STUDIES OF PARTICLE AND ATOM MANIPULATION USING FREE SPACE LIGHT BEAMS AND PHOTONIC CRYSTAL FIBRES

David Mark Gherardi

A Thesis Submitted for the Degree of PhD
at the
University of St. Andrews

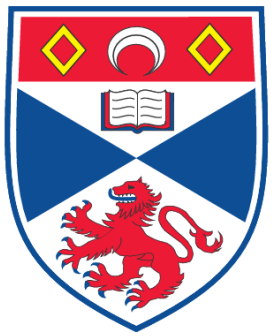

2009

STUDIES OF PARTICLE AND ATOM MANIPULATION USING FREE SPACE LIGHT BEAMS AND PHOTONIC CRYSTAL FIBRES

David Mark Gherardi

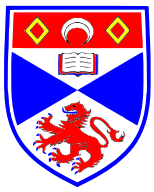

University
of
St Andrews

A thesis submitted to the
University of St Andrews in
application for the degree of
Doctor of Philosophy.

August 2008

Abstract

Light can exert optical forces on matter. In the macroscopic world these forces are minuscule, but on the microscopic or atomic scale, these forces are large enough to trap and manipulate particles. They may even be used to cool atoms to a fraction of a degree above absolute zero.

This thesis details a number of experiments concerned with the optical manipulation of atoms and micron-size particles using free space light beams and photonic crystal fibres.

Two atom guiding experiments are described. In the first experiment, a spatial light modulator is used to generate higher blue-detuned azimuthal Laguerre-Gaussian (LG) beams, which are annular beams with a hollow core. These LG beams are then used to guide laser cooled rubidium-85 atoms within the dark core over a distance of $30\ \mathrm{mm}$. The second atom guiding experiment involves attempting to guide laser cooled and thermal rubidium atoms through a hollow-core photonic crystal fibre using red-detuned light. Hollow-core photonic crystal fibres are fibres that are able to guide light with low attenuation within a hollow core. For this experiment a hot wire detection system was designed, along with a number of complex vacuum systems.

The first dual-beam fibre trap for micron-size particles constructed using endlessly single-mode photonic crystal fibre (ESM-PCF) is described. The characteristics of dual beam fibre traps are governed by the fibres used. As ESM-PCF has considerably different properties in comparison to conventional single- or multimode fibres, this dual beam ESM-PCF trap exhibits some novel characteristics. I show that the dual beam ESM-PCF trap can form trapping, repulsive and line potentials; an interference-free ‘white light’ trap; and a dual-wavelength optical conveyor belt.

DECLARATIONS

I, David Mark Gherardi, hereby certify that this thesis, which is approximately 50,000 words in length, has been written by me, that it is the record of work carried out by me and that it has not been submitted in any previous application for a higher degree.

date signature of candidate

I was admitted as a research student in January 2004 and as a candidate for the degree of Doctor of Philosophy in June 2005; the higher study for which this is a record was carried out in the University of St Andrews between 2004 and 2008.

date signature of candidate

I hereby certify that the candidate has fulfilled the conditions of the Resolution and Regulations appropriate for the degree of Doctor of Philosophy in the University of St Andrews and that the candidate is qualified to submit this thesis in application for that degree.

date signature of supervisor

In submitting this thesis to the University of St Andrews we understand that we are giving permission for it to be made available for use in accordance with the regulations of the University Library for the time being in force, subject to any copyright vested in the work not being affected thereby. We also understand that the title and the abstract will be published, and that a copy of the work may be made and supplied to any bona fide library or research worker, that my thesis will be electronically accessible for personal or research use unless exempt by award

of an embargo as requested below, and that the library has the right to migrate my thesis into new electronic forms as required to ensure continued access to the thesis. We have obtained any third-party copyright permissions that may be required in order to allow such access and migration, or have requested the appropriate embargo below.

The following is an agreed request by candidate and supervisor regarding the electronic publication of this thesis:

Access to Printed copy and electronic publication of thesis through the University of St Andrews.

date signature of candidate

date signature of supervisor

PUBLICATIONS AND PRESENTATIONS

Journal publications

D. P. Rhodes, D. M. Gherardi, J. Livesey, D. McGloin, H. Melville, T. Freegarde and K. Dholakia, "Atom guiding along high order Laguerre-Gaussian light beams formed by spatial light modulation," Journal of Modern Optics 53(4), 547556 (2006).

D. M. Gherardi, A. E. Carruthers, T. Čižmár, E. M. Wright, and K. Dholakia, "A dual beam photonic crystal fiber trap for microscopic particles," Applied Physics Letters 93, 041110 (2008).

Conference papers

D. M. Gherardi, A. E. Carruthers, T. Čižmár, R. F. Marchington and K. Dholakia, "Novel dual beam fiber traps using endlessly single mode photonic crystal fiber," (Optical Trapping and Optical Micromanipulation V) Optics + Photonics 2008, San Diego, United States, 2008. Presented by T. Čižmár.

Poster presentations

D. P. Rhodes, J. Livesey, D. McGloin, H. Melville, D. M. Gherardi, T. Freegarde and K. Dholakia, "Atom guiding along dynamically generated Laguerre-Gaussian light beams," UK Cold Atom Network conference, St Andrews, 2004.

D. M. Gherardi, D. P. Rhodes, J. G. Livesey, H. Melville, D. McGloin, D. Cassettari, K. Dholakia, J. C. Knight, F. Benabid, P. St. J. Russell and T. Freegarde, "Optical guiding using holographically generated Laguerre-Gaussian light beams and hollow core photonic crystal fibres," 17th International Conference on Laser Spectroscopy, Cairngorms National Park, 2005.

D. M. Gherardi, D. P. Rhodes, J. G. Livesey, H. Melville, D. McGloin, D. Cassettari, K. Dholakia, J. C. Knight, F. Benabid, P. St. J. Russell and T. Freegarde,

“Optical guiding using holographically generated Laguerre-Gaussian light beams and hollow core photonic crystal fibres,” QuAMP, Open University, 2005.

ACKNOWLEDGEMENTS

I hope you are sitting comfortably, as this is a long list...

My first thanks must go to my supervisor Kishan Dholakia. I owe Kishan a great debt for giving me the chance to do this PhD. Without Kishan's hard work, guidance and support this thesis would not have been possible. Cheers Kishan, I really appreciate all the effort that went into this.

Thanks must also go to my second supervisor, Donatella Cassettari, who was always on hand to answer any weird questions that I had. I'm looking forward to reading the first, of what will be many, papers from Graham, Lara, Giuseppe and Donatella. I'm sure that they are happy in the knowledge that I will never borrow anything from their lab again.

I am particularly indebted to those I have worked with in the lab: Daniel, John, Tom, Toni and Rob. In truth, having good lab mates is the secret of success for a PhD student and I am eternally grateful. Thanks for putting up with my idiosyncrasies.

I have been lucky to have worked in such an amazing group over the past four years. The many 'characters' have made life (in the lab and in the real world) that little bit more interesting: Steve L., Klaus, Graham, Dan B., Dan R., Michael S., David McG., Patience, Xanthi, Vene, Peter, Hannah, Ryan, David S., David C., Mike MacD., Maria, Joerg, Michael M., Lani, Nan, Janelle, Igor, Lynn, Carlos, Jill and Kozo. With a group that large its inevitable that I will have left somebody out; I apologise.

From our invaluable and talented glass blower, Fritz Akerboom, to the ever patient guys in the workshop, there were many people in the department who have been the solutions to a never ending stream of problems (aka a PhD). Without detailing what everybody did, I'll try to name them all: Steve Balfour, George Robb, Jimmy Lindsay, Mark Ross, Chris Booth, Scott Johnston, Aly Gillies, John Jardine, Paul Donaldson, Les Kirk and Mike Robertson. Thanks guys.

Cheers to my flatmates Phil and Alex, and the wardennial team at New Hall,

for giving me a life outside of the lab. Again, thanks for putting up with my idiosyncrasies.

I am also thankful for the time and effort that my examiners, Animesh Jha and Wilson Sibbett, put into the *viva voce* examination. Their suggestions and corrections for this thesis were gratefully received.

It seems almost inappropriate to try and thank my Mum and Dad in only a few sentences. The help that they've given me in this time can only be a fraction of what they've done for me during my life. So all I can really say is thanks for the last 28 and a bit years![1]

Finally thanks to my girlfriend Róisín. Róisín, this PhD belongs to you as much as it does to me. You've been with me through the whole experience and I truly couldn't have done this without you. Thank you.

[1] And also that I will definitely get a real job now.

Contents

1 INTRODUCTION **1**
1.1 Moving matter with light 1
1.2 Scope of thesis 2
1.3 Structure of thesis 4

2 LASER COOLING, TRAPPING AND GUIDING OF ATOMIC RUBIDIUM **6**
2.1 Chapter synopsis 6
2.2 Optical forces: an atom's perspective 6
2.2.1 The scattering force 7
2.2.2 The dipole force 10
2.3 Laser cooling and trapping 12
2.3.1 Concept of temperature 12
2.3.2 The slowing of an atomic beam 13
2.3.3 Doppler cooling and optical molasses 14
2.3.4 The magneto-optical trap 18
2.3.5 Optical dipole traps and guides 22
2.3.6 Heating effects in dipole traps and guides as a result of scattering 24

3 LASER, SPECTROSCOPY AND VACUUM SYSTEMS **27**
3.1 Chapter synopsis 27
3.2 Laser and spectroscopy systems 28
3.2.1 Spectral requirements of a rubidium-85 MOT 28
3.2.2 Cooling and Re-pump lasers 29

3.2.3 Homebuilt ECDLs 30
3.2.4 Doppler-free saturated absorption spectrsocsopy 33
3.2.5 Laser locking 36
3.2.6 Injection locking of diode laser 38
3.2.7 Tui TA-100 laser system 38
3.2.8 Ti:sapphire guide beam 40
3.3 Vacuum systems 41
3.3.1 Materials 41
3.3.2 Cleaning of vacuum components 42
3.3.3 Rubidium source 42
3.3.4 Bake-out 43
3.4 Conclusion and author's contribution 44

4 GUIDING OF ATOMS IN LG BEAMS GENERATED USING A SPATIAL LIGHT MODULATOR 45
4.1 Chapter synopsis 45
4.2 Motivation for experiment 45
4.3 Laguerre-Gaussian beams 47
4.3.1 Properties of Laguerre-Gaussian beams 47
4.3.2 Methods of generating Laguerre-Gaussian beams 52
4.4 Generation of LG beams using a phase modulating spatial light modulator 55
4.4.1 Introduction to spatial light modulators 55
4.4.2 Hamamatsu x8267 SLM 56
4.4.3 Calculation of the LG phase hologram 57
4.4.4 Experimental considerations 59
4.5 Experimental Design 61
4.5.1 Experimental aims 61
4.5.2 Chosen LG beam parameters 61
4.5.3 Vacuum Chamber 63
4.5.4 Anti-Helmholtz magnetic coils 63
4.5.5 MOT laser systems and optics 64
4.5.6 Guide beam 65

4.5.7 Mechanical Shutters 67
4.5.8 Fluorescent detection of guided atoms using photon multiplier tube 68
4.6 Experimental procedure 69
4.6.1 Forming the MOT 69
4.6.2 Adjusting the guide beam 69
4.6.3 Obtaining a data set 70
4.7 Results 70
4.7.1 Overview 70
4.7.2 Dropped cloud discrepancy 71
4.7.3 Guided data 72
4.8 Conclusion 74
4.9 Author's contribution 75

5 DESIGN OF A HOT WIRE DETECTOR AND VACUUM SYSTEM FOR FIBRE GUIDING OF RUBIDIUM ATOMS 76
5.1 Chapter synopsis 76
5.2 Motivation 77
5.3 Introduction to hot wire detectors 79
5.3.1 Ionisation potential 80
5.3.2 Residence time 81
5.4 Choice of hot wire material 81
5.4.1 Rhenium 83
5.4.2 Platinum 84
5.4.3 Tungsten 85
5.5 Channel Electron Multiplier 86
5.5.1 Efficiency of CEMs 88
5.5.2 Counting limits and damage threshold 89
5.5.3 Temperature of rhenium hot wire 91
5.6 Vacuum system: Introduction and concept 93
5.7 Design of hot wire mount and detection chamber 94
5.7.1 Requirements 94
5.7.2 Design 95

5.7.3 CEM Orientation and electrical feedthrough 97
5.7.4 Initial tests 100
5.8 Design of the source chambers 101
5.8.1 Design of single ion pump vacuum system 101
5.8.2 Design of dual pump vacuum system 103
5.8.3 Attaching the glass cell 104
5.9 Conclusion 105
5.10 Author's contribution 108

6 GUIDING OF ATOMS THROUGH HOLLOW-CORE PHOTONIC BAND GAP FIBRE 109

6.1 Chapter synopsis 109
6.2 Introduction and motivation 109
6.3 History of fibre guiding experiments carried out within group . . . 112
6.4 Hollow-core photonic band gap fibres 114
6.4.1 Introduction to HC-PBG fibres. 114
6.4.2 Fibre details 115
6.4.3 Fibre coupling and the effect of higher order modes. . . . 116
6.4.4 Optical potential within fibre 119
6.5 First attempt at vapour guiding 119
6.5.1 Aim 119
6.5.2 Experimental set-up 120
6.5.3 Experimental procedure 120
6.5.4 Results and discussion 122
6.6 Attempt at cold atom guiding 124
6.6.1 Aim 124
6.6.2 Experimental set-up 124
6.6.3 Experimental procedure 126
6.6.4 Results and discussion 128
6.7 Second attempt at vapour guiding 128
6.7.1 Aim 128
6.7.2 Experimental set-up 129
6.7.3 Experimental procedure 129

6.7.4 Results and discussion 130
6.8 Conclusions and discussion 130
6.9 Author's contribution 131

7 CHARACTERISATION OF ENDLESSLY SINGLE MODE PHOTONIC CRYSTAL FIBRES 132
7.1 Chapter synopsis 132
7.2 Motivation 133
7.3 Introduction to endlessly single-mode photonic crsytal fibre 133
7.4 Principle of operation 134
7.4.1 V number for index guiding photonic crystal fibres 134
7.4.2 Origin of the endlessly single-mode characteristic 135
7.5 Characteristics of ESM-PCF 138
7.5.1 Mode profile of ESM-PCF 138
7.5.2 Single-mode nature of ESM-PCF 140
7.5.3 Bend losses in ESM-PCF 141
7.6 Experimental characterisation 142
7.6.1 Fibres characterised 142
7.6.2 Light sources used 142
7.6.3 Fibre coupling 144
7.6.4 Testing single mode operation 146
7.6.5 Obtaining mode profiles 147
7.6.6 Characterisation of LMA-35 using 780 nm laser 148
7.6.7 Characterisation of LMA-25 fibre using 780 nm and 1070 nm lasers 149
7.6.8 Characterisation of LMA-25 and LMA-10 using supercontinuum radiation 150
7.7 Conclusion 151
7.8 Author's contribution 154

8 DUAL BEAM ENDLESSLY SINGLE-MODE PHOTONIC CRYSTAL FIBRE TRAPS 155
8.1 Chapter synopsis 155

8.2 Introduction to dual beam fibre traps and motivation to use ESM-PCF . . . 156
8.3 Nature of the axial restoring force in dual beam conventional fibre traps and dual beam ESM-PCF traps . . . 160
8.3.1 Analytical analysis of axial forces in dual beam conventional fibre traps . . . 160
8.3.2 Numerical analysis of axial forces in dual beam ESM-PCF traps . . . 164
8.4 Experimental design . . . 166
8.4.1 Requirements . . . 166
8.4.2 Isolation of fibres from the liquid sample . . . 167
8.4.3 Fibre alignment . . . 170
8.4.4 Imaging and data capture . . . 173
8.4.5 Methods for experimental calculation of the axial spring constant . . . 175
8.5 Single wavelength dual beam ESM-PCF trap . . . 178
8.5.1 Aim . . . 178
8.5.2 Experimental construction . . . 178
8.5.3 Trap stiffness . . . 180
8.5.4 Chains of particles . . . 183
8.6 Dual beam ESM-PCF trap using a supercontinuum source . . . 184
8.6.1 Aim . . . 184
8.6.2 Spectrum and coherence length of supercontinuum . . . 185
8.6.3 Experimental set-up . . . 186
8.6.4 Successful removal of interference effects . . . 187
8.7 Dual wavelength optical conveyor belt using dual beam ESM-PCF trap . . . 189
8.7.1 Aim . . . 189
8.7.2 Optical forces acting on a nanoparticle in standing wave . 189
8.7.3 Experimental set-up . . . 190
8.7.4 Results . . . 193
8.8 Conclusion . . . 193
8.9 Author's contribution . . . 194

9 OVERVIEW OF THESIS 195
9.1 Review 195
9.2 Suggested further work 198
9.2.1 HC-PBG fibre guiding experiments 198
9.2.2 Suggested applications of dual beam PCF traps in biophotonics 199

For Maureen and Granda.

Chapter 1

INTRODUCTION

1.1 Moving matter with light

The hypothesis that light can exert a force on matter was first suggested by Johannes Kepler in the 1600s [1], theoretically explained by James Clerk Maxwell in 1873 [2], and confirmed experimentally by both P. N. Lebedev in 1900 [3], and E. F. Nichols and G. F. Hull in 1901 [4]. However it was not until 1960 and the invention of the laser, that the magnitude of optical forces became sufficiently large for the controlled optical manipulation of matter to become feasible. Pioneering work by Arthur Ashkin and co-workers [5], demonstrated the optical manipulation of micron size particles using a laser, and showed that two optical forces existed; the scattering force and the gradient force. For micron size particles, the scattering force is caused by the absorption or reflection of the light by the particle, and is directed in the opposite direction to the momentum vector of the incident light. The gradient force on the other hand, arises due to the re-direction of light by the particle due to refraction. Ashkin and co-workers showed that these forces could be used to trap micron size particles using different techniques such as the counterpropagating dual beam trap [5], the optical levitator [6] and the single-beam optical tweezers [7].

Over the subsequent years, many advanced techniques have been developed. For

example, multiple particles may now be trapped and positioned in individually controllable trap sites generated using spatial light modulators [8] or acousto-optic deflectors [9]. However the basic trapping geometries demonstrated by Ashkin are still proving to be powerful tools today.

The optical forces used to manipulate micron size particles also have direct equivalents for atoms and have been used with great success to manipulate and cool numerous atomic species. Arguably the most important achievements to stem from Ashkin's initial work, were the development of laser cooling and trapping techniques, such as optical molasses [10], magneto-optical traps [11] and dipole traps [12]. The importance of these developments was emphasised by the award of the Nobel Prize in Physics in 1997 to Steven Chu, Claude Cohen-Tannoudji and William D. Phillips "for development of methods to cool and trap atoms with laser light"; and the Nobel Prize in Physics in 2001 to Eric A. Cornell, W. Ketterle and Carl E. Wieman for "for the achievement of Bose-Einstein condensation in dilute gases of alkali atoms, and for early fundamental studies of the properties of the condensates," achievements [13, 14] only made possible by laser cooling techniques.

1.2 Scope of thesis

This thesis details studies of particle and atom manipulation using free space light beams and photonic crystal fibres. The work presented in this thesis can be split into two parts.

The first part concentrates on two atom guiding experiments using optical guides. Optical atom guides generally fall into one of two categories: free space guides and fibre guides.

Free space guides are guides formed from a beam propagating in free space. In its simplest form, a free-space guide will consist of a Gaussian beam, with a frequency red-detuned[1] from atomic resonance [15]. However it is possible to

[1]For a red-detuned beam, an atom will be attracted to region of peak intensity, whereas for a blue-detuned beam an atom will be repelled from the region of peak intensity.

create more complicated free-space guides [16]. In the first experiment of this thesis, I use a spatial light modulator to generate blue-detuned high azimuthal order Laguerre-Gaussian (LG) beams, which are annular beams with hollow cores. Cold atoms within the core of these hollow blue-detuned beams will be repelled from the walls. The SLM allows us to easily change the azimuthal order of the beams and perform the first comparative study of the guiding properties of different azimuthal order LG beams.

Fibre guides are guides formed within hollow core fibres. Due to the need for a hollow core, previous experiments were limited to using hollow-core capillary fibres. These capillary fibres can be used in either a red-detuned [17] or a blue-detuned [18] guiding scheme. For the blue-detuned guiding scheme, the light is coupled into the silica annulus surrounding the core, and confined to the annulus by total internal reflection. A blue-detuned evanescent field, formed at the inner walls of the capillary, would then repel the atoms from the wall of the fibre. However, hollow-core capillary fibres are not so well suited to red-detuned guiding. As the core has a lower refractive index than the silica annulus, light is only confined to the core by weak Fresnel reflections, as total internal reflection is impossible. Consequently, the guided 'mode' suffers high attenuation rates, thus limiting the effectiveness of the guide. However, the recently developed hollow-core photonic band gap (HC-PBG) fibres are able to guide light within a hollow core, by means of a photonic band gap existing in a crystal cladding surrounding the core. The second experiment of the thesis attempts to guide rubidium atoms through these HC-PBG fibres.

The second part of this thesis details the development of a novel dual beam fibre trap. The dual beam fibre trap is an evolution of Ashkin's original counterpropagating dual beam trap geometry. Created by Constable and co-workers [19], the dual beam fibre trap extends Ashkin's original counterpropagating dual beam trap configuration [5], by delivering the beams using single-mode optical fibres. I develop the versatility of this technique again by delivering the beams using endlessly single-mode photonic crystal fibres (ESM-PCF). ESM-PCF has vastly different characteristics in comparison to conventional fibres, in that it can guide any wavelength of light in a single mode in core diameters commercially available

up to $35\,\mu\mathrm{m}$. The novel characteristics of these fibres allow us to create dual beam fibre traps with unique characteristics.

1.3 Structure of thesis

Following this introductory chapter, the thesis is structured as follows.

Chapter two describes the origin of optical forces as experienced by atoms. Doppler cooling and its application to optical molasses is discussed. The magneto-optical trap is described. The dipole force and its use in the trapping and guiding of atoms is explained, along with the role of the heating effects within dipole traps and guides.

Chapter three details the laser, spectroscopy and vacuum systems that are common to the rubidium-85 atom guiding experiments detailed in chapters 4 and 6. These systems include a homebuilt extended cavity diode laser, a master-slave laser system, a Doppler-free saturated absorption spectroscopy set-up and a Ti:sapphire laser. Vacuum techniques and procedures common to the atom guiding experiments are also detailed.

Chapter four details an experiment studying the properties of LG beams (annular modes with a dark core) when used for blue-detuned atom guiding. The theory of Laguerre-Gaussian beams and how they are generated using a phase modulating spatial light modulator is discussed. The experimental set-up, procedure and results are presented.

Chapters five and six are concerned with efforts to guide both thermal and cold rubidium through hollow-core photonic band gap fibres. Chapter five details the development of a rhenium hot wire detector, designed to detect the guided atoms. Three different metals are considered for the hot wire, with rhenium being chosen. The design of the hot wire detector is detailed. Two vacuum systems are constructed in order to guide cold and/or thermal atoms through hollow-core fibre.

Chapter six details discusses the procedure and results of the three experiments

aimed at guiding both thermal and cold rubidium atoms through hollow-core photonic band gap fibres.

Chapter seven and eight are concerned with the development of a dual beam fibre trap constructed from endlessly single-mode photonic crystal fibre (ESM-PCF). Chapter seven details the experimental characterisation of a number of ESM-PCFs. These fibres were characterised prior to their use in the novel dual-beam fibre traps described in chapter eight. The coupling and single-mode properties of the fibres are examined. Chapter eight details investigations into the properties of endlessly single-mode photonic crystal fibre when used in dual beam fibre traps.

Chapter nine provides a short summary and conclusion of the thesis.

Chapter 2

LASER COOLING, TRAPPING AND GUIDING OF ATOMIC RUBIDIUM

2.1 Chapter synopsis

This chapter explains the manifestation of optical forces on atoms. This is discussed with relevance to the laser cooling and trapping of rubidium-85; these techniques are used in the atom guiding experiments described in chapters 4 and 6. The chapter begins with an explanation of the scattering and dipole forces. I explain how the scattering force can be used to slow atomic beams using a Zeeman slower; to cool atoms in an optical molasses; and to cool and trap atoms within a magneto-optical trap. The remainder of the chapter examines how the dipole force can be used to trap and guide atoms and the influence of heating effects within these traps and guides.

2.2 Optical forces: an atom's perspective

There are two optical forces; the scattering force and the dipole force. While the scattering force will tend to accelerate an atom in the direction of the absorbed photons, the dipole force will either attract or repel the atom away from regions of

high intensity in the optical field. The scattering force is exploited for the cooling of atoms, as described section 2.3.3, but can also cause unwanted heating in optical guides, which primarily exploit the dipole force. In addition to optical forces, atoms can also be manipulated and cooled using magnetic forces. Details of these magnetic forces, which are not used in thesis, can be found in reference [20].

2.2.1 The scattering force

Albert Einstein introduced the idea that light could be thought of as consisting of discrete quanta [21], termed photons, and went on to show that each photon had a momentum p given by,

$$p = \frac{h\nu}{c} = \hbar k \tag{2.1}$$

where h is Planck's constant; ν and c are the frequency and the velocity of the light respectively; $\hbar = h/2\pi$ is the Dirac constant; and $k = 2\pi/\lambda$ is the wave vector of the incident light.

By considering this quantum mechanical view of light and the law of conservation of momentum, it is easy to imagine how radiation pressure manifests itself after the scattering of a resonant photon. On the absorption of a resonant photon, the momentum of an atom will change by a value equal to the momentum of the absorbed photon. As a result, the velocity of an atom of mass m will change by a value equal to $\hbar k/m$. As the atom is now in an unstable excited state, it will emit a photon by way of a spontaneous emission when the atom returns to the ground state. This results in the atom undergoing another change in velocity, this time in the opposite direction to the emitted photon's velocity. This viewpoint is only correct if the intensity of light is low enough so that the probability of spontaneous emission is higher than the probability of stimulated emission.

The direction of the photon emitted by spontaneous emission is dictated by a symmetric probability distribution [1]. As a consequence, as the atom goes through a number of absorption/spontaneous emission cycles, the net change in momentum

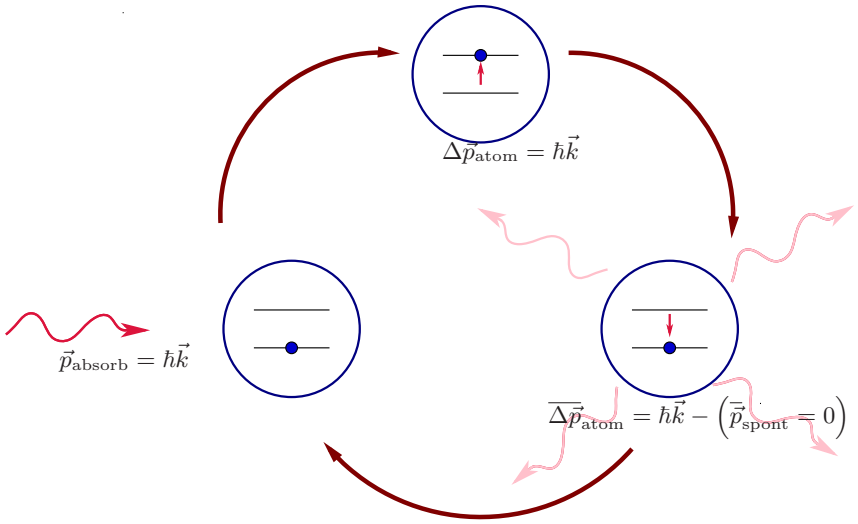

Figure 2.1: Graphical representation of the cooling cycle. On absorbing a resonant photon, the atom gains the momentum $\vec{p}_{\text{absorb}}$ of the photon. The atom then de-excites, recoiling with momentum opposite to the momentum of the emitted photon, $\vec{p}_{\text{spont}}$. As the direction of the emitted photon is dictated by a symmetric probability distribution, averaged over many cycles the average change in momentum of the atom per absorption is $\overline{\Delta\vec{p}}_{\text{atom}} = \vec{p}_{\text{absorb}} = \hbar\vec{k}$.

due to absorption, which is always in the same direction, accumulates, whereas the net change of momentum due to spontaneous emission averages to zero [1].

This cycle, represented in figure 2.1, is known as the cooling cycle as it is fundamental to the process of laser cooling, as described in section 2.3.3.

Taking rubidium-85 as our example, each absorption/spontaneous emission cycle will change the velocity of the atom by an average of $6 \times 10^{-3}\ \mathrm{m \cdot s^{-1}}$ in the direction opposite to the propagation of the beam.

The scattering rate γ_p for a two-level atom in an optical field is given by [22],

$$\gamma_p = \frac{s_0\gamma/2}{1 + s_0 + \left[2\left(\delta + \omega_D\right)/\gamma\right]^2} \tag{2.2}$$

where $\delta \equiv \omega_l - \omega_a$ is the detuning of the laser frequency ω_l from the atomic resonance ωa; $\gamma = 1/\tau$ is the angular frequency corresponding to the spontaneous

decay rate of the excited state; $\omega_D = -\vec{k} \cdot \vec{v}$ is the Doppler shift experienced by the moving atoms at velocity $\vec{v}$, where $k = 2\pi/\lambda$; and $s_0 = I/I_s$ is the ratio of the light intensity I to the saturation intensity I_s of the atomic transition, where $I_s \equiv \pi hc/3\lambda^3\tau$. The saturation intensity is the resonant intensity that results in half the maximum resonant scattering rate.

The transition of rubidium-85, $5^2\mathrm{S}_{1/2} - 5^2\mathrm{P}_{3/2}$, that is used for laser cooling has $\lambda = 780.24\ \mathrm{nm}$ and $\tau = 26.63 \times 10^{-9}\ \mathrm{s}^{-1}$ yielding an $I_s = 16.4\ \mathrm{W \cdot m^{-2}}$. This results in a scattering rate $\sim 10^7\ \mathrm{s}^{-1}$ for resonant laser light with intensity $\sim I_s$ (an intensity readily achieved by diode lasers). The maximum scattering rate is equal to $\gamma/2$, which in this case is $1.88 \times 10^7\ \mathrm{s}^{-1}$

Therefore in order to slow a thermal beam of rubidium-85 from $400\ \mathrm{m \cdot s^{-1}}$ to a stop, the atom must undergo $\sim 66,482$ scattering events. For the case of our thermal beam of rubidium, a resonant scattering rate of $10^7\,\mathrm{s}^{-1}$ would result in the beam being stopped in $6.6 \times 10^{-3}\ \mathrm{s}$.

The scattering force $\vec{F}$ and resultant acceleration $\vec{a}$ on an atom is given by,

$$F = \frac{dp}{dt} = \hbar k \gamma_p \tag{2.3}$$

$$\therefore a = \frac{F}{M} = \frac{\hbar k \gamma_p}{M}. \tag{2.4}$$

The scattering rate of $10^7\ \mathrm{s}^{-1}$ would therefore result in force of $8.5 \times 10^{-21}\ \mathrm{N}$ in the opposite direction to the beam of light. Although this may seem minuscule, it translates to the large acceleration of $6.02 \times 10^4\ \mathrm{m \cdot s^{-2}}$.

In the examples above, we have assumed that there is always an intensity $I = I_s$ of photons resonant with the atomic transition. Although this viewpoint simplifies the concept, it is experimentally non-trivial as the Doppler shift will shift the atoms out of resonance with the laser beam, as the atoms are slowed, resulting in lower scattering rates. However, the Doppler shift can be compensated for and this topic is examined in section 2.3.2.

It is worth noting at this stage that the dependency of the scattering rate and there-

fore the force, on both the velocity of the atoms and the laser detuning, see equation 2.2, is vital for the laser cooling of atoms, as described in section 2.3.3. Despite its use in laser cooling, unwanted scattering will however result in unwanted heating effects in the dipole guides and traps, as discussed in section 2.3.6.

2.2.2 The dipole force

In the presence of an electromagnetic field, the atomic energy levels of an atom become shifted, see figure 2.2. This is known as the AC-stark effect. In a two-level system the shifted energies of the ground state E_g and excited state E_e are given by [23],

$$\Delta E_g = \frac{\hbar}{2}\left(-\delta + \Omega'\right) \tag{2.5}$$

and

$$\Delta E_e = \frac{\hbar}{2}\left(-\delta - \Omega'\right), \tag{2.6}$$

where $\Omega' \equiv \sqrt{\Omega^2 + \delta^2}$ is the generalised Rabi frequency for off-resonant light with Ω being the Rabi frequency.

In the limit $\Omega \ll |\delta|$, which is applicable in the majority of atom guiding experiments where the laser is detuned from resonance to reduce the effects heating, the shifted energies are given by [23],

$$\Delta E_g = \frac{\hbar\Omega^2}{4\delta} \tag{2.7}$$

and

$$\Delta E_e = -\frac{\hbar\Omega^2}{4\delta}. \tag{2.8}$$

Therefore, shift of the energy levels acts to create a potential, termed the dipole

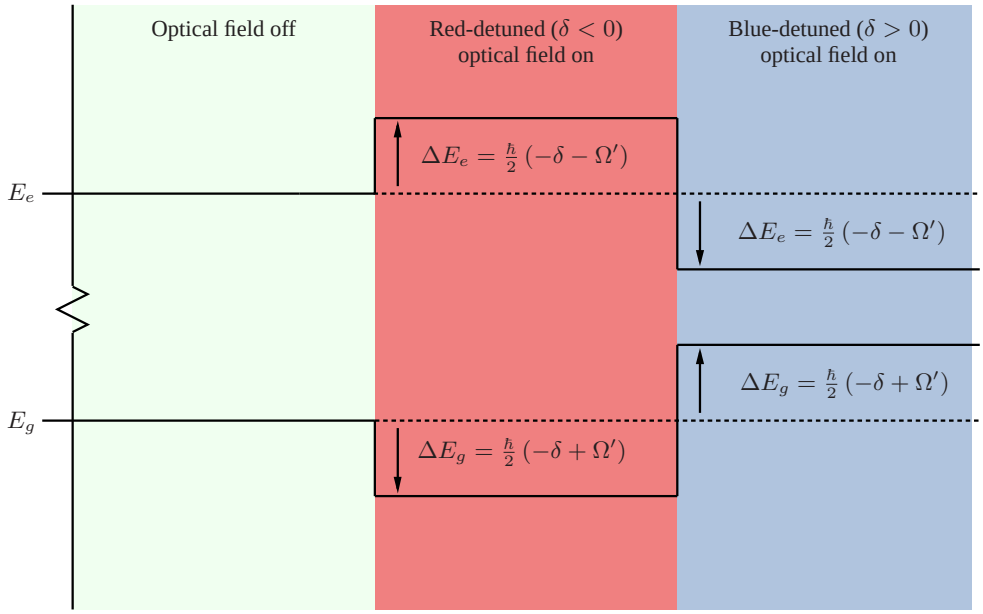

Figure 2.2: Shifting of energy levels in two-level atom due to AC-Stark shift. For the energy of ground state atom, will decrease in a red-detuned optical field and increase in a blue-detuned optical field. The opposite is true for an atom in the excited state.

potential U_{dipole}, equal to the shift on the particular atomic state. Given that $\Omega^2 = \gamma^2 I/2I_s$, the dipole potential for the ground state as a function of intensity I is given by [23],

$$U_{\text{dipole}} \simeq \frac{\hbar\Omega^2}{4\delta} = \frac{\hbar\gamma^2 I}{8\delta I_s}. \tag{2.9}$$

In an inhomogeneous field, and in the limits $\Omega \ll |\delta|$ and $\gamma \ll |\delta|$ the atom will therefore experience a force F_{dipole} given by [22],

$$\vec{F}_{\text{dipole}} = -\vec{\nabla}U_{\text{dipole}} \simeq -\frac{\hbar\gamma^2}{8\delta I_s}\vec{\nabla}I. \tag{2.10}$$

2.3 Laser cooling and trapping

2.3.1 Concept of temperature

Before introducing the techniques of laser cooling, it is important to clarify the term 'temperature' for the case of laser cooled atoms; a dilute atomic gas, contained in a vacuum, interacting with a resonant laser field. The definition of a 'temperature' in this situation is slightly inconsistent with the strictest definition of the term. The zeroth law of thermodynamics states that 'If bodies *A* and *B* are each in thermal equilibrium with a third *T*, then they are in thermal equilibrium with another' [24]; or in other words, all three bodies are the same temperature. Laser cooling relies on the scattering of resonant photons, so the atoms are constantly absorbing and scattering photons from the light field. Although these atoms are in an equilibrium state, it is wrong to consider them to be in thermal equilibrium with any other body, therefore technically forbidding us from assigning them a temperature [23]. Nevertheless, despite violating the strict definition, a meaningful temperature can be assigned to laser cooled atoms.

The velocity distribution of atoms within an optical molasses or a magneto-optical trap is accurately described by a Maxwell-Boltzmann distribution and as a consequence we can use equations from kinetic gas theory. From the kinetic theory of gases, we can assign a temperature T to an ensemble of atoms with an RMS velocity $\tilde{v}$ and an average kinetic energy $\langle E_k \rangle$. In n degrees of freedom this temperature is given by,

$$\langle E_k \rangle = \frac{1}{2} m \tilde{v}^2 = \frac{n}{2} k_B T \tag{2.11}$$

$$\therefore\ T = \frac{m\tilde{v}^2}{n k_B} \tag{2.12}$$

where k_B is the Boltzmann constant.

This definition of temperature is not only used to used to describe the kinetic energy of the cooled atoms, but also to describe the potential energy depth of the

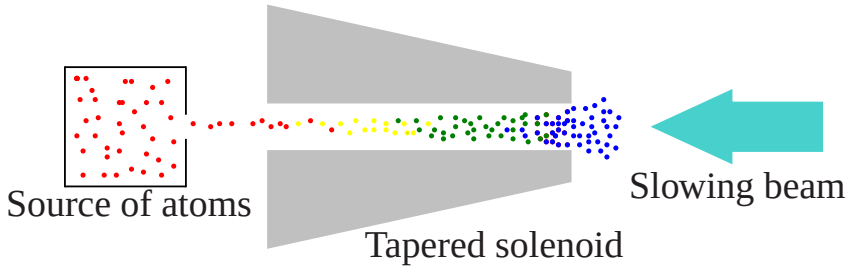

Figure 2.3: Basic schematic of the Zeeman slower. The change in colour from red to blue indicates the slowing of the atoms' velocities in the longitudinal direction only. Figure adapted from reference [23].

optical guides used within this thesis. This allows easy comparison of guide depth and kinetic energy of the atoms.

2.3.2 The slowing of an atomic beam

Consider the interaction of an atomic beam with a laser beam directed in the opposite direction. The atoms will only be absorbed by the photons if they are resonant with the atomic transition. As shown in equation 2.2, the scattering rate is a function of both the detuning δ and the Doppler shift ω_D of the laser beam relative to the atom. Therefore, in order for the photons to be absorbed and impart a force on atoms moving towards the laser, the laser must be red-detuned $\delta < 0$ from resonance . If we take for example a beam of thermal rubidium being produced by an oven at 568 K, the atoms will be travelling with an average velocity $\overline{v}$ of $402\ \mathrm{m{\cdot}s^{-1}}$. At this velocity the laser detuning δ that results in the maximum scattering rate, as calculated using equation 2.2, is $3.24\,\mathrm{GHz}$, which equates to a laser wavelength $\lambda_l = 780.247\ \mathrm{nm}$ and a scattering rate of $\sim 9.4 \times 10^6\ \mathrm{s^{-1}}$ for a laser intensity of I_s.

Each scattering changes the velocity by an average of $6 \times 10^{-3}\mathrm{m{\cdot}s^{-1}}$. After 30000 scattering events the velocity of the beam will have been reduced from $402\mathrm{ms}^{-1}$ to $222\,\mathrm{m{\cdot}s^{-1}}$. However, the atoms now experience a reduced Doppler shift, resulting in the laser no longer being in resonance with the transition. Consequently the scattering rate will have reduced from $\sim 9.4 \times 10^6\ \mathrm{s^{-1}}$ to $\sim 3.149 \times 10^3\ \mathrm{s^{-1}}$,

resulting in a far lower time averaged force compared to the on-resonance case. This would mean that the atoms would need to interact with the beam for a longer period of time to achieve the $\sim 66,482$ scattering events needed to stop the atoms (as discussed in section 2.2.1) and in reality a distance greater than experimentally feasible.

Consequently, some way is needed to keep the laser in resonance with the photons while the atoms are being slowed. This can be accomplished by sweeping the laser frequency, by using a broadband source or by changing the atomic transition frequency. The most effective method is to create a spatial dependency in the atomic resonance frequency by using an inhomogeneous d.c. magnetic field. The energy levels of an atom can be changed in the presence of a static magnetic field by way of the Zeeman effect. If the energy spacing between two levels changes as a result of this Zeeman shift, then it is possible, by having a spatially varying magnetic field, to introduce a spatial dependency to the atomic resonance frequency. A Zeeman slower utilises this effect by placing a tapered solenoid around the beam of atoms that are travelling towards the laser beam. The parameters of the solenoid and the frequency of the laser are chosen so that the laser is initially at resonance with the fast moving atoms at the entrance to the solenoid. As the beam moves through the solenoid, the changing magnetic field acts to compensate for the slowing of the beam, therefore keeping keeping the atoms continually in resonance with the laser as the beam is slowed, see figure 2.3.

At this point it should be noted that a Zeeman slower only slows the atoms and does not cool them. Although there is both a reduction in the mean velocity and the velocity spread of the atoms, the scattering force is only in one direction. Therefore it is impossible to achieve a narrow distribution around zero velocity (in any dimension), which is the desired result of a cooling scheme [1].

2.3.3 Doppler cooling and optical molasses

Laser cooling i.e. the narrowing of the atomic ensemble's velocity distribution around $v = 0$, is achieved in its simplest form in the technique called optical molasses. 1-Dimensional optical molasses is created using a pair of counter-

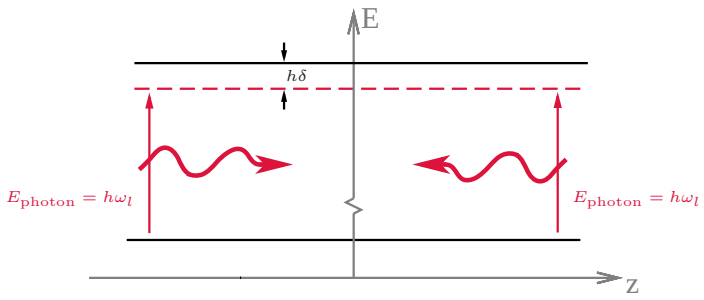

Figure 2.4: A representation of the energy levels of optical molasses. The energy levels of the atoms are shown in black, with the energies of the photons shown in red. The laser frequency is red-detuned ($\delta \equiv \omega_l - \omega_a < 0$) from the atomic resonance. As the atoms will only be preferentially scattered by photons travelling in the opposite velocity to the atom's, the atoms will be cooled. The minimum temperature achieved when $\delta = -\gamma/2$ [1].

propagating beams that are slightly red detuned from atomic resonance, see figure 2.4. For a Zeeman slower, the inhomogeneous magnetic field is required to compensate for the detrimental effects on the scattering rate as a result of the changing Doppler shift due to the slowing of the atoms. However, in optical molasses, the Doppler shift is intentionally exploited in order to generate a directional dependency in the scattering force of two counter-propagating beams. As the counter-propagating beams are red-detuned, atoms will preferentially scatter light from the beam that they are moving towards, therefore feeling a resultant force in the opposite direction to that they are moving. Consequently, the forces on the atoms act to dampen the motion in the plane of the beams, therefore cooling the atoms. This effect is known as Doppler cooling and due to the viscous nature of the force, the technique itself is known as optical molasses.

The velocity-dependent force on the atoms within optical molasses can be calculating by summing the radiation pressure forces $\vec{F}_+$ and $\vec{F}_-$ from the counter-propagating beams beams. Following on from the scattering rate equation, equation 2.2, and the resultant force equation, equation 2.4, we can calculate the forces $\vec{F}_+$ and $\vec{F}_-$ from the beams to be [23],

$$\vec{F}_{\pm} = \pm\frac{\hbar\vec{k}\gamma}{2}\frac{s_0}{1+s_0+\left[2\left(\delta \mp \left|\vec{k}\cdot\vec{v}\right|\right)/\gamma\right]^2}. \tag{2.13}$$

The sum of the forces of the two beams, $\vec{F}_{OM} = \vec{F}_{-} + \vec{F}_{+}$ gives use the total force felt by the atom. Neglecting terms of order $\left(\vec{k}\vec{v}/\gamma\right)^4$, the total force near $v = 0$ can be approximated by a linear function given by [23],

$$\vec{F}_{OM} \cong \frac{8\hbar k^2 \delta s_0 \vec{v}}{\gamma\left(1+s_0+\left(2\delta/\gamma\right)^2\right)2} \equiv \beta\vec{v}. \tag{2.14}$$

The force, $\vec{F}_{OM\delta<0}$, on atoms in the red-detuned optical molasses, where $\delta < 0$ and $\beta < 0$, is therefore,

$$\vec{F}_{OM\delta<0} \cong \beta\vec{v} = -\left|\beta\right|\vec{v}, \tag{2.15}$$

and consequently always acts to oppose the motion of the atoms.

One-dimensional (1-D) optical molasses can be used to increase the intensity of an atomic beam, as shown in figure 2.6. The atomic beam passes through one 1-D optical molasses, which cools the beam in direction transverse to the propagation direction. This results in the near collimation of the beam, as the transverse component of the velocity is now very much smaller than the velocity in the propagation direction. The beam is then focused using optical or magnetic techniques, increasing the intensity of the beam. This, however, reintroduces a velocity component in the transverse direction. A second optical molasses, situated at the focus of the beam, results in a collimated beam with is of far greater intensity than before the molasses.

In three-dimensional (3-D) optical molasses, three orthogonal pairs of counter-propagating red-detuned laser beams are used. Operating under the same principle as 1-D molasses, 3-D molasses extends the effect of Doppler cooling into 3-dimensions. It should be noted that atoms within an optical molasses are not trapped. There is no net force directing the atoms towards a trap centre and the

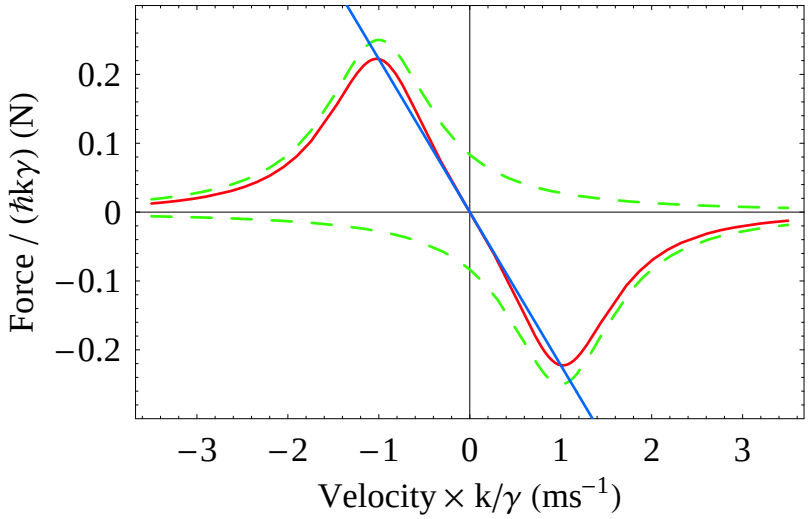

Figure 2.5: Force as a function of velocity on atoms within an optical molasses. The red curve shows the exact curve for total force $\vec{F}_{OM}$ for a $s_0 = 1$ red-detuned $\delta = -\gamma$ beam as given by equation 2.13. The green curve shows the force from each beam and the blue curve shows the linear approximation $\vec{F}_{OM\delta<0}$ for low velocities.

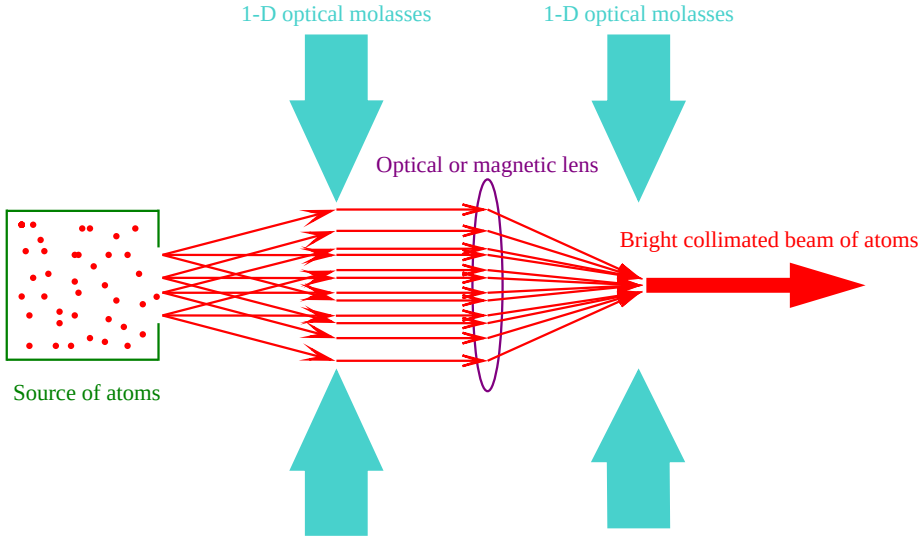

Figure 2.6: Diagram of the application of 1-D molasses to atomic beam collimation and brightening. The thermal rubidium source is collimated by the first 1-D optical molasses, focused by an optical and magnetic lens, then re-collimated by a second 1-D optical molasses. The result is a bright collimated beam of atoms with a low transverse velocity. Adapted from reference [23].

stochastic nature of the process means that there will always be a random walk; the atoms velocity will be never held at exactly zero.

The stochastic nature of the process also suggests that there should be a resultant lower limit to the temperature of the atoms as the atoms momentum can only change by integer $\hbar k$ steps and the direction of the spontaneously emitted photon is random. The minimum temperature, as suggested by this model, can be calculated by equating the viscous forces with the random heating effects. This temperature is known as the Doppler cooling limit T_D, and is given by [23],

$$T_D = \frac{\hbar\gamma}{2k_B}. \tag{2.16}$$

This limit of predicts a lower limit of $143\ \mu\mathrm{K}$ for rubidium-85, however the early optical molasses experiments measured temperatures a tenth of T_D. In order to explain these observations, it was necessary to expand the theoretical treatment from a simple two-level atom picture to the real life multi-level atom picture. This multi-level treatment resulted in the development of sub-Doppler cooling theories such as linear $\perp$ linear polarisation gradient cooling and $\sigma^+ - \sigma^-$ polarisation gradient cooling [25].

2.3.4 The magneto-optical trap

The magneto-optical trap, abbreviated as MOT, is the work-horse of the cold atom community. The MOT is able to not only cool atoms but to trap them as well, as the optical field not only acts to reduce the temperature of the atoms but also exerts a restoring force towards a trap centre. First demonstrated, with neutral sodium atoms, by Raab and co-workers in 1987 [11], a MOT is able to trap upwards of 1×10^7 atoms within regions $\sim 1\,\mathrm{mm}$ in diameter, at temperatures below $600\ \mu\mathrm{K}$ by utilising the scattering force. This is achieved, as shown in figure 2.7, through the clever use of (typically) six circularly polarised red-detuned laser beams combined with a magnetic field generated by anti-Helmholtz coils (which are coils separated by a distance equal to the radius of the coils and have currents flowing in the opposite directions) to create a spatial dependency in the scattering

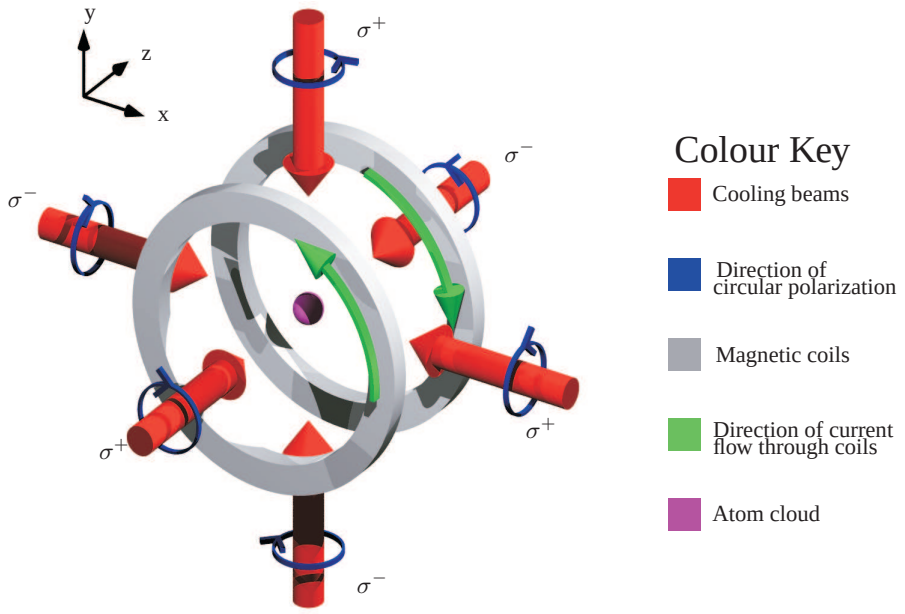

Figure 2.7: Diagram of the correct orientation of the beams and magnetic coils in a MOT. The six orthogonal beams must have the correct polarisations in order for the MOT to form. The $\sigma^{\pm}$ notation refers to the sense of rotation of the electric field around the beam axis [26]. This is different to the conventional optics notation, where circular polarisation is defined looking on to the beam. The magnetic coils are in the anti-Helmholtz configuration where they are separated by a distance equal to the radius of the coils and have currents flowing in the opposite directions.

force. Similarly to case of optical molasses, Doppler cooling also acts to create a velocity-dependent force, thereby cooling the atoms.

The position-dependent force is generated in a way similar to how the Zeeman slower compensates for the changing Doppler shift of a slowed atomic beam. The positioning of the anti-Helmholtz coils, as shown in figure 2.7, results in a magnetic field of the form,

$$B(r) = Ar, \tag{2.17}$$

where A is the magnetic field gradient, which is typically between $5\ \mathrm{G\cdot cm^{-1}} = 0.05\ \mathrm{T\cdot m^{-1}}$ and $15\ \mathrm{G\cdot cm^{-1}} = 0.15\ \mathrm{T\cdot m^{-1}}$; and r can be any plane through the

trap centre.

Figure 2.8 shows a diagram representing the energy levels of a rubidium atom in one-dimension within an anti-Helmholtz magnetic field as function of displacement from the trap centre. The energy levels of atomic transitions of the scheme, $J_g = 0 \rightarrow J_e = 1$, have three Zeeman components labelled $m = -1, m = 0, m = +1$. Placed within a magnetic field, the $m = -1$ and $m = +1$ separate by an energy proportional to the magnetic field in that region. As the $m = -1$ and $m = +1$ states have different angular momentum, and angular momentum must be conserved before and after the absorption of the photon, the two transitions will be excited by opposite circular polarisations of light.

The counter-propagating beams are adjusted to have the appropriate circular polarisations so that transition excited by the beam coming from the $+z$ is Zeeman shifted closer to resonance when displaced in the $+z$ direction and the transition of excited by the beam coming from the $-z$ direction is Zeeman shifted closer to resonance when displaced in the $-z$ direction, as illustrated in figure 2.8. An atom displaced from the centre of the trap will experience an increase in scattering force from the direction it has moved, resulting in a restoring force to trap centre. This effect, combined with the effects of Doppler cooling, results in a dense, cold and trapped cloud of atoms.

The two polarizations of the counter propagating beams are labelled as σ^+ and σ^-. This labelling refers to the sense of rotation of the electric field around the beam axis [26] and does not directly equate to the conventional optics notation of left hand and right hand polarisations. Whereas the conventional optics notation always defines circular polarisation looking towards the beam, the $\sigma^\pm$ notation defines it with regard to a certain direction. Therefore, although the counterpropagating pairs of beams are labelled with different $\sigma^\pm$ notation, they are actually the same circular polarisation as defined by optics notation. By optics notation, the pairs of beams going through the centre of the coils will be one polarisation and the remaining two pairs of beam will be the opposite polarisation, as shown in figure 2.7.

The equation describing the force an atom feels from each beam within a MOT is

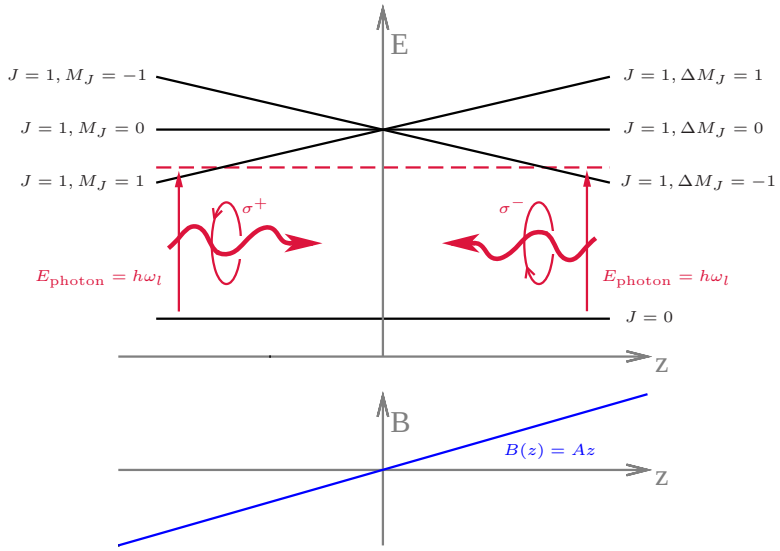

Figure 2.8: Representation of the effect of the magnetic field on the energy level of the atom, and how it affects their interaction with the cooling beams in a MOT. J refers to the total angular momentum of the atom with, with M_J being the projection of J along the three orthogonal axes [26]. The energies of the M_J levels split in the presence of the magnetic field. As the $M_J = -1$ level will absorb photons with the opposite angular momentum to those absorbed by the $M_J = 1$ levels, it is possible to generate a position-dependent force by using two beams with opposite circular polarisations.

very similar to equation 2.13 describing the force within optical molasses. In the case of the MOT, a group of terms are introduced to take account of the dependency of the force on displacement from trap centre. The force $\vec{F}_\pm$ of each beam on the atoms is given by [23],

$$\vec{F}_\pm = \pm\frac{\hbar\vec{k}\gamma}{2}\frac{s_0}{1 + s_0 + \left[2\left(\delta \mp \vec{k}\cdot\vec{v} \pm \mu' B/\hbar\right)/\gamma\right]^2}, \tag{2.18}$$

where $\mu' \equiv (g_e M_e - g_g M_g)\,\mu_B$ is the effective magnetic moment of the transition used, where $g_{g,e}$ is the Landé g-factor, $M_{g,e}$ is the magnetic quantum number and μ_B is the Bohr magneton, with the subscripts g and e refer to the ground and excited states; and B is the magnitude of the magnetic field, which for the anti-

Helmholtz coils used for a MOT is given by $B(r) = Ar$, where A is the magnetic field gradient.

In a similar way to the approximation given in equation for optical molasses, an approximate equation for the total force F_{MOT} on atoms within a MOT, valid when both the Doppler and Zeeman shift are small compared to the detuning δ of the laser, can be shown to be [23],

$$F_{MOT} = -\beta\vec{v} - \kappa\vec{r}, \tag{2.19}$$

where β is the same as in optical molasses, see equation 2.3.4, and κ is given by [23],

$$\kappa = \frac{\mu' A}{\hbar k}\beta. \tag{2.20}$$

2.3.5 Optical dipole traps and guides

By using the dipole force it is possible to create optical traps and guides. In a simplified case, a dipole trap/guide should have a larger potential depth than the temperature of the atoms intended to be trapped/guided and should minimally heat the atoms.

As stated in section 2.2.2, in the limit $\Omega \ll |\delta|$ the optical potential due to the dipole force is given by [23],

$$U_{\text{dipole}} = \frac{\hbar\Omega^2}{4\delta} = \frac{\hbar\gamma^2 I}{8\delta I_s}. \tag{2.21}$$

Given that the peak intensity I_0 of a Gaussian beam at the beam waist w_0, as a function of the power of the beam P_0, is

$$I_0 = \frac{2P_0}{\pi w_0^2}, \tag{2.22}$$

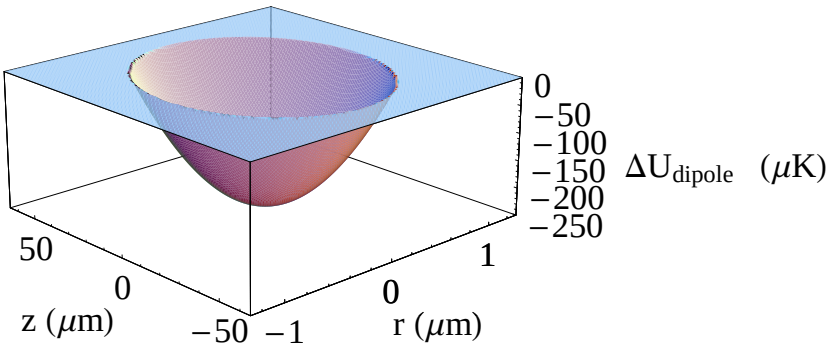

Figure 2.9: $\Delta U_{\rm dipole}$ at the focus of red-detuned Gaussian beam as a function of propagation z and transverse cross section r, for rubidium-85. Note the difference in scale of the axes. The beam parameters are $\delta = -700\,\mathrm{GHz}$, $P_0 = 10\,\mathrm{mW}$ and $w_0 = 10\,\mu\mathrm{m}$. Atoms with a temperature below $\sim 230\,\mu\mathrm{K}$ will be confined to the region of the trap shown in the picture. As $U_{\rm dipole} = -14.9\mathrm{mK}$ at the focus, hotter atoms will still be confined in the guide, albeit to a larger region than that shown in the figure.

the dipole potential $U_{\rm dipole}$ at the focus of a Gaussian beam is therefore,

$$U_{\rm dipole} = \frac{\hbar\gamma^2 P_0}{4\delta I_s \pi w_0^2} \tag{2.23}$$

More generally the dipole potential $U_{\rm dipole}\,(r,z)$ at any point of a Gaussian beam is given by,

$$U_{\rm dipole}\,(r,z) = \frac{\hbar\gamma^2 P_0}{4\delta I_s \pi w_0^2}\left(\frac{w_0}{w_0\sqrt{1+(z/z_0)^2}}\right)^2 \exp\left(\frac{-2r^2}{w_0^2\left(1+(z/z_0)^2\right)}\right), \tag{2.24}$$

where the Rayleigh range $z_0 = \pi w_0^2/\lambda$.

2.3.6 Heating effects in dipole traps and guides as a result of scattering

It is important to consider heating effects within dipole traps and guides. These heating effects fall into two categories: heating due to scattering and viscous heating effects.

Heating due to scattering

An important consideration for atoms held within an optical potential is the effect of resonant scattering. Although resonant scattering is intentionally exploited to cool and trap atoms before they are loaded into the trap, scattering acts to heat the cooled atoms once they are within the guide or trap.

For dipole traps, the momentum kick from both the absorption and spontaneous emission of photons will cause heating. As a result of the cooling cycle, the heating effect is more pronounced in the longitudinal direction, as the atoms will accumulate momentum in the direction of the beam's k vector for each absorption. We can approximate this change in momentum as a 1-D change in temperature for n scattering events, given by,

$$T = \frac{n\hbar^2 k^2}{m k_B} \tag{2.25}$$

where m is the mass of the atom, which for rubidium-85 is 1.4114×10^{-25} kg.

Although this longitudinal heating can be extremely detrimental to dipole traps, where the atom is confined in 3-D, it can be less of an issue in optical guides, where the atom is only confined in 2-D. In guide experiments, the k vector of the guide is usually in the same plane as the desired direction of motion of the atoms, so the momentum push may be exploited to accelerate or decelerate atoms through the guide.

Heating due to the spontaneous emission part of the cooling cycle can also be an issue for shallow guides. Although the spontaneous emission will be in a ran-

dom direction, and as a result the net change in momentum due to spontaneous emission for many absorption/spontaneous emission cycles will tend to zero, the magnitude of the individual recoils may be enough to impart enough energy to kick an atom out of a shallow guide. Each spontaneous emission will change the atoms temperature by $T_{\mathrm{recoil}} = \hbar^2 k^2 / m k_B$ so we can neglect spontaneous emission heating effects for guides and traps with a potential depth $U_{\mathrm{dipole}} \gg T_{\mathrm{recoil}}$.

Viscous heating

Another source of heating in the transverse direction is from an effect known as viscous heating and is explained in figure 2.10. Viscous heating results from the difference in sign of the AC-Stark shift for the ground state and the excited state. Consequently, a ground state atom will be attracted to the intensity maximum of the beam whereas an excited atom will be repelled from the intensity maximum of the beam. Therefore, if a ground state atom initially at rest at the centre of the beam is excited to an excited state, it will be then be repelled from the region of high intensity gaining kinetic energy. The atom will then undergo a spontaneous emission returning to the ground state and then be attracted to the region of high intensity again, gaining kinetic energy.

Minimising heating effects

While both the depth of the dipole trap and the scattering rate are proportional to the intensity of the light, the dependency on laser detuning is different. The scattering rate, a resonant effect, has a dependency $1/\delta^2$ while the dipole force however has a dependency of $1/\delta$. Consequently heating effects can be minimised by choosing a laser frequency far away from resonance. Neglecting any other factors, for a desired optical potential depth, it is beneficial to choose the furthest detuning δ that still yields a large enough potential well. In practice the magnitude of δ will be limited by the available power of the laser. In some cases, where a radiation pressure force may be required to push atoms along a guide, the detuning may be kept deliberately low.

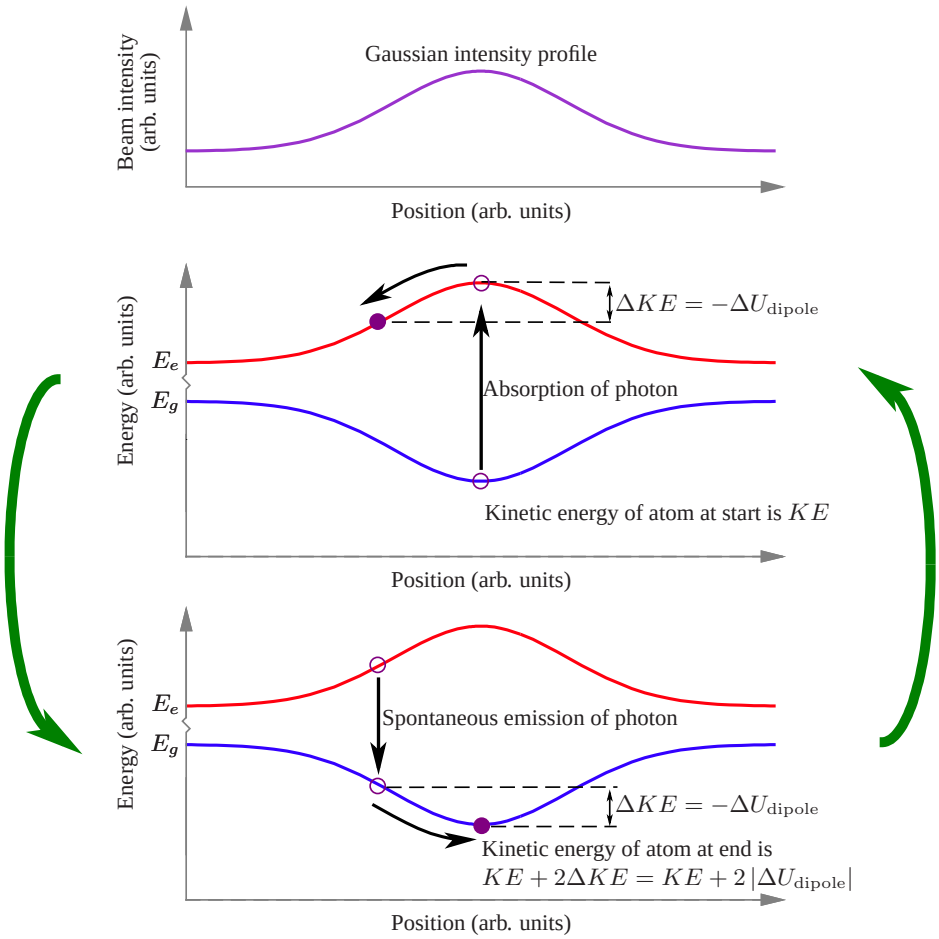

Figure 2.10: A graphical representation of viscous heating. Proportional to the intensity of light, the AC-Stark shift acts to lower the potential energy of the atom in the ground state and raise the potential energy of an atom in the excited state. The potential energy shift is given in equation 2.9. A ground state atom situated in the centre of the beam will be at the bottom of the potential well. If the atom enters an excited state by absorbing a photon, it will find itself now at the top of a potential hill. The atom will move down the hill away from the region of high optical intensity, gaining kinetic energy equal to $-\Delta U_{\text{dipole}}$, until it returns to the ground state by a spontaneous emission. Once in the ground state, the atom will roll down the potential well towards the region of high intensity. Once it reaches its original position it will have gained kinetic energy equal to $-2\Delta U_{\text{dipole}}$. In the worst case scenario, the atom will gain the full potential of the excited state as kinetic energy before decaying to the ground state and gaining the full potential of the ground state. The kinetic energy of the atom will now be twice the potential energy of the guide and will escape the guide.

Chapter 3

LASER, SPECTROSCOPY AND VACUUM SYSTEMS

3.1 Chapter synopsis

This chapter details the laser systems and vacuum procedures used as part of the atom guiding experiments described in chapters 4, 5 and 6. The extended cavity diode lasers, Doppler-free saturated absorption spectroscopy setup and frequency locking technique used to create a magneto-optical trap of rubidium-85 are described. A master-slave configuration is detailed which was used to increase the power available for the cooling transition. The Ti:sapphire laser that was used for the optical guides is detailed. I then explain briefly the vacuum requirements and how our ultra-high vacuum systems were prepared and evacuated.

3.2 Laser and spectroscopy systems

3.2.1 Spectral requirements of a rubidium-85 MOT

Rubidium-85 was used exclusively during the atomic cooling and guiding experiments carried out during this thesis. Rubidium is a common choice for such experiments due to the availability of cheap and versatile diode lasers at the wavelength needed ($780\ \mathrm{nm}$). Naturally occurring rubidium is composed of two isotopes, rubidium-85 and rubidium-87. Although the cooling of both isotopes is possible using the same laser systems, we used rubidium-85 as it has the higher abundance of $72.2\ \%$ compared to $27.8\ \%$ for rubidium-87.

Two laser frequencies are required to generate a rubidium-85 MOT. Figure 3.1 shows the absorption spectrum of the rubidium-85 $D2$ hyperfine lines. The first frequency must be red detuned by $12\mathrm{MHz}$ from the $5S_{1/2}(F=3) \rightarrow 5P_{3/2}(F'=4)$ hyperfine transition. This transition is termed the cooling transition, as it provides the characteristic MOT forces needed to cool and confine the atoms. This transition is closed, as an atom in the $5P_{3/2}(F'=4)$ state can only de-excite to the $5S_{1/2}(F=3)$ state, due to the selection rule $\Delta F = 0, \pm 1$. The second laser frequency corresponds to the $5S_{1/2}(F=2) \rightarrow 5P_{3/2}(F'=3)$ hyperfine transition which is termed the re-pump, or re-pumper, transition. This laser frequency is not used to impart any force to the atoms. Although the cooling transition is closed, an occasional off-resonant photon (approximately one in every thousand) from the cooling laser will be resonant with the $5S_{1/2}(F=3) \rightarrow 5P_{3/2}(F'=3)$ transition. Now in the $5P_{3/2}(F'=3)$ state the atom can de-excite to the $5P_{3/2}(F'=3)$ state, and fall out of the cooling cycle. However, the re-pump beam excites the atom back into the $5P_{3/2}(F'=3)$ state. From this state it can only fall back into the $5P_{3/2}(F'=3)$ state or the $5S_{1/2}(F=3)$ and consequently the atom returns to the cooling cycle.

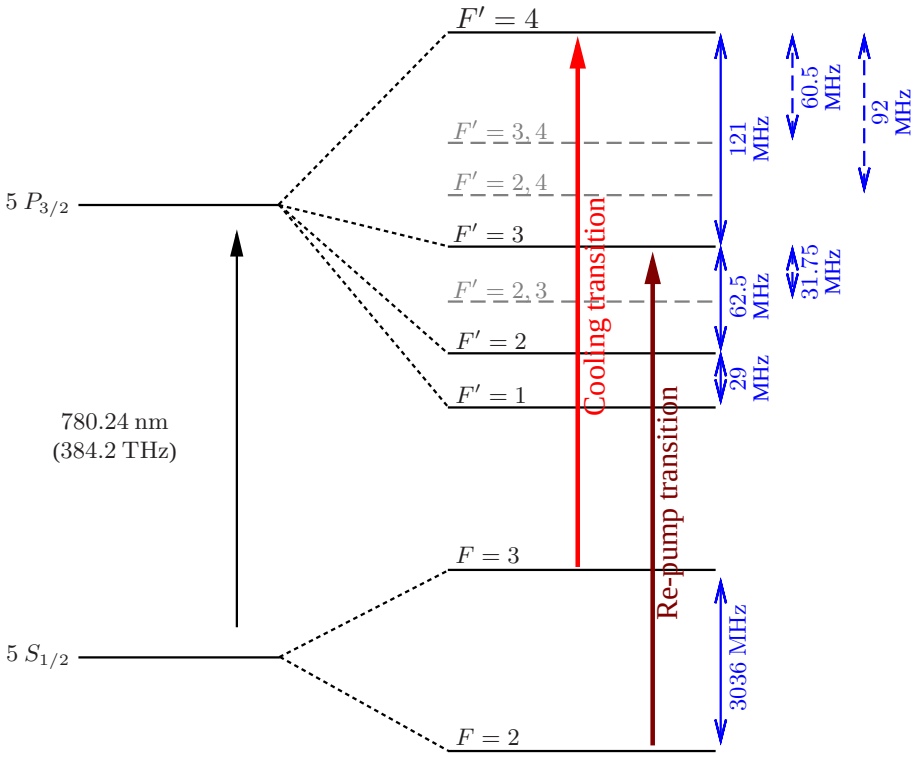

Figure 3.1: Energy level diagram of the $^{85}\mathrm{Rb}$ $D2$ lines [27]. The dotted lines show the crossover 'transitions', explained in section 3.2.4.

3.2.2 Cooling and Re-pump lasers

A number of requirements are placed on the lasers used to create a MOT. Firstly, as discussed above, there must be two frequencies of light. Secondly, the lasers must have a high enough spectral intensity and narrow enough linewidth to generate sufficient scattering events for both frequencies. These requirements are easiest met experimentally, by using low power diode lasers, that have linewidths less than the linewidth of the atomic transition, i.e. $< \Gamma = \gamma/2\pi = 5.98\ \mathrm{MHz}$ (as γ is an angular frequency, it must be divided by 2π to convert to a conventional frequency), with their output frequency stabilised to the atomic transition frequency. For the cooling laser, the intensity should be on the order of $I_s = 16.4\,\mathrm{W{\cdot}m^{-2}}$. For a $25\ \mathrm{mm}$ diameter beam, this equates to a power of $8\ \mathrm{mW}$; readily achievable by diode lasers. The intensity, linewidth and stabilisation requirements are slightly

less stringent for the re-pump laser, as they only need to generate one thousandth of the cooling scattering rate; but it is generally wise to construct the hyperfine laser with the same properties as the cooling laser so as to guarantee a satisfactory MOT.

Conventional single mode laser diodes operating at $780\ \mathrm{nm}$ do not have a sufficiently low linewidth when free-running to achieve the scattering rates needed. Consequently some mechanism is needed to narrow the linewidth of the diodes. In recent years, distributed feedback diodes and distributed Bragg reflector diodes have been developed that have an internal grating structure that forces the diode to lase with a narrow linewidth. These lasers are finding increasing use in rubidium spectroscopy due to the simplicity of their monolithic design [28].

Most commonly however, an extended cavity diode laser (ECDL) is used. An ECDL consists of a diode laser that has been placed in an extended cavity, with the output of the system taking on both the characteristics of the diode and the extended cavity. Alternatively, the output of a laser diode, termed the slave, will reduce in linewidth if a small amount of narrow linewidth 'seed' light is injected from a 'master' laser. Both ECDLs and injection locked diodes were used during the work presented in this thesis. The following sections provide the details of these laser systems.

3.2.3 Homebuilt ECDLs

Although there are numerous commercial manufacturers of extended cavity diode lasers, they are relatively simple to make from standard components [29, 30]. In the majority of my experiments, homebuilt ECDLs, combined with a homebuilt master-slave laser system provided the cooling and re-pump light. The homebuilt ECDLs used within this thesis were constructed to operate in the Littrow configuration [31]. The Littrow configuration achieves the extended cavity by orienting a diffraction grating in such a way that the 1st diffracted order is fed back into the laser with the 0th order forming the output of the laser. This cavity not only narrows the linewidth of the laser but allows it to be tuned and locked to a specific frequency.

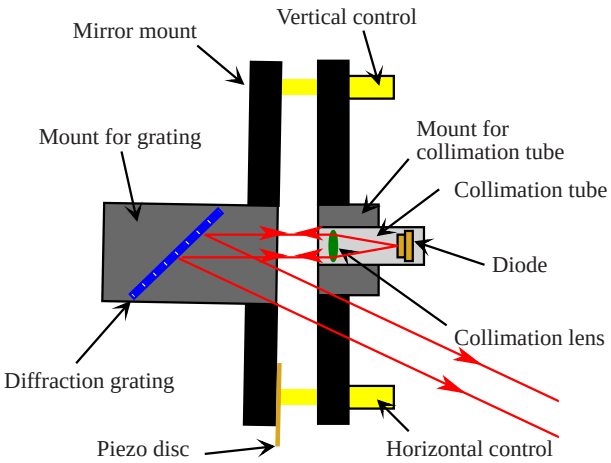

Figure 3.2: Schematic of our home-built ECDLs. With exception of the collimation tube mount and grating mount, all components were purchased from stock. The ECDL was mounted upon a Peltier element which was controlled by a commercial temperature controller.

As the output of conventional laser diodes is elliptical due to the shape of the diode itself, it is common to use anamorphic prism pairs to reshape the beam so that it becomes circular. However, for our ECDLs [30], we used a commercially available laser diode (Blue Sky Research, model: VPSL-0785-050-x-9-B) that had been modified, by the addition of a lens attached to the output facet of the laser, to produce a near circular output. This 'circularised' laser diode is based on a Hitachi HL7851G diode and produces a maximum output $50\ \mathrm{mW}$ with a typical wavelength at $25\ ^{\circ}\mathrm{C}$ of $785\ \mathrm{nm}$. As each diode is characterised by the manufacturer, we requested lasers with wavelengths as close to $780\mathrm{nm}$ as possible. As discussed later, the wavelength of the laser can be controlled by adjusting the diffraction grating and the laser temperature

Our home built ECDL, as shown in figure 3.2, was constructed around a conventional kinematic mirror mount that had been modified to hold a laser diode collimating tube containing the circularised laser diode and a collimating lens. A custom machined mount which contained the diffraction grating was designed to attach to the mirror mount where the mirror would normally be held. A piezoelectric disc was placed between the tip of the horizontal adjusting screw and the front

of the mirror mount. By applying a voltage to the piezoelectric disk, the cavity length could be adjusted. This allowed the frequency of the laser to be adjusted and locked to a reference using the servo-mechanism described in section 3.2.5. The mirror mount was attached to a Peltier element, which itself was attached to a heat sink bolted to the optical table. The Peltier element, which was controlled by a commercial temperature controller (Wavelength Electronics, model: LFI-3500), allowed the temperature of the ECDL, measured using a thermocouple, to be stabilised to better than $1\ ^{\circ}\mathrm{C}$.

The $1200\ \mathrm{lines \cdot mm^{-1}}$ diffraction grating was blazed so as to have a maximum first order efficiency at a wavelength of $300\ \mathrm{nm}$. When using the $780\ \mathrm{nm}$ diodes, approximately $20\ \%$ of the light was fed back into the diode via the diffracted first order. The remaining $80\ \%$ of the power making up the 0th order reflection constituted the $40\ \mathrm{mW}$ ouput of the ECDL.

The horizontal and vertical controls of the laser were used to align the diffraction grating so that the diffracted 1st order was accurately directed back along the path of laser output. The initial coarse alignment was carried out by observing the output of the ECDL, when running at moderate power, on a screen using a infra-red viewer. The horizontal and vertical controls were adjusted until a faint spot was seen in addition to the bright nominal output of the laser. This faint spot was as a result of the diffracted 1st order being redirected towards the diode, being reflected from the diode's front face and then reflected off the grating. The horizontal and vertical controls were then adjusted so that the nominal output and faint spot were overlapping. At this point, the drive current was reduced so that the laser was just below threshold. The mount is then adjusted with the aim of observing the laser intensity increasing again as it reaches threshold again. This 'threshold' optimisation can be repeated a number of times, each time involving finer adjustments, to fully optimise the alignment of the grating. At this stage, the ECDL is now said to be running in 'extended cavity'.

At this point it was necessary to tune the laser so that it was running at the correct wavelength; this will only be the case when both the diode and the laser cavity are correctly adjusted. The output wavelength of the ECDL can be adjusted by changing the temperature of the diode, the driving current and the position of the

grating. All of these parameters must be adjusted so that the ECDL will output the correct wavelength. This was most easily done by measuring the wavelength using a wavemeter. Once the wavelength was measured, the angle of the grating could be adjusted to bring the wavelength close to the transition. The angle of the grating could not be adjusted too far however, otherwise the ECDL would cease to be running in extended cavity. The temperature of the laser could then be adjusted; lower temperatures resulting in lower wavelengths. As our circularised laser diodes would typically have a wavelength a few nm above $780\,\mathrm{nm}$, the lasers typically needed to be cooled to between $0\,^{\circ}\mathrm{C}$ and $10\,^{\circ}\mathrm{C}$. Once the wavemeter was reading a laser wavelength close to the desired wavelength, a rubidium cell was placed in the beam. At this point fine systematic adjustments were made to the horizontal adjuster and drive current until the beam was observed, using an infrared viewer, to be resonant with the rubidium. Once the cavity and temperature were adjusted in this way, it was usual for there to be numerous possible drive currents that resulted in resonance. Although running diodes at higher currents would have yielded higher output powers, it would also would have reduced the lifetime of the laser.

The laser was then ready to be combined with the Doppler-free saturated absorption spectroscopy set-up, described in the next section. Once the saturated absorption spectroscopy trace was observed, the cavity was further adjusted to optimise the trace.

3.2.4 Doppler-free saturated absorption spectrsocsopy

The two lasers had be locked to the cooling and hyperfine transitions of the rubidium spectrum. A basic absorption spectrum of rubidium is shown in figure 3.3(a). This spectrum was taken by directing a probe beam consisting of a few mW syphoned from the output of the ECDL, through a cell of rubidium held at approximately $30\,^{\circ}\mathrm{C}$. The wavelength of the laser was scanned by applying a voltage across the piezoelectric disk, thereby changing the cavity length of the ECDL, with a photodiode reading the intensity. The output of the photodiode therefore showed us the absorption as a function of wavelength. The two peaks correspond

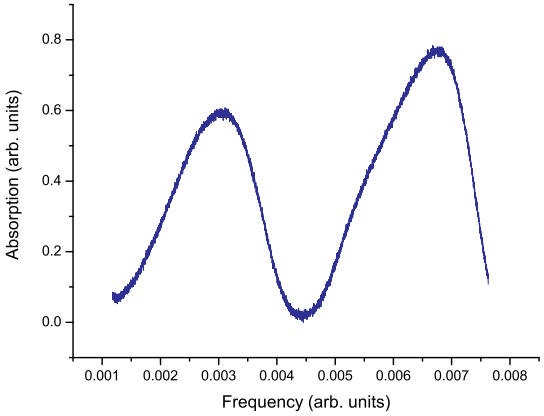

(a) Basic absorption spectrum. The rubidium-87 $F=2 \rightarrow F'$ transitions are visible on the left with the rubidium-85 $F=3 \rightarrow F'$ visible on the right. The hyperfine structure however is not visible.

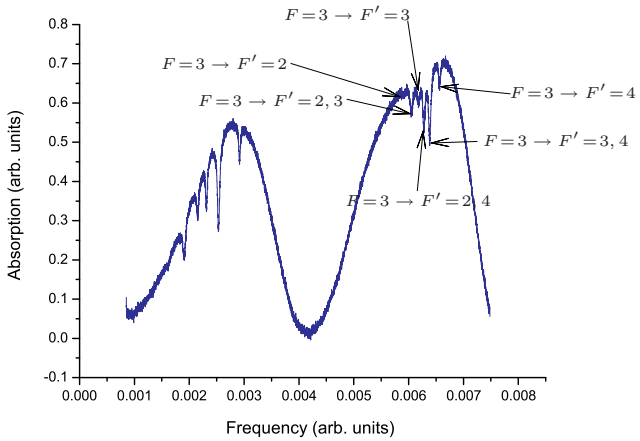

(b) Doppler-free saturated absorption spectrum. The rubidium-87 $F=2 \rightarrow F'$ transitions are visible on the left with the rubidium-85 $F=3 \rightarrow F'$ visible on the right. The hyperfine structure is visible.

Figure 3.3: Comparison between a basic absorption trace and a Doppler-free saturated absorption trace taken using our ECDL lasers. The hyperfine features visible in the sat-abs spectrum are not discernible in the basic trace. Consequently the sat-abs must be used when locking to the hyperfine transitions.

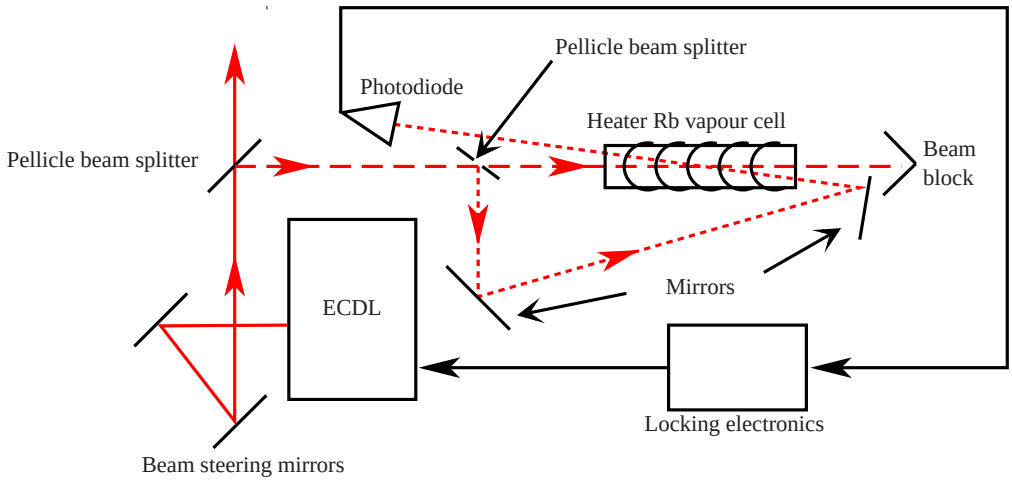

Figure 3.4: Schematic of the Doppler-free saturated absorption spectroscopy (sat-abs) set-up. A pellicle beam splitter is used to syphon a few mW of the laser power towards the sat-abs. This beam is then split into two beams; the probe beam and the pump beam. The probe beam is directed through the rubidium cell to be incident on a photodiode. A more intense pump is directed in the opposite direction to the probe beam in such a way that it overlaps the probe beam as both beams pass through the cell. As shown in figure 3.3, the addition of the pump beam allows the hyperfine features to be discerned. The signal from the photodiode is fed into locking electronics. These locking electronics, by way of negative feedback, allows the ECDL to be locked to a hyperfine transition.

to the $F = 3 \rightarrow F'$ transitions of rubidium-85 and the $F = 2 \rightarrow F'$ transition of rubidium-87. However, it is impossible to discern the finer individual transitions, as the spectrum is washed out by the thermal motion of the atoms, and resulting induced Doppler shift. As a consequence some method is required to reduce the effect of thermal motion and show finer details within the spectrum.

Doppler-free saturated absorption spectroscopy, colloquially known as sat-abs, adds an extra pump beam, travelling in the opposite direction to the probe beam, as shown in figure 3.4. The pump beam is syphoned off from the same laser beam as the pump beam; however it is configured to be more intense. The two beams are adjusted so that they overlap with each other for as great a distance as possible. The pump beam acts to saturate the rubidium transitions so they are unable

to absorb any more photons. This results in a Lamb dip in the absorption spectrum of the probe beam at the frequency corresponding to the transition frequency for atoms travelling with zero velocity (with respect to the reference frame of the apparatus). A cross over dip is also observed at frequencies corresponding to the midway between two transitions, provided that they share a common ground state and are separated by a frequency less than the Doppler linewidth [32]. An example of the sat-abs spectrum of rubidium taken using our set-up is shown in figure 3.3(b). In contrast to the basic absorption spectrum shown in figure 3.3(a), the sat-abs spectrum allows for the cooling and re-pump transitions to be discerned.

3.2.5 Laser locking

A servo-locking system was used to lock the lasers' frequencies to the cooling and re-pump transitions. The servo-locking system consisted of two negative feedback circuits, one which acted upon on the piezoelectric disc and the other which modulated the laser diode current. The piezoelectric disc was initially used to scan the laser frequency across a number of transitions, using a triangular waveform, so that the user was able to identify the appropriate transition of interest. The lock box was then adjusted, by reducing the amplitude of the waveform so that the frequency of the laser zoomed in to the transition of choice. Once fully zoomed in, the lock box was locked to that point in the waveform. By comparing the real-time voltage from the sat-abs photodiode, to the locked voltage, a phase sensitive detector generated negative feedback to return the output of the laser to that set earlier. For low-frequency compensation, below $1\mathrm{MHz}$, the piezoelectric disk was adjusted; and for high frequency compensation, up to $100\ \mathrm{MHz}$, the diode current was adjusted. Thorough details of the design, construction and operation of this system can be found in the Gavin Lancaster's thesis [33].

The re-pump laser can be directly locked to the re-pump transition as observed on the sat-abs trace. The cooling laser however must be red-detuned by $2\Gamma = 11.96\ \mathrm{MHz}$ from the cooling transition. As there are no features in the sat-abs trace to lock to at this point, the laser frequency must be shifted from one of the lockable transition frequencies. This is done using an acousto-optic modulator

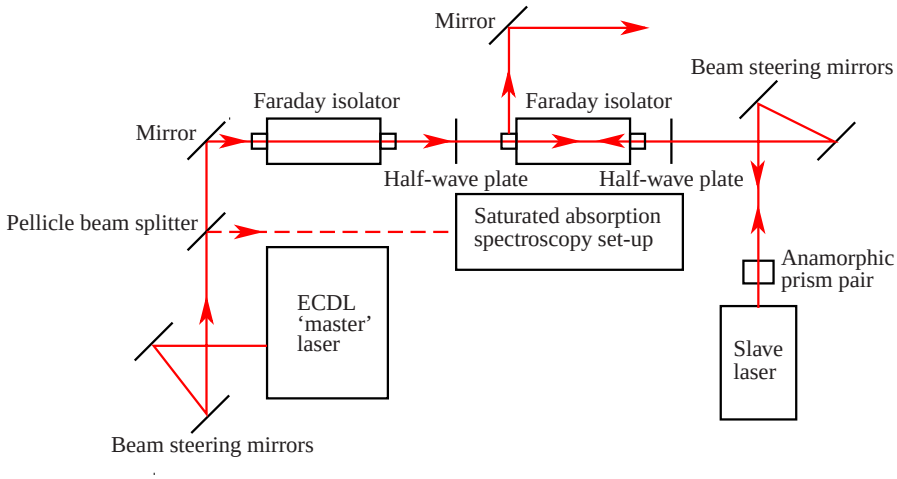

Figure 3.5: Schematic of the master-slave laser set-up. The ECDL master laser injection locks the slave laser diode with a few μW of light. Provided that the frequency of the slave laser is already close to that of the master laser, the slave laser will take on the spectral characteristics of the master ECDL [33]. This allows the use higher power laser diodes, which may not produce a narrow enough linewidth when used in an ECDL, for laser cooling experiments. The first Faraday isolator after the ECDL is to stop feedback into the ECDL. The second Faraday isolator also stops feedback, but is primarily used to separate the retro-reflected slave output beam from the co-linear seed light.

(AOM) [34]. The piezoelectric disk in an AOM produces sound waves in a crystal forming a diffraction grating. The conservation of momentum between the phonons and photons results in either a red or blue frequency shift (depending on which diffracted order is used) in the light. This frequency shift is the same magnitude as the driving frequency of piezoelectric disk. We used an acousto-optic modulator (Isle Optics, model: LM080), that had a nominal frequency of 80 MHz, which could be adjusted by ± 23 MHz. As can be seen from figure 3.1, the $5S_{1/2}(F=3) \rightarrow 5P_{3/2}(F'=2,4)$ transition is the only one suitable. By locking the laser to this transition and blue-shifting the frequency by 80 MHz, the laser will be correctly red-shifted by 12 MHz from the cooling transition.

3.2.6 Injection locking of diode laser

Aside from placing a laser diode in an extended cavity configuration, it is possible to control and improve the spectral qualities of a diode laser using a technique known as injection locking. A 'slave' laser, injected with light from a 'master' laser will take on the spectral characteristics of the master, providing that its free running frequency is sufficiently close to that of the master [33]. This technique allows higher powered diode lasers, that may not have sufficiently low linewidth when placed in an extended cavity configuration, to be used.

Our master-slave configuration used the homebuilt ECDL described above as the master laser and a temperature controlled higher powered $784\,\mathrm{nm}$ $120\,\mathrm{mW}$ diode laser (Sharp, model: GH0781JA2C [1]) as the slave. The configuration was set up is shown in figure 3.5. As with the ECDLs, the slave laser was temperature controlled using a Peltier element and commercial temperature controller. As this laser was not circularised, an anamorphic prism pair was used to circularise the beam. Correct injection locking could be confirmed by locking the ECDL to a rubidium transition, and observing if the output of the slave was resonant with a rubidium cell. The Peltier temperature and the current of the slave laser should then be adjusted until the beam is seen to be resonant with the rubidium in the cell. Once the correct Peltier temperature was found, numerous values of current would result in resonance. The highest diode current, below the maximum limit of $\sim 140\,\mathrm{mA}$, was used to gain useable optical powers up to $110\,\mathrm{mW}$.

3.2.7 Tui TA-100 laser system

During the experiments on guiding using Laguerre-Gaussian beams detailed in chapter 4, the light for the cooling transition was supplied by a commercial master oscillator power amplifier (MOPA) laser system (TuiOptics GmbH,[2] model: TA-100). The inside of this system is shown in figure 3.6. The system consisted of an ECDL (the master oscillator), beam steering mirrors, two Faraday isolators

[1] Unfortunately now discontinued.
[2] Now known as Toptica Photonics AG.

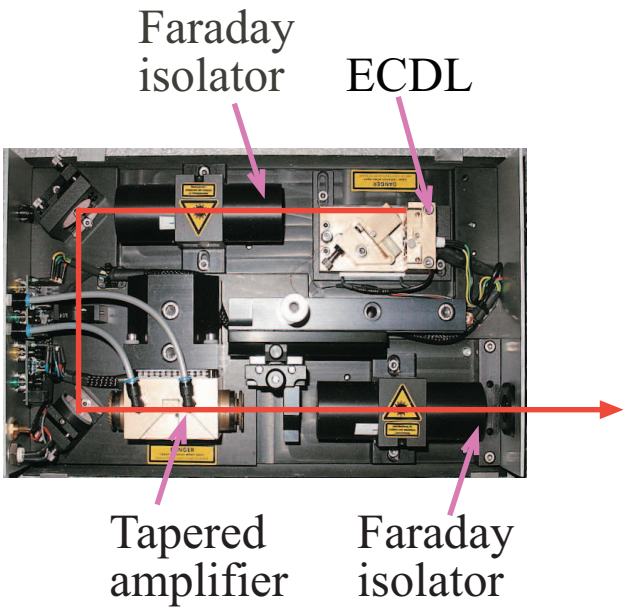

Figure 3.6: Labelled photograph of the TuiOptics TA-100 master oscillator power amplifier (MOPA) system. The system was capable of producing $500\ \mathrm{mW}$ of single frequency, narrow linewidth light. As MOPA systems are particularly vulnerable to feedback, as the amplifier will amplify any back reflected light, two Faraday isolators were included in the system. The control box is not shown.

and a tapered amplifier. The ECDL works in the same manner as the 'home-built' ECDLs described previously. While the homebuilt ECDL and the home-built master-slave setup were limited to a maximum output powers of $50\ \mathrm{mW}$ and $120\ \mathrm{mW}$ respectively, the MOPA system was able a produce $500\ \mathrm{mW}$ of single frequency light, narrow linewidth light.

The TA-100 was controlled by its own laser control system. The system had controls for the thermoelectric cooler and driving current of the ECDL; and the thermoelectric cooler and driving current of the tapered amplifier. The control systems also incorporated a servo locking device. This device worked in a slightly different manner to the homebuilt servo lock boxes, in that it used a proportional-integralderivative (PID) controller and not a phase sensitive detector to lock to the transition.

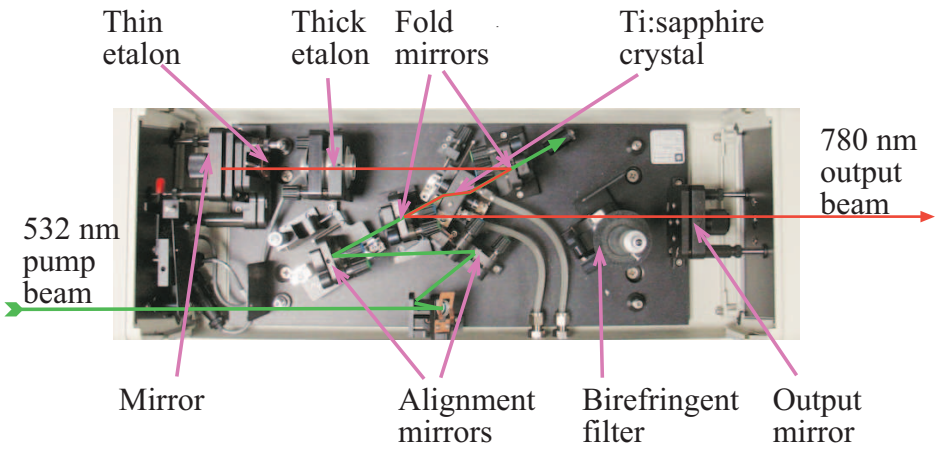

Figure 3.7: Labelled photograph of the Spectra Physics 3900S Ti:sapphire laser. The intra-cavity etalons and birefringent filter allowed the laser to operate in two tunable longitudinal modes, separated by $200\,\mathrm{MHz}$. The birefringent filter and thin etalon were tuned by adjusting actuators. The thick etalon was tuned by adjusting its temperature.

3.2.8 Ti:sapphire guide beam

ECDL based laser systems above can be useful when studying near-resonant guide beams, as they can be precisely tuned and emit a narrow linewidth single mode. However, for far-detuned guides, our diode lasers were not powerful enough. Therefore, for the guide laser we used a continuous wave tunable Ti:sapphire laser (Spectra Physics, model: 3900S), which was pumped using a $532\,\mathrm{nm}$ diode-pumped solid state laser (Spectra Physics, model: Millennia Vs) with maximum output power of $5\,\mathrm{W}$. With the intra-cavity optics used, the Ti:sapphire had a tuning range between 700 and $850\,\mathrm{nm}$, had a maximum output power of $900\,\mathrm{mW}$ and operated on two longitudinal modes separated by $200\,\mathrm{MHz}$. A schematic of the internal design of the laser is shown in figure 3.7. The inclusion within the cavity of a birefringent filter, thin etalon and temperature controllable thick etalon acted to reduce the number of longitudinal modes to two. By adjusting these elements, the laser frequency could be accurately tuned.

3.3 Vacuum systems

Atom cooling and trapping experiments must be carried out in a vacuum, otherwise the effects of the cooling or trapping technique would be negated by collisions with background gas. While it is possible to form a MOT with pressures as high as 10^{-7} mbar [35], it is desirable to maintain as good a vacuum as possible. Not only will the better vacuum increase the size of the MOT, but it will decrease the likelihood of collisions affecting guided atoms in the dipole guides. To that end, the vacuum apparatus used in these experiments were designed to approach ultra high vacuum (UHV) operation[3] with a typical base pressure of our vacuum systems being 3×10^{-9}mbar. In order to achieve UHV, there are stringent requirements for the preparation of the system and the choice of materials used within. Although a number of vacuum connection standards exist, the ConFlat standard, which consists of a gasket (usually copper) sandwiched between two 'knife-edged' flanges, yields the highest performance and was used exclusively in our UHV systems.

3.3.1 Materials

In UHV, outgassing becomes an issue. Not only can bulk outgassing prevent the system from reaching the desired vacuum level, small levels of local outgassing (i.e. outgassing from a small region such as a fingerprint) can interfere with the creation and guiding of the cold atoms. Consequently, materials were chosen and prepared so as to have as low an outgassing rate as possible. The vacuum compatible materials used within this systems included 304 and $316\mathrm{LN}$ type stainless steel, copper, MACOR (machinable glass ceramic), Kapton (a low outgassing polyimide film used for electrical insulation) and glass.

[3] Typically defined as pressures between 10^{-9} and 10^{-12} mbar.

3.3.2 Cleaning of vacuum components

Cleaning procedures for ultra high vacuum systems can be convoluted multi-step procedures that in extreme cases will include vapour washes and electropolishing. For our system however, a basic but effective cleaning practice was adequate:

1. The vacuum piece was cleaned in a solution of Liquinox (which is a residue free liquid detergent) and warm water. If the item was small enough this was done in an ultrasonic bath.

2. The piece was thoroughly rinsed under the cold water tap. Filtered or deionised water would have been preferable but tap water proved sufficient. The piece was dried using a clean room wipe.

3. If the piece was small enough, it was ultrasonically cleaned in a bath of isopropanol or acetone.

4. Before insertion to the vacuum system, the piece was wiped using a clean room wipe soaked in isopropanol or acetone. Inspection of the wipe indicated if any contamination remained on the piece. If the piece was still coarsely contaminated, the procedure was repeated in parts or in full.

It is worth noting however, that the 'odd' contaminant within a vacuum system may not necessarily guarantee that the system won't reach UHV. Indeed, on dismantling an inherited vacuum system, I discovered a quantity of blu tack within the chamber; this chamber had been operating in UHV for many years. However, the best practice when working with UHV is to adopt a suitable cleaning procedure for the experiment's needs and to strictly adhere to it.

3.3.3 Rubidium source

In all the atom guiding experiments detailed in this thesis, rubidium 'alkali metal dispensers' (SAES getters), colloquially known as getters, were used. These getters consisted of a $12\,\mathrm{mm}\times1.12\,\mathrm{mm}\times1.35\,\mathrm{mm}$ (L×W× H) sealed metal container, containing a few milligrams of rubidium. When a current of between 2 and 7.5 A

was passed through the getter, rubidium was released through a small slit in the getter. These getters provided a reliable and controllable source of rubidium in the atom guiding experiments.

3.3.4 Bake-out

In all of our vacuum systems, one or two ion getter pumps (Varian, models: VacIon Plus 40, Triode, 919-0201; and VacIon Plus 25, Triode, 911-5030), that were permanently attached and turned on, were used to maintain UHV in the system. These pumps are termed capture pumps, in that they capture, rather than remove, gases from the vacuum system. These pumps perform excellently in UHV, but as they can only operate in the pressures below $\sim 10^{-2}\,\mathrm{mbar}$, they are unable to evacuate the system down from air. Consequently a preliminary 'pumping down' stage was needed.

This pumping down stage was performed using a turbomolecular pump, backed by a diaphragm pump (Varian, model: Turbo-Dry 70). This stage usually lasted for a few days and was always accompanied by a bake-out of the system. This bake-out involved heating the system, using heat tape, to a temperature of around $100\,^{\circ}\mathrm{C}$, primarily in order to speed up the evaporation of water adsorbed on the inside surface of the system. Care was taken to raise and lower the temperature in a controlled manner, and to heat the system evenly. Once the pumping down stage was completed, the temperature was slowly lowered. At around $50\,^{\circ}\mathrm{C}$, the all-metal valve was closed, isolating the vacuum chamber from the turbomolecular pump. The ion getter pump was then turned on. The ion getter pump's controller provided a real-time reading of the current being drawn by the pump; this current was converted to a pressure. The pressure was carefully monitored at this stage, as an insufficient vacuum would result in the ion getter pump switching itself off to prevent damage. If the ion getter pump stayed on, and the pressure started to reduce, the turbomolecular pump was turned off. Care was taken at this stage to monitor the vacuum; if insufficient force have been used to close the all-metal valve, the loss of vacuum on turbomolecular pump side of the valve would result in a rapid loss of vacuum in the system. Provided the valve was correctly closed

the pressure of the system over the next $24\,\mathrm{hours}$ would approach its eventual base pressure of around $\sim 3 \times 10^{-9}\,\mathrm{mbar}$.

3.4 Conclusion and author's contribution

This chapter described the basic laser systems and vacuum procedures used in this thesis. Although the components of the laser systems, such as the lock-boxes and ECDL mounts, were largely inherited from my predecessors, I gained considerable experience during the final years of my PhD rebuilding, modifying and maintaining the system, almost entirely by myself. During the course of my PhD I completely dismantled and re-assembled the entire laser set-up on two occasions due to a lab refurbishment. I also successfully integrated the higher powered Sharp laser into the master-slave system; greatly improving the size of the MOT in the hot wire/fibre guide system. As the vacuum systems used in the hot wire/fibre guide detector system, discussed in chapters 5, were more complicated than previous systems created within the group, I introduced a more thorough vacuum cleaning procedure. This procedure was designed to ensure that any vacuum pieces that may have be coarsely contaminated by oil from the workshop could be inserted into the system with confidence.

Chapter 4

GUIDING OF ATOMS IN LG BEAMS GENERATED USING A SPATIAL LIGHT MODULATOR

4.1 Chapter synopsis

This chapter details the experimental work and results of an atom guiding experiment which utilised a spatial light modulator to generate (blue-detuned) Laguerre-Gaussian (LG) guide beams. The theory and properties of LG beams are explained with relevance to atom guiding. I then discuss the characteristics of a phase modulating spatial light modulator and how it was used to generate different azimuthal index LG beams. I then explain the construction and operation of an experiment to guide and detect clouds of cold atoms in optical guides made from the LG beams. The results of this experiment are then presented.

4.2 Motivation for experiment

High azimuthal (l) order Laguerre-Gaussian (LG) beams are annular beams; a ring of light surrounding a dark core with zero intensity. Consequently, these beams

are ideally suited to blue-detuned atom guiding, as atoms contained within the guide will be confined within the dark core, thereby minimising heating effects and other perturbations from the radiation field. By varying the parameters of the LG beam, it is possible to change the steepness of the potential well, thus changing the characteristics of the guide.

While prior studies had shown the effectiveness of LG beams for guiding [36, 37, 38], no study had been carried out to compare the guiding properties of different order LG beams. A possible reason for this, was the increased difficulty the experimenter would face if the experiment had to be repeated, numerous times, for multiple LG beams and alignments. The previous studies generated LG beams using static optical elements, such as a hologram or mode converter. The experimenter would therefore have needed to have possessed a variety of static elements and to have aligned the experiment each time the element was changed. In recent years, spatial light modulators (SLMs) have become standard equipment in optics research laboratories. Depending on the type, SLMs are able to imprint a spatial modulation on the phase, intensity, direction and/or polarisation of a laser beam. By using a phase modulating SLM, it is possible to switch between high quality LG beams of different order at a touch of a button. This would allow the experimenter the ability to change LG beams with no re-alignment.

Therefore, on paper, SLMs seemed to be well suited for generating LG beams for atom guiding. The purpose of this study was twofold. Firstly, to confirm that SLMs are able to generate LG beams suitable for atom guiding. Secondly, to carry out the first comparative study of the guiding properties of different order LG beams.

The remainder of this chapter is organised as follows. Firstly, the theory and properties of LG beams are introduced and their applicability to atom guiding experiments explored. Next, I explain how LG beams were generated using a phase modulating spatial light modulator. Our experimental set-up and procedure is then described, followed by the presentation of the results. A conclusion is then presented.

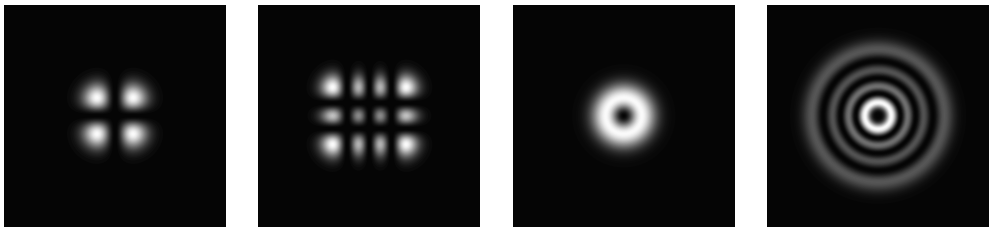

(a) Hermite-Gaussian beam, $n = 1, m = 1$. (b) Hermite-Gaussian beam, $n = 3, m = 2$. (c) Laguerre-Gaussian beam, $l = 1, p = 0$. (d) Laguerre-Gaussian beam, $l = 2, p = 3$.

Figure 4.1: Examples of calculated Hermite-Gaussian and Laguerre-Gaussian beam profiles. Hermite-Gaussian beams have rectangular symmetry and are defined by the indices n and m. Laguerre-Gaussian beams have circular symmetry and are defined by the indices l and p.

4.3 Laguerre-Gaussian beams

4.3.1 Properties of Laguerre-Gaussian beams

Laguerre-Gaussian (LG) and Hermite-Gaussian (HG) beams are known for three important properties [39]: they form a complete basis set for solutions to the paraxial wave equation; their shape is invariant on propagation[1]; and (as a result of the previous two properties) they form the transverse modes of stable resonators, such as lasers. While HG beams are described by Cartesian co-ordinates and possess rectangular symmetry, LG beams are defined in circular cylindrical coordinates and are therefore circularly symmetric, as shown in figure 4.1. Laguerre- and Hermite-Gaussian beams both form complete basis sets for the solutions to the paraxial wave equation, so it is possible to describe any LG beam as a superposition of HG beams and vice-versa [40]. As HG beams and the majority of laser cavities posses rectangular symmetry, higher order outputs from such laser cavities are more easily identified as a single high order HG beam, rather than a hard to envisage superposition of multiple high order LG beams. The rectangularly symmetric HG beams are therefore more widely known than circularly symmetric LG beams. However, LG beams have attracted increased attention not only due to their shape but also due to their other phase properties.

[1]The beams will scale radially as they diffract.

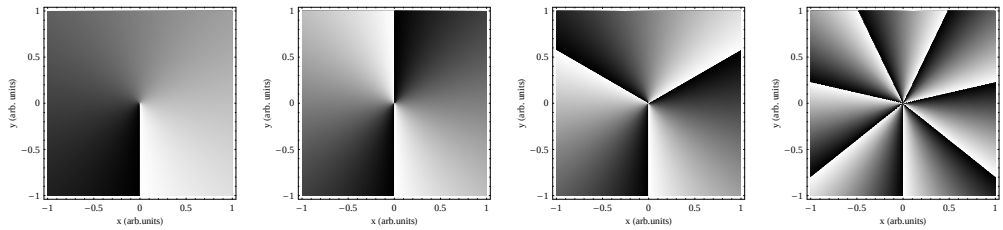

(a) Phase structure, l=1 (b) Phase structure, l=2 (c) Phase structure, l=3 (d) Phase structure, l=7

Figure 4.2: Phase profile of $p = 0$ LG beams for $l = 1, 2, 3, 7$. The transition from white to black represents the transition from 0 to 2π phase difference.

Electromagnetic field amplitude

The electromagnetic field amplitude of an LG beam is given by [41],

$$u_p^l(r,\phi,z) \propto \exp\left(-\frac{ikr^2}{2R(z)}\right)\exp\left(-\frac{r^2}{w(z)^2}\right)\exp\left(-i(2p+l+1)\psi\right) \times \exp(-il\phi)(-1)^p\left(2\frac{r^2}{w(z)^2}\right)^{l/2} L_p^l\left(\frac{2r^2}{w(z)^2}\right) \tag{4.1}$$

where L_p^l is the generalised Laguerre polynomial; λ is the wavelength of light; z is the propagation distance from the beam waist position; r and ϕ are the radial distance from and the azimuthal angle around the beam axis respectively; $R(z) = z\left(1 + (z_R/z)^2\right)$ is the wavefront radius of curvature; $z_R = \pi w_0^2/\lambda$ is the Rayleigh range; and the beam radius $w(z)$, defined at the point where the intensity falls to $1/e^2$ of its on axis value, is given by

$$w(z) = w_0\sqrt{1 + \left(\frac{\lambda z}{\pi w_0^2}\right)^2}, \tag{4.2}$$

where w_0 is the beam waist.

The term $(-i(2p+l+1)\psi)$ contained within equation 4.1 is the Gouy phase shift of the LG beam with $\psi = \arctan(z/z_R)$ being the Gouy phase shift of a

Gaussian beam.

Transverse intensity distribution

The transverse intensity distribution of a Laguerre-Gaussian beam is given by [42],

$$I(r,z) = \frac{2p!}{\pi (p+|l|)!} \frac{P_0}{w^2(z)} \exp\left(-2\frac{r^2}{w^2(z)}\right) \left(\frac{2r^2}{w^2(z)}\right)^{|l|} \times \left\{ L_p^{|l|}\left(\frac{2r^2}{w^2(z)}\right)\right\}^2 \tag{4.3}$$

Role of l and p indices

LG beams are therefore described by the indices of the generalised Laguerre polynomial; and are sometimes denoted by the nomenclature LG_p^l. The azimuthal index l refers to the number of 2π phase shifts around one circumference of the beam by the term $e^{-il\phi}$ in equation 4.1. This term causes LG beams with $l > 0$ to have a dark core; at the centre of the beam there is a phase singularity where all phases are present and therefore destructively interfere. A representation of the phase of an LG beam as l is increased is shown in figure 4.2. As l and the number of 2π phase shifts around the circumference of the beam is increased, so too does the diameter of inner ring, as shown in figure 4.3, provided that the other beam parameters are kept constant.

The p index is related to the number of radial nodes in the beam profile by the relation $p + 1$. As p is increased, the radius of the dark of the inner ring also decreases, provided that the other beam parameters are kept constant

The $e^{-il\phi}$ term also causes LG beams with $l > 0$ to possess orbital angular momentum of magnitude $l\hbar$ per photon [43]; this is distinct from the spin angular momentum possessed by circularly polarised beams. This can have consequences for the motion of atoms within these beams [44]. For our experiment, where the atom is repelled from the region of high intensity and we are primarily concerned

with the number of atoms guided rather than their precise motion, the influence of angular momentum was neglected.

Radius, intensity and steepness of inner ring

The peak to peak diameter of the inner ring of the beams changes with different values of l and p. The radius of the inner ring r_{inner} of $l > 0, p = 0$ LG beams is given by,

$$r_{\text{inner}}(l) = w(z)\sqrt{l/2}. \tag{4.4}$$

By adjusting the beam waist it is therefore possible to equalise the value of r_{inner} for different l index LG beams.

The peak intensity $I_{\max}$ of this inner ring is given by [42],

$$I_{\max} = \frac{P_0}{\pi r_{\text{inner}}^2}\frac{l^{l+1}\exp(-l)}{l!} \tag{4.5}$$

which can be approximated, using Stirling's approximation ($n! \approx \sqrt{2\pi n}\,(n/e)^n$), to within $10\,\%$ ($2\,\%$ for $l > 4$) as [45],

$$I_{\max} \approx \frac{P_0}{\pi r_{\text{inner}}^2}\sqrt{\frac{l}{2\pi}}. \tag{4.6}$$

This equation shows that for fixed inner ring radius, $I_{\max} \propto \sqrt{l}$. This means that as l is increased, both the intensity and steepness of the ring also increase. Figure 4.4 shows the calculated profiles for the $l = 1$, $l = 2$ and $l = 6$ LG beams with equalised ring diameter.

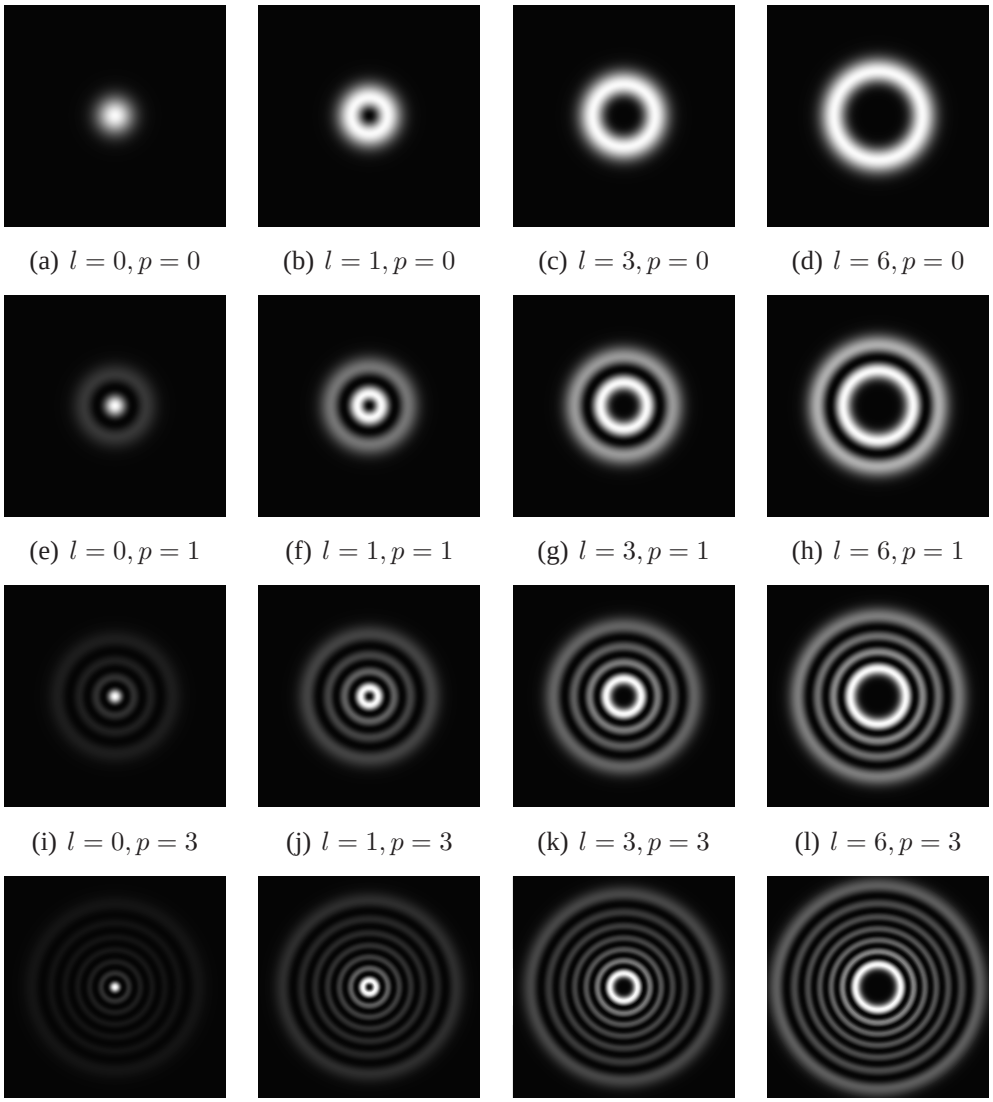

(a) $l = 0, p = 0$ (b) $l = 1, p = 0$ (c) $l = 3, p = 0$ (d) $l = 6, p = 0$

(e) $l = 0, p = 1$ (f) $l = 1, p = 1$ (g) $l = 3, p = 1$ (h) $l = 6, p = 1$

(i) $l = 0, p = 3$ (j) $l = 1, p = 3$ (k) $l = 3, p = 3$ (l) $l = 6, p = 3$

(m) $l = 0, p = 6$ (n) $l = 1, p = 6$ (o) $l = 3, p = 6$ (p) $l = 6, p = 6$

Figure 4.3: Transverse intensity profiles of various LG beams, calculated using equation 4.3. The beam parameters and transverse axes of the graphs are constant, with only the p and l parameter being changed. The intensity scale of the graphs is normalised to the peak intensity of each beam to give the highest clarity of the beam shape.

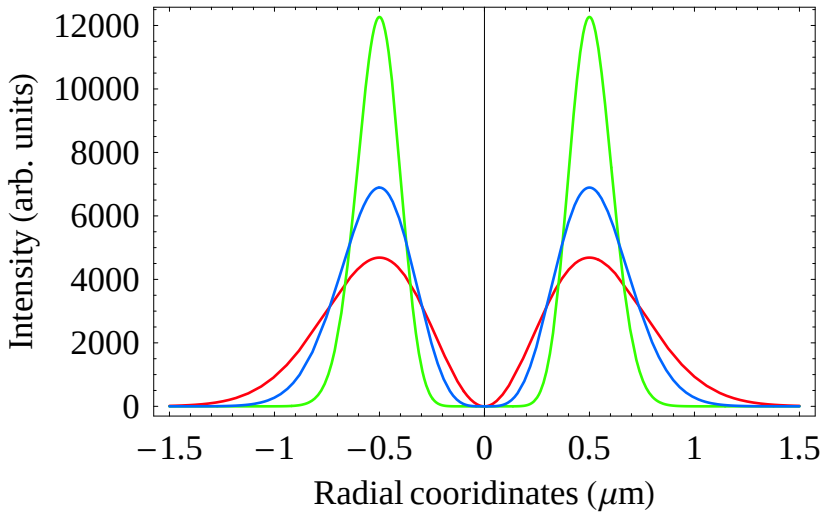

Figure 4.4: Comparison of inner ring peak intensity and steepness for $l = 1$ (in red), $l = 2$ (in blue) and $l = 6$ (in green) LG beams with a matched ring radius of $500\mu\mathrm{m}$. As l is increased, the peak intensity, width of the dark core and steepness of the inner ring also increases.

Propagation properties

Like HG beams, an LG beam's shape does not alter during propagation. The beam is still a diffracting beam so it will change in size as it propagates. LG beams will diffract at different rates depending on the LG beam's order. Figure 4.5 and figure 4.8 show the transverse profile across the diameter of $l = 1, p = 0; l = 6, p = 0; l = 1, p = 2; l = 6, p = 2$ beams of equal power. Figure 4.5 shows the profile for constant value of w_0 and figure 4.8 for constant value of the first ring diameter.

4.3.2 Methods of generating Laguerre-Gaussian beams

There are a number of ways that LG beams can be created. Although there have been some examples of lasers which output high order LG beams, the majority of laser cavities have rectangular symmetry, and therefore will output higher order HG beams if they output a higher order beam than the fundamental Gaussian. LG beams can also generated by the subsequent transformation of a Gaussian or

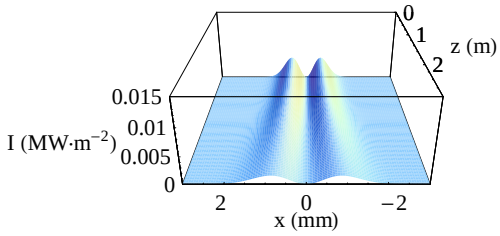

(a) $l = 1, p = 0$, diameter of inner ring$= 1$ mm

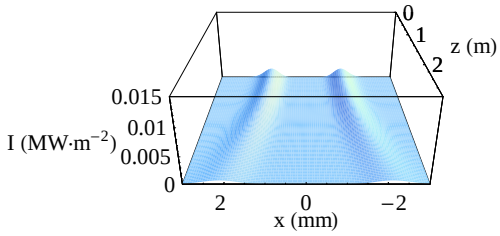

(b) $l = 6, p = 0$, diameter of inner ring$= 2.45$ mm

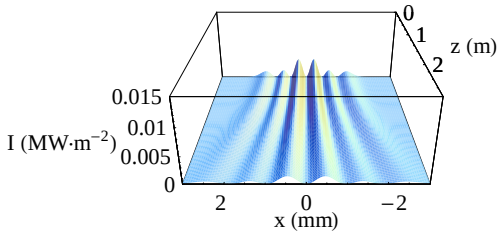

(c) $l = 1, p = 2$, diameter of inner ring$= 0.54$ mm

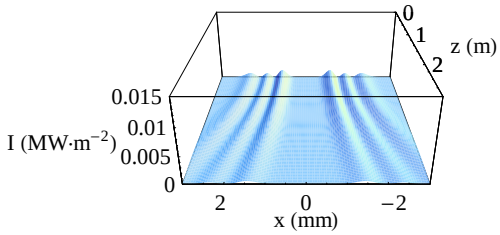

(d) $l = 6, p = 2$, diameter of inner ring$= 1.69$ mm

Figure 4.5: Transverse intensity profiles of LG beams for unmatched ring sizes on propagation. Where I is the intensity, x is the transverse coordinate and z is the propagation distance from the beam waist. Input beam parameters are $w0 = 0.71$ mm, $\lambda = 780$ nm and $P_0 = 10$ mW.

higher order HG output beam of a laser. If the output of the laser is a high order HG beam (which can be achieved, for example, with the insertion of an intra-cavity cross-wire with the wires aligned with the nodes of the desired beam), then it is possible to transform this beam into an LG beam using a mode converter consisting of two cylindrical lens. This technique has a high efficiency and generates pure LG beams. It is more practical however for LG beams to be transformed from a Gaussian beam; the nominal output beam of most laser systems. This is achieved by passing the Gaussian beam through an optical element that imprints the appropriate spatial phase and/or intensity modulation on the laser beam. Although in theory, the most versatile solution would be to modulate both the intensity and phase of the light, this is difficult from an engineering point of view. For

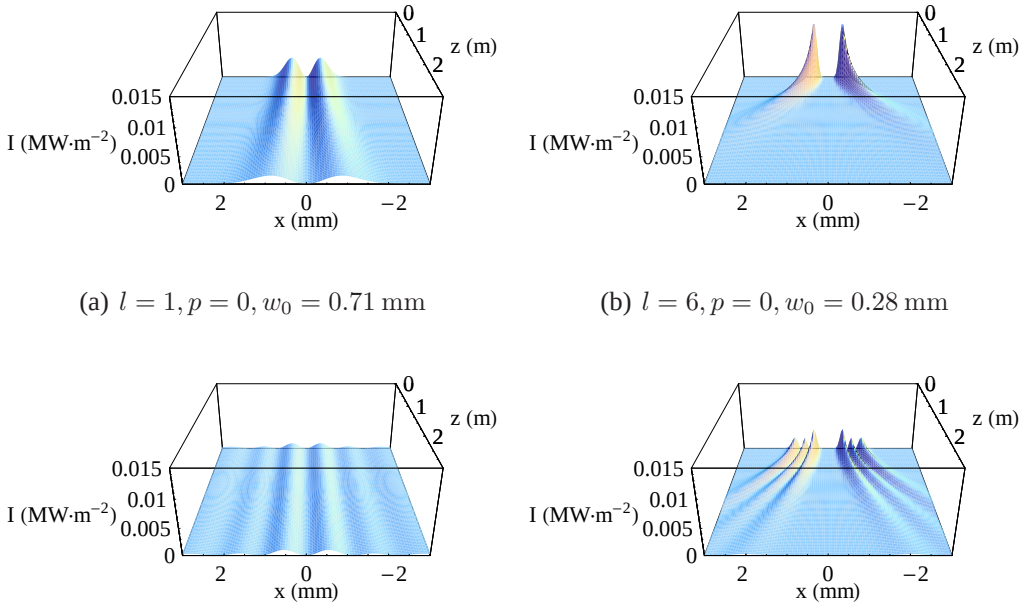

(a) $l = 1, p = 0, w_0 = 0.71\,\mathrm{mm}$

(b) $l = 6, p = 0, w_0 = 0.28\,\mathrm{mm}$

(c) $l = 1, p = 2, w_0 = 1.32\,\mathrm{mm}$

(d) $l = 6, p = 2, w_0 = 0.42\,\mathrm{mm}$

Figure 4.6: Transverse intensity profiles of LG beams for matched ring sizes on propagation. The inner ring diameter of the beams at focus is $1\,\mathrm{mm}$. Where I is the intensity, x is the transverse coordinate and z is the propagation distance from the beam waist. Input beam parameters are $\lambda = 780\,\mathrm{nm}$ and $P_0 = 10\,\mathrm{mW}$.

the purpose of LG beam generation, phase holograms are desirable over intensity holograms due to simple phase structure of the beams.

The optical elements used for this purpose fall into two categories: 'static' optical elements such as spiral phase plates [46] and holograms written on colour photographic film [41, 47] and glass plates; and the 'dynamic' liquid crystal spatial light modulators (LC-SLM). Static optical elements are simple to align, relatively cheap and can offer high efficiencies. They are limited however, in that they will only produce one beam; in order to change the indices of the LG beam, a different optical element must be inserted into the system. Although this may be acceptable for studies involving single LG beams, it poses difficulties for studies involving numerous LG beams. LC-SLMs, however, are dynamic and are therefore ideally suited for comparative investigations using different index LG beams.

4.4 Generation of LG beams using a phase modulating spatial light modulator

4.4.1 Introduction to spatial light modulators

As stated above, SLMs are dynamic optical elements that are able to spatially modulate light. The term spatial light modulator encompasses a wide range of devices, all of which will modulate either individually, or in combination, the phase, intensity, polarisation or direction of the beam. There are many different technologies used in SLMs and it is beyond the scope of this thesis to detail them. Therefore, only phase modulating liquid crystal based SLMs (LC-SLMs) are introduced in this section, as they are currently best suited to cold atom studies.

LC-SLMs, as the name suggests, use liquid crystals as the optical element performing the modulation. There are two main 'parameters' that govern the characteristics of LC-SLMs. The first is whether the liquid crystal display is ferroelectric and nematic. The second is how the liquid crystal is addressed which can either be electrically or optically.

Ferroelectric LC-SLM's offer very fast refresh rates, in the order of $1\,\mathrm{kHz}$, but are limited to binary pixel modulations; for example each pixel may be only able to cause a phase retardation of either 0 or π. High refresh rates are desirable for atom trapping experiments where it is required to move the potential well while atoms are trapped. For example Boyer and co-workers [48] use such a ferroelectric phase modulating SLM to generate multiple dipole traps for the controlled movement of Bose-Einstein condensates. For our application however, we do not change the potential during the course of the experimental run, so a high refresh rate is not required. The binary nature of ferroelectric SLMs limits the complexity of the hologram, which can reduce the quality and efficiency of the hologram. Nematic LC-SLMs are however not limited to binary modulation and the pixels can modulate the phase by varying amounts. This allows for higher efficiency and purer beam generation than ferroelectric LC-SLMs. In contrast to the ferroelectric LC-SLMs, refresh rates are limited to the order of $50\,\mathrm{Hz}$. For our application,

where more importance is placed on the characteristics of the beam and little on the refresh rate, a nematic SLM was preferable.

A key influence on the output of the SLM is as a result of how the liquid crystal is addressed. Electrically addressed LC-SLMs apply the voltage directly to individual electrodes on the liquid crystal. Consequently the profile on the LC-SLM is pixelated, corresponding to the defined areas of the electrodes. This pixelation on the hologram can result in unwanted diffraction effects. Optically addressed liquid crystals, however, use photoreactive electrodes (or similar), so that the voltage across the liquid crystal is dependant on the incident light. In order to generate a spatial variation in the voltage across the liquid crystal, the intensity of light incident on the photoreactive electrodes must have also have a spatial variation. This can be accomplished by using an intensity modulating SLM or an acousto-optic deflector to write a pattern on the photoreactive electrodes. Because the spatial variation is produced optically, it can be engineered to have a reduced pixelation effect.

4.4.2 Hamamatsu x8267 SLM

The SLM used in this study was a Hamamatsu x8267 'Programmable Phase Modulator'. The modulator consists of an optically addressed 'Parallel Aligned Nematic Liquid Crystal Spatial Light Modulator' (PAL-SLM). The PAL-SLM is optically addressed by a laser diode module, the output of which is modulated by an electrically addressed intensity modulator and then coupled using a lens to the PAL-SLM. All these devices are self-contained within the system; a schematic of which is shown in figure 4.7. The optically addressed design of the SLM results in there being no LCD pixel structure in the output. The physical size of the active area on the SLM liquid crystal is $20\ \mathrm{mm} \times 20\ \mathrm{mm}$ and has a resolution of $768 \times 768 = 589,824\ \mathrm{pixels}$.

The SLM is powered and controlled by an external drive box. The output of the PAL-SLM is set by feeding the drive box a $1024 \times 768\ \mathrm{pixel}\ 8$ bits per pixel grey-scale 'Extended Graphics Array' (XGA) analogue computer display standard signal. This was easily accomplished by connecting a laptop computer to the drive

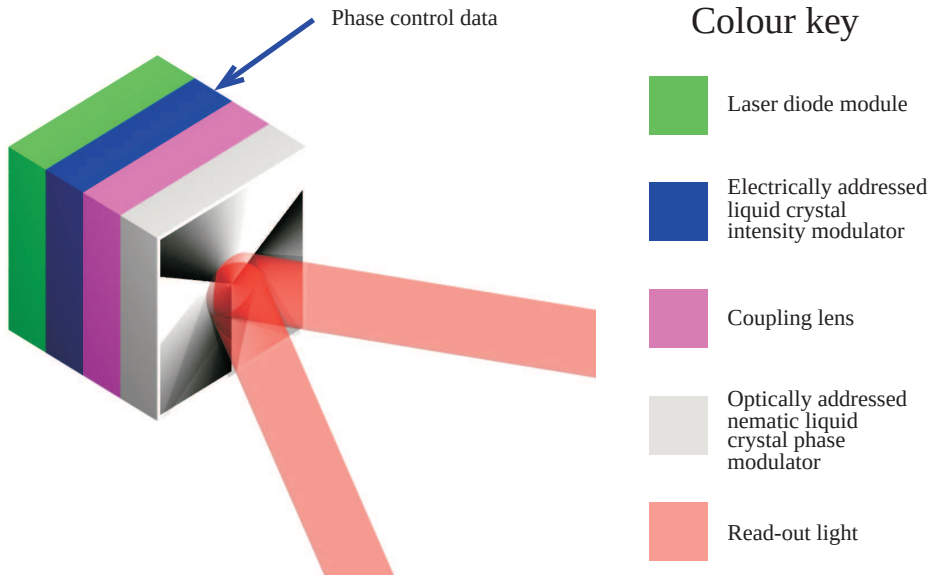

Figure 4.7: Schematic of the Hamamatsu x8267 spatial light modulator. This phase modulating SLM is optically addressed by the intensity modulated output from a laser diode. The intensity modulation is accomplished using an electrically addressed SLM. Pixelation effects are reduced by the coupling lens.

box, with the computer configured to output the appropriate resolution signal on its auxiliary monitor port. Pixels on the SLM will be set to a 0 phase shift for the black pixels of the image and scale linearly up to a 2π phase shift for the white pixels. As the resolution of the signal exceeds that of the PAL-SLM itself, the area of the input image corresponding to the hologram should only be $768 \times 768\,\mathrm{pixels}$ and be centred on the screen.

4.4.3 Calculation of the LG phase hologram

The SLM modulates incident readout light on reflection of linearly polarised light from the SLM. In order to generate the desired LG beam, the SLM must be addressed so that the readout light will be imprinted with the appropriate phase information upon reflection from the SLM. The complex amplitude $A\left(r\right)$ of the

readout beam upon reflection from the SLM can be described by [16],

$$A(r) = A_0(r)\, e^{i\psi(r)} \tag{4.7}$$

where $A_0(r)$ is the complex amplitude of the beam incident on the SLM; and $\psi(r)$ is the phase modulation on the SLM.

For our experiment, where we needed to generate LG beams with constant $p = 0$ and a variety of values of l, $\psi(r)$ can be simply made equal to the phase structure of the LG beam, $l\phi$, as given by equation 4.1. The function defining the phase profile on the SLM for a simple LG beam with $p = 0, l > 0$ can therefore be defined thus,

$$\psi(r) = mod(l\phi, 2\pi), \tag{4.8}$$

where $mod(m, n))$ gives the remainder on division of m by n.

However, it is not wise to use this simple phase profile, due to the existence of the reflected beam from the front surface of the SLM. As this beam does not pass through the liquid crystal it is unmodulated and retains its Gaussian shape. The presence of this reflected beam, which follows the same path as the modulated beam, means that it is impossible to achieve a completely dark core.

Therefore, in addition to the phase profile of the LG beam, it is beneficial to add the phase profile of a blazed grating. The blazed grating preferentially diffracts the output from the SLM into the first order, thereby removing the problem of the reflected Gaussian beam. The function defining the phase profile on the SLM for a simple LG beam with $p = 0, l > 0$ with a blazed grating of period Λ (defined at distances far away from the hologram's fork) can be defined thus [41],

$$\psi(r) = mod\left(l\phi - \frac{2\pi}{\Lambda} r\cos\phi, 2\pi\right). \tag{4.9}$$

Figure 4.8 shows an example of an $l = 1, p = 0$ and an $l = 6, p = 0$ LG beams with 15 line blazed grating. As can be seen in the figure, a phase singularity still

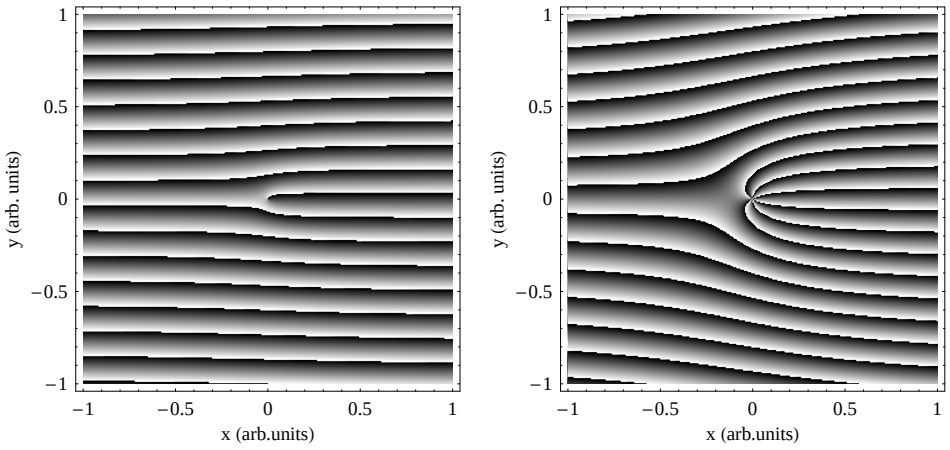

(a) $l = 1, p = 0$ (b) $l = 6, p = 0$

Figure 4.8: Phase holograms for $l = 1, p = 0$ and an $l = 6, p = 0$ LG beams with 15 line blazed grating. A phase singularity can been seen at the centre of each hologram.

exists at the centre of the hologram.

In this study, the holograms were generated using a LabVIEW program written by David McGloin.

4.4.4 Experimental considerations

The deflection of the beam, as a result of the grating can be increased by raising the number of lines on the grating. However, the efficiency of the diffracted 1st order is reduced as the number of lines is increased. This is due to the finite resolution of the PAL-SLM; as the number of lines is increased, the number of pixels between each line decreases, limiting the number of phase steps between each line. Table 4.1 shows measured values of the efficiency of the 1st diffracted order for different numbers of lines on the grating. In practice the number of lines on the grating was kept constant for all holograms ensuring that we were able to change between holograms without any deviation in the beam path. The number of lines per hologram was selected to be the lowest value that resulted in the 1st diffracted order being spatially separated from the adjacent orders for all the

Number of lines in grating	**1st diffracted order efficiency**
20	72.5 %
30	66.5 %
40	62.1 %
50	59.6 %
60	57.3 %
80	53.0 %
100	48.1 %
150	38.5 %
200	27.4 %

Table 4.1: Efficiency of the 1st diffracted order from SLM for an $l = 2, p = 0$ LG beam for different number of lines in blazed grating. Reproduced from [27].

holograms. This ensured ensured that we had the maximum efficiency hologram without any interference between the beams.

In order to keep the holograms simple, they were calculated for an incident plane wave therefore assuming that the $A_0\,(r)$ term in equation 4.7 is constant. It was therefore advantageous to expand the Gaussian output of our laser as much as possible in order to make the wavefront as close to a plane wave as possible. However, expanding the beam too much would be counter-productive as it would have reduced the power hitting the SLM, and a compromise between highest power and lowest wavefront curvature was needed. For this experiment the incident Gaussian was expanded so that it just filled the SLM without clipping the edges. This gives the lowest wavefront curvature that does not result in a loss of power in the beam. The quality of the LG beams was still observed to be high despite the deviation from the ideal plane wave. The fact that the corners of the holograms were not illuminated bears no consequence as the crucial phase singularity is situated at the centre of the hologram and no phase information was lost.

The SLM is designed to work with light reflected at normal angle of incidence. Although at normal incidence the blazed grating would spatially separate the first order from the retro-reflected zero order, the short space available on the optical table meant that it was necessary to have an additional method to fully separate the reflected beam from the incident beam. A beam splitter cube could have been

used to separate the beam, but it would have inevitably resulted in at least a $50\,\%$ loss of power as the incident and reflected beams invetiably share the same linear polarisation. The retro-reflected zeroth order beam could also have caused instabilities in the laser back along the beam line. Therefore, a more practical method, which solved the problems of spatial separation and feedback into the laser, is to direct the incident light on to the SLM at a small angle with respect to the angle of incidence, thus spatially separating the incident and reflected light. However, this must have caused a small path length change for the light and a concomitant change in phase shift. The deviated optical path through the hologram also will have reduced the quality of definition of the imprinted phase, as the light will not be travelling in the same plane as the boundaries of phase changes on the SLM. Despite this, we observed no discernable degradation in the LG beams for an angle of $\sim 5\,^{\circ}$.

4.5 Experimental Design

4.5.1 Experimental aims

The aim of this experiment was to detect and measure the fluence of dropped clouds of cold rubidium-85 atoms, created using a MOT, when dropped under gravity within various l index LG beam guides. In order to carry out a meaningful accurate study, the inner ring diameter of the LG beams was equalised.

For our experiment we needed the appropriate laser and optical set-up to generate the cold atoms. In addition an ultra high vacuum chamber was needed that had sufficient optical access to create the cold atom cloud and to allow in the LG guide beam and detection beams.

4.5.2 Chosen LG beam parameters

In order to guide the most atoms possible, it was decided that the inner ring diameter of the beams should be marginally bigger than the diameter of the cloud,

l **index**	**Dipole potential at detuning of**		
	2 GHz	**5 GHz**	**8 GHz**
3	$5.1\,\mathrm{mK}$	$2.0\,\mathrm{mK}$	$1.3\,\mathrm{mK}$
5	$6.6\,\mathrm{mK}$	$2.7\,\mathrm{mK}$	$1.7\,\mathrm{mK}$
12	$10.4\,\mathrm{mK}$	$4.2\,\mathrm{mK}$	$2.6\,\mathrm{mK}$

Table 4.2: Calculated values of dipole potential wall experienced by rubidium-85 atoms within $l = 3, 5, 12$ LG beams with fixed inner ring diameter of $2.2\,\mathrm{mm}$ at detunings of $2, 5, 8\,\mathrm{GHz}$. The power of the guide beam is $350\,\mathrm{mW}$. The potentials are expressed in Kelvin ($1\,\mathrm{K} = 6.9 \times 10^{-24}$ J) and are calculated using equation 4.10.

which was approximately $2.2\,\mathrm{mm}$. A ring diameter of $2.2\,\mathrm{mm}$ was chosen. LG beam parameters were picked to be $l = 3, 5, 12$ and detunings of $2, 5, 8\,\mathrm{GHz}$ were used. The calculated propagation distances required for the radius of the inner ring to double are: $5.6\,\mathrm{m}$ for the $l = 3$ beam; $3.4\,\mathrm{m}$ for the $l = 5$ beam; and $1.4\,\mathrm{m}$ for the $l = 12$ beam. Over the $30\,\mathrm{mm}$ guiding distance, the $l = 12$ beam, which is the most diffracting, only increases in size by $0.068\,\%$. Consequently all these beams were be considered to be a non-diffracting, constant diameter tubes over the $30\,\mathrm{mm}$ guiding distance.

Using equation for the dipole potential (equation 2.21) and the equation for the inner ring intensity (equation 4.5), the dipole potential U_{dipole} of the inner ring is given by,

$$U_{\mathrm{dipole}} = \frac{\hbar\gamma^2}{8\delta I_s}\frac{P_0}{\pi r_{\mathrm{inner}}^2}\frac{l^{l+1}\exp\left[-l\right]}{l!}. \tag{4.10}$$

Table 4.2 shows the values of U_{dipole} for our chosen beam parameters, given that the power of the beam within the trap is $350\,\mathrm{mW}$.

As the cloud temperature is at the hottest $\sim 300\,\mu\mathrm{K}$, the potential walls of all these guides were sufficient to confine the atoms. It was assumed however that the atoms would experience heating within the guide and may gain enough kinetic energy in the transverse direction to escape break through the potential walls.

4.5.3 Vacuum Chamber

The guiding chamber needed to have sufficient optical access to allow the insertion of the MOT beams, LG beam and an optical probe detection beam; and to accommodate observation cameras and the photon multiplier tube used to measure the amount of scattering from the detection beam. It also needed to be large enough to allow the transport of atoms over a distance of $\sim 30\,\mathrm{mm}$. The guiding chamber was a custom made 'drum' shaped stainless steel UHV piece, constructed by Thermo Vacuum Generators (now known as VG Scienta). As with all of our UHV pieces, the ConFlat flange standard was used. The drum piece had an inner diameter of $158\,\mathrm{mm}$ and a depth of $170\,\mathrm{mm}$. Two windows were bolted to the ends of the drum and eight access ports were positioned around the circumference. Six of these ports were sealed using windows.

One of the remaining ports was connected, via standard UHV pieces, to a $20\mathrm{l}\cdot\mathrm{s}^{-1}$ ion pump (Varian, model: VacIon Plus 25, Triode, 911-5030) running at a $3\,\mathrm{kV}$ bias. The ion pump was controlled by an ion pump controller (Varian, model: MidiVac controller, 929-5002), which also gave a continuous readout of the ion pump current. The ion pump current was proportional to the pressure of the system and was used to monitor the pressure in the chamber.

The other port was connected via a standard T-piece to an 16 pin electrical feedthrough. Three rubidium getters (see section 3.3.3) were attached to the vacuum side of 6 of the pins. Only one getter was run at a time, but due to the long turn around time for vacuum systems, it was prudent to have multiple getters. Getters may run out of rubidium after a few months of daily use, or may be unusable due to a defect.

Figure 4.9 shows an exploded diagram representing the entire system. The system was prepared and baked down as described in section 3.3.4.

4.5.4 Anti-Helmholtz magnetic coils

The large size of the trap and the need to maintain unobstructed optical access meant that the anti-Helmholtz magnetic coils had a large diameter of $\sim 140\,\mathrm{mm}$

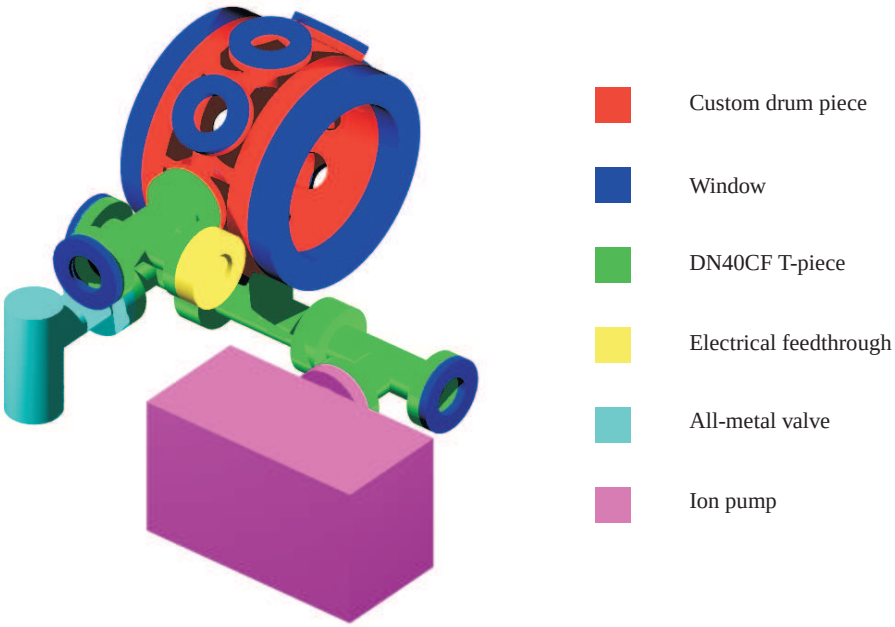

Figure 4.9: Diagram of the vacuum system used for the LG beam guiding experiment. The drum piece allowed excellent optical access for the cooling, guide and probe beams. Ultra high vacuum was maintained by an ion getter pump.

and were separated by $190\ \mathrm{mm}$. The coils were constructed from 83 turns of $1.5\ \mathrm{mm}$ diameter insulated wire and were mounted on aluminium mounts. In order to generate the required magnetic field of $\sim 10\ \mathrm{G}\ \cdot\ \mathrm{cm}^{-1}$, a current of ~ 15 amps was needed. A large amount of heat was given off by the coils and air cooling would not have been sufficient. Copper water pipes were attached to both coil mounts and were fed, via heavy duty tubing, high pressure ($120\ \mathrm{psi}$) water. This cooling method allowed the coils to run at ~ 15 amps with a steady state temperature of $\sim 35\ ^{\circ}\mathrm{C}$.

4.5.5 MOT laser systems and optics

The cooling and re-pump light was supplied by the TUI-100 laser/tapered amplifier based system and a homebuilt ECDL based system respectively. These laser systems are described in chapter 3. The cooling light passed through a me-

chanical shutter (see section 4.5.7) before being split into three beams, using two half-wave plate and polarising beam splitter pairs. The three beams were then directed directed into the trap in the three orthogonal directions. The light passed through a quarter-wave plate before entering the trap. The quarter-wave plates were adjusted so that the light possessed the correct circular polarisation (see section 2.3.4) and the half-wave plates adjusted so that each of the three beams had equal powers just before entering the chamber. On passing through the chamber, the light passed through a quarter-wave plate and was retro-reflected back into the trap, passing through the same quarter-wave plate again. In this geometry the retro-reflected beam automatically possessed the correct polarisation regardless of how the quarter-wave plate was rotated.

A single re-pump beam was directed into the trap through the top window of the chamber. From this direction the re-pump beam co-propagated with the guide. The re-pump beam was not shuttered and remained on during the guiding. As relatively few atoms were resonant with this beam, any detrimental heating effect due to scattering was minimal. The re-pump was beneficial for guiding at laser frequencies that lie between the cooling and re-pump transition. Detuning in this thesis is measured with respect to the cooling transition frequency. A laser frequency blue-detuned by less than $2\,\mathrm{GHz}$ from this frequency will be repulsive for majority of the atoms in the ground state of the cooling transition, but attractive for those in the ground state of the re-pump transition. As the re-pump beam served to the return atoms back into the cooling cycle, any losses due to this effect were minimised.

Figure 4.10 shows a representation of this set-up.

4.5.6 Guide beam

The guide beam was supplied by the Ti:Sapphire laser described in section 3.2.8. The beam was expanded to a diameter $\sim 20\,\mathrm{mm}$, so as to fill the SLM as much as possible without clipping the edges, and was directed onto the SLM at an angle of $\sim 5\,^{\circ}$. The LG beam output was passed through a region containing three pre-aligned lenses with focal lengths $f = 400\,\mathrm{mm}$, $200\,\mathrm{mm}$ and $150\,\mathrm{mm}$ all mounted

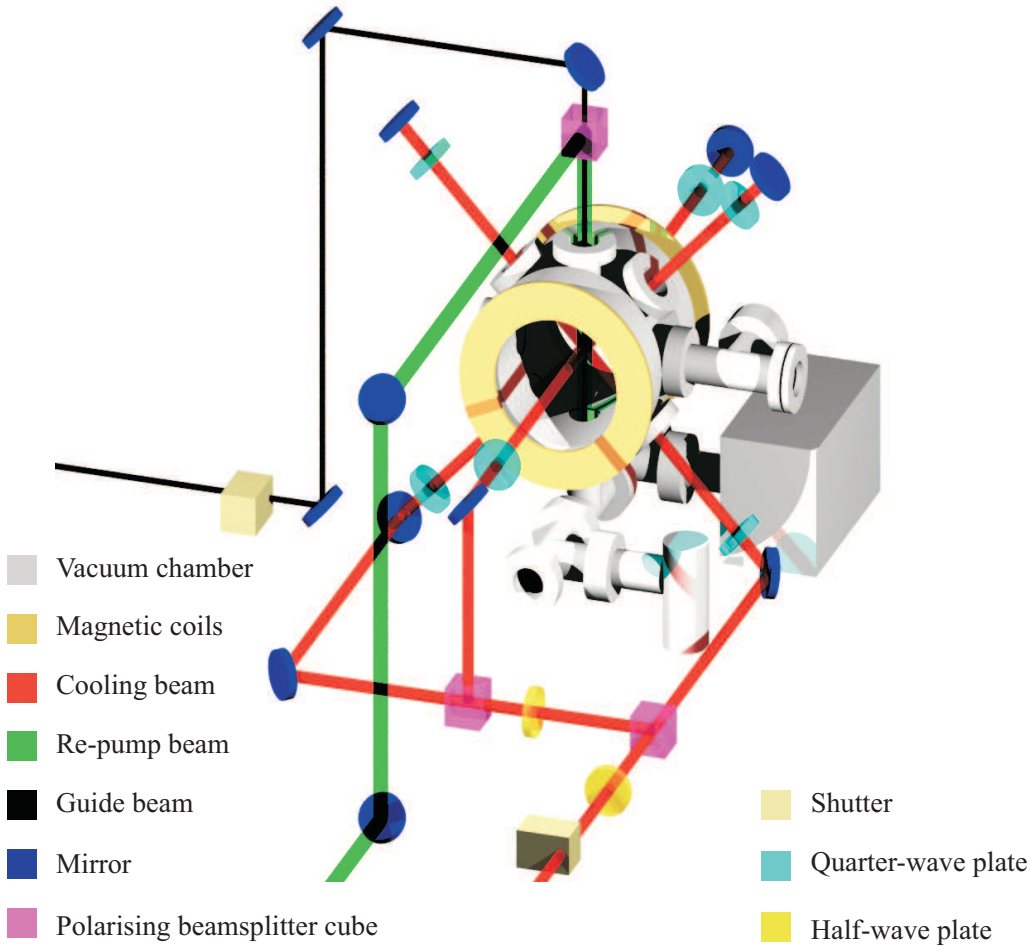

Figure 4.10: Diagram of the vacuum chamber, optics and laser beams for the LG guide experiment. The cooling beam, re-pump beam and guide beam laser systems are described in chapter 3.

on flipper mounts. A fourth lens with focal length $f = 300\ \mathrm{mm}$ was mounted on a permanent mount. The first three lenses were positioned so that their focal points all coincided with the image conjugate of the fourth lens; the combination of any one of the three lens and the fourth lens resulted in a telescope. The fourth lens then imaged the LG beam at the location of the MOT. As discussed earlier, in section 4.5.2, the LG beams were considered to be non-diffracting over the length scale of our guides. The magnification of this telescope could then be changed between three values by flipping the appropriate lens into position. These lenses were chosen so as to approximately equalise the inner diameter of the $l = 3, 5, 12$ LG beams to $2\ \mathrm{mm}$ for the purposes of the comparative study.

4.5.7 Mechanical Shutters

Mechanical shutters (Newport Corporation, model: 846HP) were used to switch on and off the cooling and guide beams. The shutters were triggered by a LabVIEW digital acquisition counter/timer card (National Instruments, model: PCI-6602) which was controlled by a LabVIEW virtual instrument program. A connector block (National Instruments, model: CB68LP) allowed the counter/timer card outputs to be connected easily to electrical wire. The counter/timer card was able to generate 0 to $+5\ \mathrm{V}$ outputs on eight channels. As the mechanical shutters opened on a positive voltage and closed on a negative voltage, two $+5\ \mathrm{V}$ card outputs are used to trigger a separate 'see-saw' circuit which then generated the required positive and negative control voltages. As the rise time of the shutters decreased as the control voltage was increased, the 'see-saw' circuit was designed to generate $30\ \mathrm{V}$ signals which resulted in a rise time of $\sim 2\ \mathrm{ms}$.

The LabVIEW VI was adapted from the pulse generator sub-VI included in LabVIEW version. The sub-VI was reproduced five times, and configured to send a $+5\ \mathrm{V}$ pulse on five channels. Two of the channels controlled the cooling beam's shutter, two controlled the guide beam's shutter and the last channel provided a trigger signal for the oscilloscope used to record the signal from the guided atoms.

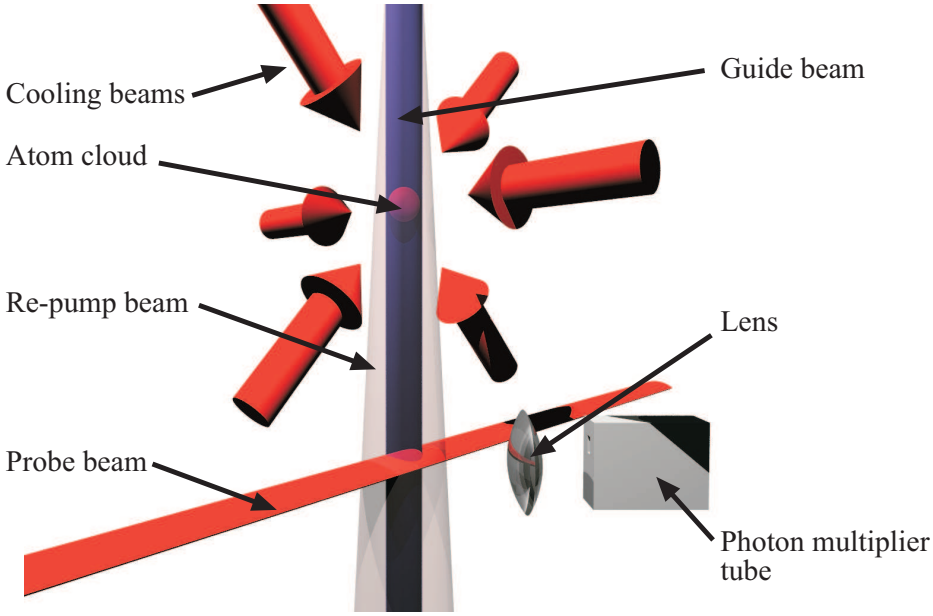

Figure 4.11: Orientation of the probe beam with respect to the MOT beams and cloud. The probe beam was $30\ \mathrm{mm}$ below the centre of the MOT. When the cooling beams were turned off and the guide beam turned on, the cloud of cold atom fell under the influence of gravity and the guide. As it passed through the probe beam, the photon multiplier tube detected the fluorescence.

4.5.8 Fluorescent detection of guided atoms using photon multiplier tube

An elliptical probe beam, of 'height' $1\ \mathrm{mm}$ and width $5\ \mathrm{mm}$, was formed using cylindrical lenses. This 'sheet of light' was directed in the plane perpendicular to the direction of travel of the free falling cloud, $30\ \mathrm{mm}$ below the centre of the MOT, as shown in figure 4.11. The probe beam was supplied by a third home built ECDL, saturated absorption spectroscopy and resonance locking system, which was locked directly to the cooling transition, i.e. unlike the cooling beams it did not need to be red-detuned. An area of fluorescence $4\ \mathrm{mm}$ in diameter, at the intersection of the centre of the guide and the plane, was imaged onto a photomultiplier tube (PMT). The voltage output of the PMT was recorded by a digital oscilloscope. The oscilloscope was triggered using the fifth channel of the pulse/counter card and was synchronised with the guide and cooling beams.

4.6 Experimental procedure

4.6.1 Forming the MOT

The cooling beams were aligned so that they were counterpropagating and overlapping at the centre of the trap and magnetic coils. The hyperfine beam was directed from the top window of the chamber so that it illuminated both the MOT but also the path of the dropped atoms. The alignment of these beams was relatively stable and only required irregular minor adjustments.

The cooling beam shutter was set to open and the guide beam shutter set to closed, using the LabView program. The lasers were locked to the appropriate transitions and the magnetic coils switched on. The rubidium getters were turned to a value between ~ 2 and ~ 4 amps. During a day of use, the current to the getters had to be increased in order to maintain the same output flux of rubidium. The size of the cloud was monitored using the CCD camera (Pulnix) and photographic lens. If the size of the cloud was seen to be smaller than previously observed, the getter current was increased. The ion pump current was also monitored as this also indicated if there was less rubidium in the chamber. This also indicated if there was too much rubidium in the chamber; which would have reduced the cloud's size due collisions with excess rubidium.

4.6.2 Adjusting the guide beam

The guide beam shutter was set to open. The LG beam LabVIEW program controlling the SLM was set to generate the hologram for the desired LG beam. The appropriate telescope lens combination was set to generate the desired LG beam ring radius in the trap. The path of the LG beam was checked so that is centred on the 'top' and 'bottom' windows of the chamber and around the cloud. By setting the guide beam to a resonant frequency of rubidium-85, the location of the LG beam at the centre of the MOT could be easily visualised as the resonant guide light was seen to ablate the cloud. Beam steering mirrors were used to adjust the

alignment if necessary. The guide beam shutter was set to closed; the system was then ready for an experimental run.

4.6.3 Obtaining a data set

The shutters for cooling and guide beams were closed. The timings for the LabView shutter control program were set. On running the program, the cooling shutter opened for approximately 10 seconds allowing the cloud to increase to maximum size. The cooling beams' shutter closed and instantaneously, the guide beam's shutter was opened. The cloud of atoms was now free to fall under the influence of gravity and the LG beam. The falling atoms passed through the guide and through the probe beam. The oscilloscope, which was triggered at the start of the experimental run by the LabView shutter control program, recorded the output voltage of the PMT as a function of time.

4.7 Results

4.7.1 Overview

For the results presented below, the cloud was dropped a distance of $30\,\mathrm{mm}$, under the influence of various LG guides. An inner ring diameter of $2.2\ \mathrm{mm}$ was used, which was just larger than the diameter of the cloud. The data collected using the PMT and oscilloscope were then fitted to a Gaussian profile using a Mathematica program. The Gaussian fit program calculated the area under the graph, giving us a measure of the atomic fluence passing through the probe, and the time it took for the atoms to travel the $5\ \mathrm{mm}$.

Ten data runs were taken for each value of l index, detuning and guide diameter size; data runs were also taken for the dropped cloud without a guide. Of the ten runs taken for each combination of parameters, between two and ten of them were usable. Data runs were deemed unusable if the data were obviously wrong due to, for example, an unlocked probe beam or incorrect synchronisation of the shutters

and trigger signal. Runs were also deemed unusable if the Gaussian fit program was unable to fit a curve to the data; this usually happened when the choice of parameters yielded a low signal.

4.7.2 Dropped cloud discrepancy

When the data were analysed it was noticed that the dropped clouds took a average time of $\sim 93\mathrm{ms}$ to travel the $30\mathrm{mm}$ distance to the probe beam. This time however was much longer than the time the cloud should have taken to travel this distance under gravity alone $\sim 78\ \mathrm{ms}$. This margin of error was too great to attribute to a misalignment of the probe beam, as a $\sim 93\ \mathrm{ms}$ free fall time would equate to a distance of $42\ \mathrm{mm}$. Therefore another explanation was needed.

During the experimental runs, when cooling beams were turned off, allowing the cloud to fall, the magnetic field was left on. The force on an atom within a magnetic field B is given by,

$$F = g_F \mu_B M_F \vec{\nabla} B \tag{4.11}$$

μ_B is the Bohr magneton , M_F is the hyperfine state of the atoms; and g-factor $g_F = 1/3$ [45].

As the atoms' hyperfine states are unknown, the exact nature of this force can not be quantified, but with a magnetic field of $10\ \mathrm{G} \cdot \mathrm{cm}^{-1} = 0.1\ \mathrm{T} \cdot \mathrm{m}^{-1}$, the magnitude of the force is approximately $0.22 M_F F_{\mathrm{grav}}$, where F_{grav} is the force due to gravity. This suggests that if the atoms where in the $M_F = -1$ state, we would have an accurate explanation for the longer drop time; however further investigation would be needed to understand the situation fully.

4.7.3 Guided data

The data is presented in the from of two graphs, with figure 4.12(a) showing the time of flight data, and figure 4.12(b) showing the fluence data, for $2, 5, 8$ GHz detunings and $l = 3, 5, 12$ index LG beams.

As would be expected, the time of flight was generally seen to increase for all detunings as l was increased [2]. This effect was due to the transient kick experienced by the atoms as a result of the scattering force. For increasing value of l, the steepness and height of the potential wall formed by the LG beam increased. As l was increased, the atoms would have penetrated less distance into the guide before the height of the potential wall was sufficient to deflect them. Consequently, as the atoms spent less time in the optical field, the effects of radiation pressure were reduced. Similarly, for all three values of l, the time of flight was clearly seen to increase for lower detunings. As the scattering force is proportional to $1/\delta^2$ the reduction in detuning reduces the magnitude of scattering force. The time of flight for $8\,\mathrm{GHz}$ detuning sets were of the order of six times longer than the $2\,\mathrm{GHz}$ detuning sets, and were approximately $2/3$ the time of flight of the dropped cloud.

The results of the fluence data show that the reduction in the time of flight of the atoms had a significant influence on the number of guided atoms. For the 2 GHz run, as the l index was increased, and the effects of radiation pressure were reduced, not only did the time of flight increase, but the fluence decreased by $\sim 25\%$. This implies that as the cloud was falling within the guide, it was being heated, either by the guide itself or by collisions with the background rubidium atoms in the vacuum chamber. The less time the atoms were in the guide, the more were guided. This trend can also be seen by comparing the different values of detuning for fixed l. For all values of l, an increase in detuning resulted in a decrease in fluence. This correlates strongly with the trend seen in the time of flight data, where for all values of l, the time of flight was seen to increase with increased detuning.

There appears to be a slight discrepancy in the data for the fluence data for $5\,\mathrm{GHz}$,

[2] Although this trend is not so clear for the case of 8 GHz detuning; this was probably due to the low guided flux and poor signal to noise ratio for this detuning.

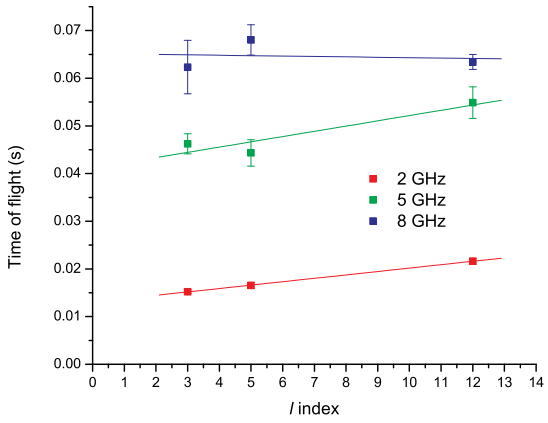

(a) Time of flight data.

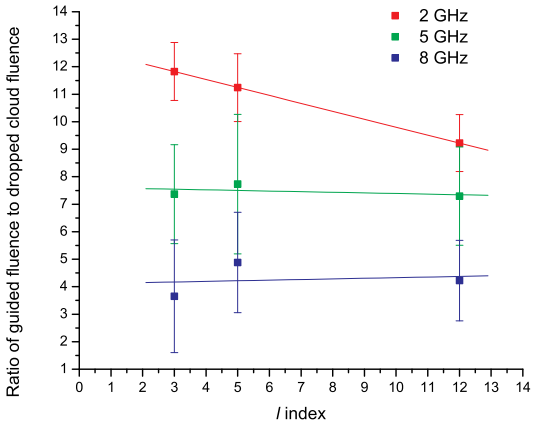

(b) Fluence data.

Figure 4.12: Fluence and time of flight data for $2.2\ \mathrm{mm}$ inner ring diameter $l = 3, 5, 12$ LG guides. The fitted lines show the overall trend of the data if the trend was linear. Error bars are plotted on the graph, but are too small to be shown for the $2\ \mathrm{GHz}$ data in figure 4.12(a). The time of flight was seen to increase for all detunings as l was decreased. The time of flight was also longer for higher detunings. Both these effects arose from the influence of radiation pressure; atoms within higher detuned and higher l guides experienced less of a radiation 'kick'. The fluence data indicated that the time of flight had a significant influence on the total number of atoms guided. Lower times of flight directly corresponded to higher fluence, as the cloud had less time to be heated by the guide or background rubidium atoms.

in that the fitted linear line was almost flat. As the time of flight data showed a strong dependency on the l index, it would have be expected that the fluence data would also exhibit a strong dependency. Nevertheless, the $8\,\mathrm{GHz}$ fluence data do appear to agree with our analysis, as although it was also relatively unaffected by different values of l, the time of flight data show this same dependency on l as well.

4.8 Conclusion

In this chapter I have explained the general properties of LG beams and how they can be used for atom guiding experiments. The role of the l and p index, in terms of the transverse beam profile and propagation characteristics were discussed. I explained how we created LG beams using a phase modulating spatial light modulator.

An experiment was described to compare the guiding properties of different azimuthal order l beams. The vacuum and optical set-up allowed a magneto-optical trap of rubidium-85 atoms to be formed. The vacuum chamber and optical set-up were detailed. I have shown that LG beams generated by a phase modulating SLM can guide cold atoms over distances of up to $30\,\mathrm{mm}$, with guided flux enhancement over dropped atoms of up to $\times 12$. The dynamic nature of the SLM allowed for the l index of the LG beams to be altered at touch of a button with no change of alignment.

Data were taken for $l = 3, 5, 12$ LG guides with an equalised ring diameter of $2.2\,\mathrm{mm}$ at detunings of $2, 5, 8\,\mathrm{GHz}$. The time of flight of the guided atoms was seen to be reduced by the increase in radiation pressure from lower l index guides and lower detunings. As a result of the atoms spending less time in the guide, the fluence was higher for guides with lower times of flight.

4.9 Author's contribution

This experiment was carried out during the first few months of my PhD and was primarily the work of Daniel Rhodes. I assisted in the day to day running of the experiment, which included the maintenance of laser systems and alignment of optics. I also carried out a number of data runs. My contribution warranted a second authorship on the published paper [45].

Chapter 5

DESIGN OF A HOT WIRE DETECTOR AND VACUUM SYSTEM FOR FIBRE GUIDING OF RUBIDIUM ATOMS

5.1 Chapter synopsis

This chapter details the design and construction of a hot wire detector and two vacuum systems designed to have the capability to detect and guide laser cooled and thermal rubidium atoms through hollow-core fibres. The detector was used in the atom guiding experiments detailed in chapter 6.

The method of operation of a hot wire detector is detailed. Platinum, tungsten and rhenium are investigated as possible hot wire materials for detecting rubidium, with rhenium being chosen. The channel electron multiplier used to detect the ions, emitted from the hot wire, is described. The method used to set the hot wire temperature is detailed. The hot wire detector was then designed, manufactured and tested.

Two variations of an ultra high vacuum system designed to facilitate the guid-

ing of atoms through hollow core fibres were constructed around the hot wire detector. Both vacuum systems were split into two chambers. A ‘source’ chamber containing the thermal and/or cooled rubidium atoms was orientated above a ‘detection’ chamber which contained an adjustable hot wire detector and channel electron multiplier. Between these two chambers was situated a mount which held two hollow-core fibres. Although the two variations of the chamber shared many common components, there were important differences with regard to the source chamber, and how the system was maintained at vacuum.

The first version of the vacuum system was designed to create and guide both cold and thermal atoms. The source chamber contained the optics, optical access and rubidium source needed to form a magneto-optical trap of rubidium-85 atoms. As I only had access to a single ion pump at the time, the two chambers were connected using a small diameter pipe. The system was found to have excellent characteristics for generating a stable MOT. The isolation was between the two chambers was less effective than was hoped; rubidium from the source chamber passed into the detection chamber and had a considerable effect on the background count of the hot wire. Although on one occasion rubidium was detected exiting the fibre, the system was too noisy to detect low flux levels as a result of optical guiding.

The second version of the vacuum system was designed to create and guide only thermal atoms. The source chamber had adequate optical access and a rubidium source, but did not need the intra-cavity optics used in the first chamber. With the addition of a second ion pump, the two chambers were isolated thereby reducing the amount of noise on the hot wire detector.

5.2 Motivation

Efforts with the aim of guiding rubidium atoms through the core of hollow-core photonic band gap fibres have been in progress within our research group since 2000. The motivation and theory for these experiments is discussed in chapter 6.

Over the years the experiment underwent a number of evolutions, as detailed in

chapter 6 and in thesis of my colleague John Livesey [49], but despite numerous improvements both in the design of the experiment and in the hollow-core photonic band gap fibres used, no guided rubidium was detected. With the experimental set-up having evolved to a stage where all other obvious prohibitive problems had been solved, it was decided that the detection system was the limiting factor in the experiment. In all the previous experiments, John had attempted to detect the guided atoms using the laser induced fluorescence detection method. While fluorescence detection methods are known for their high detection efficiency for cold atoms, they are susceptible to stray laser light, ultimately limiting the sensitivity of the technique [50]. In John's thesis [49], he calculated that the minimum detectable flux rate of his fluorescence detection system, was of the order of $10^7\,\mathrm{s}^{-1}$. He also estimated that, assuming reasonable efficiencies of the as yet unproven guide, the expected number of outputted atoms from the fibre should $\sim 5 \times 10^5$ with a maximum fibre output flux rate of $\sim 9 \times 10^5\,\mathrm{s}^{-1}$. The calculated sensitivity of the fluorescence detection system was therefore an order of magnitude less than the expected signal. We therefore concluded that there was a high probability that atoms were being guided, but that the sensitivity of the detection system was not high enough to detect them over the noise from the diffuse and specular reflection of the laser light off the glass and metal surfaces of the vacuum chamber, impinging on the photon multiplier tube (PMT).

In many of the previous successful fibre guiding experiments done outside of our group, the detection system used was a hot wire detector coupled with a channel electron multiplier [17, 18, 51, 52, 53]. Hot wire detection systems offer high detection efficiencies, are not sensitive to stray laser light and can be engineered so that they can be scanned across the aperture of the fibre; a technique used to estimate the transverse velocity of the atoms. However, their detection efficiencies are independent of the velocity of atom. Consequently they are susceptible to noise when detecting cold atoms as they will not discriminate between the low transverse velocity guided atoms and thermal background atoms. Aside from the expense of a channel electron multiplier, hot wire detectors are relatively inexpensive to build. However, as they are not commercially available they must be designed and constructed in-house.

Another related method also used with success in fibre guiding experiments involves photoionising the guided atoms and detecting the ions using a channel electron multiplier [54, 55, 56]. The main advantage of this technique is that it only photoionises atoms which are resonant with the laser beam. Consequently by using narrow linewidth lasers this type of detector could be set-up to detect only slow moving rubidium-85 atoms, thereby avoiding the unwanted detection of thermal background atoms within the system. Although the photoionisation method would have a superior signal to noise ratio over the hot wire detector, it would involve a greater outlay, as in addition to the cost of CEM, appropriate lasers would also have to purchased (if not already available).

Consequently, due to its previous success in similar experiments and its low cost in comparison to a photoionisation detector, it was decided that I should research and design a hot wire detection system for my experiment and incorporate it into a vacuum system designed for the guiding of atoms within a hollow core photonic band gap fibre. This chapter details that work.

5.3 Introduction to hot wire detectors

Hot wire detectors, which are also known as Langmuir-Taylor detectors, work in two stages; the hot wire ionisation stage and the detection stage.

The hot wire ionisation stage consists of a thin wire or ribbon heated to a high temperature by Joule heating. When an atom comes into contact with a metal, there is a chance that the valence electron(s) will become part of the metal, leaving an ion on the surface. Eventually, after a length of time known as the residence time, the ion will leave the surface of the metal. The hot wire ionisation process as shown in figure 5.1. The residence time decreases as the temperature is increased. For the case of an atom that has a lower ionisation potential than the work function of the metal, the ionisation probability will be close to unity for lower temperatures but will reduce as the temperature is increased. The equations governing these processes are discussed in sections 5.3.1 and 5.3.2.

The detection stage almost always consists of channel electron multiplier (CEM)

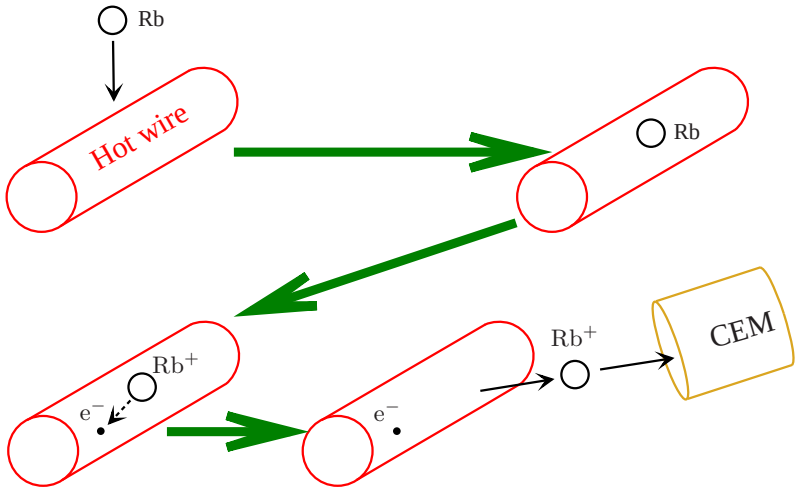

Figure 5.1: A graphical representation of the hot wire detector. The hot wire is heated by passing a DC current through it. When a neutral rubidium atom hits the hot wire, it may be ionised, with a probability given by equation 5.1. The ion will then be ejected after a residence time given by equation 5.2 and then detected by the CEM.

to detect the ion. Alternatively a microchannel plate may be used. CEMs have practically no dark noise (typically less than 0.1 counts per second) and have ion detection efficiencies ranging between $20\ \%$ and $90\ \%$, although this is a function of many parameters as will be discussed in section 5.5.1.

5.3.1 Ionisation potential

The probability P_+ that an atom will be ionised is given by the Saha-Langmuir law [50],

$$P_+ = \frac{1}{1 + \frac{g_0}{g_+} exp\left(\frac{I-\Phi}{k_B T}\right)} \tag{5.1}$$

where g_0 and g_+ are the statistical weights of the ion and atom ground states (for the case of alkali atoms $g_0/g_+ = 2$ [50]); I is the ionisation potential of the atom; and Φ is the work function of the metal used to make the hot wire.

Metal	**Φ (eV)**	**E_{ads} (eV)**	**τ_0 ($\times 10^{-13}$ s)**	**Melting point (K)**
Rhenium (Re)	4.96	2.88 ± 0.03 [57]	0.8 ± 0.3 [57]	3459
Platinum (Pt)	5.77	No data	No data	2041
Tungsten (W)	4.54	2.07 [58]	3.3 [58]	3695

Table 5.1: Values of the work function Φ, adsorption energy E_{ads}, τ_0 and melting point for tungsten, rhenium, and platinum. The absorption energy and τ_0 are specifically for rubidium on the metal.

The equation shows that the ionisation probability for a given atom is dependent upon only the temperature, the hot wire material and the atom's ionisation potential.

5.3.2 Residence time

The time that it takes for an atom to be ionised and then ejected from the surface of the hot wire is known as the residence time. The residence time is given by [50],

$$\tau = \tau_0 exp\left(E_{\mathrm{ads}}/k_B T\right), \tag{5.2}$$

where E_{ads} is the adsorption energy on the metal and τ_0 is a pre-exponential factor.

5.4 Choice of hot wire material

In order to choose the best hot wire material for rubidium, it was necessary to model the performance of the hot wire for different materials. The ability of the hot wire to ionise an atom is mainly influenced by three factors; the ionisation potential of the atom, the work function of the hot wire material and the temperature of the hot wire. As the laser systems within the laboratory were designed for rubidium, I was bound to using this atomic species for the experiment. Fortunately rubidium has the third lowest ionisation potential ($4.18\mathrm{eV}$) of the alkali atoms and

a number of metals, having a work function higher than the ionisation potential of rubidium, are potentially suitable for a rubidium detecting hot wire.

Aside from the ionisation probability and residence times, the melting point of the metal must also be considered. Firstly, it is obvious that the melting point had to be higher than the temperature of the hot wire during normal detection operation. But the wire also had to be able to sustain the high temperature 'burn-in' and 'flashes' that must to done to burn off impurities (from within the wire) and contaminants (from the vacuum system) which are on the surface of the wire. An initial 'burn-in' is carried out once the system is under high vacuum and before the hot wire is first used as a detector. 'Flashes' are carried out periodically during the operation of the hot wire to maintain the wire's cleanliness. Various procedures have been reported in the literature. Stienkemeier and co-workers reported that they left their hot wire at $\sim 2000\ \mathrm{K}$ between measurements to prevent contaminants settling on the wire [59]. Delhuille and co-workers only report that they flashed their wire at temperatures of $\geq 2200\ \mathrm{K}$ [50]. It was unclear from the literature whether the temperature required for these 'burn-ins' and 'flashes' varies depending on the metal, i.e whether the effect is a function of the work function or other purely the temperature. If the process involved surface ionisation, the temperatures needed would be different for each metal, but if the process is purely to due heat then the temperatures required should be same for all metals. Consequently, when choosing the metal I needed to consider the possibility that the hot wire would need to survive periods of temperature $\geq 2200\ \mathrm{K}$.

Three metals were considered for the hot wire: rhenium (Re), platinum (Pt) and tungsten (W). Platinum and rhenium were considered as they were both used as hot wire materials in previous rubidium fibre guiding experiments. In the capillary guiding papers of Renn and co-workers, they appear to initially use platinum, before changing to rhenium in later experiments. In the capillary guiding experiments of Ito and co-workers, a platinum wire was used. No details are given in the papers regarding their choice of metal. I also considered the use of tungsten; it would seem to be an obvious choice as it has the highest melting point of all metals and is a common filament material.

After the analysis detailed in the next section, rhenium was chosen as the hot wire

material. Although platinum had very slightly better ionisation probabilities than rhenium (due to platinum having a higher work function), its low melting point would compromise the wire's ability to survive the high temperature 'burn-ins' and 'flashes'. For tungsten, whatever small advantage that would gained from the metal's higher melting point would be offset by the far lower ionisation probability that resulted from its lower work function.

The following analysis also demonstrates that my decision to limit the choice to three pure metals was justified. Hot wires used to detect atoms with higher ionisation potentials than the work function of the pure metal wire, are sometimes made from oxidised metal wires, which have higher work functions. In the rhenium hot wire detectors that are used to detect lithium, which has a ionisation potential of $5.39\ \mathrm{eV}$, oxidising the wire can raise the work function from $4.96\ \mathrm{eV}$ to $6.09\ \mathrm{eV}$, thereby increasing the efficiency of the detector. The analysis shows however that high ionisation probabilities of near unity should be achieved using the non-oxidised pure metal and consequently no oxidation is needed. Indeed, having a hot wire with a work function greater than is needed would increase the chance that contaminants within the system would be ionised by the wire. Consequently, it is actually advantageous to not have a bigger work function than is necessary.

The sections that follow details the analysis that led us to conclude that rhenium was the best metal for the rubidium hot wire detector.

5.4.1 Rhenium

Figure 5.2 shows the theoretical ionisation probability and residence time of rubidium on a rhenium hot wire as a function of temperature. As can been seen from the graph, temperatures within the range $1263\ \mathrm{K}$ to $2488\ \mathrm{K}$ result in residence times below $1 \times 10^{-4}\ \mathrm{s}$ and ionisation probabilities above 0.95. At $1300\ \mathrm{K}$, which I decided was to be the operating temperature of the wire, the ionisation probability is 0.9981 with a residence time of $6 \times 10^{-5}\ \mathrm{s}$.

The melting point of rhenium ($3459\mathrm{K}$) is well above both the designated operating temperature and a typical burn in temperature of $2200\ \mathrm{K}$, and so would appear to

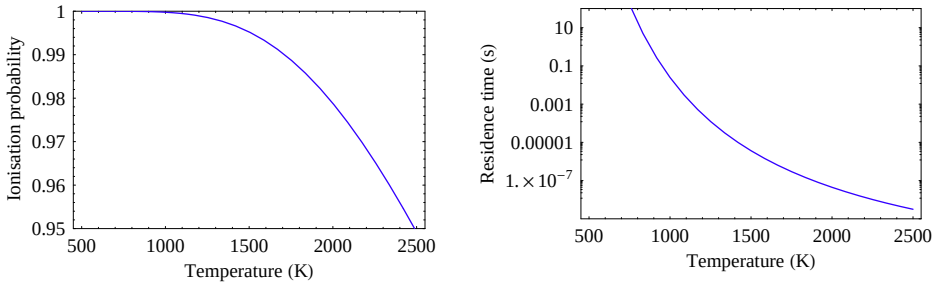

(a) Ionisation probability. (b) Residence time.

Figure 5.2: Ionisation probability and residence time of rubidium on a rhenium hot wire as a function of temperature. Calculated using equations 5.1 and 5.2.

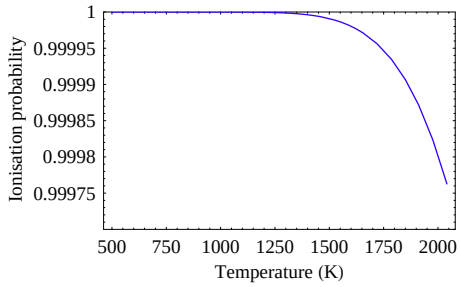

Figure 5.3: Ionisation probability of rubidium on a Tungsten hot wire as a function of temperature. Calculated using equation 5.1.

have the potential to form a long lasting and resilient hot wire.

5.4.2 Platinum

Along with rhenium, platinum is one of the main two metals commonly used in hot wire detectors. Figure 5.3 shows the ionisation probability and residence time of rubidium on a platinum hot wire as a function of temperature. As platinum has a higher work function than rhenium, for a given temperature it will have a higher ionisation probability. I was unable to find the needed data in the literature to calculate the residence time on platinum. However, as the residence time graph of rhenium and tungsten (shown in the next section) are practically identical, I assumed, with caution, for comparison's sake, that platinum had the same residence time graph as rhenium. Consequently, all temperatures greater than $1263\,\mathrm{K}$

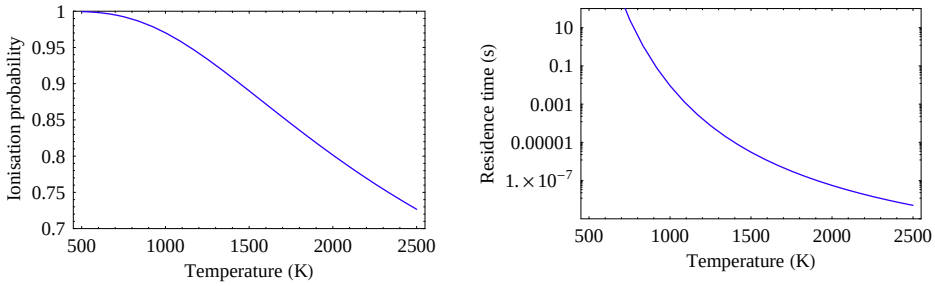

(a) Ionisation probability.

(b) Residence time.

Figure 5.4: Ionisation probability of rubidium on a Tungsten hot wire as a function of temperature. Calculated using equations 5.1 and 5.2.

(and below the melting point of $2041\ \mathrm{K}$) should result in residence times below $1 \times 10^{-4}\ \mathrm{s}$ and ionisation probabilities above 0.9997. Although these numbers are impressive, they only offer an increase in efficiency of $0.1\ \%$ over a $1300\ \mathrm{K}$ rhenium wire .

Platinum's usability as a hot wire would appear to be severely compromised by its comparatively low melting point of $2041\ \mathrm{K}$. Although it would be able to operate comfortably at the temperatures needed for normal use ($\sim 1300\ \mathrm{K}$), it would not be able to survive the 'burn-in' temperatures of $2200\ \mathrm{K}$. Consequently, rhenium must be favoured over platinum.

5.4.3 Tungsten

Tungsten would initially seem to have been the obvious choice for a hot wire as it has the highest melting point of all metals. However its low work function, in comparison to rhenium and platinum, results in much lower ionisation probabilities. Figure 5.4 shows the dependency of the ionisation probability and residence time of tungsten as a function of temperature. As can be seen from the graphs, temperatures resulting in residence times below 1×10^{-4} have ionisation probabilities below 0.937. Consequently, no advantage, save for the lower cost, would be gained by using tungsten instead rhenium.

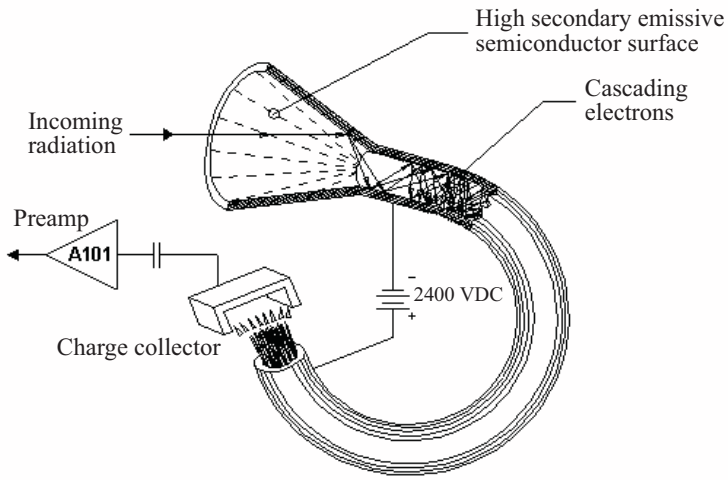

Figure 5.5: A schematic of the CEM representing the avalanche of electrons caused by a single input event. This figure is reproduced from the manual [60] of the CEM (Amptek, model: MD-502) used in my experiment.

5.5 Channel Electron Multiplier

The other important aspect of a hot wire detector is the channel electron multiplier, which is used to detect the ions emitted from the hot wire. CEMs typically consist of a ceramic, or glass, funnel with the internal surface coated in a high secondary emissive semi-conductive material. The entrance of the cone is typically held at a potential difference in the range of 1 to $3\,\mathrm{kV}$ with respect to the back of the cone, creating a continuous dynode. If a particle, be it an electron, ion or photon, hits the surface of the entrance cone with sufficient energy, the semi-conductive material will release, on average, 2 electrons. Due to the potential difference between the entrance and back of the CEM, the electrons will be accelerated along the CEM, creating an avalanche of secondary electrons as they bombard the walls. Consequently a single input event can trigger an avalanche of up to 10^7 electrons. These electrons are detected at the end of the funnel by another anode, known as the charge collector. Figure 5.5 shows a representation of this process. The charge on the collector of a CEM can detected and processed by external electronics in one of two modes: pulse counting mode, where the external electronics convert the signal into pulses representing the number of input events; and analogue, or cur-

rent measurement, mode, where the electronics convert the signal to an analogue output voltage.

A wide variety of commercial CEMs are available. However, stand-alone CEMs (i.e. CEMs that are supplied with the necessary electronics needed to run them) are rare, as CEMs are typically marketed to manufactures/consumers who need to combine the CEM with their own specialised equipment, such as mass spectrometers, and electronics. However, for this application, no advantage would be gained by designing my own external electronics and consequently I chose the only standalone CEM system available at the time. This CEM system (Amptek, model: MD-502 'Ultra-High Vacuum Electron & Ion Detector') consisted of the UHV compatible ceramic CEM which was contained in a stainless steel Faraday housing, a ceramic and gold UHV connector to facilitate the connection of the in-vacuum wiring to the CEM, and an air-side electronic controller. The electronic controller, which was powered by $9\ \mathrm{V}$ power supply, contained a high voltage DC/DC converter to supply the appropriate voltages for the anode and cathode, a charge sensitive pre-amplifier/discriminator and line driver to convert the signal on the collector to TTL output pulses and a circuit to generate test pulses. The electronic controller operated only in pulse counting mode, which was preferable for this application as I was interested in the accurate counting of discrete events. The CEM could be used for either ion or electron detection. In both cases a potential difference of $-2400\,\mathrm{kV}$ between the front and back of the CEM was kept the same, but the voltage of the CEM entrance with respect to 'ground' was changed so as to attract (repel) the wanted (unwanted) particles A switch on the remote electronic system set the appropriate voltages, as shown in table 5.2, for either ion or electron detection modes.

The dark count rate of the CEM system, i.e. the number of output pulses produced by the electronic box in absence of any stimuli, was $\sim\ 0.1$ counts per second, which is typical of CEMs in general.

	Ion mode	**Electron mode**
Cathode voltage	-2400 VDC	$+500$ VDC
Anode voltage	Ground	$+2900$ VDC
Collector voltage	Virtual ground	$+2900$ VDC

Table 5.2: CEM voltages for ion and electron detection.

5.5.1 Efficiency of CEMs

The absolute efficiency of a CEM is a complicated matter and is a function of many parameters: the type of particles being detected, how many detection events the CEM has experienced, the cleanliness of the CEM, any pre-acceleration potential in the system, the velocity and angle of the particles the input, and the mass to charge (m/z) ratio. Different individual CEMs, even of the same model, may also have different efficiencies. Consequently, it is difficult to fully predict the efficiency of the CEM. For the purposes of this study, where I did not have an accurate method of measuring the efficiency of the CEM, I turned to the literature. Amongst the numerous publications on CEM efficiency, the two most recent [61, 62] provide the most useful data for my experiment. In both these papers, the detection efficiencies are given as a function of kinetic energy and mass of the ion. Although neither of these papers provide data for rubidium, the clear relationship between the detection efficiency and the mass of the ion makes it possible to predict the efficiency for rubidium from the data presented. In the work of Krems and co-workers [62], the detection efficiency for a krypton ion with an energy $2.4\,\mathrm{keV}$ (the front of the CEM is biased at $2.4\,\mathrm{kV}$) is ~ 0.3. As krypton is only $1\,\mathrm{a.m.u}$ lighter than rubidium, I assumed that the efficiency is similar. In the work of Gilmore and Seah [61], the detection efficiencies of argon and xenon ions with energies of $2.4\,\mathrm{keV}$ are measured as ~ 0.54 and ~ 0.38 respectively. Give that the mass of rubidium is midway between these two atoms, the efficiency for rubidium will lie between these two values at around ~ 0.46.

The difference in measured efficiencies could possibly be a result of the Krems study having used a 20 year old CEM, which they measured to have a lower efficiency than a modern CEM. However, this illustrates the difficulty in fully predicting the CEM efficiency. Nevertheless, I assumed that the CEM efficiency was

0.38, the average of the two values.

5.5.2 Counting limits and damage threshold

For each discernible input event, the external CEM electronic unit will output a $+5\,\mathrm{V}$ pulse of width $220\,\mathrm{ns}$, with a pulse pair resolution of $250\,\mathrm{ns}$. Consequently, the CEM can sustain count rates of up to $\sim 4 \times 10^6$ counts per second before the counting statistics become non-linear, as the CEM electronics are unable to distinguish between the individual pulses. As the input flux is increased beyond this threshold, the output count rate will reduce to zero.

This behaviour was important to bear in mind, as large count rates which could damage the CEM could go unnoticed. The CEM could only sustain a total number of between 10^{11} and 10^{12} counts during its lifetime. Although this number seems high and could not realistically be achieved from the detection of the guided atoms, it can easily be achieved within seconds if the CEM is close enough to a source of thermionic electrons, such as the hot wire.

Aside from the potentially damaging effect of high flux rates, it would seem that lower flux rates of thermionic electrons could also add noise to the system as the CEM would not differentiate between counts generated by ions and those generated by electrons. However, the front surface of the CEM, when operated in ion detection mode, has a potential bias of $-2400\,\mathrm{V}$. As the energy barrier eV due to this potential is very much greater than the kinetic energy $3kT/2$ of the thermal ions (assuming that they were in thermal equilibrium with the wire before being ejected), this potential will act to prevent the electrons reaching the CEM.

However, it is still useful to gauge the influence of thermionic electrons on the CEM in absence of this potential, if only to understand the risks involved with accidentally switching the CEM to electron counting mode. The Richardson-Dushman law states that the emitted current density, $J\,(\mathrm{A}\cdot\mathrm{m}^{-2})$, of a metal with work function Φ at temperature T is given by,

$$J = AT^2 e^{-\Phi/k_B T} \tag{5.3}$$

where,

$$A = \frac{4\pi m k_B^2 e}{h^3} = 1.20173 \times 10^6 \ \mathrm{A \cdot m^{-2} \cdot K^{-2}}.$$

The number of electrons N_e given off by the wire is therefore given by,

$$N_e = 6.241506 \times 10^{18} A_{\mathrm{wire}} J \tag{5.4}$$

where $A_{\mathrm{wire}} = 1.18 \times 10^{-6}\ \mathrm{m}$ is the surface area of the $5\ \mathrm{mm}$ long hot region of the $75\ \mu\mathrm{m}$ diameter wire. Taking into account that the CEM was to be situated approximately $18\ \mathrm{mm}$ away from the hot wire and had an aperture of diameter $1.8\ \mathrm{mm}$, we can calculate the number of ions impinging on the entrance of the CEM as a function of temperature. Figure 5.6 shows a calculated plot of the number of electrons incident on the CEM due to thermionic emission. It shows that for high temperatures, considerable amounts of electrons would be directed towards the entrance aperture; at $2000\,\mathrm{K}$ the CEM would reach its lifetime fluence limit in approximately one second.

Consequently, despite the repulsive effect due to the bias on the front of the CEM, it would seem wise, considering the catastrophic consequences, to turn off the CEM during the 'burn-in' and 'flashing' periods in case the CEM was accidentally switched to electron counting mode.

At the designated running temperature of $1300\ \mathrm{K}$ the number of electrons hitting the CEM is calculated to be $\sim 1800\ \mathrm{s^{-1}}$. This calculated number was far higher than was experimentally measured later, with approximately 100 counts per second being measured when the hot wire was on (rubidium getters off) and the CEM operating in ion counting mode. This number increased dramatically, when the CEM was switched to electron counting mode, implying that the positive bias on the front of the CEM, when operating in ion counting mode, was indeed repelling the thermionic electrons.

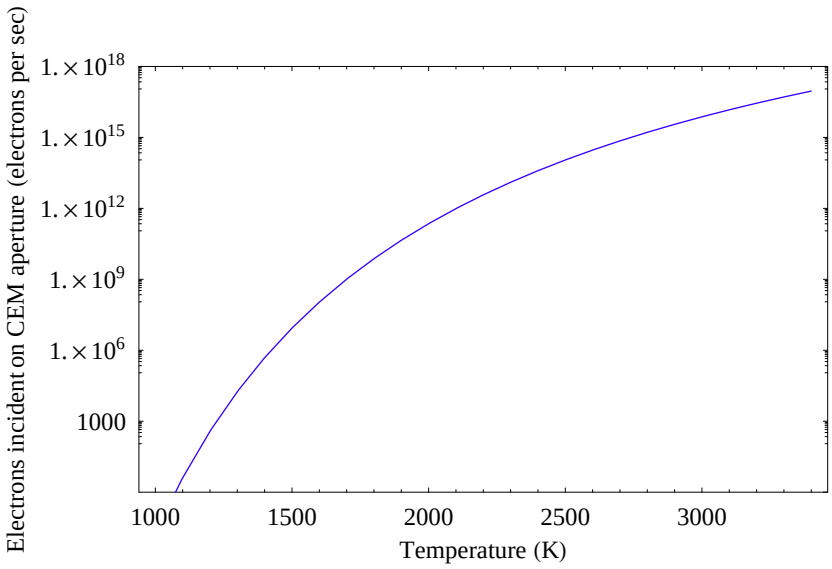

Figure 5.6: Number of electrons that would hit the aperture of the CEM due to thermionic emission when front of the CEM has no repulsive bias. When operating in ion mode the front of the CEM is biased by $-2400\,\mathrm{V}$. This potential repels most of the thermionic electrons.

5.5.3 Temperature of rhenium hot wire

Due to the sensitive temperature dependency of the hot wire's characteristics, it was necessary to have a method of knowing the temperature of the hot wire. Although measuring the temperature directly would have been almost impossible, I could have used an indirect measurement method, such as a pyrometer or spectrometer. Another method is to work out theoretical temperature of wire as function of the current. This was the method that I initially elected to use due to a lack of pyrometer or spectrometer and continued to use throughout the experiment due to its success.

The equilibrium temperature of a hot wire results from the equilibrium between Joule heating due to the current passed through the wire and radiative, conductive and convective loses [63]. As the wire was to be situated in UHV, there would be no convective loses due to background gas. Conductive loses could also be ignored, as the wire had a high surface area to volume ratio and was long com-

Description	**Temperature (K)**	**Current (A)**
Normal running temperature	1300	0.228
Typical flash temperature	1700	0.390
Melting point	3459	1.614

Table 5.3: Table of the hot wire temperatures used during the experiments and currents needed to generate them for the $75\ \mu\mathrm{m}$ diameter Rhenium hot wire.

pared to its diameter. The temperature of the wire would be lower near to its mounts/electrical contacts, but would be sufficiently close to theoretical model in the central region of the wire away from these contact. Consequently, it was a good approximation to model the equilibrium temperature as an equilibrium between Joule heating and radiative losses. In this case the equation linking the wire's temperature to the flowing current is given by [63],

$$T = \left(\frac{I^2 \rho}{2\epsilon\sigma\pi^2 r^3} \right)^{1/4} \tag{5.5}$$

where $\sigma = 5.670400 \times 10^{-8}\ \mathrm{W{\cdot}m^{-2}{\cdot}K^{-4}}$ is the Stefan-Boltzmann constant.

The resistivity and emittance of a material are functions of temperature. The approximate resistivity ρ of Rhenium between $1200 < T < 2000\ \mathrm{K}$ is fitted by the equation $\rho = 26.0 \times 10^{-8} \times (1 + 1.27 \times 10^{-3} \times T)$ [50]. The approximate emittance ϵ of Rhenium between $300 < T < 3000\ \mathrm{K}$ is fitted by the equation $\epsilon = 0.0852 \times (1 + 1.15 \times 10^{-3} \times T)$ [50].

The ratio ρ/ϵ, contained in equation 5.5 is a slow function of temperature and only changes by $\sim 1.1\ \%$ between $1500\ \mathrm{K}$ and $2500\ \mathrm{K}$. I therefore assumed that $\rho/\epsilon = 3.24 \times 10^{-6}\ \Omega{\cdot}\mathrm{m}$, which is the value at $1300\ \mathrm{K}$.

Therefore, for the $75\ \mu\mathrm{m}$ diameter hot wire, equation 5.5 reduces to the form,

$$T = 2722 \times \sqrt{I}, \tag{5.6}$$

where I is the current passing through the wire. Table 5.3 lists a number of temperatures

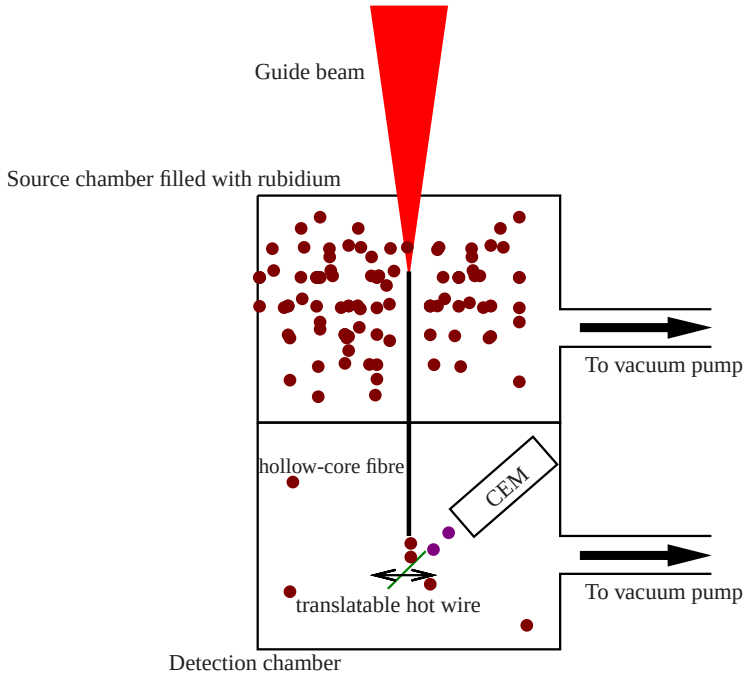

Figure 5.7: Concept of vacuum chamber. Thermal or laser cooled rubidium (not shown) is guided from the source chamber, through the hollow-core fibre into the detection chamber. The guided atoms are then detected by the hot wire and the CEM.

5.6 Vacuum system: Introduction and concept

Following on from John Livesey's work described in section 6.3, I continued to use a gravity assisted vertical guiding orientation. In this configuration, the vacuum system was split into two chambers, the source chamber sitting above a detection chamber, connected by a hollow-core fibre. The source chamber needed to have sufficient optical access for the guide beam and cooling beams (if needed) with the bottom holding a translatable hot wire and CEM. Both chambers needed to be maintained at UHV, and be relatively well isolated from one another to minimise migration (by paths other than through the hollow-core fibres) of rubidium from the source chamber to the detection chamber. A representation of this concept is shown in figure 5.7.

Two variations of an ultra high vacuum system based on this concept were de-

signed. Although they shared the same detection chamber, there were a number of differences with regard to the source chamber, and how the system was maintained at vacuum.

5.7 Design of hot wire mount and detection chamber

This section details the construction of the hot wire mount and detection chambers. Both the hot wire mount and detection chambers were identical for both versions of the vacuum system.

5.7.1 Requirements

I placed a number of requirements on the design of the hot wire mount. Firstly, as alluded to earlier in the chapter, a rhenium hot wire (Advent Research Material Ltd, model: RE545607) diameter of $75\ \mu\mathrm{m}$ was used. This diameter of wire is typical of hot wires used in fibre guiding experiments and allows for an acceptable resolution level when scanning the hot wire while still keeping the wire wide enough to intersect an adequate proportion of the atoms. The wire had a purity of $99.99\ \%$, and was annealed making it relatively flexible and resilient to manipulation.

Secondly, it was decided that the mount should hold two independently switchable hot wires i.e. two wires that could be turned on separately from each other. As the guided atoms will diverge when leaving the fibre, the distance between the fibre exit and hot wire plays an important role. As the hot wire detector was to be used in both cold atom guiding experiments and thermal atom guiding experiments, the resultant divergence would be vastly different for each case. Therefore I decided to have two wires separated vertically by $10\ \mathrm{mm}$ to allow us the choice between high detection sensitivity and high resolution when measuring the divergence of the guided atoms. The presence of the second wire also gave us a redundancy

in the system in case of premature breakage. This condition placed demands on the design of the mount as it needed to be able to provide an individual electrical supply to each wire.

Secondly, the hot wire had to be moveable, not only so that it could be scanned across the output of the fibre in order to profile the transverse velocity distribution of the atoms, but so that it could be moved away from the CEM during the initial 'burn-in' phase, when it was wise to keep the hot wire away from the CEM to avoid contamination. This condition placed demands on the mechanical rigidity of the mount as it needed to securely hold the $70\,\mu\mathrm{m}$ wire during these movements.

Finally, the hot wire mount needed to be able to be constructed from UHV compatible materials.

5.7.2 Design

The hot wire detector mount was designed so that it would fit in a (HxDxW: $35 \times 35 \times 35\,\mathrm{mm}$) 6-way 'cube' vacuum piece DN40CF (Caburn, model: 408008), which formed the backbone of the detection chamber. The system was designed so that the fibre would come through the top port of the cube, with the CEM positioned in the horizontal port facing the hot wire.

Figure 5.8, shows the design and dimensions of the hot wire mount. The hot wire mount was designed to provide the largest range of motion possible within the confines of the cube. The hot wire mount was designed to be attached to a linear motion vacuum feedthrough (Caburn, model: 660006), which had a adjustable in-vacuum arm length between $90\,\mathrm{mm}$ and $141\,\mathrm{mm}$, giving a range of $51\,\mathrm{mm}$. Attached to the arms of the linear translator was a stainless steel tuning fork shaped piece, that allowed the hot wire mount to be freely translated without touching the fibres. Attached perpendicularly and hanging straight down the arms of the 'fork', were short MACOR (a machinable ceramic with excellent UHV characteristics) arms. The MACOR material served two important functions. It has low thermal conductivity, which limiting the cooling effect of the mount on the hot wire. It is also an electrical insulator, and thus allowed the separately controllable hot

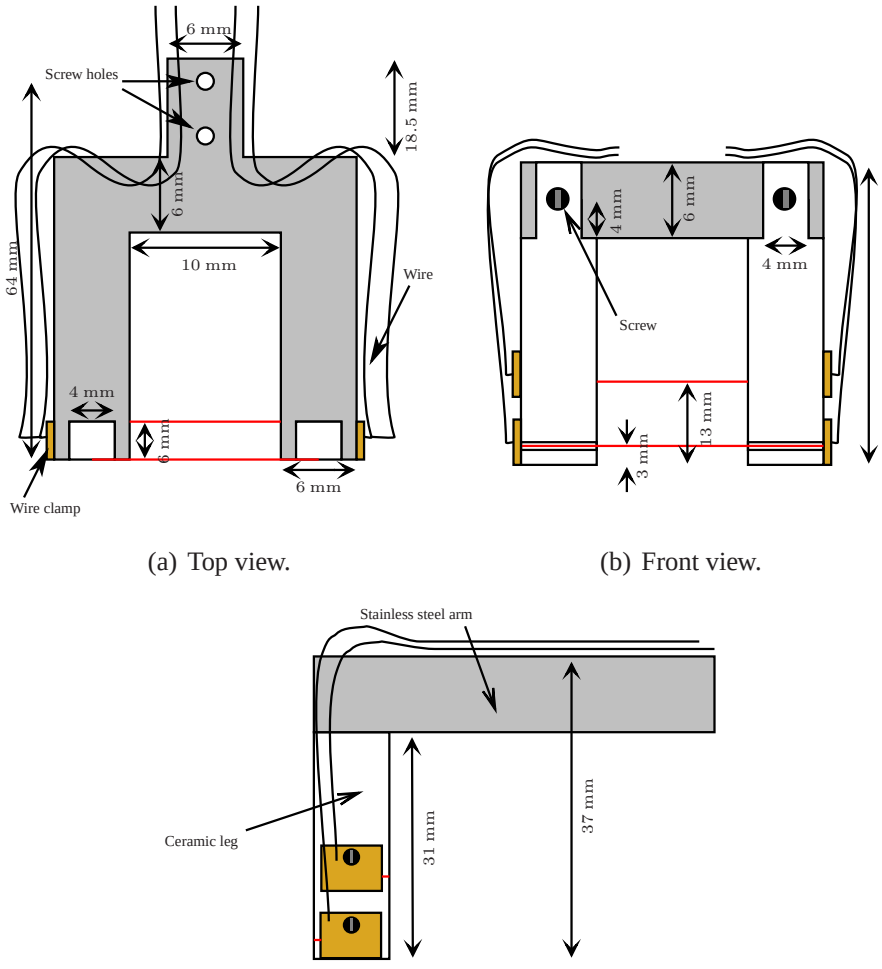

(a) Top view.

(b) Front view.

(c) Side view.

Figure 5.8: Schematic of the hot wire mount. The mount held two hot wires. The mount was attached to the arm of the linear translator by two screws. The cabling from the electrical contacts led to a electrical feedthrough.

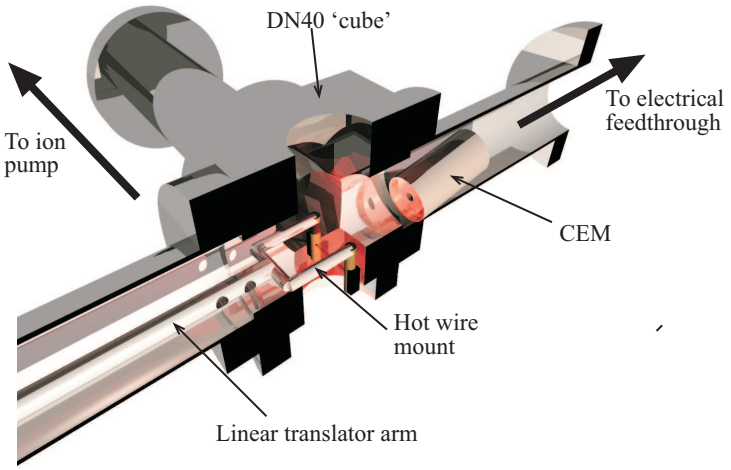

Figure 5.9: Diagram of the hot wire mount and channel electron multiplier as orientated in the detection chamber. The system was designed so that the fibre would hang down vertically through the top port of the cube. Not shown are the electrical feedthroughs.

wires to be attached to the arms without any additional electrical isolation. The hot wires were secured to the ceramic arms by separate copper contacts which screwed directly into the ceramic arm. Brazed onto these contacts were vacuum compatible Kapton coated wires, which led to a multi-pin electrical feedthrough.

The hot wire mount as it was situated within the detection chamber, is shown in figure 5.9. A $33\,\mathrm{l{\cdot}s^{-1}}$ ion pump (Varian, model: VacIon Plus 40, Triode, 919-0201) pump was used to maintain this chamber at UHV.

5.7.3 CEM Orientation and electrical feedthrough

The CEM was oriented facing the hot wire as shown in figure 5.10. Although the $-2400\,\mathrm{V}$ potential at the front of the CEM would attract the ions, I was unsure how strong this effect would be in deflecting ions initially emitted from the wire in the opposite direction. Consequently the CEM was placed as close as possible to the hot wire (at a distance of $18\,\mathrm{mm}$) and was angled downwards by $18\,^\circ$. Figure 5.10 shows that both hot wires were situated in the field of view of the CEM.

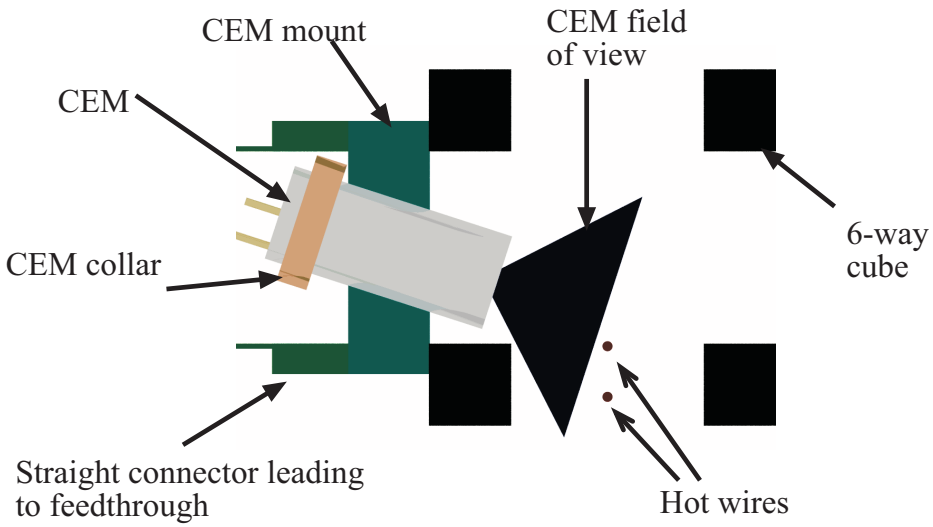

Figure 5.10: Orientation and field of view of CEM. The CEM is angled downwards by $18\,^{\circ}$. The front of the CEM is $18\,\mathrm{mm}$ away from the hot wire.

Due to the $2.4\mathrm{kV}$ potential needed for the CEM, the electrical feedthrough needed to be more robust than the multi-pin feedthroughs used for the hot wire and rubidium getter connections. The 4-pin electrical feedthrough used (Caburn, model: 9232004) was rated to $5\,\mathrm{kV}$ and used the SHV-5 (safe high voltage, $5\,\mathrm{kV}$ and $5\,\mathrm{A}$ maximum) connection standard on the air-side of the feedthrough. As the CEM controller is by nature very sensitive to charge, it is best to minimise the effects of electrical noise in the system. Consequently, I used a co-axial in-vacuum cable for the collector with non-shielded cables used for the anode and cathode. Although the feedthrough was designed to work with co-axial SHV-5 connectors on the air-side and proprietary co-axial connectors on the vacuum side, the 4 pins shared a common ground. Potentially, if all the shielded cables that were grounded at the point of the external controller were again grounded at the point of the vacuum feedthrough, a ground loop may have been formed. To avoid this eventuality, the cables were wired in the configuration shown in figure 5.11.

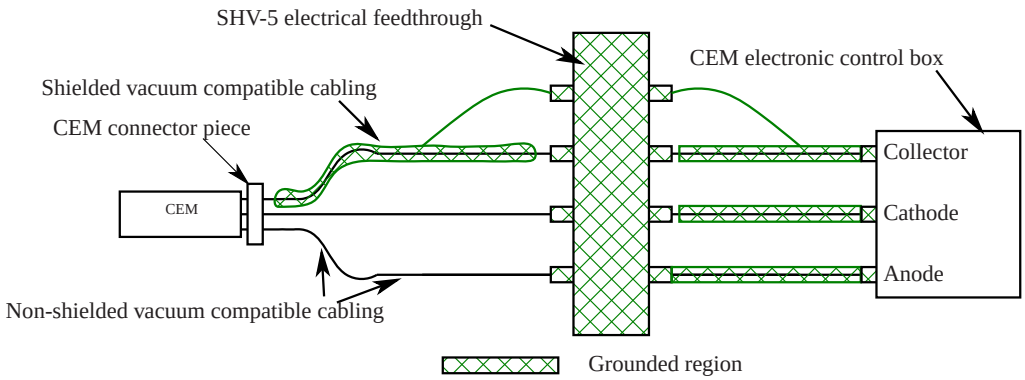

Figure 5.11: Illustration of the air-side and vacuum-side wiring between the external CEM control box and the CEM. The wiring is designed to minimised the impacts of ground loops. The 4th pin is utilised to provide an isolated ground for the in-vacuum collector cable.

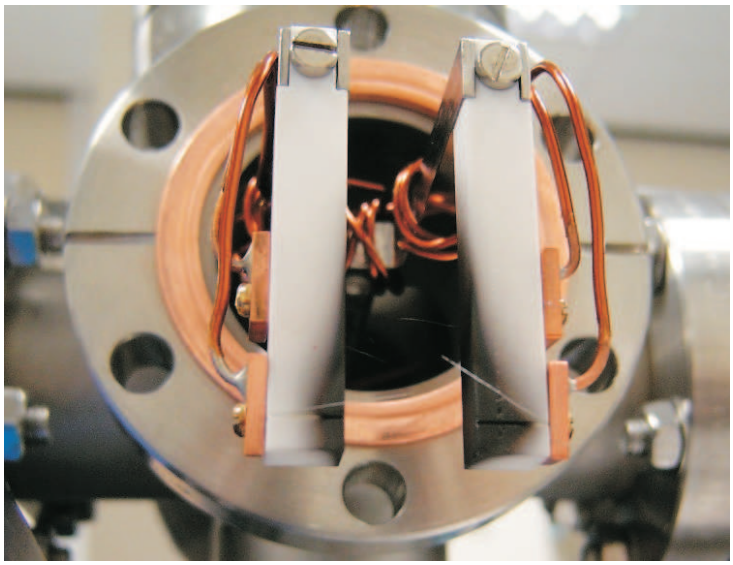

Figure 5.12: Photograph of the broken hot wire. It failed within a number of seconds after being raised to a temperature above $\sim 1000\ \mathrm{K}$. The ceramic arms became coated in a black/dark yellow residue, signalling the presence of rhenium heptoxide ($\mathrm{Re_2O_7}$) which is formed rapidly when heated rhenium when is exposed to air.

5.7.4 Initial tests

In order to confirm that the hot wire would operate how I expected, with regard to the temperature-current relationship and the manoeuvrability and longevity of the hot wire, I placed the hot wire and 'cube' in a simple vacuum system. For my first attempt, I pumped the system down for approximately ten minutes using the turbo-pump (Varian, model: Turbo-Dry 70) before closing the all-metal valve. I found however, that the hot wire would only survive for a number of seconds at temperatures above $\sim 1000\,\mathrm{K}$ before the wire would break midway between the two mount arms. In the process of breaking, the ceramic arms became coated in a black/dark yellow residue, as shown in figure 5.12, signalling the presence of rhenium heptoxide ($\mathrm{Re_2O_7}$) which is formed rapidly when heated rhenium when is exposed to air. As I assumed that this was due to the presence of air in the system, I decided to increase the vacuum by baking out the system and add a $33\,\mathrm{l{\cdot}s^{-1}}$ ion pump (Varian; model: VacIon Plus 40, Triode, 919-0201). During the bake-out of this second set-up it was discovered that I had not tightened the all-metal valve sufficiently in my first attempt, confirming my suspicion that the wire had oxidised. It is possible that the wire would have survived in the first set-up if the valve had been fully closed, as the turbo-pump should have evacuated most of the oxygen from the system.

By eye, the colour temperature of the hot wire appeared to match the theoretical temperature given by equation 5.6. The wire was heated to a maximum temperature of $2700\,\mathrm{K}$ (sustained for $10\,\mathrm{sec}$) and was left on for $9\,\mathrm{hours}$ at $1300\,\mathrm{K}$, without breaking. The hot wire mount was translated back and forth a large number of times without affecting the wire.

Although this test yielded no information about its capability to detect rubidium, it showed that the hot wire and mount were mechanically sound.

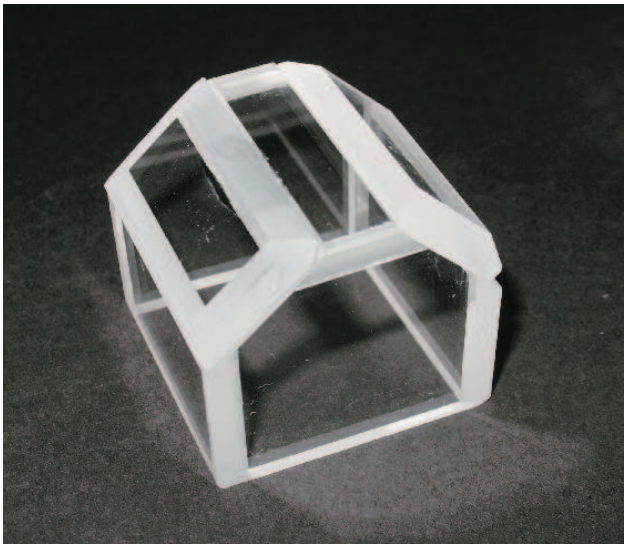

Figure 5.13: Modification for the cube used in the single ion pump vacuum system. The angled windows allow the cooling beam to pass through the glass at normal incidence.

5.8 Design of the source chambers

Two versions of the vacuum system were built. The two versions differed with regard to the source chamber and how the chamber was maintained at vacuum. The two versions were named the ‘single ion pump system’ and the ‘dual ion pump system’.

5.8.1 Design of single ion pump vacuum system

For the single ion pump system which was designed to perform both cold atom guiding and thermal atom guiding experiments, the source chamber system, as shown in figure 5.14, contained mounted mirrors and quarter-wave plates needed to generate a MOT. It also contained rubidium getters and an electrical feedthrough. Excellent optical access was needed in order to accommodate the MOT and guide beams.

A glass cube was attached to the flange. Due to the desire to keep the length

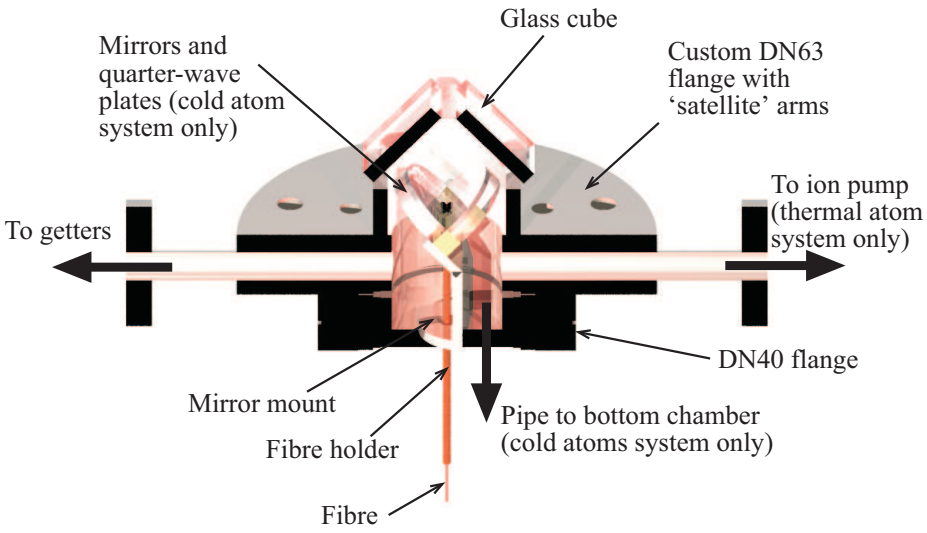

Figure 5.14: Diagram of the source chamber. In the single ion pump system, the glass cube was modified (as shown in this figure) so that the cooling beams windows were perpendicular to the beams. A pipe connected the source chamber to the detection chamber so that both chambers could be maintained at vacuum using the same pump. The dual ion pump system, was designed purely for thermal atom guiding, and consequently did not have the intra-cavity mirrors shown in this figure. The glass cube was not modified as no cooling beams were used. The source chamber, which was completely isolated from the detection chamber, was maintained at vacuum using a separate ion pump connected to one of the satellite arms on the custom made DN63 flange.

of the fibre as close to 8cm as possible, I directly glued glass cubes (Hellma, model:700.037 OG) to the metal flange, as described in section 5.8.3. The cube was sized (H x W x D) $15\ \mathrm{mm} \times 15\ \mathrm{mm} \times 15\ \mathrm{mm}$. Due to the orientation of the intra-vacuum MOT mirrors which are angled at 45° to the flange face, the top cube was modified in order to make the face of the glass perpendicular to the beams. This was done by cutting two 45° slices across the sides of the cube, leaving a 10mm diameter gap to allow the insertion of the guide beam. Two windows were then made from a another 'donor' cube and glued on to the cube to form an air tight 'glass house' using the EpoTek H70 epoxy. This modification was carried out by our glass blower Fritz Akerboom and is shown in figure 5.13.

A fibre holder, which held the fibre in place between the two chambers was de-

signed to have two main characteristics. Firstly, it needed to firmly hold the fibre to protect it and minimise movement. Secondly, the possibility of thermal rubidium migrating around the fibre and getting from the MOT chamber to the hot wire chamber needed to be minimised. The fibre holder was machined out of machinable glass ceramic called MACOR which has excellent vacuum characteristics. The mounts were machined to accommodate two fibres side by side. Having two fibres in the system gave us a redundancy in case one became damages or had become blocked during assembly or the bake out. The fibre holder was attached using a weak clamp to the mirror mount.

As I only had access to a single ion pump at the time, one ion pump (Varian, model: VacIon Plus 40, Triode, 919-0201) was used to maintain UHV in the whole system. Consequently, the source and detection chamber needed to be linked together in such a way that would allow the simultaneous pumping of both chambers but with minimal noise on the detector due to the migration of thermal rubidium from the MOT chamber into the hot wire chamber. A small diameter pipe led from the source chamber to the detection chamber where the ion pump was situated. The pipe was directed in such a way as to direct the rubidium towards the ion pump and away from the hot wire. The intention was that rubidium would migrate along the pipe, be directed towards the ion pump on exit, and be captured within the pump without influencing the hot wire detector.

5.8.2 Design of dual pump vacuum system

The dual ion pump system used the same detection chamber but small modifications to the source chamber and the way that the system was maintained at vacuum. As this vacuum system was designed to guide only thermal atoms, the intra-vacuum mirrors and wave plates were not included in the system. An unmodified glass cube was used as no cooling beams were required.

The main improvement of this system over the single ion pump system was the complete isolation (with exception of the hollow core of the fibres) between the source and detection chambers. Although the single ion pump system had been designed to minimise direct ‘line of sight’ pathways between the source and de-

tection chamber, I did not seal any small gaps as the two chambers were already connected via a pipe. However excess noise was a problem with the single ion pump system and I decided to remove all pathways between the two chambers. This was achieved by sealing all possible routes from the source chamber to the detection chamber using Torr Seal epoxy. The satellite arm on the DN63 flange, that was not used for the getters, as shown in figure 5.14, was connected to a second ion pump (Varian; model: VacIon Plus 25, Triode, 911-5030). This modification removed the effect of thermal rubidium migrating from the source chamber to the detection chamber.

5.8.3 Attaching the glass cell

In order to give us the optical access required for the MOT and guide beams, glass cells were used in the source chamber. Metal to glass vacuum seals are however notoriously difficult to make, due to the mismatch in thermal expansion coefficients of the two materials. In commercial components, this thermal mismatch is alleviated by using an intermediate Kovar joint or a stainless steel/graded glass transition. I was unable to use such a transition however as these seals can add $50\ \mathrm{mm}$ or more to each transition, potentially doubling the length of the $80\ \mathrm{mm}$ long fibre. As had been done in previous work within the group, it was decided to glue a glass cube directly to a flange.

The technique of directly epoxying glass cubes to flanges results in high failure rates, both within our group and elsewhere. During my period in the group, the failure rate was approximately 50%. The epoxyied cube typically fractured during the periods during or after thermal change. These periods occured during the high temperature curing of the EPO-TEK epoxy (described below) and the subsequent cooling down, during or just after the chamber bakeout. The cubes that survived the first few days after the bakeout were extremely reliable and survived for periods up to a year until the vacuum system was dismantled and they were forceable removed.

There are numerous UHV compatible glues available. For the single ion pump vacuum system, and the preceding chambers constructed by John, EPO-TEK H77

two component epoxy resin was used. Although this glue has proven to be form mechanically strong and air-tight vacuum seals and to produce negligible outgassing, it had a number of undesired characteristics. In order for the glue to cure in a reasonable length of time, it had to be cured at temperatures over $100\ ^{\circ}\mathrm{C}$. Consequently, the glue would cure when the glass and metal were thermally expanded; the glass cube would then experience a large amount of stress and strain as it cooled down to room temperature. This effect was further amplified by the rigid nature of the glue. Fracture rates for this glue during this work was $100\ \%$, however on one occasion I was able to patch up the fracture by epoxying a glass slide over the fracture areas. This patched cube then survived the subsequent return to vacuum.

For the dual ion pump version of the system, I substituted the H77 epoxy for Varian Torr Seal two component vacuum resin. This Torr Seal epoxy was chosen as it could be cured at room temperature, thus avoiding bonding the cube to the metal when they thermally expanded. Although this glue could not be baked over $120\ ^{\circ}\mathrm{C}$, which would be prohibitive for some bake-down procedures, my bake-downs did not typically go above $100\ ^{\circ}\mathrm{C}$.

5.9 Conclusion

A complete hot wire system and associated vacuum system was designed, as shown in figure 5.15. In order to maximise the hot wire detector's ability to detect rubidium, three different metals were modelled for the hot wire. Rhenium was shown to have the best characteristics. I calculated the temperature of the hot wire as a function of current. A moveable hot wire detector with two independently switchable hot wires was designed and manufactured. Two vacuum systems designed to contain the hot wire and guide cold and thermal atoms through hollow-core fibres were constructed.

In conclusion, I note the characteristics of my hot wire detector observed during the subsequent months of use.

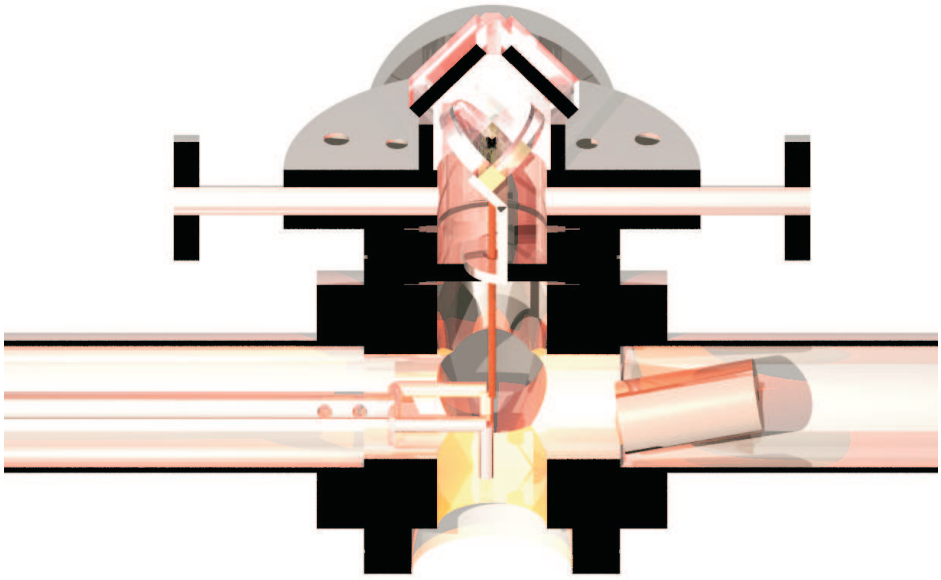

Figure 5.15: Diagram of the complete vacuum system. This diagram represents the single ion pump system, with small modifications carried out for the dual ion pump system, as discussed in section 5.8.2

Hot wire temperature

The hot wire temperature appeared to be well described by equation 5.5. The cooling effect of the hot wire mount meant that only the central $\sim 4\,\mathrm{mm}$ of the total hot wire length of $10\,\mathrm{mm}$ was glowing.

Burn-ins and flashing

Aside from the initial 'burn-in', which was required to initially clean the wire after being placed in vacuum, it was found that flashing was not necessary. The cleanliness of my system ensured that no contaminants came into contact with the hot wire while in the vacuum.

Hot wire noise

There were two distinct forms of hot wire noise. A slowly varying background noise was observed due to ionisation of rubidium and other background gas in the chamber. The magnitude of this noise was especially large in the single ion pump chamber and was influenced by the pressure of rubidium in the source chamber. This reading could vary from 300 to > 1000 counts per second. The dual ion pump system reduced this noise to approximately 130 counts per second, independent of the pressure in the source chamber. Transient bursts of noise were also observed, corresponding to the ionisation of contaminants in the wire as they migrated to the surface [50]. These bursts could be easily subtracted from data runs as they were easily distinguishable above the nominal count rate.

Sensitivity of CEM to electrical noise

My initial suspicion that the CEM and its electronic control box would be sensitive to electrical noise was confirmed. Unless all of the metal surfaces surrounding the CEM system were grounded, such as the vacuum system, CEM control box and optical table, the CEM control box would generate large quantities of pulses. I also noticed that the CEM would pick up noise from the ion pumps, with more noise being generated when the pump was drawing more current. This effect could only be fully removed by turning off the pump, however this action also stopped the formation of the MOT, due to loss of vacuum.

Ability to detect rubidium

In the next chapter I discuss the efforts made to guide rubidium through hollow-core fibres. Although largely unsuccessful, on one occasion rubidium was detected exiting the fibre. This result demonstrated that the hot wire detector was capable of detecting guided atoms. However, further work would be needed to calibrate and characterise the sensitivity of the detector.

5.10 Author's contribution

This work was carried out partly in conjunction with John Livesey. John contributed to the design of the 'glass house' cube, while the mirror mounts were a legacy from John's previous experiments. The overall design of the trap was greatly influenced by John's work and his conclusions. John also assisted in the construction and bolting together of one iteration of the trap. Steve Balfour, from our mechanical workshop, manufactured the pieces for the hot wire mount, with Steve, George Robb and Jimmy Lindsay (also from the workshop) carrying out some modifications to the vacuum pieces. Aside from this assistance, the design, construction and characterisation of the hot wire was carried out by myself.

Chapter 6

GUIDING OF ATOMS THROUGH HOLLOW-CORE PHOTONIC BAND GAP FIBRE

6.1 Chapter synopsis

This chapter details the work carried out with the aim of guiding rubidium atoms through hollow-core photonic band gap fibres. The properties of hollow-core fibre guides are discussed with comparison to free space guides. A brief introduction to hollow-core photonic band gap (HC-PBG) fibre is presented with details of the particular fibres used in this experiment. Two thermal atom fibre guiding experiments and one cold atom guiding experiment are attempted.

6.2 Introduction and motivation

The guiding of atoms through flexible hollow core fibres is of great importance to atom optics. Although free-space atom guides are relatively easy to align (as it is usually possible to situate all the optical elements outside of the vacuum chamber) and offer almost infinite flexibility to choose any desired guide shape

(using, for example, a spatial light modulator [16]), fibre guides have some useful and unique characteristics. The fibre may be used to form a variable throughput guide between two chambers that are hermetically isolated from each other, with only the small diameter hole of the fibre core linking them. By placing a bend in the fibre guide, it would also be possible to guide atoms around a curve. This curve would act as a longitudinal velocity filter as atoms above a certain longitudinal velocity threshold will not be guided around the bend. These properties suggest that such a method would be ideal for loading a high vacuum 'science' chamber with cold atoms from a 'source' chamber filled with thermal rubidium. Fibre guides are also well suited to generating atom interferometers. If the diameter of the potential barrier is similar to the de Broglie wavelength of the atoms, then it is possible to guide atoms in a single mode, analogous to the single mode guiding of light through optical fibres [64]. If a fibre was then constructed in the form of a Y-splitter then Y-combiner the coherent atomic ensemble could be made to split into two paths and then be recombined, forming a Mach-Zehnder interferometer [65]. If the matter waves of the two atomic beams in the two arms were still coherent, interference effects would be seen.

Inevitably, the core of any fibre based atom guide must be hollow. Prior studies of fibre guiding have been limited to using hollow core capillary fibres. For blue-detuned guiding, the light can be coupled into the silica annulus [18], or doped region [55], surrounding the core, forming an evanescent barrier to atoms. However, for red-detuned guiding, where the light must inevitably be confined to the core, hollow-core capillary fibres have limitations. Conventional silica fibres guide light in the core using total internal reflection (TIR), which is not possible in hollow-core capillary fibres where the core has an index of refraction less than the surrounding walls [1]. The first fibre guiding experiment by Renn and co-workers [17] used red-detuned light that was coupled into grazing incidence modes in the core of the capillary. These modes are formed from the weak Fresnel reflections from the air-silica interface. However, these modes suffer high

[1] Waveguides known as 'attenuated total internal reflection hollow waveguides' [66] are in fact able to guide light in a hollow core using TIR. The air or gas core which has a refractive index $n \approx 1$ is surrounded by a doped cladding, which for a narrow band of wavelengths has a refractive index of $n < 1$. However, these guides have only been demonstrated to work in the mid-IR range, limiting their usefulness.

attenuation rates as they are not truly guided modes. For the $40\ \mu\mathrm{m}$ diameter hollow capillary fibre used by Renn and co-workers [17, 51] the $1/e^2$ attenuation length was $\sim 3.1\ \mathrm{cm}$, which they estimate limits the distance over which atoms can be successfully guided to $\sim 20\ \mathrm{cm}$. This attenuation length is also inversely proportional to the cube of the hole diameter, which would further limit the effectiveness of the guides when attempting to guide atoms through a small core fibre in a single mode.

During the last decade, photonic crystal fibres (PCF) have proved to be a revolution in fibre technology. PCFs are characterised by their 2-dimensional periodic lattice of high and low refractive index regions in the transverse plane. PCFs generally fall into one of two categories; those which guide light by modified total internal reflection, known as index guiding fibres, and those which guide light using a photonic band gap, known as photonic band gap fibres. Index guiding fibres, a type of which known as endlessly single-mode photonic crystal fibre is used elsewhere in this thesis (see chapter 7), are unsuitable for atom guiding experiments as they invariably have a solid core. However, as photonic band gaps fibres guide light using a photonic band gap, there is no requirement for the core to have a higher refractive index than the cladding. Consequently, photonic band gap fibres can have cores with a lower refractive index than the cladding. Although solid core examples do exist [67], the majority are hollow-core photonic band gap (HC-PBG) fibres.

Although a new and evolving technology, these HC-PBG fibres would seem well suited to fibre guiding experiments. In contrast to the grazing incidence modes within capillary guides, the modes of a correctly engineered HC-PBG fibre would be essentially lossless over the distances that experimentalists would want to guide atoms. Additionally, it should be possible to make fibres with core sizes sufficiently small enough to guide atoms in a single mode. The aim of the work presented in this chapter is to investigate these HC-PBG fibres when used in atom guiding experiments.

Overall aim of the experiments

The aim of the following experiments was to guide rubidium atoms from one part of the vacuum chamber to another using the optical dipole force. As described in chapter 5, I elected to use a gravity assisted guiding geometry, where the source chamber was situated directly above the detection chamber, with the HC-PBG fibre connecting the two chambers. The hot wire, designed to detect the guided rubidium atoms, and the vacuum system are described in chapter 5.

Previous work has shown that it is possible to guide both thermal atoms [17, 18, 55] (i.e. non-cooled atoms, generally at room temperature or above) and cold atoms [53] (i.e. atoms that have been cooled using laser cooling techniques) through fibre guides. Thermal atom guiding experiments are generally easier to set-up as they do not require the complicated laser systems required for laser cooling. Cold atom guiding experiments, however, can produce higher guided flux rates due to the increase in the number of atoms with sufficiently low transverse velocity. In the rest of this chapter, I detail attempts at both thermal and cold atom guiding.

6.3 History of fibre guiding experiments carried out within group

Efforts with the aim of guiding rubidium atoms through hollow core photonic band gap fibres have been in progress within our research group since the year 2000. The experiments detailed in this chapter follow on from those performed by John Livesey in his successful pursuit of the PhD [49]. Consequently, by the time I 'inherited' the experiment a number of unsuccessful attempts had already been made to guide atoms through hollow-core photonic band gap fibres.

With the first demonstration of a HC-PBG fibre having only been made in 1999, early work within the group was hampered by the infancy of the technology. For the purposes of this experiment, the fibres needed to guide light a few nanometres either side of the resonant wavelength of rubidium at $780\ \mathrm{nm}$. Given that the di-

mensions of the crystal lattice must be on the length scale of the wavelength of the light, these fibres were more difficult to make than fibres guiding at longer wavelengths, as the dimensions of the fibre had to be scaled accordingly. It was not until after 2003, before Bath were able to supply us with a fibre (model: FB-BG-19c-800, described below) with adequate guiding characteristics in this wavelength range [68].

Aside from the improvements in the fibre technology, advances were also made in how the atoms were loaded into the fibre. The first guiding system attempted to guide thermal atoms (i.e. atoms at room temperature or above that were not cooled) through the fibre, in a similar configuration to that of Renn and co-workers. This was then replaced with an apparatus which facilitated the 2-D cooling (transverse plane) of the atoms, in theory increasing the number of atoms able to be guided. This was then superseded by an apparatus that attempted to load the fibre guide using a low-velocity intense source of atoms (LVIS) [69], created by an imbalance in the MOT beams. Although in theory this system should have been well suited to the experiment, in reality it was difficult to couple the LVIS into the fibre. At the conclusion of John's work, an apparatus was designed which enabled a fully formed MOT to be positioned directly above the fibre entrance, and then coupled into the fibre under the influence of the guide beam and gravity.

Despite this experimental evolution and the accompanied solution of numerous obstacles along the way, no guided atoms were ever conclusively detected. While the failure of the group's early fibre guiding experiments could always be attributed to a limiting factor, such as a poor fibre or an obvious flaw in the design of the experiment, the experiment had now evolved to a stage were there was no obvious reason why atoms were not being guided.

At this point our analysis of the situation led us to believe that atoms were being guided, but the number was too small to detect using the fluorescence detection system that had been used for all atom guide experiments in the group to date. In John's conclusions, he calculated that the expected number of outputted atoms from the fibre should be $\sim 5 \times 10^5$ with a maximum fibre output flux rate of $\sim 9 \times 10^5 \mathrm{s}^{-1}$. This value was an order of magnitude less than estimated sensitivity of the fluorescence detection method. This prompted me to design the hot wire

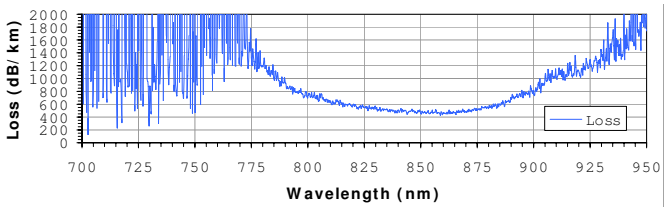

(a) FB-BG-7c-800 fibre. $8.9\mu\mathrm{m}$ core diameter.

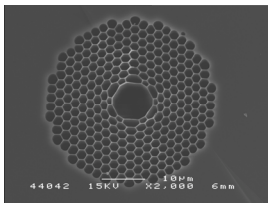

(b) SEM image of FB-BG-7c-800 fibre.

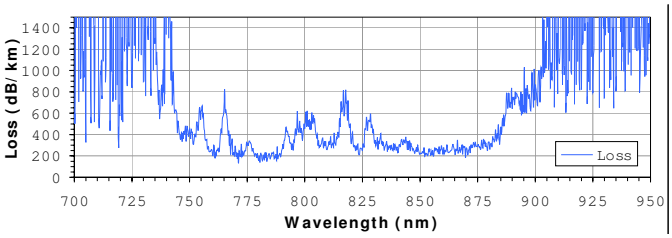

(c) FB-BG-19c-800 fibre. $11.7\mu\mathrm{m}$ core diameter.

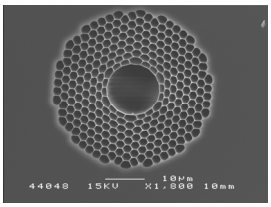

(d) SEM image of FB-BG-19c-800 fibre.

Figure 6.1: Transmission losses and scanning electron microscope (SEM) images of the hollow-core photonic band gap fibres supplied by our collaborators in Bath.

detector and improved vacuum systems as detailed in chapter 5. The experiments in this chapter detail the application of these systems to fibre guiding experiments.

6.4 Hollow-core photonic band gap fibres

6.4.1 Introduction to HC-PBG fibres.

As stated above, hollow-core photonic band gap (HC-PBG) fibres are fibres that guide light within a hollow core by means of a photonic band gap. Figures 6.1(b) and 6.1(d) shows scanning electron micrographs of the faces of the two HC-PBG fibres used in this thesis, as described below. The fibres are created from a preform of thin walled silica tubes, typically stacked in a triangular lattice, with a number of absent capillaries in the centre of the preform forming the eventual core. This preform is then fused together, and drawn at high at temperatures of $\sim 1900\,^{\circ}\mathrm{C}$. As the fibre is drawn, the preform collapses into the form of the hollow core photonic band gap fibre, with collapse ratios as high as $50,000:1$ having been

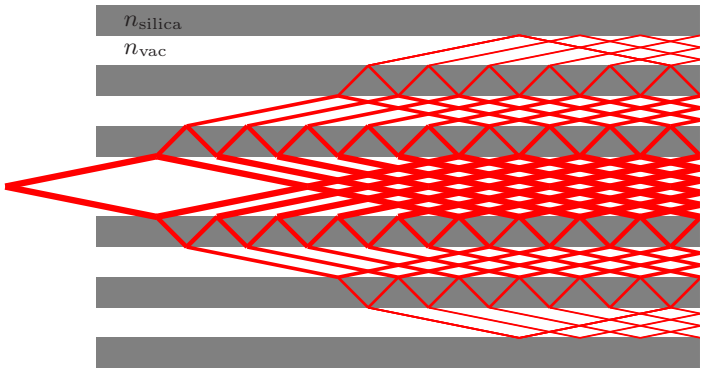

Figure 6.2: The mode is formed in the core due to the constructive interference of the Bragg reflections from the refractive index boundaries. As the condition for constructive interference is dependent on the wavelength, only certain wavelength ranges, falling within this wavelength band gap, will be guided. This figure is modified from reference [71].

achieved [70].

With correct design, the crystal structure will have a band gap for a range of frequencies where light will not propagate. This band gap is as a result of wavelength dependent Bragg reflections from the multiple refractive index interfaces [71], as shown in figure 6.2. The core of fibre, which is formed by the emission of 3, 7 or 19 capillaries [72] at the centre of preform, introduces a defect in the lattice. Such fibres are termed 3c, 7c and 19c fibres. Light, with a wavelength within the band gap that is coupled into the core will be confined within the core by the band gap.

6.4.2 Fibre details

Our collaborators from the Centre for Photonics and Photonic Materials at the University of Bath supplied us with two HC-PBG fibres. The first fibre, designated FB-BG-19c-800, had a core diameter of $11.7\mu\text{m}$ formed by the omission of 19 cells from the centre of the lattice. Figure 6.1(a) shows the transmission loss of this fibre as a function of wavelength, as measured by Bath. For $780\ \text{nm}$, which is the laser wavelength that is needed for the dipole guiding of rubidium, the loss is shown to be $200\ \text{dB}\cdot\text{km}^{-1}$. The second fibre, designated FB-BG-7c-800, had a

core diameter of $8.9\mu\mathrm{m}$ formed by the emission of 9 cells from the centre of the lattice. Figure 6.1(a), shows the specified transmission of this fibre as a function of wavelength. For $780\ \mathrm{nm}$ the loss is $1200\ \mathrm{dB{\cdot}km^{-1}}$ which is higher than for the FB-BG-19c-800 fibre.

Over a distance of $10\ \mathrm{cm}$ which is a typical guide distance, if $10\ \mathrm{mW}$ of power is coupled into each fibre, the $11.7\mu\mathrm{m}$ core diameter FB-BG-19c-800 (attenuation of $200\ \mathrm{dB{\cdot}km^{-1}}$) will output $9.95\ \mathrm{mW}$, with the $8.9\mu\mathrm{m}$ core diameter FB-BG-7c-800 fibre (attenuation of $1200\ \mathrm{dB{\cdot}km^{-1}}$) outputting $9.73\ \mathrm{mW}$. The attenuation rates of these fibres are therefore sufficiently low enough so as to have little effect on atom guiding.

6.4.3 Fibre coupling and the effect of higher order modes.

In order to achieve the highest coupling and transmission efficiency it is important to preferentially couple into the fundamental mode. This is accomplished by matching the spot size of the focussed coupling beam to the mode field diameter of the fundamental mode, using equation 7.5. The mode field diameter of these fibres, as specified by Bath University, is 0.92 times the core diameter.

Aside from the benefit of maximising the power within the capillary, there are two other reasons why optimising the spot size to the mode field diameter is critical. Firstly, if too large a focussed spot size is used, then light will be incident upon the crystal lattice. In this coupling region, the confining potential that keeps the atoms away from the walls within the fibre, is not so well defined, possibly leading to losses in the atom guide. Such an effect was seen in the HC-PBG fibre guiding work of Takekoshi and Knize [2] [56], where it resulted in a longitudinal cut-off velocity below which no atoms were guided.

Secondly, a smaller spot size than necessary will increase the likelihood that higher order modes will also be excited within the fibre. As well as causing the fibre output to deviate from the expected LP_{01} mode profile, a superposition

[2]This paper was similar to the work presented in this chapter and was published mid-way through my efforts.

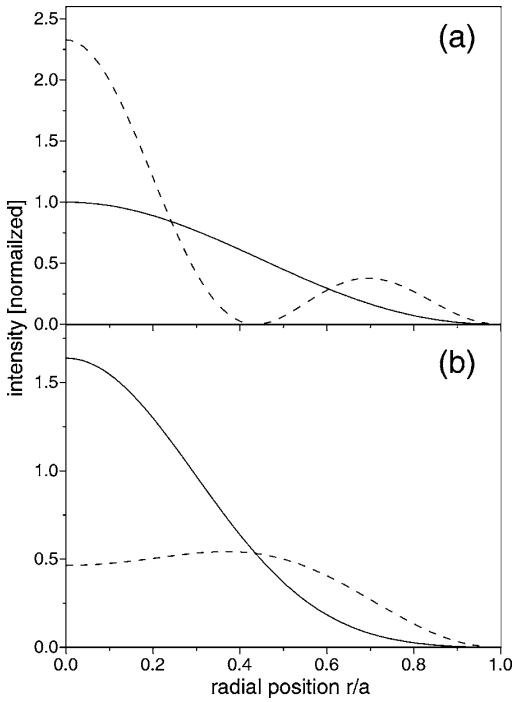

Figure 6.3: Figure a shows the radial intensity of the EH11 (solid curve) and EH12 (dashed curve) modes for a straight hollow-core optical waveguide. Figure b shows the superposition of these modes when both are coupled into the waveguide with a power ratio of 25:1 in favour of the EH11 fundamental mode. The solid curve shows the case when the interference of the modes is additive with the dashed curve illustrating when the interference is subtractive. The mode flips between the two cases of additive and subtractive interference, with a periodicity of $\sim 150\mu\mathrm{m}$ for a $12\mu\mathrm{m}$ core diameter fibre, as it propagates along the fibre. Both graphs are normalised with regard to power. This figure is reproduced from reference [73].

of modes can cause beating effects along the length of the fibre, as the different modes have different longitudinal wave vectors. In the work of Pfeifer and Downer [73], they show that the beating of the EH_{11} and EH_{12} modes, even with a power ratio of 25:1 in favour of the fundamental mode, can cause substantial periodic changes in the mode profile as it propagates along the fibre, as shown in figure 6.3. For a hollow-core optical fibre with a core diameter of $12\mu\mathrm{m}$ the periodicity of these beats in the mode profile is $\sim 150\mu\mathrm{m}$.[3] As this modulation of the optical field would at best cause some uncertainty in the guiding potential and at worst induce heating effects in the atoms, as the atoms would experience a dipole potential 'roller-coaster', it is best to avoid such an effect by carefully optimising the spot size of the coupling beam.

This problem may also be magnified by the modal qualities of PCF. All 7c and 19c HC-PBG fibres support numerous modes in the core; with a typical 7c HC-PBG fibre supporting up to 14 modes and a typical 19c HC-PBG fibres supporting up to 45 modes [72]. Recently a 3c HC-PBG fibre has been demonstrated to be single mode [72]. However this beating phenomenon may still exist in such 'single-mode' fibres as higher order modes may propagate short distances (up to a few thousands of wavelengths [74]) along the fibre before the single-mode operation is achieved. [74, 73].

Consequently it is of great importance to match as closely as possible the spot size of the coupling beam to the mode field diameter of the fibre. Under experimental conditions, I achieved coupling transmission efficiencies of $\sim 35\,\%$. Although I did not have a long enough length of fibre to characterise whether the transmission efficiency was due to coupling loss or attenuation within the guide, I believe that this loss was mainly due to coupling loss. Although this transmission effiency was maximised as best as possible, the $65\,\%$ loss of power, presumably at the fibre entrance, poses serious questions regarding where this optical power goes and the shape of the guide's potential in the coupling region.

[3] This is calculated using an equation which assumes that the mode field diameter is 0.64 the size of the core diameter. Although this is not same ratio as for PCF, the equation still gives us a good indication of the length scale of the periodicity, with the periodicity reducing for smaller core sizes.

6.4.4 Optical potential within fibre

In order to take into account the Doppler shift of the atoms with respect to the laser beam, the equation for the dipole potential of an atom in the far-detuned limit, as given by equation 2.21, is modified to become,

$$U_{\text{dipole}} = \frac{\hbar\gamma^2 I}{8\left(\delta - k\cdot\vec{v}_z\right) I_s}. \tag{6.1}$$

where $\vec{v}_z$ is the velocity component atom in the direction of the beam propagation. For a rubidium atom at room temperature travelling in the same direction, the average red Doppler shift is $1.38\ \text{GHz}$

The fundamental mode of this type of HC-PBG fibre is roughly Gaussian in shape [68]. Given that the $1/e^2$ mode field diameter of the fundamental mode is 0.92 times the core diameter D_{core}, the dipole potential as a function of laser power P_0 is given by,

$$U_{\text{dipole}} = \frac{\hbar\gamma^2 P_0}{4\left(\delta - k\cdot\vec{v}_z\right) I_s \pi \left(0.46 D_{\text{core}}\right)^2}. \tag{6.2}$$

6.5 First attempt at vapour guiding

6.5.1 Aim

The first experiment was to try to guide thermal rubidium atoms. All reports to date of red-detuned guiding in hollow core capillaries have used a thermal source of atoms.

Aside from the being easier to setup than experiments involving cold atoms, the high longitudinal velocity of the thermal atoms through the fibre minimises the time that the atoms spend within the guide. As discussed in section 7.6.3, the optical potential within the guide may be distorted, especially near the coupling

region. Consequently, the shorter period spent in the guide will reduce the atoms' exposure to inhomogeneities in the optical potential.

This experiment was designed to essentially reproduce the red-detuned capillary guiding experiments of Renn and co-workers [17, 51], but for HC-PBG fibres.

6.5.2 Experimental set-up

The vacuum chamber used for this experiment was the single ion pump system as described in detail in chapter 5. In brief, the system consisted of two sub-chambers. The top chamber contained rubidium getters, excellent optical access and the intra-cavity mirrors needed for the cold atom experiment as described in the next section. The intra-cavity mirrors were not used in this experiment as I did not want the atoms to be cooled. The bottom chamber contained the hot wire detector (consisting of a hot wire and CEM) and an ion pump. A small $3\ \mathrm{mm}$ diameter pipe linked the two chambers so that the two chambers could be maintained at UHV using a single ion pump. A fibre holder allowed for two fibres to run between the two chambers.

For this experiment, I loaded the fibre holder with two of the $11.7\mu\mathrm{m}$ core diameter hollow core photonic band gap fibres (model:FB-BG-19c-800). Both fibres were $\sim 8\ \mathrm{cm}$ long with the output of the fibre $\sim 11\ \mathrm{mm}$ away from the hot wire. The two fibres gave the experiment a redundancy in case one fibre was contaminated or became damaged during the experiment.

6.5.3 Experimental procedure

The guide beam was supplied by the Ti:Sapphire laser described in section 3.2.8. The beam passed through an AOM (Isle Optics, model: LM080), which was used to turn the beam on and off. The frequency shift of the AOM does not need to be taken into account due to the large detunings, with respect to the rubidium transitions, used. The beam was steered towards the top of the trap and then coarsely coupled into the fibre using the beams steering mirrors and a convex lens

with focal length $f = 38.1\ \mathrm{mm}$ which was mounted on an xyz linear positioning stage (Newport, model: 562 series). The diameter of the beam before entering the lens was $3.5\ \mathrm{mm}$. The resultant spot size was therefore $10.8\ \mu\mathrm{m}$.

A basic laser pointer was then pointed at the output end of the fibre. Despite the absence of a coupling lens, a small amount of light was coupled into the fibre and exited from the input end. The coupling lens, was adjusted so that pointer beam passed through the middle of the lens. The guide beam's beam steering mirrors were then adjusted so that the guide beam and the laser pointer light emitted from the fibre overlapped over as long a beam path as was observable. The laser pointer was then removed. A power meter was then used monitor the output power from the fibre. A glass slide placed before the power meter directed a small percentage towards a lens which imaged the end of the fibre on a CCD camera. This method allowed the output mode to be observed simultaneously while optimising the transmission efficiency. As the fibre was multimode, it was important to not only optimise the power, but to optimise the shape of the mode so that it looked Gaussian.

The hot wire detector was then manoeuvred to a position directly under the fibre. This was done by observing the influence of diffraction, in the fibre's output, from the hot wire. The hot wire was set to a temperature of $1300\ \mathrm{K}$ and allowed to stabilise for ~ 10 minutes. The CEM was then turned on.

By heating up the rubidium getters, the source chamber filled with thermal rubidium, building up to a pressure of $\sim 10^{-7}\ \mathrm{mbar}$. As the getters were situated along a small diameter pipe away from the entrance of fibre, rubidium in this chamber was considered to be at room temperature.

A LabVIEW VI was then used to control the AOM and turn the guide on and off, with an adjustable period. The LabVIEW program then recorded the number of pulses being being generated by the CEM control box.

In principle, the introduction of a red-detuned guide beam, with sufficient power to guide the atoms and sufficient detuning to minimise heating effects, should result in the atoms being guided through the fibre. The guided atoms would then increase the signal being detected by the hot wire detector.

6.5.4 Results and discussion

This attempt at vapour guiding produced only a partial result. As shown in figure 6.4, a clear increase in the detected flux was observed when the red-detuned (from both the rubidium-85 and rubidium-87 $D2$ transitions) guide beam was turned on. Initial optimism was quickly subdued when the same effect was seen for a blue-detuned (from both the rubidium-85 and rubidium-87 $D2$ transitions) guide beam; indicating that the dipole force was not the cause of this observation. I am still not entirely sure how to explain this effect. As the influence of the dipole force had been discounted, the only other optical force was due to the scattering. As seen in the LG guide beam experiment in chapter 4, increased scattering force can mean an increase in flux due to the reduction of time spent in the guide. Such an explanation would not apply in this situation as the increase in velocity would only have been very small compared to the high velocity of the thermal atoms.

One possibility was that the laser, by heating effects or otherwise, had increased the desorption of rubidium deposited on the walls of the fibre core, thus increasing the quantity of rubidium leaving the fibre. This seems unlikely however, as a similar effect was not seen when the getters were turned off.

Also apparent from the data, as can be seen from figure 6.4, is that the flux rate built up slowly when the guide beam was turned on. This build up correlated with a curious effect seen when viewing the output of the fibre. If coupling was maximised, and subsequently the laser turned off for more than ~ 10 seconds, the coupling efficiency would be greatly reduced on the re-introduction of the laser. Over the next few seconds, the coupling would improve back to the previous level. The time scale of this build up in coupling matched the build up in atom flux. The nature of this reduction in coupling suggested that heating effects in the fibre were causing some form of elastic mechanical deformation.

Despite trying numerous guide parameters and different pressures of rubidium in the source chamber, I was unable to produce a conclusive result. When the pressure of the source chamber was high enough to observe any effect, it was always independent on detuning. Consequently, it was decided to switch to the cold atom guiding method, as this should have increased the number of atoms

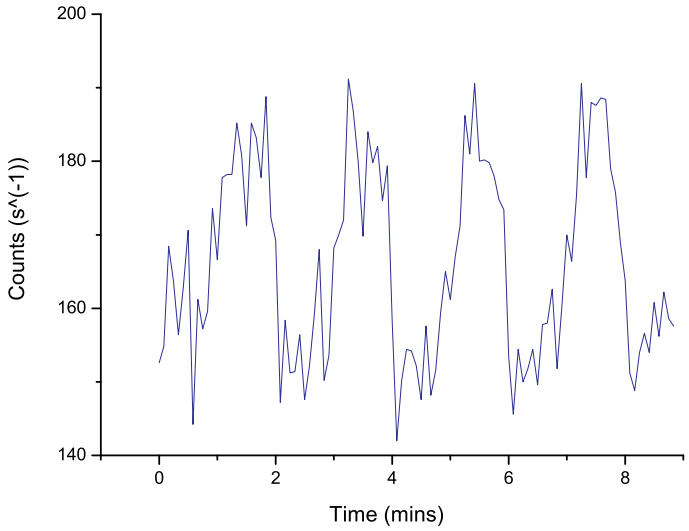

(a) $4.5\,\mathrm{mW}$ guide power at $16\,\mathrm{GHz}$ red detuning resulting in a potential well depth of $1.01\,\mathrm{K}$. On-off period of $2\,\mathrm{mins}$.

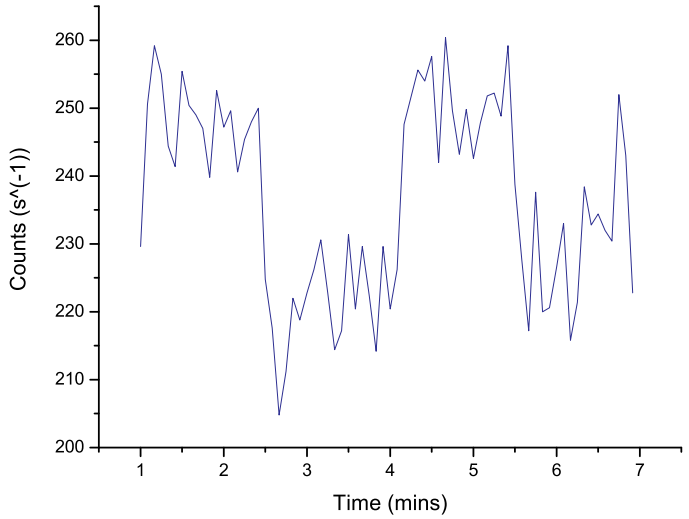

(b) $4.9\,\mathrm{mW}$ guide power at $11\,\mathrm{GHz}$ blue detuning resulting in a potential wall height of $1.6\,\mathrm{K}$. On-off period of $3\,\mathrm{mins}$.

Figure 6.4: Data taken for thermal guiding for blue- and red-detuned guide. An increase in flux is observed when both detunings are present, indicating that mechanism is not due to the dipole force. Note the gradual increase in flux rate as the laser is turned on. This coincided with an observed increase in coupling.

with sufficiently low enough transverse velocity to be guided, without needing high vapour pressures in the source chamber.

6.6 Attempt at cold atom guiding

6.6.1 Aim

This experiment was aimed at guiding cold atoms through the HC-PBG fibre. By using a magneto-optical trap, a cloud of cold rubidium-85 atoms, with a temperature $\leq 600\mu\mathrm{K}$, could be formed above the HC-PBG fibres in the source chamber. This cloud would then be dropped on the cloud while simultaneously turning on the guide beam. This approach would allow a large number of atoms to be directed into the fibre with low enough transverse velocity to be guided. This avoided the need to generate the high pressures of rubidium in the sample chamber needed for vapour guiding.

6.6.2 Experimental set-up

The vacuum chamber used for this experiment was the same single ion pump system, as described in detail in chapter 5, used for the above vapour guiding experiment. The intra-cavity mirrors were now utilised to create the MOT. As there was no need to bring the vacuum system back up to air between the vapour guiding experiment and this experiment, the same two $11.7\mu\mathrm{m}$ core diameter hollow core photonic band gap fibres (model:FB-BG-19c-800) were used.

Cooling and guide lasers

The cooling and re-pump beams were supplied by the master-slave system and a homebuilt ECDL based system respectively. These laser systems are described in chapter 3. The cooling light passed through an AOM (Isle Optics, model: LM080), which not only provided the necessary frequency shift to the cooling

beam as described in section 3.2.5, but allowed the beam to be quickly and accurately switched on and off. Subsequent to the AOM, the beams was split into three beams of equal power beams, using two half-wave plate and polarising beam splitter pairs. Two of the these beams were directed to hit the two intra-vacuum mirrors/quarter-wave plates. The beams passed through quarter-wave plates before entering the trap. The quarter-wave plates were adjusted so that the light possessed the correct circular polarisation. Beam steering mirrors were used to ensure that the beams were hitting the mirrors/quarter-wave plates squarely and so that they were retro-reflected back along the same path. The third beam was passed through a correctly adjusted quarter-wave plate and then through the 'V' gap between the mirrors. An exterior mirror/quarter-wave plate assembly was adjusted to retro-reflect this beam back through the trap. Each arm of the cooling beams had a power of $8\ \mathrm{mW}$ and was $\sim 10\ \mathrm{mm}$ in diameter.

The $20\ \mathrm{mW}$ re-pump beam was directed in to the trap by way of a mirror positioned just above the exterior retro-reflecting mirror/quarter-wave plate assembly. A diverging lens was used to expand the beam to ensure that it filled the trapping and guiding area.

The guide beam was the same Ti:sapphire laser used in the vapour guiding experiment.

Magnetic coils

The anti-Helmholtz magnetic field was supplied by two $25\ \mathrm{mm}$ diameter coils separated by $30\ \mathrm{mm}$. The coils were constructed from ~ 60 turns of insulated wire. The coils were mounted on two optical lens mounts (Newport, model: LH-1). The mounts were modified so that the coils could be positioned nearer the flange surface, allowing the magnetic field centre to be close to the optical axes centre of the MOT. The coils were secured to the mount by loops of wire. A current of ~ 5 amps was needed to produce an adequate MOT. The coils only needed air cooling, however continuous running was avoided as they could reach temperatures over $60\ ^{\circ}\mathrm{C}$.

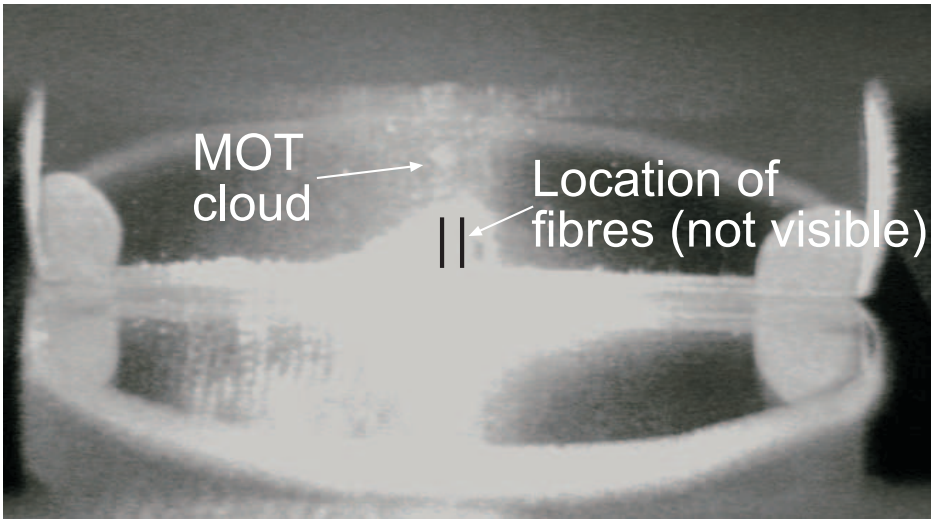

Figure 6.5: Picture of an example cloud of atoms within my MOT. The approximate position of the two fibres, not visible in the original photo, are marked. The two mirrors and quarter-wave plates (epoxied to the surface of the mirrors) are visible. The cloud was estimated to contain minimum number of 1×10^6 atoms and be $0.6\,\mathrm{mm}$ in diameter.

A method was needed to adjust the position of the cloud so that it was situated directly above the fibre entrance. Positional adjustments in one axis could be facilitated by changing the balance of the currents in the anti-Helmholtz coils. For the other two axes, shim coils were used. A single shim coil was positioned on each of the two axes around $50\,\mathrm{mm}$ away from the trap centre. The clouds position was adjusted by passing the current in the correct direction through the coils. The shim coils consisted of 50 turns of insulated wire and were $\sim 60\,\mathrm{mm}$ in diameter. By running up to $1.5\,\mathrm{A}$ current through the coil, sub-millimetre adjustments could be made to the position of the cloud.

6.6.3 Experimental procedure

The guide beam was coupled in to the beam as described in section 6.5.3. With the guide beam turned off and the cooling beams turned on, the lasers and magnetic coils were set to form the MOT. If needed, the rubidium getters were turned on by passing a current of between $\sim 2\,\mathrm{A}$ and $\sim 5\,\mathrm{A}$. The guide beam shutter was set to

open and the Ti:sapphire laser tuned to a near-resonant frequency.

Two cameras were positioned around the source chamber to image the MOT. The guide beam was tuned to a resonant frequency of rubidium and then turned on. The cloud was then manoeuvred, by adjusting the current through the anti-Helmholtz coils and shim coils, until it was as close as possible to the fibre entrance and centred on resonant beam. As the beam was on-resonance, the position of the cloud with respect to the beam could be visualised from the ablation of the cloud. After alignment, the frequency of the guide beam was set to the desired detuning.

The hot wire was set-up in the same manner as in the thermal guiding experiment and set to the same temperature of $1300\ \mathrm{K}$. The CEM was then turned on. The guide beam AOM was set to off and the cooling beam shutter set to open. A LabVIEW vi program was programmed to control the cooling beam and guide beams AOMs. The cooling beams were allowed in for $0.75\ \mathrm{s}$ before being switched off. After a $2.5\ \mathrm{ms}$ delay (to allow for any experimental mistiming), the guide beam was introduced. After another $0.75\ \mathrm{s}$ the cycle restarted and continued for as long as programmed. During these 'guide on' and 'guide off' periods the LabVIEW program counted the number of pulses for each period outputted by the CEM electronics.

Data analysis

Each experimental run lasted up to $15\ \mathrm{min}$, and consequently a large number of 'guide on' and 'guide off' bins were were acquired (600 on and 600 off bins for a $15\ \mathrm{min}$ run). The data was then inspected to gauge the influence of ion burst activity. Occasionally, the hot wire would produce a short and intense burst of ions, due to an impurity migrating to the surface of the wire. These spikes needed to be manually removed from the data as they would greatly influence the analysis. The off bins were then summed and then subtracted from the sum of the ion bins.

6.6.4 Results and discussion

Despite changing numerous parameters of the experiment, no signal was detected from the guided atoms. Many combinations of guide detuning and powers were used, with both fibres being used. Despite the rubidium pressure in the top chamber not being as high as for the vapour guiding experiment, significant noise was still present in the bottom chamber. The origin of this noise was mainly from background rubidium within the chamber. For getter currents of 1.5 A, which was the typical current needed for an adequate MOT, the background counts approached average values of $1200\,\mathrm{s}^{-1}$. Any guided atom counts that may have been present in the on bins minus off bins calculations were not discernible from the random variation due to the background noise.

At this point, it was decided that in order to stand any chance of detecting guided atoms, the two vacuum chambers needed to be completely isolated from each and pumped using two separate ion pumps. This would remove the pathways for rubidium to migrate from the source chamber to the detection chamber, thus decreasing the noise on the hot wire detector.

6.7 Second attempt at vapour guiding

6.7.1 Aim

The problems with noise in the previous two experiments prompted the modification of the vacuum system to the dual ion pump system as described in section 5.8. As cold atom guiding has to date never been achieved in a red-detuned (capillary or HC-PBG) fibre guide by any research group, it was decided that I should concentrate on vapour guiding. It was also decided to include in the system a $40\ \mu\mathrm{m}$ core diameter hollow-core capillary fibre, as well as the $8.9\mu\mathrm{m}$ core diameter FB-BG-7c-800 fibre. This would allow us the possibility to perform a direct repeat of the Renn experiments [17, 51] using hollow core capillary fibres and then compare the guiding through these fibres to the guiding through HC-PBG fibres. In addi-

tion, the smaller diameter 7c HC-PBG fibre was used, as this fibre would support a smaller number of higher order modes than the larger core 9c fibre [72] used in the previous tow experiments.

6.7.2 Experimental set-up

The experimental set-up was similar to that used in the previous thermal atom guiding experiment, discussed in section 6.5.2. For this experiment, the dual ion pump vacuum system was used, as detailed in section 5.8.2. With the addition of a second ion pump, and the isolation of the source and detection chambers, this vacuum system was designed to reduce the noise on the detector as a result of thermal rubidium migrating around the chamber. By reducing the noise on the hot wire detector, the sensitivity should be increased.

6.7.3 Experimental procedure

The laser was coupled into the fibre as described in section 6.5.3. The guide beam was passed through an AOM in order to provide fast and repeatable switching. A signal generator was used to control the AOM and gate a LabVIEW counting program, which recorded the number of pulses generated by the CEM control box. The program was identical to that used during the cold atom fibre guiding experiment described in section 6.6.3. It was programmed to output a text file with the sums of the counts detected by the CEM during each of the guide's on and off periods. In contrast to the cold atom fibre guiding experiment, where the shuttering frequency of guide was limited (to 0.66 Hz) by the time it took for the MOT cloud to form, the guide beam for this experiment was shuttered by up 20 Hz.

The getters were run at a comparatively high current of $6\,\mathrm{A}$, producing a rubidium pressure in the source chamber of $\sim \times 10^{-7}\,\mathrm{mbar}$.

6.7.4 Results and discussion

The improved vacuum system proved to be successful in reducing the noise in the detection chamber, with a typical background count rate of 130 counts per second. However no guided atoms were detected from either the HC-PBG fibre or the hollow-core capillary fibre. Possible reasons for this are discussed in the conclusion.

6.8 Conclusions and discussion

This chapter has detailed my unsuccessful attempts at guiding thermal and cold rubidium atoms through hollow-core photonic band gap fibre.

The first experiment which attempted to guide thermal rubidium through a HC-PBG fibre produced a detectable signal from apparently 'guided' atoms. However, I quickly ruled out the influence of the optical dipole force in this result, and were unable to confirm the exact cause of the observed signal. High noise in the detection chamber as a result of thermal rubidium migrating into this chamber from the source chamber, prompted us to switch to a cold atom experiment.

The second experiment attempted to guide laser cooled rubidium, generated in a MOT, through the same HC-PBG fibres. The MOT served to increase the number of atoms which had sufficiently low transverse velocity to be guided. Again, no signal was observed, with the assumption that excess noise from the thermal rubidium in the vacuum chamber was still blocking the signal.

The third experiment was another attempt at thermal rubidium guiding. The high level of noise in the previous two experiments had prompted us to design the dual ion pump vacuum system as described in section 5.8.2. The modifications to the vacuum set-up reduced the noise as intended, but no rubidium was detected exiting either a HC-PBG fibre or a hollow-core capillary. There are a number of possible reasons for this. Firstly, as this experiment was constructed during the last few weeks of my experimental work, the system was not under vacuum for long before the experiment was attempted. Consequently, it is possible that the small

diameter core of the fibres had not achieved sufficient enough vacuum for the guided to atoms to pass through without heating. Secondly, the highest pressure of rubidium that could be achieved in the source chamber was approximately $\sim 10^{-7}\,\mathrm{mbar}$. This is an order of magnitude less than the pressure of $10^{-6}\,\mathrm{mbar}$ used by Renn and co-workers in their experiment [17]. Other possible reasons include insufficient coupling efficiency and insufficient fibre preparation procedure.

It is worth noting that during the course of these experiments Takekoshi and Knize published details of their successful experiment guiding thermal rubidium through a HC-PBG [56]. Of interest, was their observation that low velocity atoms were not being guided through the fibre. An effect they attributed to insufficient coupling. Additionally, Klaus Sengstock's group has also been working on a cold atom guiding experiment using HC-PBG for over two year with no results having been presented to date.

6.9 Author's contribution

With the exception of a few weeks assistance from John Livesey during the early stages of the first thermal guiding experiment, the experiments were carried out entirely by myself.

Chapter 7

CHARACTERISATION OF ENDLESSLY SINGLE MODE PHOTONIC CRYSTAL FIBRES

7.1 Chapter synopsis

This chapter provides an overview of the properties of endlessly single mode photonic crystal fibres (ESM-PCF) and details the characterisation of the ESM-PCFs used during the course of my PhD. These fibres were characterised as part of my work described in chapter 8 to create a dual beam fibre trap using ESM-PCFs.

Three core diameters ($10\ \mu\mathrm{m}$, $25\ \mu\mathrm{m}$ and $35\ \mu\mathrm{m}$) of ESM-PCF, purchased from Crystal Fibre A/S [75] were characterised for laser wavelengths of $780\ \mathrm{nm}$ and/or $\sim 1070\ \mathrm{nm}$. In addition to characterising the fibres for these laser wavelengths, the fibres were also characterised for broadband radiation generated using a supercontinuum source.

The characterisation of the fibres involved optimising coupling efficiencies, understanding the experimental conditions resulting in single-mode and multimode output and measuring the mode profiles of the fibre.

7.2 Motivation

In the next chapter I discuss the use of endlessly single-mode photonic crystal fibres (ESM-PCFs) in dual beam fibre traps. The characteristics of dual beam fibre traps are heavily influenced by the fibres used to create them. Previous to this study, all dual beam fibre traps had been constructed from conventional single-mode or multimode fibres. As I shall discuss in this chapter, ESM-PCFs have novel characteristics in comparison to conventional fibres. Consequently, I believed that a dual beam fibre trap constructed from ESM-PCF had the potential to exhibit unique and useful characteristics. However, prior creating the dual beam trap, it was important to characterise the fibres.

7.3 Introduction to endlessly single-mode photonic crsytal fibre

In recent years, photonic crystal fibres have come to the fore [70]. Photonic crystal fibres (PCF) are fibres which have a 2-dimensional periodic lattice of high and low refractive index regions in the transverse plane. With appropriate design of this lattice, PCF crystals fibres can exhibit vastly different properties compared to conventional fibres. PCF fibres can fall into one of two classes; index guiding fibres, which guide light by modified total internal reflection, and photonic band gap fibres, which guide light using a photonic band gap. In this chapter I discuss a type of PCF known as endlessly single-mode photonic crystal fibre (ESM-PCF), which fall under the class of index guiding fibres. Photonic band gap fibres, which are used for another experiment described in this thesis, are described in section 6.4.

In 1996, Knight and co-workers published the first experimental demonstration of a photonic crystal fibre [76]. This fibre was shown to have a unique characteristic, in that it was single mode for every optical wavelength that they were able to measure for, from $337\ \mathrm{nm}$ to $1550\ \mathrm{nm}$ [77]. This was despite the core having a diameter of $4.6\ \mu\mathrm{m}$, which in a typical conventional single mode fibre would have a single mode cut-off wavelength of $\sim 550\ \mathrm{nm}$. As a result of this unique

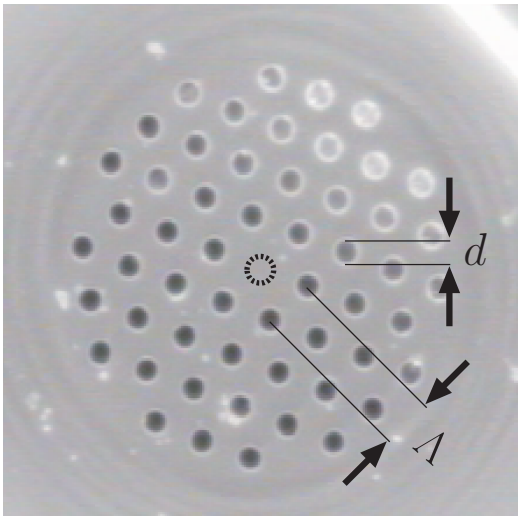

Figure 7.1: Micrograph of LMA-25 fibre, illustrating the diameter d of the air holes and the pitch Λ. The dashed circle in the centre of picture marks the location of the absent air hole, forming the $2\Lambda = 25\ \mu\mathrm{m}$ diameter core of the fibre.

property, these fibres were named endlessly single-mode photonic crystal fibres. In contrast to conventional fibres, where the number of modes is dependant on the ratio of the core radius to wavelength of light, the number of modes in a correctly designed ESM-PCF, shown in figure 7.1, will only be dependant on the ratio of the air hole diameter d to the spacing between the air holes, known as the pitch Λ. Therefore, as it was later shown experimentally [78], with the appropriate ratio d/Λ, these fibres could operate in the same manner with far larger core sizes by simply scaling up dimensions of the fibre. Consequently for larger core diameters, ESM-PCF is also known commonly as large mode area photonic crystal fibre (LMA-PCF).

7.4 Principle of operation

7.4.1 V number for index guiding photonic crystal fibres

In order to explain how ESM-PCFs work, it is instructive to use a modification of the theories used for conventional optical fibres. It is common to parametrise

conventional step index fibres by the V number. For a step index fibre, this V number is given by [79],

$$V_{SIF}(\lambda) = \frac{2\pi\rho}{\lambda}\sqrt{n_c^2 - n_{cl}^2} = \frac{2\pi\rho}{\lambda}NA, \tag{7.1}$$

where λ is the wavelength of light; ρ is the core radius; and n_{cl} and n_c are the refractive indices of the cladding and core respectively. $NA = n\sin\theta$ is the numerical aperture of the fibre where n is the index of refraction of the medium outside of the fibre and θ is the half-angle of the cone of light.

For a particular step index fibre if $V_{SIF} < 2.405$ (which is the solution of the first zero of the Bessel function) the fibre will be single mode and if $V_{SIF} > 2.405$ the fibre will be multimode. For photonic crystal fibres, this equation is modified to take into account the natural length scale of the fibre, namely the separation of the fibre holes, known as the pitch Λ [79]. The V number for an index guiding PCF is given by [79],

$$V_{PCF}(\lambda) = \frac{2\pi\Lambda}{\lambda}\sqrt{n_c^2(\lambda) - n_{cl}^2(\lambda)} = \frac{2\pi\Lambda}{\lambda}NA(\lambda), \tag{7.2}$$

where $n_{cl}(\lambda)$ and $n_c(\lambda)$ are the effective refractive indices of the core and cladding of the PCF respectively.

Single-mode operation occurs if $V_{PCF} < \pi$ and multi-mode operation if $V_{PCF} > \pi$ [79].

7.4.2 Origin of the endlessly single-mode characteristic

The origin of the endlessly single mode property of ESM-PCF, is the wavelength dependent 'effective refractive index' of the fibre's microstructured cladding. For the fundamental mode, the wavelength of the mode in the transverse plane can be thought of as being too large to fit in between the holes of the cladding and

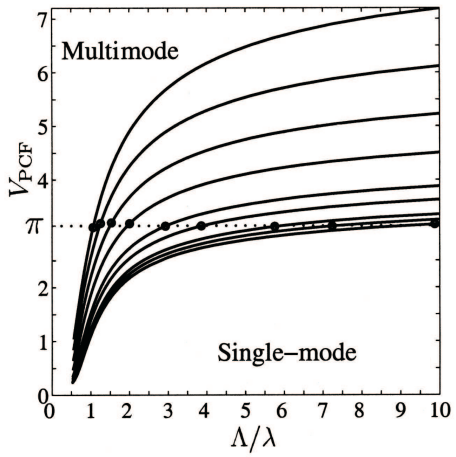

Figure 7.2: Reproduced from reference [79], this figure shows the numerical results of the V number for PCFs with different d/Λ values (from the bottom,$d/\Lambda = 0.43, 0.44, 0.45, 0.475, 0.50, 0.55, 0.60, 0.65, 0.70$) , as a function of Λ/λ. The dotted line represents the $V_{PCF} = \pi$ boundary between the single-mode and multimode regime, with the circles representing the points where the curves intercept this line.

is therefore confined to the core. However the higher transverse wavelengths of higher order modes experience less of the holey region and leak away through the silica. Consequently, if the holes are made bigger, the fibre is more likely to become multimode as the silica regions play less of a role. If the holes are made too small however, the fibre becomes very susceptible to bend losses [77], as discussed in section 7.5.3. It should be noted that all the modes in PCF are leaky, due to the finite extent of the cladding. Single-mode operation of the fibre results from the higher order modes attenuating more rapidly than the fundamental mode. Section 7.5.2 discusses how this property can have implications for achieving single-mode operation of short fibres.

By computationally modelling the structure it is possible to calculate the values of n_{cl} and n_c for the structure for various air hole diameters [79, 80]. Figure 7.2, reproduced from reference [79], shows the calculated values of V_{PCF} as a function of the ratio Λ/λ for different d/Λ ratios. As can be seen in the graph, the large values of d/Λ, which correspond to fibres with large air holes, result in fibres which are multimode for short wavelengths. As d/Λ is decreased, the fibre approaches a

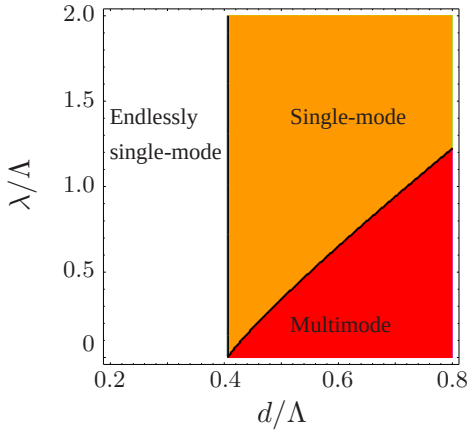

Figure 7.3: The 'phase' diagram illustrating the mode regimes of index guiding photonic crystal fibres as a function of air hole diameter d, the pitch Λ and the wavelength of light λ. Calculated using equation 7.3 taken from reference [80]. The endlessly single mode boundary line is at $d/\Lambda = 0.406$.

regime where it is single-mode for all optical wavelengths. The 'phase' boundary λ^*/Λ, where the fibre changes between single and multimode operation, has been shown to be given by the equation [80],

$$\lambda^*/\Lambda \simeq \alpha \left(d/\Lambda - d^*/\Lambda\right)^{\gamma} \tag{7.3}$$

where $\alpha = 2.80 \pm 0.12$; $\gamma = 0.89 \pm 0.02$; and d^*/Λ is the calculated value of the endlessly single mode transition equal to 0.406.

Figure 7.3 shows the 'phase' diagram resulting from equation 7.3. Therefore, by choosing the ratio d/Λ to be less than 0.406, an index guiding PCF will be endlessly single mode.

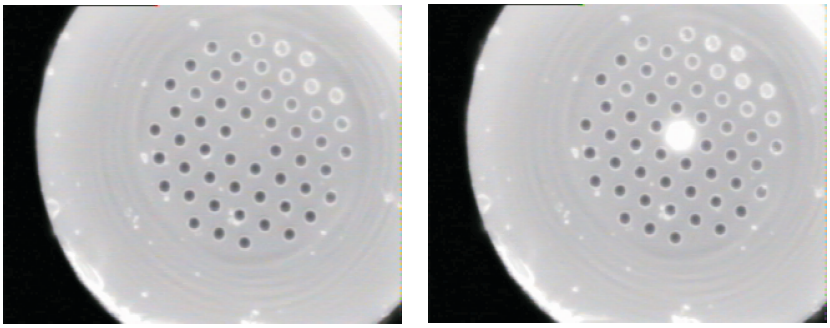

(a) (b)

Figure 7.4: Figure 7.4(a) shows a micrograph of an illuminated end face of the LMA-25 fibre. Figures 7.4(b) shows the same fibre with the laser turned on; the mode is visible in the core of the ESM-PCF

7.5 Characteristics of ESM-PCF

7.5.1 Mode profile of ESM-PCF

Due to the characteristic hexagonal shape of the core of photonic crystal fibres, the transverse and axial (along direction of propagation) mode profile is different compared to conventional single mode fibres. The mode profile of single-mode conventional fibres are approximately Gaussian and consequently the propagation of the mode closely follows the typical relation for a propagating Gaussian beam. However, the output mode of ESM-PCFs do not follow this Gaussian dependency. Due to the presence of the holes surrounding the core, the transverse profile takes on a hexagonal shape, as shown in figure 7.5.1. Although this has an obvious effect on the transverse profile of the PCF, the effect is minimal for intensities over $1/e^2$ where the intensity is closely approximated by a Gaussian [81]. Somewhat surprisingly however, this hexagonal shape also results in the PCF having propagation characteristics completely different from the normal Gaussian dependency of conventional fibres.

On propagation, the hexagonal transverse mode profile is seen to undergo two 30° rotations, as shown in figure 7.5. This behaviour is as a result of the interference between the different Gaussian elements of the decomposition of the PCF's

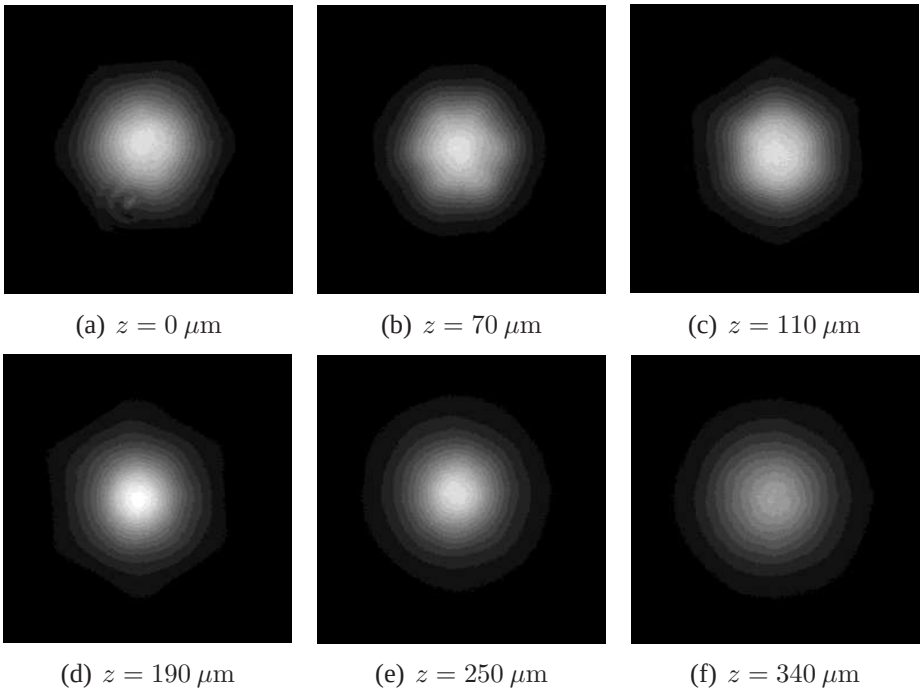

(a) $z = 0\,\mu\mathrm{m}$ (b) $z = 70\,\mu\mathrm{m}$ (c) $z = 110\,\mu\mathrm{m}$

(d) $z = 190\,\mu\mathrm{m}$ (e) $z = 250\,\mu\mathrm{m}$ (f) $z = 340\,\mu\mathrm{m}$

Figure 7.5: Micrographs of the transverse mode profile of the $25\,\mu\mathrm{m}$ core diameter ESM-PCF (LMA-25) taken at various propagation distances. The mode is seen to undergo the first 30° rotation by $110\ \mu\mathrm{m}$ (figure 7.5(c)) with the second 30° rotation by $340\ \mu\mathrm{m}$ (figure 7.5(f)). The shape of the mode is more easily seen in the low intensity regions. In regions with intensity greater than $1/e^2$ the mode is approximately Gaussian. The colour depth of the images has been reduced to highlight the shape of the mode.

fundamental mode [82].

This hexagonal mode also results in the on-axis intensity reaching a peak value, or focus, at a finite propagation distance after the fibre. This feature is in contrast to conventional single mode fibre where the intensity reduces on propagation, approximated closely by the normal Gaussian relation. The focal distance increases with increasing ratio λ/Λ. By modelling the output mode of the fibre, Dabarian and co-workers [81] were able to show how the focal length changes, as shown in figure 7.6. Figure 7.11, in section 7.6.7, shows an example of the on-axis intensity profile for a $25\ \mu\mathrm{m}$ diameter fibre (Crystal Fibre, LMA-25) using the $1070\ \mathrm{nm}$ laser. As will be shown later in chapter 8, this longitudinal intensity profile can have important implications for how the trap works.

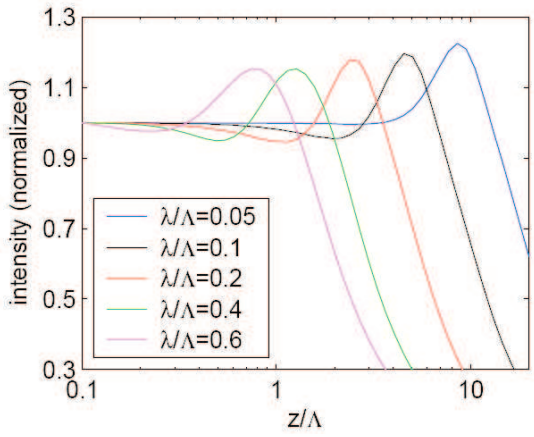

Figure 7.6: Reproduced from reference [81], this figure shows the calculated variation of electric field intensity at the centre of the fibre as a function of propagation distance z for various values of λ/Λ. With decreasing λ/Λ, the mode comes to a sharper focus with an increasing focal length.

7.5.2 Single-mode nature of ESM-PCF

The definition of single-mode operation in photonic crystal fibres is not as clear cut as in conventional fibres. In conventional step and graded index fibres, guided modes are those modes which are evanescent in the cladding whereas leaky modes are those which have oscillatory fields in the cladding therefore allowing power to escape [83]. For ESM-PCF, where light is confined by the effective refractive index of a finite holey cladding layer, all the modes are leaky [83]. Consequently, the declaration that an ESM-PCF fibre is operating in a single mode must be made on a more arbitrary basis than in the case of conventional fibres. As higher order modes suffer higher attenuation rates than the fundamental modes, after a certain length, the power in the attenuated mode will be so much greater than the power in the other modes, that the fibre can be considered to be operating in a single mode. As is the case with conventional fibres, the term single-mode applies to the most common case where in fact two fundamental modes with orthogonal polarisations exist.

Argyros and co-workers [83] proposed that a PCF fibre can be considered to be operating in a single mode after a certain length L_{sm} if the fundamental mode has

attenuated no more than $20\ \mathrm{dB}$ of its original value, and the second least leaky mode has attenuated by at least $40\ \mathrm{dB}$. Or in other words, a PCF is considered to operation in a single mode regime if after a certain length L_{sm} the modes have attenuated such that the output power of the fundamental mode is 100 times greater than the power of any other mode in the output.

As discussed in the work by Grassi and co-workers [84], when working with ESM-PCF fibres purchased from Crystal Fibre, L_{sm} can be as high as $2\ \mathrm{m}$; fibre lengths below this length can guide a higher order mode. The fibre is more likely to be multimode for lower wavelengths, larger core diameters and when the fibre is kept straight.

7.5.3 Bend losses in ESM-PCF

Theory predicts that there will be both a short wavelength and long wavelength band edge for the bend loss in index guiding PCFs [85]. In reality however, the long wavelength band edge only occurs at $\lambda > \Lambda/2$ [85], which is outside of the usual operating parameters of an ESM-PCF and in any case is typically located in the non transparent regime of silica [86]. Therefore, only the short wavelength edge of the bend loss profile is important. The critical bending radius R^*, below which the losses increase dramatically, is given for the short wavelength edge as [86],

$$R^* \propto \Lambda^3/\lambda^2. \tag{7.4}$$

Therefore, the fibre's tolerance to bends decreases with increasing core size or decreasing wavelength. In the extreme case of a short wavelength within a large core, bend losses may be so high as to cause almost complete attenuation of the fundamental mode for small bends. However, as is discussed in section 7.6, by putting a bend in the fibre, L_{sm} can be reduced drastically compared to when the fibre is kept straight.

7.6 Experimental characterisation

7.6.1 Fibres characterised

Crystal Fibres A/S [75] are currently the only commercial manufacturer of photonic crystal fibre. Crystal Fibre manufacture six different core diameters of ESM-PCF ($8\,\mu\mathrm{m}$, $10\,\mu\mathrm{m}$, $15\,\mu\mathrm{m}$, $20\,\mu\mathrm{m}$, $25\,\mu\mathrm{m}$ and $35\,\mu\mathrm{m}$) which are named large mode area photonic crystal fibres (LMA-PCF)[1]. I decided to purchase and characterise 3 core sizes of fibre: LMA-10 ($10\ \mu\mathrm{m}$ core diameter), LMA-25 ($25\ \mu\mathrm{m}$ core diameter) and LMA-35 ($35\,\mu\mathrm{m}$ core diameter). Table 7.1 shows selected parameters of the fibres. The LMA-35 fibre was chosen as it was the largest core diameter available and I was interested to see how the low numerical aperture would influence the dynamics of the dual beam fibre trap, described in chapter 8. I chose the LMA-25 fibre as the laser wavelengths that I initially intended to use, $780\,\mathrm{nm}$ and $1070\ \mathrm{nm}$, were technically out of the recommended operating range with regard to bend losses (see section 7.5.3) of the LMA-35 fibre. For the LMA-25 fibre, $1070\ \mathrm{nm}$ was well within, and $780\ \mathrm{nm}$ on the borderline, of the recommended range. I also chose the LMA-10 fibres; the intended laser wavelengths were well within its recommended operating range and was also suitable for wavelengths down to $405\,\mathrm{nm}$, therefore making the fibre potentially useable for practically any wavelength that I might decide to use in further studies. It may also have been useful to have had a ESM-PCF with an NA that was more close to that of the conventional single mode fibre.

7.6.2 Light sources used

Two lasers with different wavelengths were used for the characterisation of the fibres: a continuous wave Ti:sapphire (Spectra Physics, model: 3900s), as described in section 3.2.8, with a maximum power of $\sim 800\ \mathrm{mW}$ and operating at $780\ \mathrm{nm}$; and a continuous wave fibre laser (IPG, model: YLM-5-1070LP) with a

[1] Polarising and polarisation maintaining versions are also available but were not used in this thesis.

Fibre name	**Core diameter**	**Mode field diameter**
LMA-10	$10 \pm 1\ \mu\mathrm{m}$	$7.5 \pm 1.0\ \mu\mathrm{m}$
LMA-25	$25.2 \pm 0.4\ \mu\mathrm{m}$	$19.8 \pm 2.0\ \mu\mathrm{m}$
LMA-35	$35.0 \pm 0.5\ \mu\mathrm{m}$	$26.0 \pm 2.5\ \mu\mathrm{m}$

Table 7.1: The specifications (as published by the manufacturer) of the three core sizes of ESM-PCF used. The fibres were all manufactured by Crystal Fibre A/S, who describe the fibres as large mode area photonic crystal fibre. The mode field diameter is constant for all wavelengths.

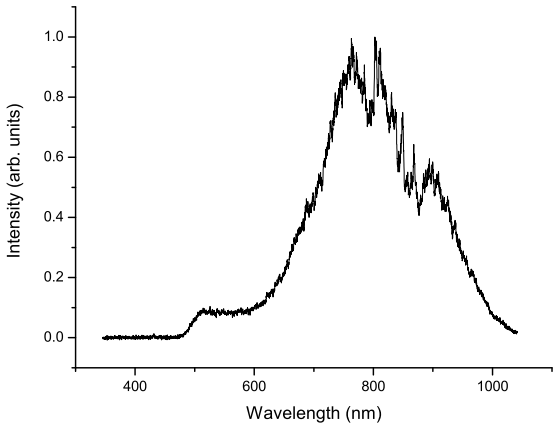

Figure 7.7: Measured spectrum of the supercontinuum. The bandwidth at FWHM is approximately $\sim 200\,\mathrm{nm}$.

maximum power of $5\ \mathrm{W}$ and operating at $1070\ \mathrm{nm}$.

In addition to these lasers, a commercial supercontinuum radiation source was also used. The supercontinuum source (Fianium, model: SC-500-6) produced broadband radiation generated in a highly nonlinear photonic crystal fibre pumped using a mode-locked fibre laser based on a core-pumped Yb-doped fibre (operating at a repetition rate of approx $10\ \mathrm{MHz}$, providing transform limited pulses of approx $4\ \mathrm{ps}$) and a high power cladding pumped fibre amplifier. When running at the maximum power of the $6.3\ \mathrm{W}$, the supercontinuum was quoted by the manufacture to emit pulsed radiation, with a repetition rate of $40\,\mathrm{MHz}$ and a pulse duration less than $10\mathrm{ps}$, at a central wavelength of $1060\mathrm{nm}$ and an emission bandwidth from $450-1750\mathrm{nm}$, when operating at maximum output power. Because of

the nature of the supercontinuum generation, the maximum emission bandwidth is achieved when the laser is running at maximum power, therefore the laser was run at this power during all experiments. However the emission bandwidth of the supercontinuum was measured to be $\sim 130\,\mathrm{nm}$, as shown in figure 7.7, which is considerably less than the quoted emission bandwidth of $450 - 1750\,\mathrm{nm}$. This bandwidth is still very much greater than that of the laser sources used in this thesis.

The choice of the optics when using the supercontinuum was important so that the spectrum of the laser was minimally affected. Ion-plated silver mirrors (Comar, model: 25MX06) were used as they have greater than 95% reflectance in the range $400 - 2000\,\mathrm{nm}$.

7.6.3 Fibre coupling

As with conventional single-mode fibres, I achieved the best coupling into ESM-PCF when the spot size of the focussed beam closely matched the mode field diameter of the fibres. However, unlike conventional single mode fibres where the mode field diameter is larger than the core of the fibre, the mode field diameter of a PCF is smaller than the core. The mode field diameters of the fibres are given in table 7.1.

The spot size, $2w_0$, of a focussed Gaussian beam is given by,

$$2w_0 = \frac{4\lambda}{\pi}\frac{f}{D} \tag{7.5}$$

where w_0 is the beam waist of the focussed beam; λ is the wavelength of light; f is the focal length of the lens; and D is the diameter of the beam illuminating the lens.

However, for microscope objectives a numerical aperture (NA) is typically specified rather than a focal length or beam diameter. Given that the numerical aperture

Fibre name	**Mode field diameter**	**Focal length of coupling lens (1 mm diameter input beam)**	
		at 780 nm	**at 1070 nm**
LMA-10	$7.5 \pm 1.0\ \mu\mathrm{m}$	$7.6 \pm 1.0\ \mathrm{mm}$	$5.5 \pm 0.7\ \mathrm{mm}$
LMA-25	$19.8 \pm 2.0\ \mu\mathrm{m}$	$20.0 \pm 2.0\ \mathrm{mm}$	$14.6 \pm 1.5\ \mathrm{mm}$
LMA-35	$26.0 \pm 2.5\ \mu\mathrm{m}$	$26.2 \pm 2.5\ \mathrm{mm}$	$19.1 \pm 1.8\ \mathrm{mm}$

Table 7.2: Focal length of lens that would be required to generate a focussed spot size equal to the mode field diameter for the ESM-PCFs for a $1\,\mathrm{mm}$ diameter input beam.

is given by $NA = n\sin\theta = n\sin\arctan\left(D/\left(2f\right)\right) \simeq D/\left(2f\right)$, we can rewrite the equation 7.5 as,

$$2w_0 \simeq \frac{2\lambda}{\pi}\frac{1}{NA} \tag{7.6}$$

This equation assumes that the back aperture of the objective lens is filled completely. If the back aperture is underfilled, the value of NA for the objective should be multiplied by the ratio of input beam diameter to the diameter of back aperture.

In contrast to conventional single mode fibres which require relatively high NA objectives to produce the appropriate spot size (typically less than $7\ \mu\mathrm{m}$) the large spot sizes required for the LMA-25 and LMA-35 fibres mean that (comparatively) low NA optics must be used. Table 7.2 shows the focal length of the lenses, as calculated using equation 7.5, that must be used to achieve the appropriate spot size for the three fibres when using a input beam diameter of $1\ \mathrm{mm}$.

Coupling was achieved using two beam steering mirrors (IR dielectric for the lasers and ion plated silver mirrors for the supercontinuum) and a linear translation fibre coupling stage (Elliot Scientific, model: MDE510). It was found that the optimisation of the angle of the input beam and the distance between the lens and fibre were the most critical for maximising the coupling efficiency. If the coupling stage was adjusted using the lateral linear translators so that the fibre input and objective were perfectly in line with each other, excellent coupling could then be achieved by adjusting only the beam steering mirrors and the linear actuator

controlling the distance between the objective and fibre input. After coupling was optimised by this method, small adjustments of the lateral linear translators would only result in small increases to the coupling efficiency.

Initially, I was concerned over how the broadband nature of the supercontinuum source would affect the coupling. As the spot size of the focus of the coupling lens is proportional to the wavelength λ, as shown in equation 7.5, it was impossible to match the spot size with the mode field diameter for all wavelengths of the supercontinuum spectrum. This potentially could have caused the output from the fibres to have had a drastically narrower bandwidth than the input. However, optimising the spot size for the supercontinuum's central wavelength resulted in fibre output having adequate bandwidth for the experiments needs and a coupling efficiency close to those achieved using the laser sources.

By correctly matching the spot size to the mode field diameter and optimising the optical alignment, I routinely achieved coupling efficiencies between $50\,\%$ and $70\,\%$.

7.6.4 Testing single mode operation

Due to space and cost considerations, I intended on using lengths of fibre less than $2\,\mathrm{m}$. Due to the characteristics of ESM-PCF, as discussed section 7.5.2, fibres this short are not guaranteed to output a single mode. Consequently, for each fibre and wavelength combination, the mode output had to be checked. A number of methods were used to test whether or not the fibres were operating in a single mode. It was possible to check if the fibre was operating in a multimode regime by observing the output of the fibre. When changing the launch conditions, the output of a fibre operating in a single mode will only change intensity and will not change shape. Therefore, if when scanning one of the lateral axes of the fibre launch stage, the mode was observed to change shape, the fibre was not operating in a single mode.

It was also possible to observe the contribution of higher order modes in the fibre by rotating a linear polariser in front of the output. If the input light to the fibre is

linearly polarised, the fundamental mode will be the same polarisation, provided that the fibre is kept free of mechanical stress. Higher order modes however may have a different polarisation. By placing a linear polariser with its transmission perpendicular to the polarisation axis of the fundamental mode, it was possible to observe any higher order modes. Care was taken however to keep the fibre free of mechanical stress. By placing optical fibres in a curve, the silica undergoes stress induced birefringence. This effect is utilised in fibre polarisation controllers where loops of the fibre, forming fractional wave plates, are used to control the polarisation of the light within the fibre. It was therefore important to keep the fibres straight or if curved, make sure that the plane of the curve is perpendicular or parallel to the direction of linear polarisation of the light, therefore assuring the light remains linearly polarised. If this rule was not followed, the linear polarised light became elliptically or circularly polarised, reducing the usefulness of the rotating polariser analysis method.

7.6.5 Obtaining mode profiles

Mode profiles were obtained by imaging the output of the fibre using a 100x long working distance objective (Mitutoyo, model: M Plan Apo) onto either an anologue CCD (Pulnix, model: PE2015) or a digital CCD (Basler, model: A641f), with the latter camera offering better image quality and higher resolution. The objective and camera setup were attached to an xyz linear positioning stage (Newport, Model: 562 Series) using a cage plate assembly. The xyx stage was then adjusted so that the objective imaged the end facet of the fibre. The intensity of the image was then adjusted either by adding neutral density filters (which often compromised the image), reducing the shutter speed of the camera (only possible using the Basler CCD camera) or reducing the power of the input light to the fibre. A micrograph could then be taken of the mode.

In order to measure the mode profile of as it propagated, the xyz was translated along the path of the beam, thereby imaging the mode as it propagated. Successive micrographs were then taken at intervals of $5\ \mu\mathrm{m}$ or $10\ \mu\mathrm{m}$, up to a distance of $500\ \mu\mathrm{m}$. These micrographs were then analysed using a MATLAB program

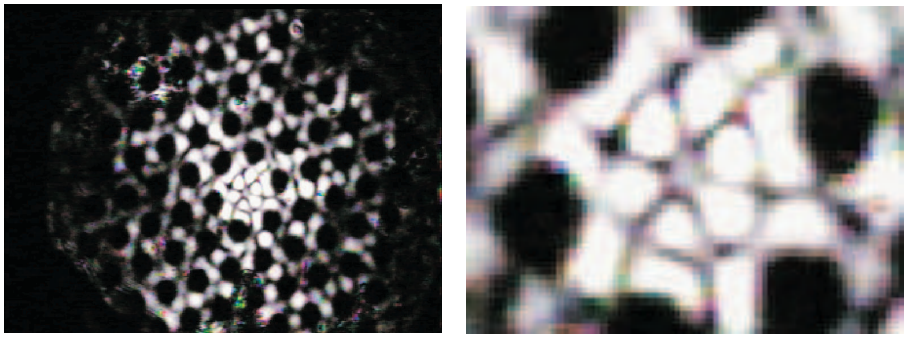

(a) (b)

Figure 7.8: Micrographs of a higher order mode in a straight $1.7\ \mathrm{m}$ long LMA-35 fibre, $780\,\mathrm{nm}$ laser radiation. The higher order mode was preferentially excited by misaligning the coupling stage on one of the lateral axes. Figure 7.8(a) shows the higher order mode and the cladding. The illumination in the cladding indicates that power from the higher order mode is leaking into the cladding. Figure 7.8(b) zooms in to show the detail of the mode.

written by Tomáš Čižmár.

7.6.6 Characterisation of LMA-35 using 780 nm laser

When using the lowest wavelength laser, $780\ \mathrm{nm}$, with the largest core size fibre, LMA-35, I found that the fibre was operating in a multimode regime for a straight $2\ \mathrm{m}$ long fibre. When changing the coupling conditions, the output from the fibre was seen to change considerably. Although some definite modes where discernible, as shown in figure 7.8, the wide variety of complex shapes the output mode formed when changes were made to the coupling suggested that a large number of modes where present in the fibre.

By placing the fibre in a loop ($420\ \mathrm{mm}$ in diameter), it was possible to operate the LMA-35 fibre in a single mode. Single mode operation was confirmed by observing no change in the mode structure on changing the launch conditions and by observing no higher order modes using the crossed polariser method. However, as well as attenuating the higher modes, the curve also severely attenuated the fundamental mode as well. In contrast to the minimum of $32\ \%$ transmission efficiency achieved for the straight fibre, the looped fibre was only able to achieve

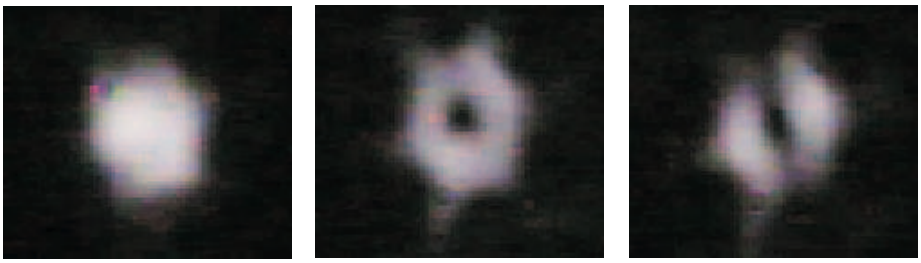

(a) Primarily LP_{01} mode. (b) Primarily LP_{11} mode. (c) Combination of LP_{01} and LP_{11} modes.

Figure 7.9: Micrographs of a higher order mode in a straight $2\ \mathrm{m}$ long LMA-25 fibre using $1070\ \mathrm{nm}$ laser radiation. The three subfigures show the higher order modes which were preferentially excited by misaligning the coupling stage on one of the lateral axes. Figure 7.9(a) is primarily one of the fundamental LP_{01} modes; Figure 7.9(b) appears to be primarily the LP_{11} mode [87]; and figure 7.9(c) appears to be a combination of these two modes [84].

$7\ \%$ transmission efficiency. Consequently the maximum laser power of $800\ \mathrm{mW}$ would only yield have yielded a fibre output power $27.9\ \mathrm{mW}$, when using two fibres, which would be insufficient for statistfactory operation of a dueal beam fibre trap. It should be noted that at this point, I had not yet discovered the importance of angular alignment to the coupling and it is probable that these efficiencies are very much lower than possible. Despite this insufficiency, the results are still instructive as the main loss in the fibre was shown to be from the bend losses and would not be recoverable from optimising coupling alone.

7.6.7 Characterisation of LMA-25 fibre using 780 nm and 1070 nm lasers

At this point, due to the difficulties in achieving single-mode output with adequate transmission efficiency using the LMA-35 fibre, I decided to switch to the LMA-25 fibre and also characterise the fibre using the $1064\ \mathrm{nm}$ laser. At this point I realised the importance of angular alignment when coupling into the fibre, and consequently the transmission efficiencies increased.

Coupling $1064\ \mathrm{nm}$ laser radiation into a $2\ \mathrm{m}$ long straight fibre, resulted in mul-

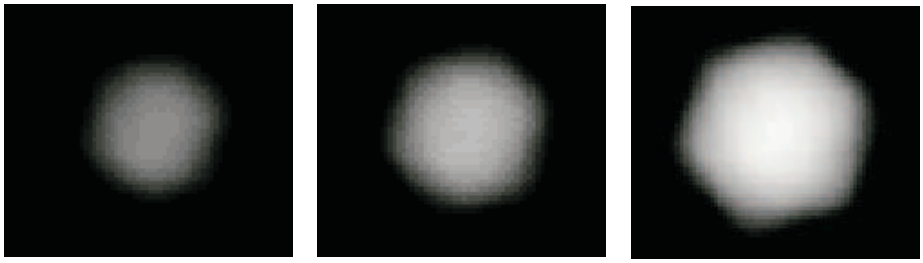

(a) (b) (c)

Figure 7.10: Micrographs of the single mode output of the curved LMA-25 for different degrees of misalignment in one of the coupling stage's lateral axes. As the coupling is altered only the intensity of the mode is affected; no change in mode shape is observed.

timode output, but in contrast to the LMA-35 fibre used with $780\ \mathrm{nm}$ which appeared to support a large number of higher order modes, the output only appeared to consist of two modes, as shown in figure 7.9. Initial attempts at achieving a single mode output with the curved $2\ \mathrm{m}$ long straight fibre proved very successful and it was decided to cut the fibre in half. With the fibre now cut down to a $1\ \mathrm{m}$ length and positioned in a $300\ \mathrm{mm}$ diameter semi-circular loop, the fibre was single-mode, as shown in figure 7.6.7, with a transmission efficiency of $\sim 70\ \%$. The profile of the mode was taken as it propagated away from the fibre end. The profile is similar in shape to the theoretical profiles discussed in section 7.5.1. In the near field the axial intensity, as shown in figure 7.11, is seen to reduce in intensity before coming to a focus at a distance of $\sim 130\ \mu\mathrm{m}$ away from the fibre end. After this focus point, the intensity falls away with distance.

In a similar curved configuration, the LMA-25 when used with $780\ \mathrm{nm}$ laser radiation also yielded a single mode output, with an efficiency of $\sim 50\ \%$.

7.6.8 Characterisation of LMA-25 and LMA-10 using supercontinuum radiation

Supercontinuum radiation was used with both the LMA-25 and LMA-10 fibres. Single mode output was achieved in curved $1\ \mathrm{m}$ long lengths of each fibre. LMA-

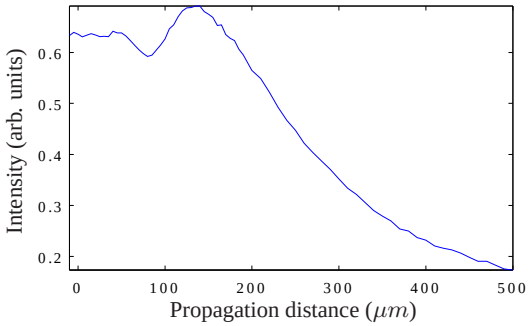

Figure 7.11: On-axis propagation intensity profile of single-mode output from LMA-25 fibre. The laser wavelength used is $1070\,\mathrm{nm}$. In the near field region, the intensity dips then reaches a peak at a distance of $\sim 130\ \mu\mathrm{m}$ away from the fibre end. After this point the intensity decays with increased distance.

10 was single-mode in nearly straight lengths of fibre, whereas the LMA-25 fibre needed bends similar to those used for $780\ \mathrm{nm}$ and $1064\ \mathrm{nm}$ lasers.

Due to the broadband nature of the supercontinuum radiation, the ouput modes had to observed with different wavelengths of light. This was achieved by placing $50\ \mathrm{nm}$ band pass holographic filters in front of the fibre output and observing the mode. In certain circumstances, such as the straight LMA-10 fibre, the fibre would output a single mode for longer wavelengths of light, but would start to operate in two modes when the wavelength of light went below a certain value, for example $550\ \mathrm{nm}$.

The output spectrum from a curved $1.5\ \mathrm{m}$ length of LMA-25 is shown in figure 7.12. Although the spectrum will have been attenuated by both the fibre and the preceding optics, it does not deviate greatly from the output of the supercontinuum source, as shown in figure 7.7.

7.7 Conclusion

Three commercial ESM-PCF fibres, purchased from Crystal Fibre A/S, were experimentally characterised for $780\ \mathrm{nm}$, $1064\ \mathrm{nm}$ and supercontinuum radiation. Optimal coupling was found to be achieved when the spot size of the focussed

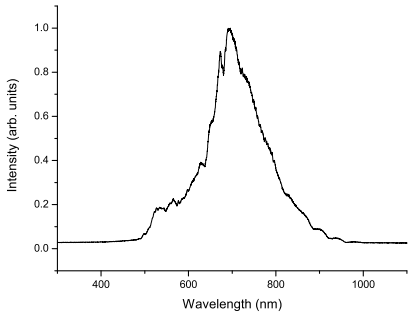

Figure 7.12: This figure shows the output spectrum of LMA-25 using the supercontinuum source. The spectrum does not deviate noticeably from the nominal output of the laser, as shown in figure 7.7. The LMA-25 is 1.5 m long and is curved to suppress higher order modes.

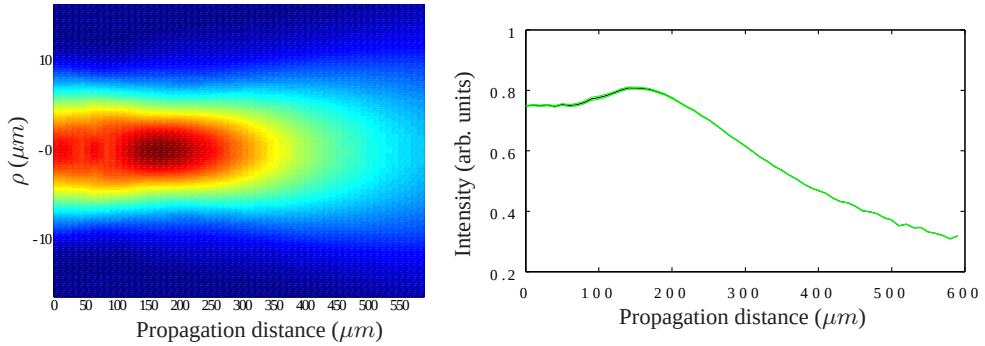

(a) Transverse mode profile on propagation.

(b) Axial intensity profile.

Figure 7.13: Mode profile of the LMA-25 when used with the supercontinuum source. Figure 7.13(b) show the transverse mode profile on propagation and figure 7.13(a) shows how the maximum intensity of the mode, located on the central axis, varies with propagation.

coupling beam matched the mode field diameter of the fibre. Optimisation of the angle of the coupling beam was found to be crucial for maximising the transmission efficiency. By optimising the focal spot size, the position of the focus relative to the fibre and the angle of the beam, coupling efficiencies of $\sim 70\,\%$ were routinely achieved for both the LMA-25 and LMA-10 fibres for the two lasers and $\sim 50\,\%$ for the supercontinuum.

It was found that under real life experimental conditions, single-mode output was not assured for lengths of fibre under $2\,\mathrm{m}$. In straight fibres under $2\,\mathrm{m}$ higher order modes were always present for all the radiation sources. By placing the fibre in a $300\ \mathrm{mm}$ diameter semi-circular loop (or similar), the fibres could be made to operate in a single mode, as the induced bend losses reduced the length of the fibre needed to attenuate the higher order modes. The bends also increased the attenuation of the fundamental mode. The influence of higher order modes was seen to be greater for larger core sizes and shorter wavelengths. For bent fibres, the attenuation of the fundamental mode was also greater for larger core sizes and shorter wavelengths. Consequently for the LMA-35 fibre used with the $780\ \mathrm{nm}$ laser, the radii bends needed to attenuate the higher modes, also resulted in high attenuation of the fundamental mode. However, the bends needed to yield single-mode output for LMA-25 and LMA-10 fibres did not considerably attenuate the output of the fundamental mode.

Consequently, LMA-35 fibre was deemed unsuitable for use in the dual beam fibre trap described in chapter 8. The LMA-25 and LMA-10 fibres were both deemed useful. For both fibres (the LMA-25 in particular) it was noted that the output should be confirmed as being single-mode when the fibres were either re-cleaved or repositioned.

The beam profiles of the LMA-25 and LMA-10 fibres were measured. The characteristic propagation output profile of the modes were recorded for the $1070\ \mathrm{nm}$ and supercontinuum radiation. These profiles were important for the understanding the correct operation of the fibre trap constructed in chapter 8.

7.8 Author's contribution

The characterisation of the ESM-PCF fibres was carried out in conjunction with Antonia Carruthers and Tomáš Čižmár. The characterisation of the fibres at $780\mathrm{nm}$ and $1064\,\mathrm{nm}$ was performed mainly by me, with the characterisation using the supercontinuum performed with the assistance of Antonia. The analysis of the mode profiles was performed by Tomáš.

Chapter 8

DUAL BEAM ENDLESSLY SINGLE-MODE PHOTONIC CRYSTAL FIBRE TRAPS

8.1 Chapter synopsis

This chapter details the construction and characterisation of a number of dual beam fibre traps constructed using endlessly single mode photonic crystal fibres. The unique properties of endlessly single mode photonic crystal fibres, as described in chapter 7, are exploited to create dual beam fibre traps with novel properties. These dual beam ESM-PCF traps are the first reported use of photonic crystal fibre in fibre traps.

Firstly, the theoretical characteristics of a dual beam fibre trap constructed from conventional fibre is compared to one constructed from ESM-PCF. I show that by changing the fibre separation, the trap stiffness of an ESM-PCF trap can be made to have positive, negative or near zero values. Whereas a positive trap stiffness results in the typical confining force, a negative trap stiffness yields a repulsive (from trap centre) potential, and a near zero trap stiffness yields a near line potential.

Secondly, the experimental characteristics of single wavelength fibre trap operating at $1070\ \mathrm{nm}$ are described. Confining, repulsive and line potentials are observed. However, the characteristics of this trap were dominated by standing wave effects caused by the presence of the square capillary holding the sample. Long chains of particles were observed to form in this trap with standing wave effects seen to influence the separation of the particles.

Thirdly, the endlessly single mode characteristic of the PCF was exploited to form the first dual beam fibre trap formed with broadband supercontinuum light. As the coherence length of the supercontinuum radiation was less than the particle-particle and capillary wall-particle separation, the interference effects from the capillary were removed. Long chains of particles were also observed in this trap, this time with particle separations governed by binding effects.

Fourthly, a dual wavelength optical conveyor belt was constructed using ESM-PCF. For this experiment, interference between the two trapping arms was intentionally exploited for both wavelengths to form two standing wave traps superimposed on each other. By adjusting the phase difference between the two arms of the beams, the positions of the nodes and anti-nodes of the standing wave changed, thus moving the particles; this technique is known as an optical conveyor belt [88]. As different species of particles are influenced to different degrees by certain wavelengths of standing wave, the dual wavelength optical conveyor belt was used to selectively move two sizes of trapped particles.

Finally, the potential applications of dual beam PCF traps to the field of biophotonics are discussed. The possibility to trap cells at one wavelength and interrogate them with another wavelength is explored.

8.2 Introduction to dual beam fibre traps and motivation to use ESM-PCF

In 1970, Ashkin created the first stable optical trap using the counter-propagating dual beam geometry [5], as shown in figure 8.1. Held within a counter-propagating

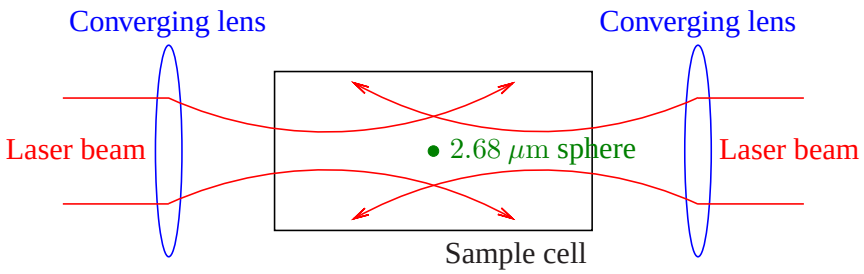

Figure 8.1: The configuration of Ashkin's original optical trap [5]; the counter-propagating dual beam fibre trap. The two diverging counter-propagating beams are created using converging lenses. In order to generate the correct axial force, the location of the focal point of these lenses must be closer to the lens than the desired trap centre.

dual beam trap, a particle will be confined axially by the difference in scattering force from the two diverging beams and radially by the sum of the gradient force from the two beams. Although this technique was initially superseded by single beam optical tweezers [7], which continue to be used with great success for a variety of applications [89], it was revisited and re-engineered by Constable and co-workers in 1993 [19]. By delivering the divergent beams using optical fibres, as shown in figure 8.2, Constable and co-workers greatly increased the versatility of the technique, and spawned renewed interest in this method.

Dual beam fibre traps are constructed by carefully aligning two counter propagating optical fibres and ensuring that the outputs from both fibres are powerful enough to move the particle and of equal magnitude. Unlike optical tweezers, which confine particles using mainly the gradient force, fibre traps confine particles using both the gradient force and the scattering force. As a result of the diverging nature of the beams, when a particle is axially displaced from the trap centre, it will experience a stronger scattering force from the fibre it moves towards and a weaker scattering force from the fibre it moves away from [1]. Consequently, the particle experiences an axial restoring force towards an equilibrium point where the scattering forces from the two fibres cancel. When displaced in a radial direction, the particle will experience a restoring force towards the central

[1]There is also an axial component of the gradient force due to the divergence of the beams, but due to its small magnitude it is usually ignored.

axis of the beam as a result of the gradient force. In fibre traps, the radial force is greater than the scattering force. For a trap constructed from conventional single mode fibre, Wei and co-workers [90] measured the radial force to be 3.6 greater than the axial restoring force due to scattering. This difference in magnitudes originates from the additive nature of the radial force and the differential nature of the axial restoring force due to the scattering.

These dual beam fibre traps have been shown to have some useful characteristics, and in many cases the technique is preferred over optical tweezers. Dual beam fibre traps have a large capture range, do not use focussed light therefore reducing the likelihood of light induced damage to the (biological) sample, can be easily aligned, and allow the trapping and imaging optics to be easily decoupled from each other. These features have contributed to the successful use of dual beam fibre traps in Raman spectroscopy studies [91], in optical binding studies [92], for the optical stretching of cells [93], and within integrated [94] and microfluidic devices [95, 96].

In many ways the characteristics of the trap are heavily influenced by the fibres used. Until the studies presented in this thesis, fibre traps had only been implemented using conventional single-mode or multimode fibres. Multimode fibres can be sometimes preferred when a simple trap is needed, as they are easy to couple into, can sustain high optical powers and generate a highly divergent beam. However, multi-mode fibre traps suffer from hot spots due to the interference of the different modes. Consequently the potential is not smooth and particles can become trapped in one of the many locations corresponding to the hot spots. This characteristic renders multimode fibres unsuitable for experiments that need well defined potentials, such as for optical stretching and binding studies. Consequently, for many applications, single-mode fibres are desirable or necessary, in that they produce smooth and well-defined potentials.

As described in chapter 7, endlessly single-mode photonic crystal fibre (ESM-PCF) has vastly different characteristics in comparison to conventional fibres. Specifically, ESM-PCF can guide any wavelength of light in a single-mode in large core diameters (commercially available up to $35\ \mu\mathrm{m}$) and has a hexagonal shaped mode with the output intensity coming to a ‘focus’ a finite distance from

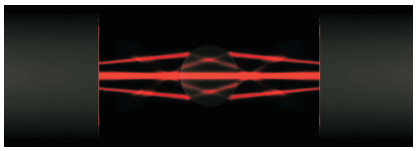

(a) Representation of fibre trap.

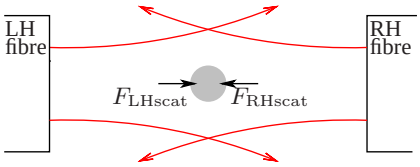

(b) Forces balance when sphere trapped in centre.

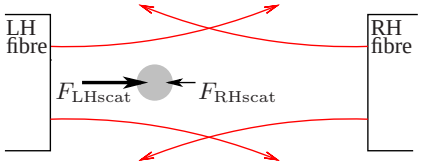

(c) Axial displacement results in a restoring force towards centre due to the difference in scattering forces.

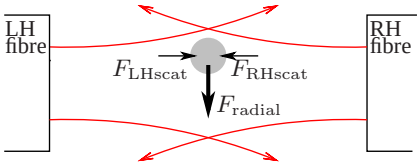

(d) Radial displacement results in a restoring force towards centre due to the sum of gradient forces.

Figure 8.2: The dual beam fibre trap, represented graphically in figure 8.2(a). Figure 8.2(b) shows the gradient and scattering forces acting upon the sphere when the sphere is held at the trap centre. Figure 8.2(c) shows the forces acting upon the sphere when the sphere is displaced in an axial direction. Figure 8.2(d) shows the forces acting upon the sphere when the sphere is displaced in a radial direction. F_{LHscat} and F_{LHscat} are the scattering forces from the left and right fibre respectively. F_{radial} is the sum of the gradient forces due to both beams.

the fibre end. By virtue of these properties, a dual beam fibre trap constructed using ESM-PCFs had the potential to exhibit novel characteristics.

The initial motivation was to examine the properties of a fibre trap constructed from ESM-PCF when using a single wavelength conventional laser source. Subsequently the focus of the investigation changed to examining the characteristics of a white light dual beam fibre trap, in an effort to neutralise interference effects observed in the single wavelength trap as a result of the capillary sample holder. Finally, I was able to exploit the endlessly single-mode nature of the fibres to form an dual wavelength optical conveyor belt

8.3 Nature of the axial restoring force in dual beam conventional fibre traps and dual beam ESM-PCF traps

The scattering forces from the two fibres play the most important role in determining the characteristics of the dual beam ESM-PCF trap. As was shown in chapter 7, the axial (propagation) intensity profile of ESM-PCFs is markedly different to conventional fibre, in that the mode profile comes to a focus at a finite distance away from the end face. Although this property has little bearing on the gradient/radial restoring force, as the maximum intensity of the beams is always situated on-axis, it does have major implications for the axial restoring force.

In order to understand how the axial mode profile of ESM-PCF influences the axial restoring force, I modelled the axial force profile for both conventional and ESM-PCF dual beam fibre traps.

8.3.1 Analytical analysis of axial forces in dual beam conventional fibre traps

The total scattering force experienced by a dielectric sphere is given by [97],

$$F_{\text{scat}} = \frac{n_1}{c} Q_{\text{scat}} P, \tag{8.1}$$

where n_1 is the refractive index of the medium surrounding the sphere; P is the power of the incident ray hitting the sphere; and Q_{scat} is the fraction of the light's momentum transferred to the sphere.

For a fibre trap the resultant axial force of the two beams on the particle is given by,

$$F_{\text{axial}} = \frac{n_1}{c} Q_{\text{scat}} P_{\text{sphereleft}} - \frac{n_1}{c} Q_{\text{scat}} P_{\text{sphereright}} \tag{8.2}$$

where $P_{\text{sphereleft}}$ and $P_{\text{sphereright}}$ are the quantity of power incident on the sphere from the left and right fibres respectively.

The output of conventional single-mode fibres is accurately approximated by a Gaussian. Using this Gaussian approximation, the power P_{sphere} intercepted by a sphere of radius R_{sphere} situated in the output of a fibre, as function of axial distance z from the beam waist w_0 and radial displacement ρ from the beam axis, is given by [98],

$$\begin{aligned} P_{\text{sphere}}(z,\rho) = {} & \frac{2P_0}{\pi w^2(z)} \exp\left[\frac{-2\rho^2}{w^2(z)}\right] \\ & \times \int_0^{2\pi} \int_0^{R_{\text{sphere}}} \exp\left[\frac{-2r^2}{w^2(z)}\right] \exp\left[\frac{-4r\rho\cos r}{w^2(z)}\right] r\, dr\, d\theta, \end{aligned} \tag{8.3}$$

where $w(z) = w_0\sqrt{1 + \left(\frac{z\lambda}{\pi w_0^2}\right)}$.

If the two beam are of equal power and have identical profiles, the scattering forces of the two beams will cancel at half the separation of the fibres; this point is the trap centre. For a trap with fibre separation S, we can therefore rewrite the equation 8.2 as a function of displacement d from trap centre and radial displacement

from the beam axis ρ, thus,

$$F_{\text{axial}}(d,\rho) = \frac{n_1}{c} Q_{\text{scat}} \frac{2P_0}{\pi w_{\text{left}}^2(d)} \exp\left[\frac{-2\rho^2}{w_{\text{left}}^2(d)}\right] \times \int_0^{2\pi}\int_0^{R_{\text{sphere}}} \exp\left[\frac{-2r^2}{w_{\text{left}}^2(d)}\right] \exp\left[\frac{-4r\rho\cos r}{w_{\text{left}}^2(d)}\right] r\,dr\,d\theta - \frac{n_1}{c} Q_{\text{scat}} \frac{2P_0}{\pi w_{\text{right}}^2(d)} \exp\left[\frac{-2\rho^2}{w_{\text{right}}^2(d)}\right] \times \int_0^{2\pi}\int_0^{R_{\text{sphere}}} \exp\left[\frac{-2r^2}{w_{\text{right}}^2(d)}\right] \exp\left[\frac{-4r\rho\cos r}{w_{\text{right}}^2(d)}\right] r\,dr\,d\theta, \quad (8.4)$$

where $w_{\text{left}}(d) = w_0\sqrt{1+\left(\frac{(S/2+d)\lambda}{\pi w_0^2}\right)}$ and $w_{\text{right}}(d) = w_0\sqrt{1+\left(\frac{(S/2-d)\lambda}{\pi w_0^2}\right)}$.

Using this equation, it is possible to visualise the axial force within a conventional fibre trap. Figure 8.3 shows an example force profile within a conventional fibre trap . As can be seen from the profile, the on-axis axial force is always directed towards the trap centre.

We can also assign a trap stiffness (also known as spring constant) k to the trap by,

$$F_{\text{axial}} = -kd \quad (8.5)$$

$$\therefore\ k = -\frac{F_{axial}}{d} \quad (8.6)$$

and is evaluated around the position $d = 0$.

As can be seen in figure 8.4 the trap stiffness k reaches a maximum value when the fibre separation S is approximately twice the Rayleigh range of the fibre beams [19]. This is an important characteristic to bear in mind when designing fibre traps, as it may go against the first instinct that the closer the fibres are together the stronger the trap.

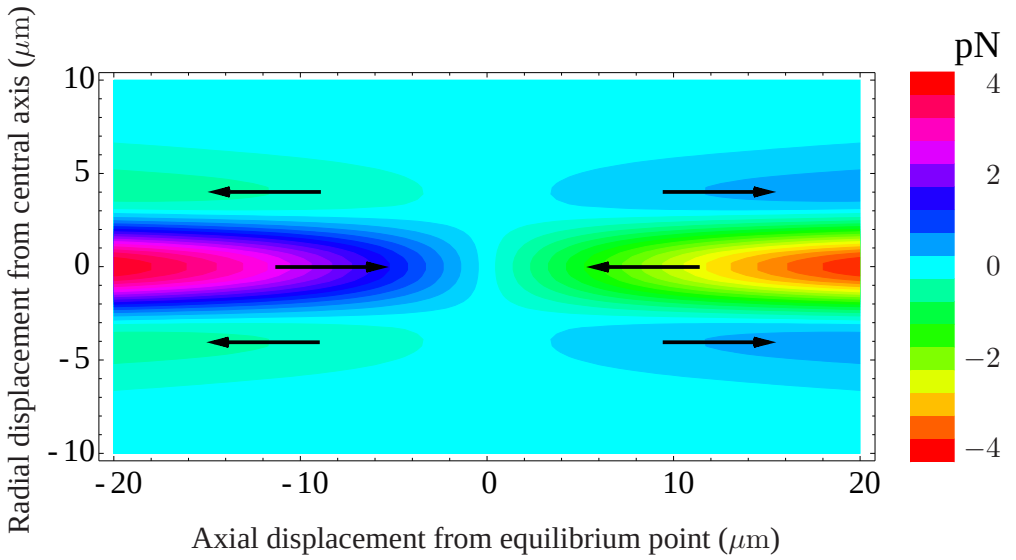

Figure 8.3: Axial force profile calculated using equation 8.4 for a $3\ \mu\mathrm{m}$ diameter polystyrene bead in water, with trap parameters: fibre separation $S = 40\ \mu\mathrm{m}$; $\lambda = 1070\ \mathrm{nm}$; beam waist or mode field radius $w_0 = 3.1\ \mu\mathrm{m}$; and laser power $P_0 = 30\ \mathrm{mW}$. The arrows denote the direction of the force.

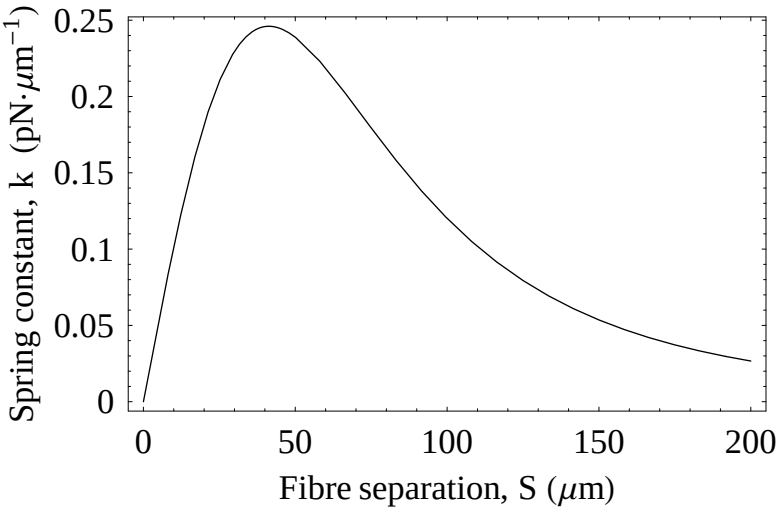

Figure 8.4: The calculated value of the spring constant k of a fibre trap as a function of fibre separation. The spring constant k is maximum at a value around $40\ \mu\mathrm{m}$. The trap stiffness is calculated for a $3\ \mu\mathrm{m}$ diameter polystyrene bead in water and with trap parameters: $\lambda = 1070\ \mathrm{nm}$; beam waist or mode field radius $w_0 = 3.1\ \mu\mathrm{m}$; and output power $P_0 = 30\ \mathrm{mW}$. The Rayleigh range of the beams is $28.2\ \mu\mathrm{m}$.

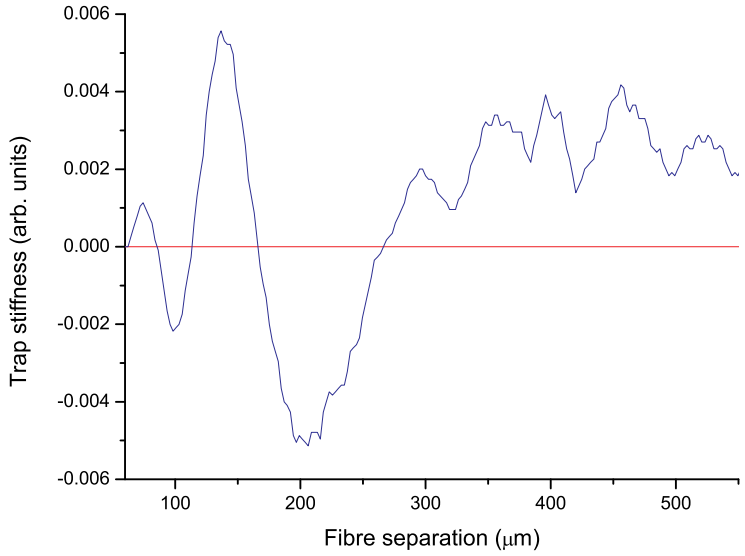

Figure 8.5: Axial trap stiffness of dual beam ESM-PCF fibre trap as function of fibre separation. The red line indicates zero trap stiffness boundary. Values above this line result in a confining potential and values below this line result in a repulsive potential.

8.3.2 Numerical analysis of axial forces in dual beam ESM-PCF traps

ESM-PCFs have a longitudinal intensity profile greatly different to conventional fibres, as shown in chapter 7. As a consequence of the hexagonal shape of mode, the mode on propagation rotates through two 30° rotations [82] and comes to a focus a finite distance away from the end of the fibre [81]. The hexagonal shape of the mode and its rotation on propagation had little consequence to the operation of the trap, as this behaviour only affects the lower intensity region of the mode; the mode closely resembles a Gaussian for intensities greater than $1/e^2$ [81].

Of great importance however, was how the mode comes to a focus. For conventional fibre traps, as shown in figure 8.4, all values of fibre separation S result in a positive axial spring constant, i.e. the sphere will always feel an axial force towards the point midway between the fibres. By changing the trap separation only

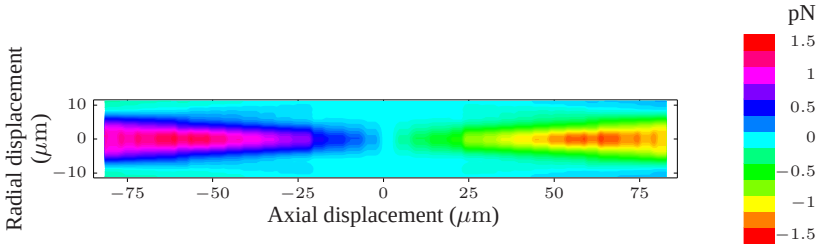

(a) 356 μm fibre separation resulting in a conventional 3-d trapping potential.

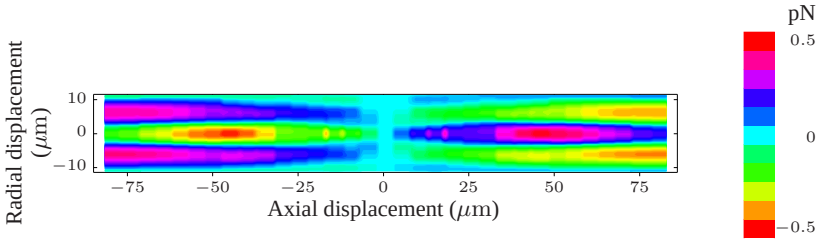

(b) 175 μm fibre separation resulting in an axially repulsive/radially confining potential.

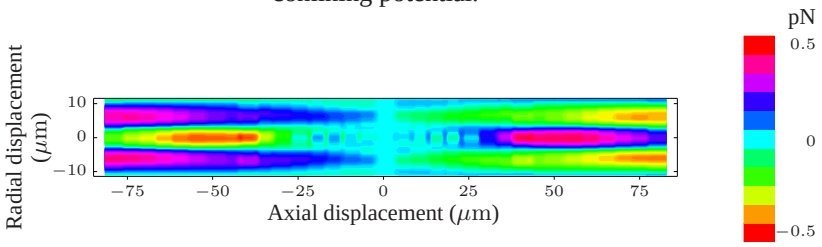

(c) 165 μm fibre separation resulting in a radially confining weak axially confining/repulsive 'line' potential. With increasing displacement, the axial potential appears to alternate between weakly confining and weakly repulsive potentials before changing to greatly repulsive. The alternating confining and repulsive potentials could result in multiple weak traps.

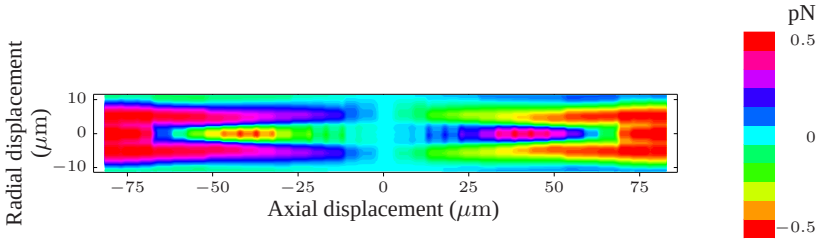

(d) 264 μm fibre separation resulting in a radially confining and weak axially repulsive 'line' potential. With increasing displacement the axial potential changes from weakly repulsive to greatly repulsive.

Figure 8.6: Numerical calculations of the axial force profiles for a 3 μm polystyrene sphere situated in water, while held in a dual beam ESM-PCF trap, for different fibre separations. The magnitude and value of the axial potential can be altered by changing the fibre separation; resulting in conventional 3-d trapping, axially repulsive and 'line' potentials. The radial potential is always confining. The fibre profile used for this calculation was that of the 25 μm diameter core LMA-25 fibre with laser wavelength $\lambda = 1070$ nm. The force was calculated for an output power $P_0 = 30$ mW.

the magnitude of the force profile will change. However, for a dual beam fibre trap constructed of ESM-PCF, the dependence of the force profile on fibre separation is much more complicated. As the on-axis output intensity is maximum at a finite distance ($\sim 130\ \mu\mathrm{m}$ with $\lambda = 1070\ \mu\mathrm{m}$ for the $25\ \mu\mathrm{m}$ diameter core LMA-25 fibre) away from fibre, as discussed in section 7.6.7, changing the fibre separation can not only change the magnitude of the axial spring constant, but can make the spring constant negative or make it close to zero. Figure 8.5 shows the variation of the axial spring constant with fibre separation. Using the measured mode profile of the LMA-25 fibre, it is possible to numerically calculate the force profile of the dual beam ESM-PCF with varying fibre separations. Figure 8.6 shows calculated profiles for a separation of $356\ \mu\mathrm{m}$, which results in a positive spring constant; $175\ \mu\mathrm{m}$ which results in a negative spring constant; and $165\ \mu\mathrm{m}$ and $264\ \mu\mathrm{m}$ which result in a spring constant that is close to zero, resulting in a line potential.

8.4 Experimental design

8.4.1 Requirements

In order to investigate experimentally the properties of dual beam ESM-PCF traps, a stable and versatile apparatus was assembled. Aside from the basic requirements of fibres, sample and imaging optics, a number of other more stringent requirements needed to be met. Although the trap was relatively easy to coarsely align, it was crucial to be able to align the fibres to a high accuracy. I also needed to be able to change the fibre separation in an easy manner. Due to the holey nature of the PCF, it was also necessary to isolate the sample from the fibres. Finally, all the laser and opto-mechanical systems needed to be extremely stable in order to achieve meaningful and repeatable data. The following sections detail the design and evolution of the apparatus.

8.4.2 Isolation of fibres from the liquid sample

As the properties of the ESM-PCF are derived from the lattice of air holes in the cladding, it was important to keep these holes free from contamination. For this experiment, where I wanted to trap particles suspended in a liquid medium, there was the possibility that the fibre could come into contact with this liquid. If his had happened, capillary action would have resulted in the liquid propagating millimetre distances up the fibre, destroying the properties of the photonic crystal, resulting in a messy output mode. Therefore, one of the first issues to be addressed, was how I would isolate the medium from the fibres. Three options were considered.

Commercially available sealed fibres

The manufacturer of the ESM-PCFs used in this thesis, Crystal Fibre A/S [75], is able to heat treat the ends of the fibres in such a way that the air holes collapse and hermetically seal the ends. These sealed fibres could then have come into contact with liquid without suffering any adverse problems. I did not choose this method as, although the sealed fibre ends would have allowed the fibre to be connectorised and re-polished, past experiences with fibre traps in the group suggested that it would be necessary to have to re-cleave the fibres on a semi-regular basis. As re-cleaving the fibre would have removed the sealed ends, I decided that it was not worth the time or money required to purchase them.

Polymer sealing

It was also possible to seal the holes of a PCF using UV curable polymer (or adhesive) [99, 100]. This method involves placing the ends of the fibre in UV curable polymer, allowing the polymer to be drawn into the holes by way of capillary action and then curing the polymer after a certain length of time (and therefore propagation distance up the fibre) using UV light. The fibre can then be cleaved to yield a clean end facet. Although this method would change the mode field diameter (and consequently the numerical aperture) of the fibre and possibly reduce

the mode quality, it seemed to be a promising solution. However, I elected to use the following method first.

Hollow square capillary

Instead of modifying the fibre and therefore potentially introducing uncertainties to the mode profile, I decided that it would be better to isolate the sample from the fibre using some form of sample chamber. I chose to use a hollow square borosilicate micro-capillary with an inside diameter of $100\ \mu\mathrm{m}$ and an outside diameter of $200\ \mu\mathrm{m}$ (VitroCom, model: VitroCELL 8510-100). This isolation method had certain advantages in that it allowed the samples to be sealed, re-used and easily swapped; and also opened up the possibility of delivering the sample through the capillary using a microfluidic system. Subsequent to the initiation of my set-up, Lincoln and co-workers [96] reported the use of a similar dual beam fibre trap configuration, using conventional fibres, involving a square capillary and microfluidic setup. However, as will be shown later in this chapter, the capillary introduced undesirable standing waves in the trap region.

The glass walls of the capillary and the liquid (water) sample change the path of the beam due to refraction. The equivalent propagation distance z_{equivair} through air only, can be worked out by the equation [96],

$$z_{\mathrm{equivair}} = \left(\frac{z_{\mathrm{air}}}{n_{\mathrm{air}}} + \frac{z_{\mathrm{glass}}}{n_{\mathrm{glass}}} + \frac{z_{\mathrm{water}}}{n_{\mathrm{water}}} \right) n_{\mathrm{air}}, \tag{8.7}$$

where $Z_{\mathrm{air}}, Z_{\mathrm{glass}}$ and Z_{water} are the propagation distances through the air, glass and water regions respectively; and $n_{\mathrm{air}} = 1.00, n_{\mathrm{glass}} = 1.47$ and $n_{\mathrm{water}} = 1.33$ are the refractive indices of air, glass and water respectively. This equation was used to convert the calculated fibre separation distances in air, to capillary wall to fibre separation distances (a more easy value to measure experimentally), as shown in figure 8.7.

The polymer micro-sphere solution were prepared by diluting drops of the con-

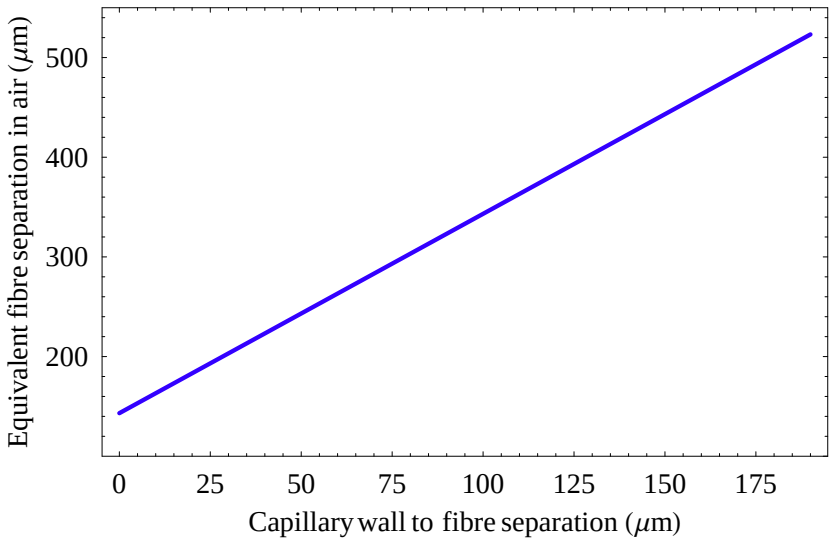

Figure 8.7: Graph converting capillary wall separation to equivalent fibre separation in air alone. The presence of the capillary changes the path of the beam due to diffraction.

centrated sphere solution, as supplied by the manufacturer, with the appropriate quantity (worked out by trial and error) of de-ionised water in a centrifuge tube. The solution was then vigorously mixed by placing the centrifuge tube in a vortex mixer.

One end of a $\sim 25\mathrm{mm}$ length of capillary was held into the prepared sample for a few seconds, allowing the sample to be drawn into the capillary by capillary action. The capillary was then removed from the sample and sealed by pushing each end into a wax sealant designed for this purpose (Hawksley, Model: Cristaseal). If correctly sealed, the sample would remain useable for a few days or more.

The capillary was attached to a microscope slide, using a thin sliver of electrical trap, so that majority of the capillary extended beyond the edge of the slide. The slide could then be easily labelled and attached to an xyz linear positioning stage.

8.4.3 Fibre alignment

Two methods of alignment were used during the investigation. Initially a v-groove slide was used but this was later abandoned in favour of a free-space method.

V-groove alignment

In order to accurately align the capillary in a repeatable way and to ensure the fibres were co-linear, I used a 20×20 mm slide that had been etched with a ~ 100 μm deep v-groove (Adamant Kogyo Co., Ltd.). A slot was cut in this slide so that the height of square capillary could be freely adjusted between the fibres without any hindrance from the v-groove slide. The v-groove slide was then glued to a normal slide to increase stability and two small sections of slide were positioned over each of the grooves. The fibres were then placed facing each other in the grooves. By adding pressure to the small sections of slides, using electrical tape, a weak clamp was formed which held the fibres in the v-groove. The v-groove slide set-up is shown in figure 8.8.

Figure 8.9 shows the apparatus used in addition to the v-groove. External to the v-groove, each fibre was also attached to an xyz linear positioning stage (Newport, model: 562 Series). The stages allowed the fibres to be manoeuvred into place on the v-grooved slide. Once held in the v-groove, the separation of the fibres could be controlled by adjusting the appropriate axis of the xyz stages; the v-groove slide ensured that the fibres remained approximately co-axial as the separation was adjusted.

The capillary was then manoeuvred into position using the xyz linear positioning stage and the rotation stage. The height and position was adjusted to optimise trapping and locate an optimal area of the sample.

Although in principle, this arrangement should have ensured exact alignment, in reality this method proved to have two problems. Firstly, the fixed alignment was not as accurate as was later achieved using manually adjusted linear positioning and rotation stages. This was possibly due to mechanical torque being exerted on

the slide, thus destroying the alignment; or due to the centre of the fibres not being concentric with the cladding. Although adequate and repeatable results were achieved for single particles, the lack of any freedom in the lateral or rotational alignment of the fibres was detrimental when studying multiple particle chains.

Secondly, it was observed during the setting up of the supercontinuum experiment, that the output of the fibre could be severely affected by applying pressure or an abrupt bend near the output end of the fibre. This was presumably as a result of the bend or pressure induced deformity introducing a mode-conversion loss, also known as transition loss, where an abrupt change of curvature results in modal distortion [101] therefore coupling light into higher order modes. I observed that in such situations, a speckle pattern would appear not only in the the mode output but also in the crystal structure of the fibre, suggesting that the fibre was operating in many modes.

Although I could not confirm whether the v-groove set-up induced such mode-conversion problems, as it was impossible to measure the output of the fibre while situated in the v-groove, I assumed that there was a high likelihood that it would, due to the pressure on the fibre from the slide clamps. Subsequent to this discovery, the v-groove method was abandoned.

Free-space alignment

Figure 8.9 shows the experimental set-up, identical to that used with the v-groove slide, however it requires more careful adjustment to compensate for the absence of the slide. Although alignment in free-space was generally more labour intensive than when using the v-groove, having more degrees of freedom usually resulted in superior alignment. Using the xyz positioning stages and rotation stages, the fibres and hollow square capillary were coarsely positioned by eye and then using the microscope. Subsequent to this coarse alignment, a number of fine alignment techniques were used. By blocking one of the coupling beams, and then placing a power meter at the back of the coupling objective facing the input end of the ‘off’ fibre, it was possible to measure the power being coupling between the output ends of the left fibre and right fibre. The coupling could then be optimised by

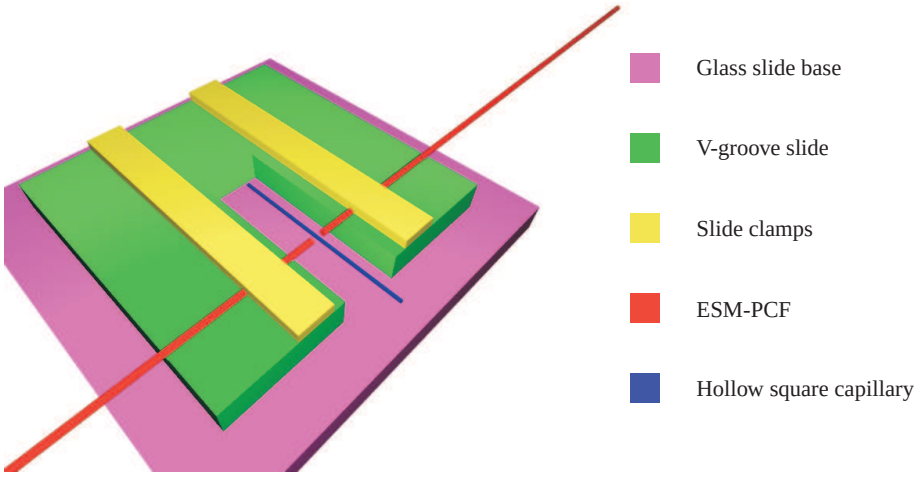

Figure 8.8: Diagram of the fibre alignment when using the v-groove slide. The two ESM-PCF fibres were held in the v-groove by the two clamps that were made from small sections of microscope slide. The separation of the fibres was controllable using one axis of the xyz linear translators; the v-groove insured that the fibres remained relatively co-axial. The square capillary was attached to a microscope slide (not shown), which was then attached to a rotation stage and an xyz linear translator, allowing the sample to be aligned correctly and moved.

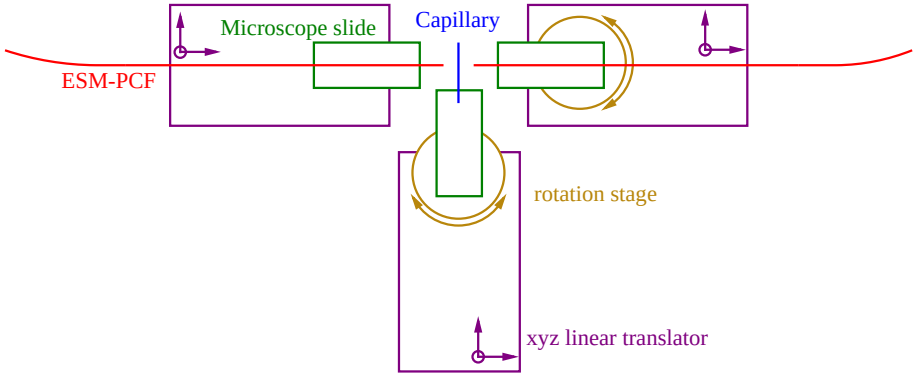

Figure 8.9: Schematic of the fibre trap assembly. The fibres were mounted on glass slides which were then attached to two xyz linear positioning stages. One of the slides was also mounted to a rotation stage; this allowed the fibres to be adjusted so that they were co-linear. The capillary was mounted on a slide which was attached to a rotation stage and an xyz linear translator stage. This allowed the capillary to be aligned correctly and the sample to be moved. When used, the v-groove slide (not shown) was positioned between the two xyz linear translators.

adjusting the xyz linear translators and the rotation stages holding the right hand fibre and the capillary.

It was also possible to optimise the alignment by observing the behaviour of the trapped particles. Misalignment could be manifested in a number of ways, for example, by blocking one of the beams the particle is seen to move in an unexpected direction. Furthermore, arrays of particles were particularly sensitive to misalignment.

As with the v-groove set-up, the capillary's height and position was adjusted to optimise trapping and locate an optimal area of the sample.

The free-space alignment method was not immune to the pressure/bend induced mode conversion problems that may have affected the v-groove alignment method, as the fibres still had to be securely mounted. However it was relatively easy to observe the mode output of the fibres after they had been secured. If any mode conversion effects were observed, the fibre was simply re-positioned and re-secured in a way that resulted in a clean mode.

8.4.4 Imaging and data capture

Imaging was accomplished using an upright homebuilt microscope system. The microscope was constructed using a cage assembly which held 100X long working distance microscope objective (Mitutoyo, model: M Plan Apo), a $200\ \mathrm{mm}$ tube lens and a camera (Basler, model: A641f), shown in figure 8.10. The square capillary sample chamber was illuminated from below. For the initial single wavelength trapping study a conventional light bulb was used, with short pass coloured glass filter mounted before the camera in order to block out scattered $1070\ \mathrm{nm}$ laser light.

The light bulb and short pass filter method was unsuitable for the supercontinuum experiment, as the spectrum of the supercontinuum overlapped with the spectrum of the light bulb, making it impossible to filter out the scattered light without filtering out the illumination as well. Consequently, the light bulb and short pass filter were replaced with a $220\ \mathrm{mW}$, $455\ \mathrm{nm}$ light emitting diode (Lumileds, model:

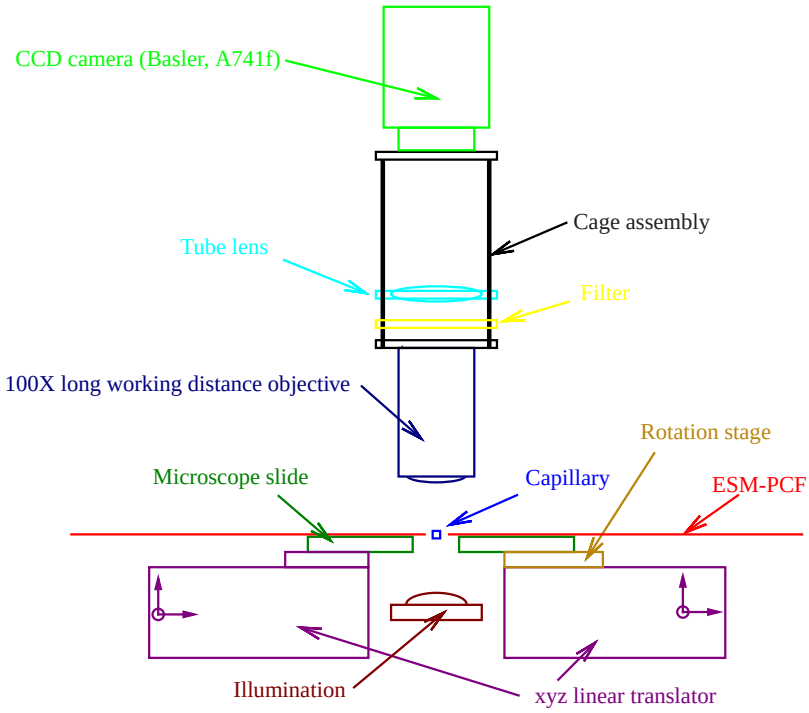

Figure 8.10: Side on view of the fibre trap setup, showing the orientation of the illumination and microscope optics. The long working distance objectives used was a 100X with an NA of 0.70 of (Mitutoyo, model: M Plan Apo). The illumination and filter were removed when wanting to observe the scattered light from the trapped particle. When used, the v-groove slide (not shown) was positioned between the two xyz linear translators.

LUXEON I LXHL-MRRB) and a $50\ \mathrm{nm}$ bandpass filter centred on $450\ \mathrm{nm}$ (Comar, model:450 IU 25). This method of illumination was successful as the spectral power of the supercontinuum was virtually zero in this wavelength range.

In both set-ups, the scattered light from the trapped sample could be observed by turning the illumination down or off and removing the filter.

Observation and recording of the image was accomplished using a fast digital CMOS camera (Basler, model: A741f) and a LabVIEW program.

8.4.5 Methods for experimental calculation of the axial spring constant

We used two different methods for experimentally calculating the axial spring constant. The first method centred around the measurement of a displaced particle's position or velocity as it returned to the trap centre under the influence of the trapping beams and the drag of the liquid medium. The second method involved tracking the motion of the trapped particle and calculating the trap stiffness from the particle's position distribution using the equipartition method.

Drag method

When axially displaced, the particle will feel a restoring force F_{axial} directed towards the trap centre as a result of equation 8.2. As the particles movement in the fluid (water) medium is over damped, we can make an approximation that at each point in its motion F_{axial} will be balanced by the drag force, given by Stokes's law as $F_{\text{drag}} = 6\pi\mu R_{\text{sphere}} v_d$, where $\mu\,(= 1.002 \times 10^{-3}\ \text{Pa}\cdot\text{s})$ is the dynamic viscosity of the liquid (water at $20\ ^{\circ}\text{C}$); R_{sphere} is the radius of the sphere; and v_d is the sphere's velocity. Therefore, the trap stiffness k is given by,

$$k = -\frac{F_{axial}}{d} \tag{8.8}$$

$$= -\frac{F_{\text{drag}}}{d} \tag{8.9}$$

$$= -\frac{6\pi\mu R_{\text{sphere}} v_d}{d} \tag{8.10}$$

Therefore by measuring the velocity v_d of the sphere as a function of displacement d, it is possible to calculate k. Similarly, by integrating equation 8.10, k can be calculated by knowing the particle's position with respect to time.

In order to acquire the relevant data for these calculations, a mechanical shutter (Newport, model: 845P Series) was placed in the each of the beam paths prior to

the coupling stages, allowing the individual on/off control of both fibres. These shutters were set-up in the same configuration as described in section 4.5.7; a LabView program was used to control the timings. This program controlled the shutters in the following way:

- Both fibres turned 'on'.
- Left fibre turned 'off'; sphere rapidly displaced to left as a result of scattering force from right fibre.
- Left fibre turned 'on' again; sphere moves to trap centre as a result of F_{axial}.
- Right fibre turned 'off'; sphere rapidly displaced to right as a result of scattering force from left fibre.
- Right fibre turned 'on' again; sphere moves to trap centre; sphere moves to trap centre as a result of F_{axial}.
- Routine re-started.

The sphere was displaced in both directions, it assess the impact of any misalignments that may have gone unnoticed during the set-up. The timings of the program would generally need to be re-set when the parameters of the trap were altered, e.g. the laser power, particle size e.t.c, to reflect the change in velocities and required time scale of the experiment.

Equipartition method

Using the equipartition theorem it is possible to relate average 1-D kinetic energy E_{KE} of a particle to its temperature T by,

$$\langle E_{\mathrm{KE}} \rangle = \frac{1}{2} k_B T. \tag{8.11}$$

As the potential of the particle trapped within the dual beam fibre trap is harmonic, as $F_{\mathrm{axial}} = -kd$, the relationship between the energy of a trapped particle and its

displacement can be written as $E_{\mathrm{KE}} = E_{\mathrm{axial}} = \frac{1}{2}kd^2$. Therefore, we rewrite equation 8.11 as,

$$\frac{1}{2}k_BT = \frac{1}{2}k\left\langle d^2\right\rangle. \tag{8.12}$$

Therefore, by knowing the temperature T and measuring $\langle d^2\rangle$, which is the average value of d^2 (otherwise known as the variance of d), we can calculate the trap stiffness k.

In an extension of this argument [102], it is possible to determine the trap stiffness using the complete distribution of the particle's displacement d. The relative probability $P\left(d\right)$ of finding a particle at displacement d is given by the Boltzmann factor as,

$$P\left(d\right) \propto \exp\left(\frac{-E_{\mathrm{KE}}}{k_BT}\right) = \exp\left(\frac{-kd^2}{2k_BT}\right), \tag{8.13}$$

which is a simple Gaussian function. Therefore by fitting this function to a distribution of the particle's displacement, it is possible to calculate k.

Choice of method

Each method offered certain advantages over the other. The advantage of the drag method over the equipartition method, was that it was relatively insensitive to drifts in the set-up. The equipartition particle method required a large quantity of positional data in order for the data to be statistically valid, with a typical video being $10\ \mathrm{min}$ long at $50\ \mathrm{fps}$. This method was particularly sensitive to perturbations and drift in the set-up. Even small drifts could cause problems since the tails of the Gaussian distribution, which have few counts, play a disproportionate role in calculating the Gaussian fit [102]. Consequently useable videos of this time scale were difficult to obtain, as other spheres (or contaminants in the sample) would migrate into the trapping region, possibly due to heating ef-

fects. These particles would then become trapped thereby perturbing the position of the original trapped particle(s). Even small perturbations due to vibrations, or laser and opto-mechanical drift could greatly influence the data generated using the equipartition method.

The equipartition method did however allow the quantitative analysis of standing wave traps to be observed, something which would have been difficult to do using the displacement method.

8.5 Single wavelength dual beam ESM-PCF trap

8.5.1 Aim

The aim of this experiment was to investigate the properties of a dual beam ESM-PCF trap when using single frequency light. This single wavelength configuration is the nominal configuration for all other dual beam fibre traps. This investigation would give us a comparison between this dual beam ESM-PCF trap and other conventional dual beam fibre traps.

8.5.2 Experimental construction

For this experiment a linear polarised near-infrared laser (IPG, model: YLM-5-1070-LP) was used. The laser test sheet quotes the central emission wavelength and emission bandwidth as $1070.7\,\mathrm{nm}$ and $0.34\,\mathrm{nm}$ respectively, when the laser is running at the nominal output power of $5\,\mathrm{W}$. The laser therefore had a coherence length of $3.37\,\mathrm{mm}$.

The beam was directed through a Faraday isolator (Linos, model: FI-1060-8 SO) to reduce the influence of back reflections on the laser. The beam was then passed a half-wave plate and then a Glan-laser calcite polariser (Newport, model: 10GL08) with an extinction ratio $> 100,000:1$. This ensured that the polarisation of the beam was kept constant. By adjusting the half-wave plate, the power

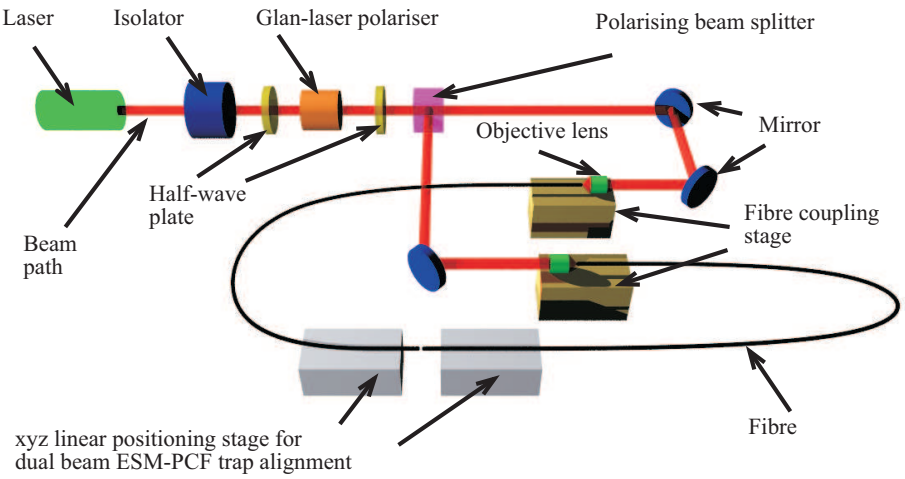

Figure 8.11: Diagram showing the optical set-up needed for the single wavelength fibre trap. All optics are chosen to be compatible with the $1070\ \mathrm{nm}$ laser. The v-groove fibre alignment set-up and the microscope set-up, not shown in this diagram, are illustrated in figures 8.8, 8.9 and 8.10.

could to be turned up or down while keeping the laser operating at its nominal $5\ \mathrm{W}$ output. The beam was then passed through another half-wave plate and a polarising beam splitter cube in order to split the beam into two arms of approximately equal power, adjustable using the half-wave plate. The beams in each arm were then steered, using two mirrors per arm, towards fibre coupling stages (Elliot Scientific, model: MDE510) that held 10X objectives (Newport, model: M-10X) and one end of the optical fibres. Coupling was optimised as described in section 7.6.3. The fibres were coiled in a $\sim 300\ \mathrm{mm}$ diameter semi-circular loop in order to ensure single mode operation (see section 7.6.6). Figure 8.11 shows a diagram of this fibre coupling set-up.

For this experiment, the fibres were aligned using the v-groove method described in section 8.4.3. It was not discovered until after this experiment that the v-groove set-up may have caused the fibre output to become multimode, due to bend/pressure induced mode conversion. Despite abandoning the v-groove method as a precaution, I do not believe that the data presented in this section was adversely affected by using the v-groove.

8.5.3 Trap stiffness

As shown in section 8.3.2, the magnitude and sign of the trap stiffness of a dual beam ESM-PCF trap can be altered by changing the separation of the fibres. As shown in figure 8.5, for the $1070\ \mathrm{nm}$ laser, for fibre separations below between $165\ \mu\mathrm{m}$ and $264\ \mu\mathrm{m}$ the potential, in the axial plane, should be repulsive (i.e. the particle will be repelled from the central point between the fibres); for a fibre separation equal to $165\ \mu\mathrm{m}$ or $264\ \mu\mathrm{m}$, there should be near to flat axial potential, resulting in a line trap; and for fibre separations greater than $264\mu\mathrm{m}$ a conventional trapping potential results [2]. All three types of potential were observed.

Trapping potential

Initial attempts of measuring the trap potential using the drag method, resulted in an unexpected result; when the sphere was returning back to the equilibrium position (from each direction), it appeared to stop before it reached the mid-point between the two fibres. This behaviour suggested the presence of a standing wave potential superimposed on top of the nominal fibre trap potential. Far away from the trap centre where the force due to the fibre trap potential was high, the standing wave potential was not influential. However, once the particle approached the trap centre, and the restoring force consequently reduced, the standing wave potential started to dominate. The spheres became trapped in this potential and were not returned to the trap centre corresponding to the minimum of the global potential.

These observed standing wave effects could not have been due to interference between the two fibre outputs as the path difference between the two fibre trap arms was very much greater than the coherence length of the laser ($3.37\ \mathrm{mm}$). Consequently, these standing waves originated from the interference of each beam with its only reflection from the capillary walls.

In order to quantify the nature of this potential, and confirm its existence, I used the equipartition method, as described in section 8.4.5. By recording the position

[2] Other theoretical 'regions' of trapping, line and repulsive potentials should exist, but they correspond to fibre separations too low to be achieved using the capillary.

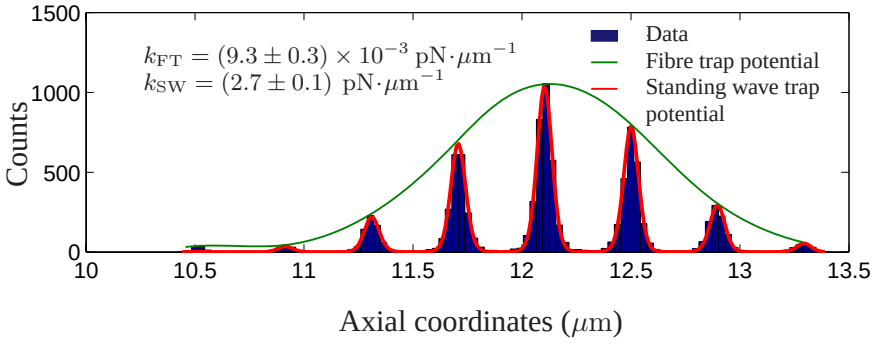

Figure 8.12: Histogram of a $2\ \mu\mathrm{m}$ diameter particle's distribution in the single wavelength dual beam ESM-PCF trap. The output power of each fibre was $300\ \mathrm{mW}$ and the fibres were positioned $120\ \mu\mathrm{m}$ away from the capillary's walls. The spring constants were worked out from the probability distribution of the particle's position as described in section 8.4.5.

of a trapped particle for a sufficient length of time and frame rate, it was possible to map both the fibre trap and standing wave potential. As shown in figure 8.12, the histogram of the positions of the particle during the recorded run clearly show both a global confining potential, due to the normal dual beam fibre trap potential, but also the standing wave potential. The standing wave potential was measured to be over 100 times greater than the fibre trap potential.

Line potential

The 'line' trap potential was difficult to achieve; according to the numerical simulations, it is practically impossible to reduce the trap stiffness to exactly zero over a finite distance, as the intensity profiles of the two fibres will never perfectly overlap. Fine alignment was critical to reduce the magnitude of these forces.

Problems also arouse quantifying the nature of the line potentials. While it was possible with careful alignment to achieve a potential which was radially confining but appeared to exert little force, it was difficult to quantify the potentials exact nature. Figure 8.13, shows an example of a particle's movement within a line trap. As the axial force was minimal, the sphere would appear to drift along the axial direction of the trap as a result of Brownian motion but it would appear

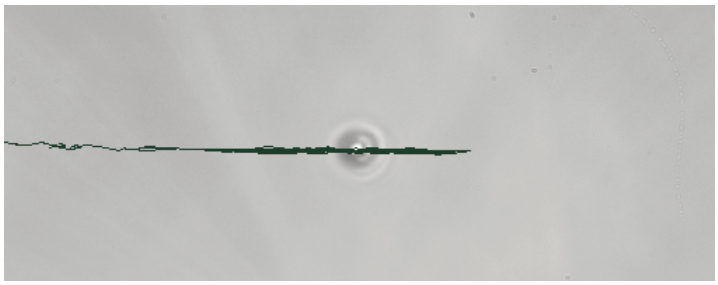

(a) Position of sphere in line trap.

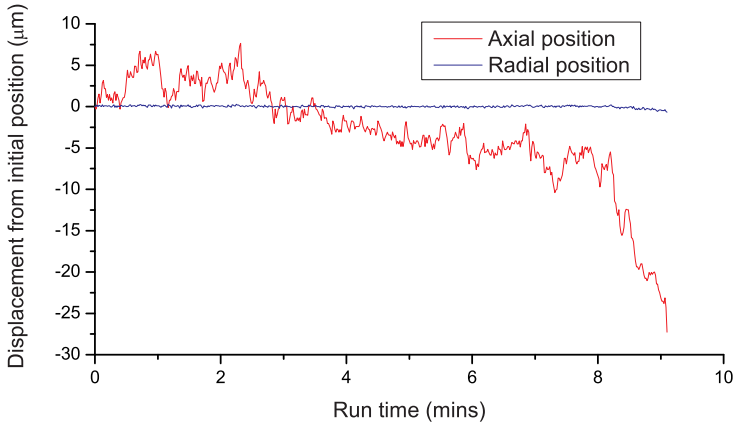

(b) Graph of axial and radial position against time.

Figure 8.13: Path of a $2\ \mu\mathrm{m}$ polystyrene sphere when held in a line trap with output power of $360\ \mathrm{mW}$. Fibres were separated from the outer capillary walls by $\sim 52\ \mu\mathrm{m}$ which corresponds to a fibre separation in air of $247\ \mu\mathrm{m}$. According to my model, this separation should have resulted in a weak inverse trap, but was observed experimentally to result in a near line trap. The discrepancy may have arisen as a result of a change in the fibre's beam profile, possibly as a result of a cleave. Figure 8.13(a) shows the path of the sphere in the capillary. Figure 8.13(b) shows a plot of the axial and radial position as a function of time. The radial position does not vary by more than $0.5\ \mu\mathrm{m}$ from its initial position, whereas the axial position varies by more than $15\,\mu\mathrm{m}$. The sphere stays within the line trap for over $8\,\mathrm{min}$ before moving into a region where the axial potential pushes it into the left capillary wall. This graph was generated using Graham Milne's StAT particle tracking program [103].

to preferentially wander in one direction until it collided with the wall of the capillary. This nature would suggest that the axial potential was not perfectly flat, and that there was still a slight repulsive potential pushing the spheres away from the 'trap' centre. The sphere was tightly confined in the radial direction by the gradient force.

Repulsive potential

Repulsive potentials were observed, but as they resulted in the spheres being repelled from the centre and into the walls of the capillary, it was impossible to measure the trap stiffness in my current set-up. It would be possible to make this measurement by tracking the path of a sphere which had been placed between the two fibres using a helper tweezer [104]. This method was not used however due to the predicted difficulty creating a tight enough focus using the low numerical aperture long working distance objectives that were needed for the experiment.

8.5.4 Chains of particles

By using a dense sample of microspheres it was possible to see chains of over 15 particles spanning the entire inner diameter of the capillary, as shown in figure 8.14. Instabilities were seen in these chains as more particles entered the chain area. Because of the standing wave potential, it was highly unlikely that chains were purely governed by optical binding effects. It was common to see a gap in the periodicity in the chain where there was twice the usual spacing between the spheres. This implies that the standing wave potential was dominating the characteristics of the chain, as if the spheres were optically bound (in the absence of any other negative influence) no irregular sphere spacings would be observed [105].

(a) Long chain of over 16 spheres. Dimers are formed in some locations. These spheres were situated in a larger capillary than used elsewhere with an inside diameter of 200 μm and an outside diameter of 400μm

(b) Chain of 4 spheres. One sphere is separated from its adjacent sphere by twice the distance of the others.

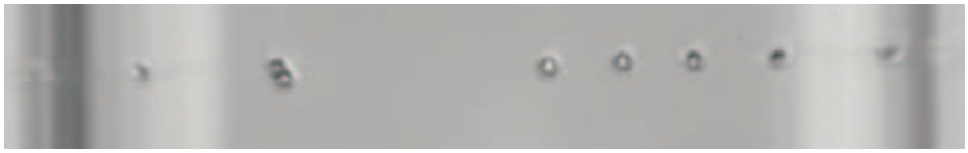

(c) Chain of 8 spheres. A discontinuity is seen in the chain.

Figure 8.14: Examples of particle chains observed when working with a dense sample. The chains above were taken during a static period, i.e. the spacing of the chain was the same for many seconds. The non constant spacings in the chain implies that the standing wave potential was heavily influencing the separation.

8.6 Dual beam ESM-PCF trap using a supercontinuum source

8.6.1 Aim

The characterisation of the single wavelength ESM-PCF trap showed that the capillary introduced standing wave traps formed from the reflection of the beams with the capillary walls and the properties of the trap was dominated by these effects. Although a basic solution may have been to have sealed the fibre ends using UV curable polymer, as discussed in section 8.4.2, thus allowing the capillary to removed completely, standing waves could still be formed from the reflections from the fibre faces. For optical binding studies, the effects of standing waves can be extremely detrimental. It was therefore decided that I take advantage of the end-

lessly single mode nature of the fibres and use a supercontinuum source instead of a laser. As the emission bandwidth of a supercontinuum is generally $> 100\ \mathrm{nm}$, the resultant coherence length is generally $< 10\ \mu\mathrm{m}$. This would therefore result in no standing wave effects from the walls of the capillary. The position of spheres within bound arrays can also be influenced by interference effects between adjacent spheres [106]. If the emission bandwidth was large enough so that the coherence length was less than the separation of the particles held in bound chains, the supercontinuum trap could remove such effects.

8.6.2 Spectrum and coherence length of supercontinuum

The spectrum of the supercontinuum was measured after the fibres to ensure that it was not altered. Although each measured spectrum was slightly different to those taken before it, due to changes in coupling and how the fibre was positioned, the spectrum shown in figure 8.15 was characteristic of all the spectra.

The coherence length L is given by,

$$L = \frac{\lambda^2}{n\Delta\lambda} \tag{8.14}$$

where λ is the central wavelength of the source; $\Delta\lambda$ is the bandwidth; and n is the refractive index of the medium.

Although the spectrum of the supercontinuum is irregular and the assignment of a simple bandwidth is somewhat arbitrary, a value of $\sim 120\ \mathrm{nm}$ would be a conservative estimate. Using $690\ \mathrm{nm}$ as the peak wavelength, I arrive at a figure of $2.98\,\mu\mathrm{m}$ for the coherence length in water. This value is sufficiently low to obviate the formation of standing waves from reflections not only from the capillary walls, but also from trapped spheres within a bound array, as long as their separation are greater than $2.98\ \mu\mathrm{m}$

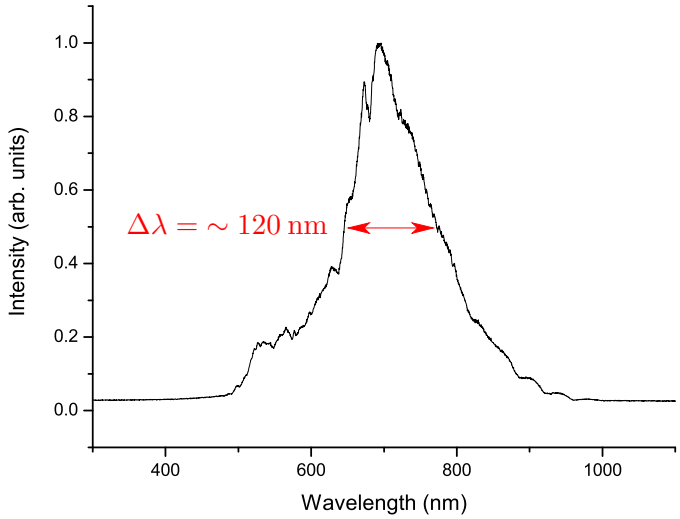

Figure 8.15: This figure shows the output spectrum of LMA-25 using the supercontinuum source. The LMA-25 fibre is 1.5 m long and is curved to suppress higher order modes. The bandwidth is measured at the FWHM point to be $120\,\mathrm{nm}$; resulting in a calculated coherence length of $2.98\ \mu\mathrm{m}$.

8.6.3 Experimental set-up

The supercontinuum source (Fianium, model: SC-500-6) used during this experiment had a maximum output power of 5 W, a quoted central wavelength of $1060\,\mathrm{nm}$ and an emission bandwidth from $450 - 1750\,\mathrm{nm}$ when operating at maximum output power. In reality however, the measured bandwidth of the supercontinuum was very much lower than the specification suggested with the spectra being very similar to that taken after the fibre, as shown in figure 8.15. Nevertheless, because of the nature of the supercontinuum generation, the maximum emission bandwidth was achieved when the laser was run at maximum power, and consequently the laser was run at this power during all the experiments.

The choice of the optics when using the supercontinuum was important so that the spectrum of the laser was minimally affected. Figure 8.16 shows a schematic of the set-up. Subsequent to the unpolarised output of the supercontinuum, a 50:50 beam splitter was used to divide the beam into the two arms. In each arm, a Glan-Thompson prism was used to polarise the beam and allow the intensities of

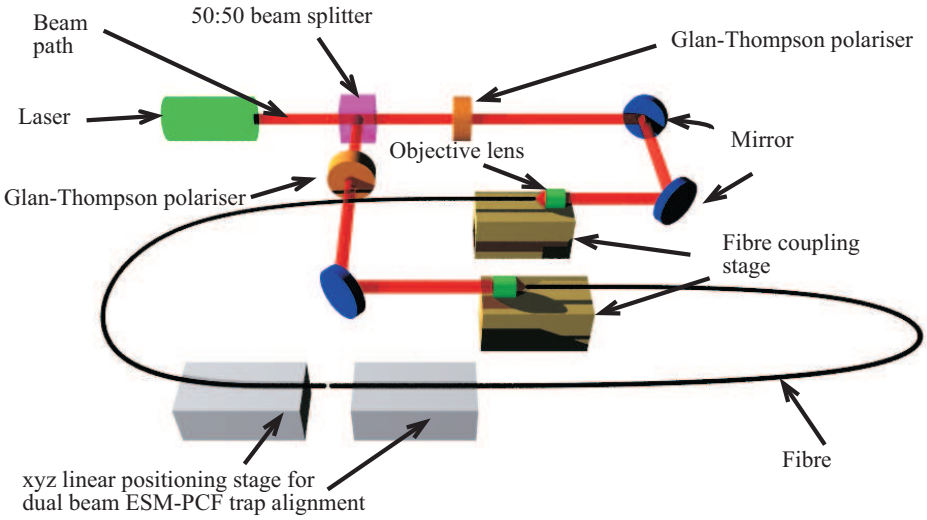

Figure 8.16: Schematic of the optical setup used for the supercontinuum dual beam ESM-PCF trap.

the arms to be equalised; this resulted in a high loss of power. Ion-plated silver mirrors (Comar, model: 25MX06) were used as they have $> 95\ \%$ reflectance in the range $400 - 2000\ \mathrm{nm}$.

The beams in each arm were then steered using two mirrors towards the same fibre coupling stage (Elliot Scientific, model: MDE510) holding a 10X times objective (Newport, model: M-10X) and one end of the optical fibres. The fibres were coiled in a $\sim 300\ \mathrm{mm}$ diameter semicircular single loop in order to ensure single mode operation (see chapter 7.6.8).

The v-groove slide was abandoned at this point as I had discovered that exerting a pressure or inducing micro-bends in the fibre would induce higher order modes in the fibre, therefore compromising the quality of the output.

8.6.4 Successful removal of interference effects

Although it was immediately clear that the observed effects from the capillary induced standing waves were absent in the supercontinuum dual beam fibre trap, I was unable to reproduce an equivalent graph to figure 8.12, where I measured

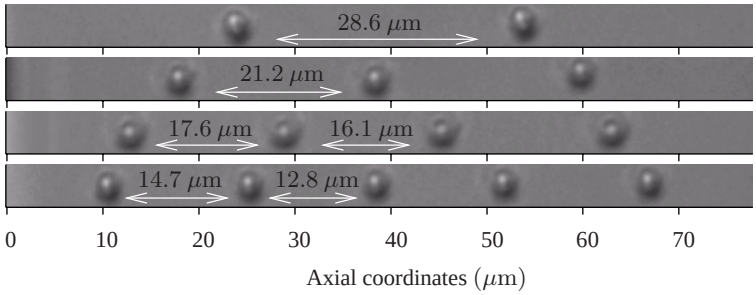

Figure 8.17: Optically bound arrays of $1.3\ \mu\mathrm{m}$ diameter polystyrene particles trapped in the white light dual beam ESM-PCF trap. The output power is $115\,\mathrm{mW}$ in each arm and the capillary wall to fibre separation is $140\,\mu\mathrm{m}$. Arrays with more spheres are seen to been more closely packed, and the separation between the interior spheres is less than between the exterior spheres. This behaviour was also recently observed in conventional fibre traps and is as a result of the inner spheres experienced stronger binding forces [107]. This observation confirms the absence of standing wave effects, as the separation of the arrays of particles using the $1070\ \mathrm{nm}$ laser was dictated by the periodicity of the standing wave. In this case, the separation would appear to be dictated by binding effects.

the particle's position distribution in the single wavelength trap. It was found that the stability of the particle, due to an instability in the supercontinuum, was too low to produce a mappable potential. These instabilities may have been caused by power or polarisation fluctuations in the output of the supercontinuum. As I did not have access to a suitable Faraday isolator, feedback was a problem and may have caused the fluctuations.

We were however able to show that the spacing of optically bound chains was not influenced by any standing wave effects. Figure 8.17 shows examples optically bound chains of particles. The spacing of the spheres was seen to decrease as the number of particles increased. The separation of the spheres was also seen to be greater for the spheres at the exterior of the chain. This inhomogeneous spacing was recently reported for bound arrays held in a conventional single mode trap and is as a result of the inner spheres experiencing stronger binding forces [107]. This behaviour contrasts with that seen in chains formed in the single wavelength ESM-PCF trap, where the spacing between the spheres was constant. This demonstrated that the supercontinuum had removed any interference effects due to the capillary.

8.7 Dual wavelength optical conveyor belt using dual beam ESM-PCF trap

8.7.1 Aim

As demonstrated above, particles can become trapped in standing wave potentials. Optical conveyor belt traps [88] are generated by intentionally interfering two counterpropagating beams and moving the nodes of the standing wave by adjusting the phase difference between the beams. The sensitivity of particles to a standing wave potential is governed, among other things, by the wavelength of the light, the particle's radius and its refractive index. Zemánek and co-workers [108] calculated that a for a given wavelength of light, some particles will be extremely sensitive to the standing wave and become strongly trapped, whereas other particles will experience little confining force at all.

Previous to this work, optical conveyor belts have only been demonstrated using a single wavelength. Theoretically, a dual wavelength standing wave trap should be able to selectively move two species of particles. It was therefore decided to attempt this experiment using the a modification of the dual beam ESM-PCF trap. In principle when trapping (in an array) a mixture of the two sizes, it should be possible to selectively move each size of particle by adjusting the phase difference of the appropriate beam.

8.7.2 Optical forces acting on a nanoparticle in standing wave

Before attempting the experiment, the two species of particles needed to be selected: one which would be sensitive to $1064\ \mathrm{nm}$ and insensitive to $780\ \mathrm{nm}$; and one which would be sensitive $780\ \mathrm{nm}$ and insensitive to $1064\ \mathrm{nm}$. In the work of Zemánek and co-workers [108], they investigate the force experienced by a nanoparticle in a Gaussian standing wave. Figure 8.18 shows a reproduction from the relevant graph in their paper. From this graph, I was able to estimate that two sizes of polystyrene particles in our inventory were suitable: $600\ \mathrm{nm}$ diameter,

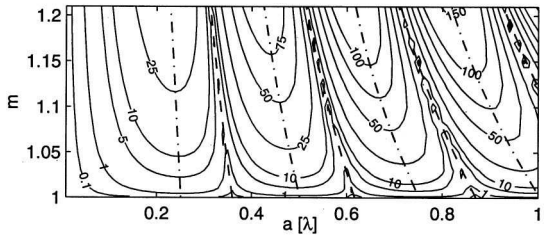

Figure 8.18: Reproduced from reference [108], this graph shows the maximum axial trapping force experienced by a nanoparticle situated in a standing wave trap as a function of particle radius a (expressed in units of wavelength) and the ratio m of the refractive index of the particle to the refractive index of the medium. Although the magnitude of the forces were calculated for the certain set of parameters with laser power $P = 30\ \mathrm{mW}$ and laser wavelength $\lambda = 1064\ \mathrm{nm}$, the particles radii, as a function of λ, that are most and least sensitive to the standing waves are constant.

sensitive to $1064\ \mathrm{nm}$ and insensitive to $780\ \mathrm{nm}$; and $500\ \mathrm{nm}$ diameter, sensitive to $780\ \mathrm{nm}$ and insensitive to $1064\ \mathrm{nm}$.

8.7.3 Experimental set-up

The experimental set-up for this experiment was more complicated than the previous experiments. Not only did I have to successfully couple two wavelengths (from separate sources) into the fibre, I also needed a method of adjusting the phase difference between the arms. The experimental set-up is shown in figure 8.19.

The lasers used were: a $780\ \mathrm{nm}$ Ti:Sapphire(Spectra-Physics, model: 3900S), described in section 3.2.8, with a maximum power of $800\ \mathrm{mW}$ and a coherence length of $300\ \mathrm{mm}$; and a single frequency $\sim 1064\ \mathrm{nm}$ fibre laser (IPG Photonics, model: YLR-10-1064-LP-SF) with a maximum power of $10\ \mathrm{W}$ and a coherence length of $\sim 3\ \mathrm{km}$.

The coupling of both wavelengths into the fibre was facilitated by a $780\mathrm{nm}$ narrow band polarising beam splitter, positioned as shown in figure 8.19, which allowed both beams to be of the same linear polarisation and be independently aligned.

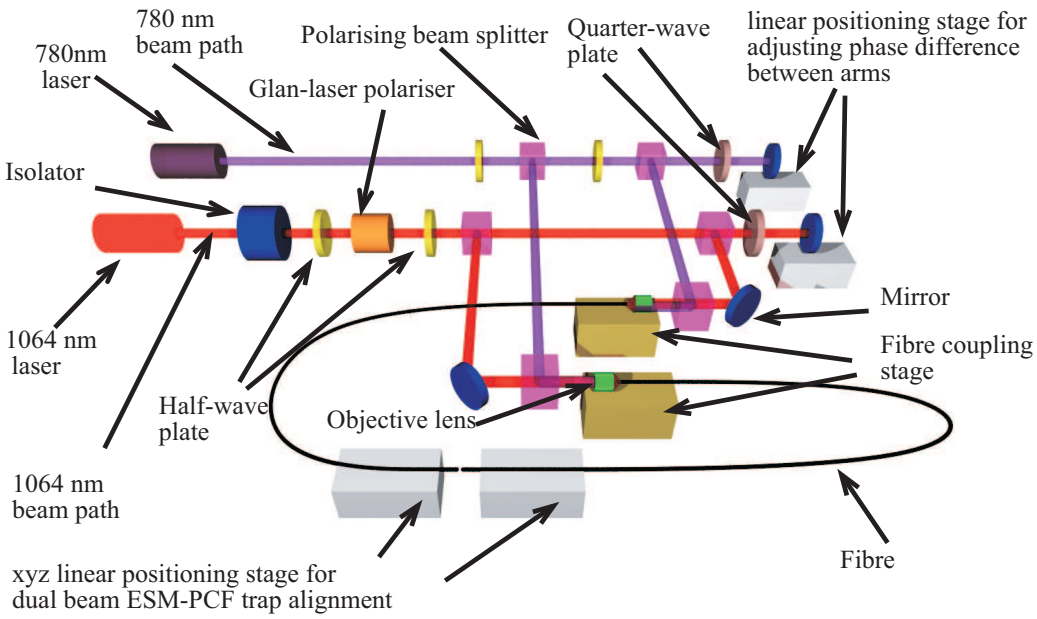

Figure 8.19: Schematic of the optical setup used for the dual beam optical conveyor belt. The beam splitter cubes immediately before the fibre coupling stages were narrow band $780\ \mathrm{nm}$ polarising beam splitters. As $1064\ \mathrm{nm}$ light passed through these beam splitter cubes regardless of polarisation; this setup allowed the $780\ \mathrm{nm}$ and $1064\ \mathrm{nm}$ beams to share the same polarisation on input to the fibre.

Although the two wavelengths did not have to be the same polarisation (although the two arms did) it allowed us a slight advantage. It was extremely important in this experiment that the fibres were only curved in a plane parallel or perpendicular to the polarisation of the input beam. If this had not been the case, the light would no longer have been linear polarised. To be sure, the output of the fibre was checked for polarisation; a task which was made easier by having the two wavelengths at the same polarisation.

The phase difference for each wavelength was adjusted by using a half-wave plate, polarising beam splitter, quarter-wave plate and retro-reflecting mirror mounted on a linear translator. The half-wave plate was adjusted to allow all the light to pass through the cube, with the quarter-wave plate adjusted so that the retro-reflected beam was reflected when it went back into the cube. The path length of each beam could then be altered independently by adjusting the appropriate

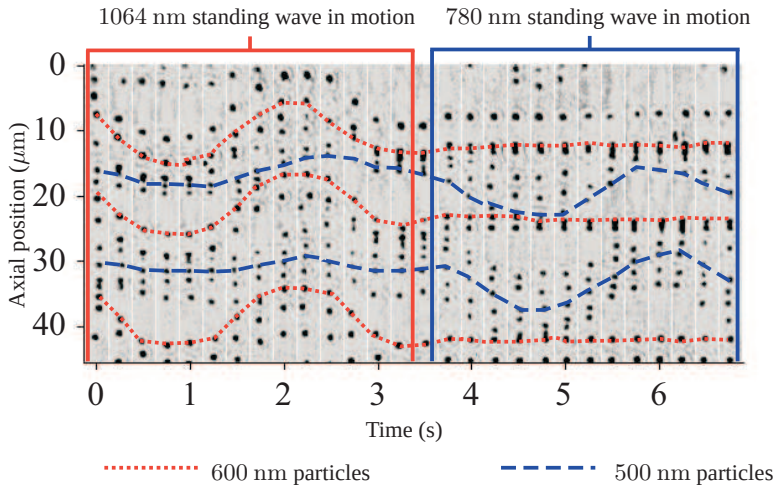

Figure 8.20: This diagram shows snapshots of the motion of an array of $500\ \mathrm{nm}$ and $600\ \mathrm{nm}$ polystyrene particles held within a dual wavelength ($1064\ \mathrm{nm}$ and $780\ \mathrm{nm}$) standing wave trap. The output powers are approximately $70\ \mathrm{mW}$ per wavelength per arm. As the two particle sizes are sensitive to standing waves of different wavelengths, it was possible to selectively move the each particle size within the trap by adjusting the phase difference between the arms of the appropriate beam. The $500\,\mathrm{nm}$ diameter spheres were calculated to be sensitive to $1064\,\mathrm{nm}$ standing wave and insensitive to $780\ \mathrm{nm}$ standing wave; while $500\ \mathrm{nm}$ diameter sphere were sensitive to $780\ \mathrm{nm}$ standing wave and insensitive to $1064\ \mathrm{nm}$ standing wave. The graph shows however that the $500\ \mathrm{nm}$ particles moved when the $1064\,\mathrm{nm}$ standing wave was in motion. This may have been due to binding effects or as a result of the particles not being as insensitive to the $1064\ \mathrm{nm}$ radiation as I estimated.

linear translator. This caused a change in phase difference between the two beams resulting in the position of the nodes and anti-nodes to change.

The coupling lens had a focal length of $35\ \mathrm{mm}$. The coupling lens was chosen to optimise the coupling efficiency for the $780\ \mathrm{nm}$ laser, as this laser was less powerful than the $1064\ \mathrm{nm}$ laser. The fibres were aligned using the free space method and the sample was held in the regular hollow square capillary.

8.7.4 Results

A dense sample containing approximately equal amounts of $500\ \mathrm{nm}$ and $600\ \mathrm{nm}$ diameter polystyrene microspheres was used. It was found that optimisation of the alignment was critical to the correct operation of the conveyor belt. Once a stable chain was achieved, it was possible to preferentially move each particle size by adjusting the phase difference between the arms of the relevant laser, using the linear translator.

Figure 8.20 shows that the two sizes of particles could be individually controlled by moving the different standing waves. This effect was most pronounced when the $780\ \mathrm{nm}$ standing wave was in motion. While the $500\ \mathrm{nm}$ particles clearly moved, the $600\ \mathrm{nm}$ particles were virtually static. The effect was not as pronounced when the $1064\ \mathrm{nm}$ standing wave was in motion. Both particles were seen to move; with $600\ \mathrm{nm}$ particles being influenced more than the $500\ \mathrm{nm}$ particles (which should have been insensitive to this wavelength). There are two possible reasons for this behaviour. It was possible that one of the particle sizes was not as insensitive to its 'insensitive wavelength' as I estimated. It was also possible that optical binding effects meant that despite the $500\ \mathrm{nm}$ particle being insensitive to the $1064\ \mathrm{nm}$ standing wave, it was influenced by the movement, as a result of binding effects, of the $600\ \mathrm{nm}$ particles.

8.8 Conclusion

In this chapter I have explored, for the first time, the use of endlessly single-mode photonic crystal fibre in dual beam fibre traps. The influence of the non-Gaussian mode profile on the axial force was numerically calculated and compared to that of single mode fibre. I predicted that, by adjusting the separation of the fibres, the spring constant of the trap could not only be changed in magnitude, but could be changed from negative to positive. I also predicted that for some separations the axial force would be close to zero.

We constructed a stable apparatus which allowed the confinement of the liquid

sample from the holey fibres and the accurate alignment of the fibres. The properties of a single wavelength trap were explored. I experimentally realised the predicted confining potentials, repulsive potentials and line potentials. Long chains of particles were seen to form in dense samples. It was found that the capillary sample holder was introducing standing wave effects due to reflections. The influence of these standing wave traps was quantified.

In order to neutralise the standing wave effects not only from the capillary but from reflections from fibre ends and optically bound particles, I utilised the endlessly single-mode characteristic of the fibres to form the first dual beam white light fibre trap. Using a broadband (low coherence length) supercontinuum source I was able to form chains of particles, that were spaced as a result of optical binding effects, with no observable influence from standing waves.

The endlessly single-mode characteristic of the fibres allowed us to form the first dual wavelength optical conveyor belt. Using the same geometry as the dual beam fibre traps, interference between the two arms of the trap were intentionally exploited to form standing wave traps. As two wavelengths of light were used, two standing wave traps were formed. By choosing two diameters of polystyrene particles that were each sensitive to a different one of the wavelengths I was able to independently control the movement of each size of particle with a chain.

8.9 Author's contribution

This experiment was carried out in conjunction with Antonia Carruthers and Tomáš Čižmár. The analytical and numerical analysis of the axial force profiles for dual beam conventional and ESM-PCF fibre traps were carried out by myself. The design of the fibre alignment setup was mine, with the construction and operation of the single wavelength experiment carried out by myself. The construction and operation of the dual beam supercontinuum trap was carried out by Antonia and me. The optical conveyor belt experiment, which was Tomáš's idea, was constructed and operated by Tomáš and me. Video analysis and calculation of trap constants was performed by Tomáš.

Chapter 9

OVERVIEW OF THESIS

9.1 Review

In this thesis I have presented a range of studies, concentrating on the manipulation of particles and atoms using free space light beams and photonic crystal fibres.

Before the cold atom guiding experiments were attempted, the laser systems for the MOT and guide beams needed to be setup. The MOT beams were supplied by home-built extended cavity diode lasers (or, for the LG guide experiment, a master oscillator power amplifier system), which were locked to the relevant transition, as observed using Doppler-free saturated absorption spectroscopy, by a servo-locking system. While the $40\ \mathrm{mW}$ output of the ECDL was sufficiently powerful to supply the re-pump beam, a homebuilt master/slave system was used to increase the power available for the cooling beam to $110\ \mathrm{mW}$. A commercial continuous wave tunable Ti:sapphire laser, with a maximum power of $800\ \mathrm{mW}$, was used for the guide beams. With the exception of the laser systems used in the LG atom guiding experiment, I set-up, maintained and operated these laser systems. During this process a new higher powered laser diode was included into the master/slave system to increase the size of the cooled cloud of rubidium-85 atoms.

Laguerre-Gaussian atom guides were used to guide free-falling cold atoms within

a vacuum. These LG guides were generated dynamically using a phase modulating spatial light modulator. The SLM allowed us to carry out the first comparative study of the guiding characteristics of different azimuthal order LG guides [45]. Atoms were guided within $l = 3, 5, 12$ LG guides with an equalised ring diameter of $2.2\mathrm{mm}$ at detunings of $2, 5, 8\mathrm{Ghz}$. Within these guides, the cold atoms could be guided over distances of up to $30\mathrm{mm}$, with a guided fluence enhancement (over an unguided dropped cloud) of up to $\times 12$. The time of flight of the guided atoms was seen to decrease for lower l index beams and lower detunings, due to the increase in radiation pressure and as a result, the atoms spent less time in the presence of the optical field. Consequently the fluence was higher for those guides that resulted in lower times of flight. This experiment was carried out during the initial stages of my PhD, when I assisted my colleague Daniel Rhodes, who performed the majority of the work. I assisted in the overall running of the experiment and performed some of the data runs by myself.

A hot wire detection system was designed to detect guided rubidium atoms exiting a photonic band gap fibre. The characteristics of rhenium, tungsten and platinum hot wires were modelled, with rhenium being chosen as the hot wire material. A translatable mount that held two independently switchable hot wires was designed and constructed. The hot wire was combined with a channel electron multiplier to form the hot wire detector. This hot wire detector was then incorporated into two twin chambered vacuum systems. With the exception of occasional assistance and useful advice from John Livesey, the design and construction of the hot wire detector and vacuum systems was my own.

The first vacuum chamber was designed to be used in an experiment designed guide either thermal or cold atoms (created in a MOT) through a hollow-core photonic band gap fibre guiding. When the top chamber was filled with thermal rubidium, atoms were detected exiting the fibre when the guide laser was turned on. However, this result was unexplainable as the atoms were guided for both red- and blue-detuned frequencies. As the top and bottom chambers were connected, so that they could both be pumped using the same ion pump, high background noise levels were recorded in the detection chamber due to the migration of thermal rubidium. This prompted us to switch to the planned cold atom experiment. A

MOT of approximately 1×10^6 atoms was formed in the top chamber, making use of the intra-vacuum optics. The cooling beams were then turned off, and the guide beam (which have been coupled into the fibre) turned on, allowing the atoms to fall under the influence of gravity and the guide beam. The guided fluence was calculated by comparing the total number of counts detected by the CEM during the period when the cloud was forming and comparing it to the total number of counts when the cloud was meant to be guided onto the hot wire. The thermal noise in the system led us to automate the system so that hundreds of data points could be accumulated. Despite this action, no guided atoms were detected. With the exception of a few week of assistance from John Livesey with the thermal atom guiding experiment, this experiment was carried out by myself.

The second vacuum chamber was designed to alleviate the problem of thermal rubidium migrating from the rubidium chamber to the detection chamber. With the addition of a second ion getter pump, the rubidium chamber and detection chamber could be completely isolated, with the only path available to the atoms being through the fibre. This experiment was designed to be optimised to for thermal atom guiding and did not have the capability to form cold atoms. In addition to a hollow-core photonic band gap fibre, a hollow-core capillary was also inserted into the system. Despite numerous attempts, no rubidium was detected exiting the fibres. This experiment was carried out solely by myself.

My next piece of work entailed characterising and understanding the experimental characteristics of endlessly single-mode photonic crystal fibre, with the aim of using it to develop a novel dual beam fibre trap. Three core diameters ($10\ \mu\mathrm{m}$, $25\ \mu\mathrm{m}$ and $35\ \mu\mathrm{m}$) were characterised for laser wavelengths of $780\ \mathrm{nm}$ and/or $\sim 1070\ \mathrm{nm}$. The fibres were also characterised for broadband radiation generated using a supercontinuum source. The characterisation of the fibres involved optimising coupling efficiencies, understanding the experimental conditions resulting in single-mode and multimode output and measuring the mode profiles of the fibre. This work was carried out conjunction with Antonia Carruthers, who assisted with the work involving the supercontinuum, and Tomáš Čižmár who assisted with the processing of the fibre profiles.

Finally, a number of novel dual beam fibre traps where constructed using the

$25\ \mu\mathrm{m}$ diameter ESM-PCF fibres. As the hexagonal mode causes the mode to come to a focus at a finite distance away from the fibre end, I showed that it was possible to not only create conventional trapping potentials, but to create repulsive and line potentials. The characteristics of the trap were heavily influenced by the square capillary sample holder, which was required to isolate the liquid medium from the holey fibre. The reflections from the square capillary resulted in a standing wave potential being superimposed upon the global fibre trap potential. Consequently, by exploiting the endlessly single-mode characteristic of the PCF, I showed that interference effects can be removed by using a broadband low coherence length supercontinuum source. I then went on to demonstrate the dual wavelength optical conveyor belt. Two particle sizes were chosen so that the two particles would be sensitive (insensitive) to different wavelengths. By individually moving the standing wave of each wavelength, I was able to observe the selective movement of each size of particle when a mixture of particles were held in a chain.

9.2 Suggested further work

9.2.1 HC-PBG fibre guiding experiments

There are a number of options for future work with the hollow-core photonic band gap fibre guiding experiment. Although the guiding of thermal rubidium through HC-PBG fibres has now been reported [56], cold rubidium guidance has still not been achieved. Consequently, any further experiments must have cold rubidium guidance as the ultimate goal. Nevertheless it may still be wise to attempt to repeat the thermal rubidium experiment first, as I know that it can be successful. I propose that the following improvements may increase the likelihood of success.

Firstly, state of the art fibres should be used. The fibres used in the experiment have now been superseded by fibres with improved transmission efficiencies and with different lattice patterns, such as those with a Kagome structure lattice. These Kagome structure fibres have been used with success in an experiment to observe

electromagnetically induced transparency in a rubidium filled HC-PBG fibre. Not only do these fibres have higher transmission efficiencies, but the Kagome structure fibres are less susceptable to the effects of surface modes which may influence the guided atoms [109].

Secondly, if a thermal rubidium guiding experiment is performed, the pressure of rubidium in the source chamber should be increased by at least an order of magnitude. Using the getters, the pressures were an order of magnitude less than those reported elsewhere [17]. The solution to this problem may involve replacing the getters with some form of heated rubidium oven. It may also be worthwhile investigating whether a further stage in the bake-out/evacuation procedure, aimed at reducing residual gas within the chamber by way of an additional getter material, might allow higher rubidium vapour pressures to be achieved within the source chamber. Additionally, pacifying the surface of the glass cell, thereby making it less reactive to rubidium, may have a similar effect.

Thirdly, the sensitivity of the hot wire detector should be calibrated. However, there would appear to be no easy way of doing this in the current vacuum set-up.

Fourthly, a theoretical analysis of the effects of higher order modes within the fibre would be a worthwhile endeavour. Even without an associated experimental result, such a theoretical analysis could easily be published.

Finally, the noise on the CEM caused be the electrical noise from the ion pumps should be minimised. Although this is not a problem for the thermal atom guiding experiments, as it does not matter if the ion pump is turned off, it is a major problem for the cold atom experiments, as the ion pump cannot be turned off without adversely affecting the cloud.

9.2.2 Suggested applications of dual beam PCF traps in biophotonics

In the last decade, fibre traps have shown to have important applications in the field of biophotonics. Jess and co-workers combined a dual beam fibre trap with a

microscope system designed to obtain Raman spectra of trapped cells [91]. In the works of Guck and co-workers [93, 110], they use a dual beam fibre trap to stretch cells, a technique they named the 'optical stretcher', in an effort to differentiate whether cells are cancerous.

My dual beam ESM-PCF trap has potential applications in biophotonics. For the optical stretcher, the low numerical aperture of the fibres may enhance the stretching force. Additionally, the ease with which multiple wavelengths can be delivered would allow, for example, the simultaneous delivery of $1064\,\mathrm{nm}$ light for trapping and $395\,\mathrm{nm}$ light for excitation of a green fluorescent protein marker. I attempted a proof of principle experiment using a cell stained with fluorescent dye and a portion of the supercontinuum output which had been filtered of the wavelengths around the dye's emission wavelength; however the spectral power of the supercontinuum in the region of the dye's excitation wavelength was not sufficient to generate a measurable result.

An attempt was also made to trap a cell using $780\,\mathrm{nm}$ light and measure using a microscope objective the Raman spectra from the cell's scattered light. However, using a basic spectrometer, I was unable to extract the cell's low intensity Raman signal from noise. I was however able to observe the large Raman signal from silica. This is a known obstacle to such experiments, as the signal from the silica will completely mask the signal from the sample. To combat this effect, I propose that by replacing the solid core ESM-PCFs with hollow-core photonic band gap fibres, the Raman signal from the silica could be greatly reduced. Furthermore, it may be possible to not only deliver the excitation light but also collect the Raman spectra in the fibres as well. I believe such a technique could allow the simplification of the current techniques used in Raman microscopy. Work is planned within the group to investigate the feasibility of this technique.

Bibliography

[1] R. S. Adams and E. Riis, “Laser cooling and trapping of neutral atoms,” Progress in Quantum Electronics **21**(1), 1–79 (1997).

[2] J. C. Maxwell, *A treatise on electricity and magnetism*, vol. 2, p. 391 (1873).

[3] P. N. Lebedev, “Experimental examination of light pressure,” Annalen der Physik **6**, 433 (1901).

[4] E. F. Nichols and G. F. Hull, “A Preliminary Communication on the Pressure of Heat and Light Radiation,” Phys. Rev. (Series I) **13**(5), 307–320 (1901).

[5] A. Ashkin, “Acceleration and trapping of particles by radiation pressure,” Physical Review Letters **24**(4), 156–& (1970).

[6] A. Ashkin and J. M. Dziedzic, “Optical levitation by radiation pressure,” Applied Physics Letters **19**(8), 283–& (1971).

[7] A. Ashkin, J. M. Dziedzic, J. E. Bjorkholm, and S. Chu, “Observation of a single-beam gradient force optical trap for dielectric particles,” Optics Letters **11**(5), 288 (1986).

[8] J. E. Curtis, B. A. Koss, and D. G. Grier, “Dynamic holographic optical tweezers,” Optics Communications **207**(1–6), 169–175 (2002).

[9] W. H. Guilford, J. A. Tournas, D. Dascalu, and D. S. Watson, “Creating multiple time-shared laser traps with simultaneous displacement detection

using digital signal processing hardware," Analytical Biochemistry **326**, 153–166 (2004).

[10] S. Chu, L. Hollberg, J. E. Bjorkholm, A. Cable, and A. Ashkin, "3-dimensional viscous confinement and cooling of atoms by resonace radation pressure," Physical Review Letters **55**(1), 48–51 (1985).

[11] E. L. Raab, M. Prentiss, A. Cable, S. Chu, and D. E. Pritchard, "Trapping of neutral sodium atoms with radiation pressure," Physical Review Letters **59**(23), 2631–2634 (1987).

[12] S. Chu, J. E. Bjorkholm, A. Ashkin, and A. Cable, "Experimental Observation of Optically Trapped Atoms," Phys. Rev. Lett. **57**(3), 314–317 (1986).

[13] M. H. Anderson, J. R. Ensher, M. R. Matthews, C. E. Wieman, and E. A. Cornell, "Observation of Bose-Einstein Condensation in a Dilute Atomic Vapor," Science **269**(5221), 198–201 (1995).

[14] K. B. Davis, M. O. Mewes, M. R. Andrews, N. J. van Druten, D. S. Durfee, D. M. Kurn, and W. Ketterle, "Bose-Einstein Condensation in a Gas of Sodium Atoms," Phys. Rev. Lett. **75**(22), 3969–3973 (1995).

[15] L. Pruvost, D. Marescaux, O. Houde, and H. T. Duong, "Guiding and cooling of cold atoms in a dipole guide," Optics Communications **166**, 199–209 (1999).

[16] D. McGloin, G. Spalding, H. Melville, W. Sibbett, and K. Dholakia, "Applications of spatial light modulators in atom optics," Optics Express **11**(2), 158–166 (2003).

[17] M. J. Renn, D. Montgomery, O. Vdovin, D. Z. Anderson, C. E. Wieman, and E. A. Cornell, "Laser-guided atoms in hollow-core optical fibers," Physical Review Letters **75**(18), 3253–3256 (1995).

[18] M. J. Renn, E. A. Donley, E. A. Cornell, C. E. Wieman, and D. Z. Anderson, "Evanescent-wave guiding of atoms in hollow optical fibers," Phys. Rev. A **53**(2), R648–R651 (1996).

[19] A. Constable, J. Kim, J. Mervis, F. Zarinetchi, and M. Prentiss, "Demonstration of a fiber optical light-force trap," Optics Letters **18**(21), 1867–1869 (1993).

[20] E. A. Hinds and I. G. Hughes, "Magnetic atom optics: mirrors, guides, traps, and chips for atoms," Journal of Physics D: Applied Physics **32**(18), R119–R146 (1999).

[21] A. Einstein, "On a heuristic viewpoint concerning the production and transformation of light," Annalen der Physik **17**, 132–148 (1905).

[22] H. J. Metcalf and P. van der Straten, "Laser cooling and trapping of atoms," Journal of the Optical Society of America B: Optical Physics **20**(5), 887–908 (2003).

[23] H. J. Metcalf and P. van der Straten, *Laser cooling and trapping* (Springer, 1999).

[24] Halliday, Resnick, and Walker, *Fundamentals of Physics,* 6th ed. (Wiley).

[25] J. Dalibard and C. Cohen-Tannoudji, "Laser cooling below the Doppler limit by polarization gradients: simple theoretical models," Journal of the Optical Society of America B: Optical Physics **6**(11), 2023 (1989).

[26] C. J. Foot, *Atomic Physics* (Oxford University Press, 2005).

[27] D. P. Rhodes, "Experimental studies of cold atom guding using hollow light beams," Ph.D. thesis, University of St Andrews (2005).

[28] S. Kraft, A. Deninger, C. Trck, J. Fortgh, F. Lison, and C. Zimmermann, "Rubidium spectroscopy at 778-780 nm with a distributed feedback laser diode," Laser Physics Letters **2**(2), 71–76 (2005).

[29] A. S. Arnold, J. S. Wilson, and M. G. Boshier, "A simple extended-cavity diode laser," Review of Scientific Instruments **69**(3), 1236–1239 (1998).

[30] G. P. T. Lancaster, W. Sibbett, and K. Dholakia, "An extended-cavity diode laser with a circular output beam," Review of Scientific Instruments **71**(10), 3646–3647 (2000).

[31] T. W. Hänsch, “Repetitively Pulsed Tunable Dye Laser for High Resolution Spectroscopy,” Appl. Opt. **11**(4), 895–898 (1972).

[32] D. W. Preston, “Doppler-free saturated absorption: Laser spectroscopy,” American Journal of Physics **64**, 1432–1436 (1996).

[33] G. P. T. Lancaster, “Experimental studies of diode lasers and cold atom guiding,” Ph.D. thesis, University of St Andrews (2001).

[34] E. A. Donley, T. P. Heavner, F. Levi, M. O. Tataw, and S. R. Jefferts, “Double-pass acousto-optic modulator system,” Review of Scientific Instruments **76**(6), 063112 (pages 6) (2005).

[35] C. Wieman, G. Flowers, and S. Gilbert, “Inexpensive laser cooling and trapping experiment for undergraduate laboratories,” American Journal of Physics **63**(4), 317–330 (1995).

[36] S. Kuppens, M. Rauner, M. Schiffer, K. Sengstock, W. Ertmer, F. E. van Dorsselaer, and G. Nienhuis, “Polarization-gradient cooling in a strong doughnut-mode dipole potential,” Phys. Rev. A **58**(4), 3068–3079 (1998).

[37] M. Schiffer, M. Rauner, S. Kuppens, M. Zinner, K. Sengstock, and W. Ertmer, “Guiding, focusing, and cooling of atoms in a strong dipole potential,” Applied Physics B **67**, 705–708 (1998).

[38] D. P. Rhodes, G. P. T. Lancaster, J. Livesey, D. McGloin, J. Arlt, and K. Dholakia, “Guiding a cold atomic beam along a co-propagating and oblique hollow light guide,” Optics Communications **214**, 247–254(8) (15 December 2002).

[39] M. A. Bandres and J. C. Gutiérrez-Vega, “Ince–Gaussian modes of the paraxial wave equation and stable resonators,” Journal of the Optical Society of America A **21**(5), 873–880 (2004).

[40] A. E. Siegman, *Lasers*, chap. 16.4, p. 648 (University Science Books, 1986).

[41] J. Arlt, K. Dholakia, L. Allen, and M. J. Padgett, "The production of multiringed Laguerre-Gaussian modes by computer-generated holograms," Journal of Modern Optics **45**(6), 1231–1237 (1998).

[42] J. Arlt, T. Hitomi, and K. Dholakia, "Atom guiding along Laguerre-Gaussian and Bessel light beams," Applied Physics B **71**(4), 549–554 (2000).

[43] L. Allen, M. W. Beijersbergen, R. J. C. Spreeuw, and J. P. Woerdman, "Orbital angular momentum of light and the transformation of Laguerre-Gaussian laser modes," Physical Review A **45**(11), 8185–8189 (1992).

[44] W. L. Power, L. Allen, M. Babiker, and V. E. Lembessis, "Atomic motion in light beams possessing orbital angular momentum," Physical Review A **52**(1), 479–488 (1995).

[45] D. P. Rhodes, D. M. Gherardi, J. Livesey, D. McGloin, H. Melville, T. Freegarde, and K. Dholakia, "Atom guiding along high order LaguerreGaussian light beams formed by spatial light modulation," Journal of Modern Optics **53**, 547–556 (2006).

[46] W. C. Cheong, W. M. Lee, X.-C. Yuan, L.-S. Zhang, K. Dholakia, and H. Wang, "Direct electron-beam writing of continuous spiral phase plates in negative resist with high power efficiency for optical manipulation," Applied Physics Letters **85**, 5784–+ (2004).

[47] M. A. Clifford, J. Arlt, J. Courtial, and K. Dholakia, "High-order Laguerre-Gaussian laser modes for studies of cold atoms," Optics Communications **156**(4-6), 300–306 (1998).

[48] V. Boyer, R. M. Godun, G. Smirne, D. Cassettari, C. M. Chandrashekar, A. B. Deb, Z. J. Laczik, and C. J. Foot, "Dynamic manipulation of Bose-Einstein condensates with a spatial light modulator," Physical Review A **73**(3), 031402 (2006).

[49] J. G. Livesey, "Atom guding in free-space light beams and photonic crystal fibres," Ph.D. thesis, University of St Andrews (2007).

[50] R. Delhuille, A. Miffre, E. Lavallette, M. Büchner, C. Rizzo, G. Trénec, J. Vigué, H. J. Loesch, and J. P. Gauyacq, "Optimization of a Langmuir–Taylor detector for lithium," Review of Scientific Instruments **73**(6), 2249–2258 (2002).

[51] M. J. Renn, A. A. Zozulya, E. A. Donley, E. A. Cornell, and D. Z. Anderson, "Optical-dipole-force fiber guiding and heating of atoms," Physical Review A **55**(5), 3684–3696 (1997).

[52] H. Ito, K. Sakaki, M. Ohtsu, and W. Jhe, "Evanescent-light guiding of atoms through hollow optical fiber for optically controlled atomic deposition," Applied Physics Letters **70**(19), 2496–2498 (1997).

[53] D. Muller, E. A. Cornell, D. Z. Anderson, and E. R. Abraham, "Guiding laser-cooled atoms in hollow-core fibers," Physical Review A **61**(3), 6 (2000).

[54] H. Ito, T. Nakata, K. Sakaki, M. Ohtsu, K. I. Lee, and W. Jhe, "Laser spectroscopy of atoms guided by evanescent waves in micron-sized hollow optical fibers," Physical Review Letters **76**(24), 4500–4503 (1996).

[55] H. Ito, K. Sakaki, W. Jhe, and M. Ohtsu, "Evanescent-light induced atom-guidance using a hollow optical fiber with light coupled sideways," Optics Communications **141**(1-2), 43–47 (1997).

[56] T. Takekoshi and R. J. Knize, "Optical guiding of atoms through a hollow-core photonic band-gap fiber," Physical Review Letters **98**(21) (2007).

[57] M. D. Scheer and J. Fine, "Kinetics of desorption. III. Rb+ , K+, and Na+ on Rhenium," The Journal of Chemical Physics **39**(7), 1752–1755 (1963).

[58] O. K. Husmann, "Alkali-ion desorption energies on polycrystalline refractory metals at low surface coverage," Phys. Rev. **140**(2A), A546–A551 (1965).

[59] F. Stienkemeier, M. Wewer, F. Meier, and H. O. Lutz, "Langmuir–Taylor surface ionization of alkali (Li, Na, K) and alkaline earth (Ca, Sr, Ba) atoms

attached to helium droplets," Review of Scientific Instruments **71**(9), 3480–3484 (2000).

[60] AMPTEK inc., *Amtektron UHV Model MD-502 Operating Manual*.

[61] I. Gilmore and M. Seah, "Static SIMS: ion detection efficiencies in a channel electron multiplier," Applied Surface Science **144-145**, 113–117 (1999).

[62] M. Krems, J. Zirbel, M. Thomason, and R. D. DuBois, "Channel electron multiplier and channelplate efficiencies for detecting positive ions," Review of Scientific Instruments **76**(9), 093305 (pages 7) (2005).

[63] M. Knobel, P. Allia, C. Gomez-Polo, H. Chiriac, and M. Vazquez, "Joule heating in amorphous metallic wires," Journal of Physics D: Applied Physics **28**(12), 2398–2403 (1995).

[64] R. G. Dall, M. D. Hoogerland, D. Tierney, K. G. H. Baldwin, and S. J. Buckman, "Single-mode hollow optical fibre for atom guiding," Applie Physics B: Lasers and Optics **74**, 11–18 (2002).

[65] D. Pritchard, M. Chapman, T. Hammond, D. Kokorowski, A. Lenef, R. Rubenstein, E. Smith, and J. Schmiedmayer, "Atom Interferometers and Atomic Coherence," Fortschritte der Physik **46**(6-8), 801–808 (1998).

[66] C. C. Gregory and J. A. Harrington, "Attentuation, modal, and polarization properties of n less than 1, hollow dielectric waveguides," Applied Optics **32**(27), 5302 (1993).

[67] F. Luan, A. K. George, T. D. Hedley, G. J. Pearce, D. M. Bird, J. C. Knight, and P. S. J. Russell, "All-solid photonic bandgap fiber," Opt. Lett. **29**(20), 2369–2371 (2004).

[68] G. Bouwmans, F. Luan, J. Knight, P. S. J. Russell, L. Farr, B. Mangan, and H. Sabert, "Properties of a hollow-core photonic bandgap fiber at 850 nm wavelength," Opt. Express **11**(14), 1613–1620 (2003).

[69] J. G. Livesey, D. P. Rhodes, D. McGloin, K. Dholakia, and J. F. Allen, "Transient response of a cold atomic beam in the presence of a far-off resonance light guide," Journal of Modern Optics **50**(11), 1751–1755 (2003).

[70] P. Russell, "Photonic crystal fibers," Science **299**(5605), 358–362 (2003).

[71] R. F. Cregan, B. J. Mangan, J. C. Knight, T. A. Birks, P. S. Russell, P. J. Roberts, and D. C. Allan, "Single-mode photonic band gap guidance of light in air," Science **285**(5433), 1537–1539 (1999).

[72] M. N. Petrovich, F. Poletti, A. van Brakel, and D. J. Richardson, "Robustly single mode hollow core photonic bandgap fiber," Opt. Express **16**(6), 4337–4346 (2008).

[73] T. Pfeifer and M. C. Downer, "Direct experimental observation of periodic intensity modulation along a straight hollow-core optical waveguide," J. Opt. Soc. Am. B **24**(5), 1025–1029 (2007).

[74] W. Klaus and W. R. Leeb, "Transient fields in the input coupling region of optical single-mode waveguides," Opt. Express **15**(19), 11,808–11,826 (2007).

[75] Crystal Fibre A/S, `http://www.crystal-fibre.com`.

[76] J. C. Knight, T. A. Birks, P. S. Russell, and D. M. Atkin, "All-silica single-mode optical fiber with photonic crystal cladding," Optics Letters **21**(19), 1547–1549 (1996).

[77] T. A. Birks, J. C. Knight, and P. S. Russell, "Endlessly single-mode photonic crystal fiber," Optics Letters **22**(13), 961–963 (1997).

[78] J. Knight, T. Birks, R. Cregan, P. Russell, and J.-P. de Sandro, "Large mode area photonic crystal fibre," Electronics Letters **34**(13), 1347–1348 (1998).

[79] N. A. Mortensen, J. R. Folkenberg, M. D. Nielsen, and K. P. Hansen, "Modal cutoff and the V parameter in photonic crystal fibers," Optics Letters **28**(20), 1879–1881 (2003).

[80] B. T. Kuhlmey, R. C. McPhedran, and C. M. de Sterke, "Modal cutoff in microstructured optical fibers," Optics Letters **27**(19), 1684–1686 (2002).

[81] A. Dabirian, M. Akbari, and N. A. Mortensen, "The radiated fields of the fundamental mode of photonic crystal fibers," Optics Express **13**(11), 3999–4004 (2005).

[82] N. A. Mortensen and J. R. Folkenberg, "Near-field to far-field transition of photonic crystal fibers: symmetries and interference phenomena," Optics Express **10**(11), 475–481 (2002).

[83] A. Argyros and I. M. Bassett, "Counting modes in optical fibres with leaky mode," in *Symposium on optical fiber measurements*, p. 135 (Boulder, Colorado, USA, 2002).

[84] A. M. Grassi, F. Casagrande, M. D'Alessandro, and S. Marinoni, "Single-modeness of short large mode area fibers: An experiemental study," Optics Communications **273**(1), 127–132 (2007).

[85] T. Sorensen, J. Broeng, A. Bjarklev, E. Knudsen, and S. E. B. Libori, "Macro-bending loss properties of photonic crystal fibre," Electronics Letters **37**(5), 287–289 (2001).

[86] M. D. Nielsen, N. A. Mortensen, M. Albertsen, J. R. Folkenberg, A. Bjarklev, and D. Bonacinni, "Predicting macrobending loss for large-mode area photonic crystal fibers," Optics Express **12**, 1775 (2004).

[87] A. Witkowska, S. G. Leon-Saval, A. Pham, and T. A. Birks, "All-fiber LP11 mode convertors," Optics Letters **33**(4), 306–308 (2008).

[88] T. Čižmár, V. Garcés-Chávez, K. Dholakia, and P. Zemánek, "Optical conveyor belt for delivery of submicron objects," Applied Physics Letters **86**(17), 174101 (pages 3) (2005).

[89] K. Dholakia, P. Reece, and M. Gu, "Optical micromanipulation," Chemical society reviews **37**, 42–55 (2008).

[90] M.-T. Wei, K.-T. Yang, A. Karmenyan, and A. Chiou, "Three-dimensional optical force field on a Chinese hamster ovary cell in a fiber-optical dual-beam trap," Optics Express **14**(7), 3056–3064 (2006).

[91] P. Jess, V. Garces-Chavez, D. Smith, M. Mazilu, A. Riches, C. S. Herrington, W. Sibbett, and K. Dholakia, "A dual beam fibre trap for Raman microspectroscopy of single cells," Journal of Pathology **210**, 28–28 (2006).

[92] N. K. Metzger, K. Dholakia, and E. M. Wright, "Observation of bistability and hysteresis in optical binding of two dielectric spheres," Physical Review Letters **96**(6) (2006).

[93] J. Guck, R. Ananthakrishnan, T. J. Moon, C. C. Cunningham, and J. Käs, "Optical Deformability of Soft Biological Dielectrics," Physical Review Letters **84**(23), 5451–5454 (2000).

[94] S. Cran-McGreehin, T. F. Krauss, and K. Dholakia, "Integrated monolithic optical manipulation," Lab on a Chip **6**(9), 1122–1124 (2006).

[95] F. U. Gast, P. S. Dittrich, P. Schwille, M. Weigel, M. Mertig, J. Opitz, U. Queitsch, S. Diez, B. Lincoln, F. Wottawah, S. Schinkinger, J. Guck, J. Kas, J. Smolinski, K. Salchert, C. Werner, C. Duschl, M. S. Jager, K. Uhlig, P. Geggier, and S. Howitz, "The microscopy cell (MicCell), a versatile modular flowthrough system for cell biology, biomaterial research, and nanotechnology," Microfluidics and Nanofluidics **2**(1), 21–36 (2006).

[96] B. Lincoln, S. Schinkinger, K. Travis, F. Wottawah, S. Ebert, F. Sauer, and J. Guck, "Reconfigurable microfluidic integration of a dual-beam laser trap with biomedical applications," Biomedical Microdevices **9**(5), 703–710 (2007).

[97] R. B. Liebert and D. C. Prieve, "Force exerted by a laser-beam on a microscopic sphere in water - designing for maximum axial force," Industrial & Engineering Chemistry Research **34**, 3542–3550 (1995).

[98] N. R. Barbeau, "Power deposited by a Gaussian beam on a decentered circular aperture," Applied Optics **34**(28), 6443 (1995).

[99] K. Nielsen, D. Noordegraaf, T. Sorensen, A. Bjarklev, and T. P. Hansen, "Selective filling of photonic crystal fibres," Journal of Optics A - Pure and Applied Optics **7**(8), L13–L20 (2005).

[100] Y. Y. Huang, Y. Xu, and A. Yariv, "Fabrication of functional microstructured optical fibers through a selective-filling technique," Applied Physics Letters **85**(22), 5182–5184 (2004).

[101] J. C. Baggett, T. M. Monro, K. Furusawa, V. Finazzi, and D. J. Richardson, "Understanding bending losses in holey optical fibers," Optics Communications **227**, 317–335 (2003).

[102] K. C. Neuman and S. M. Block, "Optical trapping," Review of Scientific Instruments **75**(9), 2787–2809 (2004).

[103] G. Milne, "Optical Sorting and Manipulation of Microscopic Particles," Ph.D. thesis, University of St Andrews (2007).

[104] N. K. Metzger, E. M. Wright, and K. Dholakia, "Theory and simulation of the bistable behaviour of optically bound particles in the Mie size regime," New Journal of Physics **8**(8), 139 (2006).

[105] W. Singer, M. Frick, S. Bernet, and M. Ritsch-Marte, "Self-organized array of regularly spaced microbeads in a fiber-optical trap," Journal of the Optical Society of America B-Optical Physics **20**(7), 1568–1574 (2003).

[106] V. Karásek, K. Dholakia, and P. Zemánek, "Analysis of optical binding in one dimension," Applied Physics B **84**, 149–156 (2006).

[107] R. Gordon, M. Kawano, J. T. Blakely, and D. Sinton, "Optohydrodynamic theory of particles in a dual-beam optical trap," Physical Review B (Condensed Matter and Materials Physics) **77**(24), 245125 (pages 5) (2008).

[108] P. Zemánek, A. Jonáš, and M. Liška, "Simplified description of optical forces acting on a nanoparticle in the Gaussian standing wave," Journal of the Optical Society of America A: Optics, Image Science, and Vision **19**(5), 1025–1034 (2002).

[109] F. Benabid (Centre for Photonics & Photonic Materials, University of Bath.), Private communication.

[110] J. Guck, R. Ananthakrishnan, H. Mahmood, T. J. Moon, C. C. Cunningham, and J. Kas, "The optical stretcher: A novel laser tool to micromanipulate cells," Biophysical Journal **81**(2), 767–784 (2001).

Thank you.

You’ve read the whole of my thesis.

Reward yourself with an apple.

Go on; you’ve deserved it!

Cheers.

∴